Searches for new physics with leptons and invisible particles at the ATLAS experiment at the LHC

Gabriel Gallardo

St Edmund Hall

University of Oxford

A thesis submitted for the degree of

Doctor of Philosophy

Hilary Term 2021

Abstract

The Standard Model of Particle Physics (SM), while successful at describing almost all subatomic phenomena observed to date, has some glaring open questions: the Higgs boson mass is unstable at high energies, there is no dark matter candidate, and the prediction and measurement of $(g-2)_\mu$ are in tension. Supersymmetric (SUSY) extensions to the Standard Model could provide possible answers to all these problems, and some SUSY particles could be produced at the Large Hadron Collider. This thesis describes three areas of work aimed at finding evidence for SUSY at the ATLAS Experiment of the Large Hadron Collider. First, the performance and development of the ATLAS $E_{\mathrm{T}}^{\mathrm{miss}}$ trigger is discussed. Many theorised SUSY process are predicted to produce events with $E_{\mathrm{T}}^{\mathrm{miss}}$, a large imbalance in the momentum sum of detectable particles, as SUSY particles could escape detection. The $E_{\mathrm{T}}^{\mathrm{miss}}$ trigger aims to select such events during data-taking to be saved to disk for analysis. Next, a search for new physics in events with four or more leptons is described. This search is optimised for certain SUSY models, but is also sensitive to a wide range of beyond-the-Standard-Model (BSM) processes. No significant deviation from the SM is observed. From this observation, limits are set on general gauge-mediated SUSY models, R-parity violating SUSY models, and BSM contributions. Finally, a machine-learning-based strategy is proposed to probe an experimentally challenging but phenomenologically favoured range of SUSY parameters in events with two leptons and $E_{\mathrm{T}}^{\mathrm{miss}}$. The strategy is found to not only be competitive with a more traditional cuts-based strategy, but it also provides the event yields necessary for the measurement of SUSY particle properties.

Acknowledgements

Whenever I count my supporters and friends, I'm always surprised by how many there are. Without the help of these people, this thesis would never have come to be.

Before I thank anyone else on this list, I must thank God for blessing me with this wonderful experience and the friends with whom to share it. I have grown so much all thanks to his loving care.

"It takes a village" I must thank my family: my parents Robi and Let, and my sister Mika. Our household is a loving and supportive household. I felt you had my back as I stepped out and followed my dreams. I thank also my extended family, especially my paternal grandmother Blanche, Tita Cara and Uncle David, Tita Marita and Uncle Jim, and my cousins Ayden and Teresa. Your unconditional support and care means so much to me. I am also grateful for the prayers of my family in heaven: my siblings Rachel and Joshua, my maternal grandparents Lolo Marcelo and Lola Naty, and my paternal grandfather "Grumpy" Bert. I hope I've made you proud.

I relied so much on the support and prayers of the communities in which I grew up, particularly those of the BLD Community and St. Teresa's Parish in Hong Kong.

I thank teachers from my school days for their mentorship and their faith in me, especially Moses Tsang, Grace Mak, Chris Lau, Ming Lee, Ken Yiu, and Nancy Chung. I thank William, Bryan, Matthew, Hugo, and Yau for their friendship throughout school and beyond.

I'm grateful for the formation by my university lecturers, particularly M.K. Yip, C.C. Ling, K.M. Lee, X.D. Cui, W. Yao, and Judy Chow. It was wonderful to learn physics with Juno, Enoch, Sandy, and Amruth.

My love of particle physics was kindled by my early mentors Dongliang Zhang, Jeanette Lorenz, Nicola Orlando, and Junjie Zhu. Special thanks to Prof. Yanjun Tu because, while raising two newborns and founding the experimental particle physics group at The University of Hong Kong, she took the time to supervise my Bachelor's thesis and continued to supervise me as her research assistant after my graduation.

Maybe the real D.Phil. was the friends we made along the way I am so thankful for the companionship of my friends. You give me so much support.

I'm grateful for my physics friends from my pre-PhD days: Bradley Dice, Nina Coyle, Alex Brown, Kaustuv Datta, Lau Tak Shun, and Jacky.

While in Geneva, I was blessed by the MFC community. I'm so grateful that I met Emz, Anne, Kristine, AC, Lorenz, Paps, Chiara, and Gelo; Mark, Faith, Cynthia and the Delfin family; Bimbo and Claire, and their children Raeven, China, Sam, and Aaron. Particularly heartfelt thanks go out to the Colina family: Jake and Hydee, and their children Jacques and Julien. You welcomed me into your family and made me feel at home.

I thank the parish of St. John XXIII, particularly Fr. Paul, and members of the 11:30 am choir: Jill, Ken, Albert, Sharmilla, Larry, Eden, Mary.

I also thank the friends I made at CERN for accompanying me on the PhD journey: Elliot, Yvonne, Jay, Melissa, Matt, Neil, Meirin, Dani, Rupert, jess, Tom, Jake, Candice, Riccardo, Marc, Adrian, and Malte.

I'm grateful to the Oxford Particle Physics department for the warmth with which it welcomed me and the friends I made there: Jonas, Ynyr, Eimear, Aaron, Ludo, Miglė, Maria Giovanna, Martina, Ewan, Josh, Lawrence, Alex Goldsack, Jon, Jesse, Santiago, Mikkel, Jason and Jordan, Michael, Hayden, James, Frederico, Kamil, Siyuan, and Iza. I thank also the academics, especially Todd, Farrukh, Claire, Daniela, and Ian for keeping an eye on us.

At Teddy Hall, my time was wonderfully spent with Jae and Won, my dudez Yusuf, James, Reza, Licio and his wife Isabella. Special thanks to Hannah Markay for inspiring me by your kindness and your altruism.

The Oxford University Catholic Chaplaincy supported me greatly both spiritually and socially. Thanks so much to the chaplains Fr. Matthew, Fr. Nick, Fr. Ian, Fr. Keith, Alvea, and Becky; to members of the 9pm choir Megan, Mitch, John, Matthew, and Claire; to the God in the Quad group Colin, Claudia, Joanna, and Rasa; to my fellow postgrads Josh, Anna, Katy, Riccardo, Rasa, and Christopher; and specially to Catherine Fleischer, Lucia Švecová, and James Sinclair.

Living at Grandpont House was among the highlights of my D.Phil. Many thanks to all those who helped make my stay an enjoyable one: Fr. Andrew, Jim, Xavier, Bas, Paul, Victor, Alvaro, Fr. Ramon, Fr. Joseph, Sam, Bakht, Jaime, Chema, Luis, Giuseppe, Peter B, Peter T, Diego, and Maarten. I could always count on your support. A special shout-out to our cook, Carla, for making such wonderful meals.

There are some friends who have always been there and will be no matter what. David, Justin, Joycelyn, Nanor, Ericka, Jess, Christopher, Anna and Clement, Ashley,

Fernanda, Benjamin: I am so grateful that you have always been just a phone call away. Your love means the world to me.

"If I have seen further it is by standing on the shoulders of giants" I'm thankful to those who have mentored me professionally in one way or another: Stefania Xella, Jiri Masik, Catrin Bernius, Stewart Martin-Haugh, Sarah Williams, Jeff Dandoy, Mike Hance, Zach Marshall, Federico Meloni, Laura Jeanty, T.J. Khoo, Chris Pollard, Steven Schramm, Rosa Simoniello, Will Kalderon, Will Fawcett, Larry Lee Jr., Claudia Merlassino, and Bill Balunas. Thank you for the engaging discussions, nuggets of wisdom, fun stories, and kind encouragement.

I thank the Oxford Particle Physics admin team Sue Geddes, Kim Proudfoot, and Jennifer Matthews for helping me get through all the bureaucratic red tape. I never had to worry about any of it.

I thank my colleagues: fellow MET trigger enthusiasts Kenji, Renjie, Moritz, Antonia, Manfredi, Allen, Ben, and Ava; two-leptoners Sonia, Margherita, Jordi, Daniel, Francesco, Eric; and four-leptoners Marian and Daniel. Particular thanks to Johannes Junggeburth who inspired me by the speed, clarity and dedication in his work. Extra special thanks to the magnificent Tina Potter, whose warmth, skill, and leadership I will never forget.

Thank you to my examiners Jeff Tseng and Simon George for taking the time to make sure I did a good job.

My studies would not have been possible without the generous financial support of the Oxford-CS Wu Scholarship, the Oxford University Sub-department of Particle Physics, the Science and Technology Facilities Council, and all the contributors to ATLAS and CERN.

"If you want to go fast, go alone. If you want to go far, go together." "You're an independent researcher now. You're your own boss." is one of the first things my supervisor, Alan Barr, said to me (and still says to me whenever I ask him for help). I thank him for his faith in me and respect for me as a researcher. He taught and inspired me to think through my problems myself, but was never too far away if ever I needed his guidance.

I thank Angelica Tong for being a kind, steady, and faithful companion; you have seen me at my worst and have always accepted me.

I thank Carol Mak, my D.Phil. buddy, my rock, my home-away-from-home, my fellow sojourner in faith, for being a dear friend to whom I could always turn.

Preface

Chapter 1 introduces the work of this thesis, while Chapters 2 and 3 are dedicated to describing the theory and experimental methods respectively that form the basis for the work described in this thesis.

The remaining three major chapters describe work I did with the ATLAS Experiment, which consists of more than 3000 active authors. The contributions to the experiment which are wholly or largely my own are highlighted below. In this thesis, any figure or table taken from other sources or produced by collaborators will be noted as such in the caption. Figures which have been approved by ATLAS for publication in peer-reviewed journals (conference notes) have the label "**ATLAS**" ("**ATLAS** Preliminary") in the figure.

$E_{\mathbf{T}}^{\mathbf{miss}}$ Trigger This chapter describes work I did as one of the main contributors to the ATLAS $E_{\mathrm{T}}^{\mathrm{miss}}$ trigger. I was a junior member of the team from Oct 2017 to Jul 2018, and then served as their software coordinator for two years, from Aug 2018 to Jul 2020. During my tenure in the group, I shouldered the following responsibilities:

- I analysed the performance of the $E_{\mathrm{T}}^{\mathrm{miss}}$ trigger algorithms on ATLAS Run-2 data. For this, I produced data samples required for the studies, wrote part of the analysis software, and frequently discussed my findings with collaborators. The corresponding section in this thesis consists of work that is largely or wholly my own. My work, together with that of collaborators, has been published in the *Journal of High Energy Physics* [1].

- I completely rewrote the $E_{\mathrm{T}}^{\mathrm{miss}}$ trigger software. This was part of an experiment-wide initiative to migrate to a new software framework called AthenaMT. I took advantage of this opportunity to rewrite the $E_{\mathrm{T}}^{\mathrm{miss}}$ trigger software to be more readable and easier to maintain. This work, from conception to implementation, and documented in this thesis, was almost entirely my own, with some assistance from senior members of the ATLAS $E_{\mathrm{T}}^{\mathrm{miss}}$ trigger and ATLAS trigger groups. Further improvements the $E_{\mathrm{T}}^{\mathrm{miss}}$ trigger software were later implemented on the basis of my work.

- I led the development and optimisation of the `pufitjet` algorithm. This involved, again, producing samples, writing analysis software, and discussing findings with collaborators. Documented in this thesis are my own studies, which together with additional studies by collaborators, inform the experiment on the suitability of the algorithm's use in ATLAS data-taking from 2022 onwards.

Searching for new physics in final states with four leptons This chapter describes an analysis in which I was one of the lead analysers. My main contributions include the following:

- I developed the analysis strategy by designing and optimising signal regions. This mainly involved testing the effect of different variables on the sensitivity of the analysis. The variables I considered include m_{eff}, $E_{\text{T}}^{\text{miss}}$, and the quality and number of physics objects (jets, b-jets, tau leptons, and light leptons). I also considered how our sensitivity was impacted by the magnitude of experimental uncertainties. All this work, largely mine, is described in the relevant section of this thesis.

- I validated our datasets in distributions of key variables for unexpected features, such as unexplained excesses, deficits, or shapes, and inconsistencies in modelling. I reported my findings to my collaborators, and in some cases helped track down and mitigate the source(s) of the errant behaviour. This work is not documented explicitly in this thesis.

I am indebted to my collaborators for other key parts of the analysis, including background estimation, uncertainty evaluation, statistical interpretation, and analysis preservation. They were also responsible for writing the majority of the analysis software. Their contributions are included in this thesis for completeness.

The work described in this chapter was presented at the 2020 International Conference on High Energy Physics [2], and in my poster at the 2020 International Conference on Particle Physics and Astrophysics [3]. A paper based on this work has been thoroughly reviewed by the ATLAS Collaboration and has been submitted to the *Journal of High Energy Physics* [4].

Searching for SUSY in final states with two leptons The final analysis chapter is dedicated to a machine-learning-based method I developed to extend the searches described in Refs. [5, 6]. This involved the following:

- I produced simulated signal samples. To do this, I simulated physics processes with MadGraph-based simulation software from ATLAS, and I simulated the detector's response with an analysis class I wrote for the ATLAS-internal `SimpleAnalysis` framework [7].
- I selected a machine-learning classifier, and optimised its sensitivity to the targeted signal models by selecting input variables and tuning hyper-parameters. This was done jointly with a collaborator.
- I designed candidate signal regions based on the classifier output and evaluated the sensitivities of the regions.
- I developed the analysis software needed to train, apply, and optimise the classifier, and to produce results in the form of tables and plots.
- I compared my machine-learning approach to a traditional cuts-based approach developed by my collaborators.

Analysis collaborators were responsible for producing samples of real and simulated data used in my studies. They were also responsible for developing the traditional cuts-based approach and the data-driven background estimation methods. Their work is described in the relevant parts of this thesis for completeness.

Contents

1 Introduction

Where did we come from? Why are we here? How did the universe come to be? Why is the universe the way it is? Humankind has been asking these questions for millennia. In this thesis, the author attempts to answer them from the perspective of fundamental particle physics. The big idea is this: if we know what the fundamental constituents of the universe are and how they interact, then we could possibly dial back the clock to see how it all began, or dial the clock forward to see how it would all evolve and end.

First, the story so far is recapped in Chapter 2. Our current best understanding of fundamental particle physics is the Standard Model of Particle Physics. Its key features are reviewed, and where it still falls short is highlighted. Supersymmetry is introduced as a possible extension to the Standard Model, then there is discussion of how it solves the Standard Model's open problems and how one might search for evidence to support it.

Next, Chapter 3 describes ambitious undertakings aimed at testing our understanding of fundamental physics like never before — the Large Hadron Collider and the ATLAS Experiment. The Large Hadron Collider is the world's largest machine; it accelerates protons to near the speed of light and crashes them into each other. ATLAS studies the debris of these collisions events to measure the parameters of

the Standard Model to great precision and to search for evidence of "new" beyond-the-Standard-Model physics.

The original work in this thesis is concerned with (a) the performance of and improvements to ATLAS and (b) using data collected by ATLAS to search for new physics. This work is described in the chapters to follow.

A key ATLAS subsystem is discussed in Chapter 4. This system selects proton-proton collision events which have large momentum imbalance to be saved to disk at the time of data-taking for later analysis. This momentum imbalance is known as $E_{\mathrm{T}}^{\mathrm{miss}}$. The $E_{\mathrm{T}}^{\mathrm{miss}}$ trigger is essential to the ATLAS physics program as many theorised beyond-the-Standard-Model processes give rise to events which have the signature of $E_{\mathrm{T}}^{\mathrm{miss}}$. Described in this chapter are original efforts by the author to characterise the performance of the $E_{\mathrm{T}}^{\mathrm{miss}}$ trigger, and to prepare it for future data-taking runs.

Chapter 5 describes an effort to search for new physics which produces, in the final state, four Standard Model particles known as leptons. The author was responsible for the optimisation of this analysis to be sensitive to certain supersymmetric models. The results of this search greatly extended previous limits on supersymmetric and non-supersymmetric new physics.

In Chapter 6, a machine-learning-based strategy is proposed to search for strategic but unprobed supersymmetric models. The strategy, which is interested in final states with two leptons and $E_{\mathrm{T}}^{\mathrm{miss}}$, has the potential to probe parameter space favoured by experimental observations in tension with the Standard Model.

Finally, the thesis is summarised in Chapter 7.

2 Theory

The worldview of particle physics is that the universe is made up of indivisible, fundamental particles. The dynamics and evolution of our macroscopic universe is governed by the interactions between these particles.

This chapter aims to provide a brief overview of the particle theory underlying and motivating the experiments described in later chapters. It is based heavily on Refs. [8, 9].

We first review some core concepts in Section 2.1. Section 2.2 introduces the prominent theory which describes fundamental matter and its interactions — the *Standard Model* (SM). The SM is not without its problems, leading to the proposal of a class of theories known as *supersymmetry* (SUSY), which are introduced in Section 2.3.

2.1 Core concepts

This thesis uses natural and Heaviside-Lorentz units, that is

$$\hbar = c = \epsilon_0 = \mu_0 = 1, \text{ and } \hbar c = 197\,\text{MeV fm}. \tag{2.1}$$

The probability of particle interactions is quantified by the *cross section* σ [8]:

$$\sigma = \frac{\text{number of interactions per unit time per target particle}}{\text{incident flux}}. \tag{2.2}$$

To illustrate the factors which influence the cross section, let us consider a two-body to two-body scattering process in the centre-of-mass frame: the cross section of this process is dependent on the momenta of the initial and final state particles p_i and p_f, the centre-of-mass energy $\sqrt{s}$, and the matrix element $\mathcal{M}_{fi}$ integrated over the solid angle $d\Omega$ [8]:

$$\sigma = \frac{1}{64\pi^2 s}\frac{p_f}{p_i}\int |\mathcal{M}_{fi}|^2 d\Omega. \tag{2.3}$$

The Lorentz-invariant matrix element $\mathcal{M}_{fi}$ contains the interesting physics. It is often useful to write $\mathcal{M}_{fi}$ as a perturbative expansion: for initial and final states $|i\rangle$ and $|j\rangle$, which can each contain any number of particles, $\mathcal{M}_{fi}$ is proportional to

$$\mathcal{M}_{fi} \propto \langle f|\hat{H}|i\rangle + \sum_{j\neq i}\frac{\langle f|\hat{H}|j\rangle\langle j|\hat{H}|i\rangle}{E_i - E_j} + ..., \tag{2.4}$$

where $\hat{H}$ is the interaction Hamiltonian, and the ellipses are higher order perturbations.

In order to find the matrix element for a process, we consider the *Lagrangian density* $\mathcal{L}[\Psi, \partial_\mu \Psi]$ (referred to simply as *Lagrangian* for simplicity) of the system. The Lagrangian is a functional of quantum fields and their spacetime derivatives. Fundamental particles are excitations of their corresponding quantum fields, therefore their properties and interactions are governed by the corresponding terms in the Lagrangian. An example of a Lagrangian, the Standard Model Langrangian, is shown in Eq. 2.22 later in this chapter. $\mathcal{L}$ is integrated over spacetime to give the action S [10]:

$$S = \int \mathcal{L}\, d^4x. \tag{2.5}$$

The Euler-Lagrange equations of motion, which describe the propagation and interactions of quantum fields and their particle excitations, are derived by requiring $\delta S = 0$. Such a derivation gives the *Feynman rules*, which are used to compute $\mathcal{M}_{fi}$ [10].

It is often convenient to represent particle interactions as *Feynman diagrams*. Each line and vertex in a diagram corresponds to a factor in the corresponding contribution to $\mathcal{M}_{fi}$. Figure 2.1 shows an example of a possible interaction in the Standard Model, where the electron field interacts with the photon field.

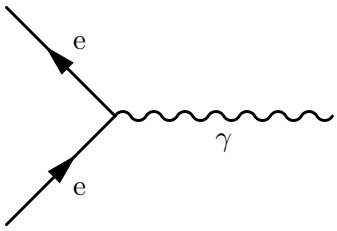

Figure 2.1: An example interaction between the electron and photon fields

2.2 The Standard Model

The Standard Model of particle physics is composed of three kinds of fundamental particles: spin-$\frac{1}{2}$ fermions, spin-1 vector bosons, and a spin-0 scalar boson. The particles are excitations of quantum fields. Particles interact because their respective fields interact. The fermions make up matter, and the vector bosons mediate the interactions between fermions. The *Higgs mechanism* is responsible for fermion masses, and for the eponymous scalar boson.

The Standard Model has been experimentally tested to high precision. For example, the cross sections measurements of various Standard Model production processes by the ATLAS experiment have been observed to agree well with theoretical predictions (Figure 2.2).

This section is heavily based on Refs. [8], and draws inspiration from the treatment in Ref. [12]. Additional references are taken from Refs. [10, 13, 14].

2.2.1 Particle content

The particles which make up the Standard Model (Figure 2.3) are organised as follows. There are twelve fermions in the Standard Model: six quarks and six leptons, all with spin $\frac{1}{2}$. The quarks are organised into three pairs, or generations, with each generation increasing in mass. Each generation of quarks has an up-type quark (with electric charge $Q = \frac{2}{3}$) and a down-type quark ($Q = -\frac{1}{3}$). The leptons are also organised into three generations, each generation of leptons has a charged lepton ($Q = -1$)

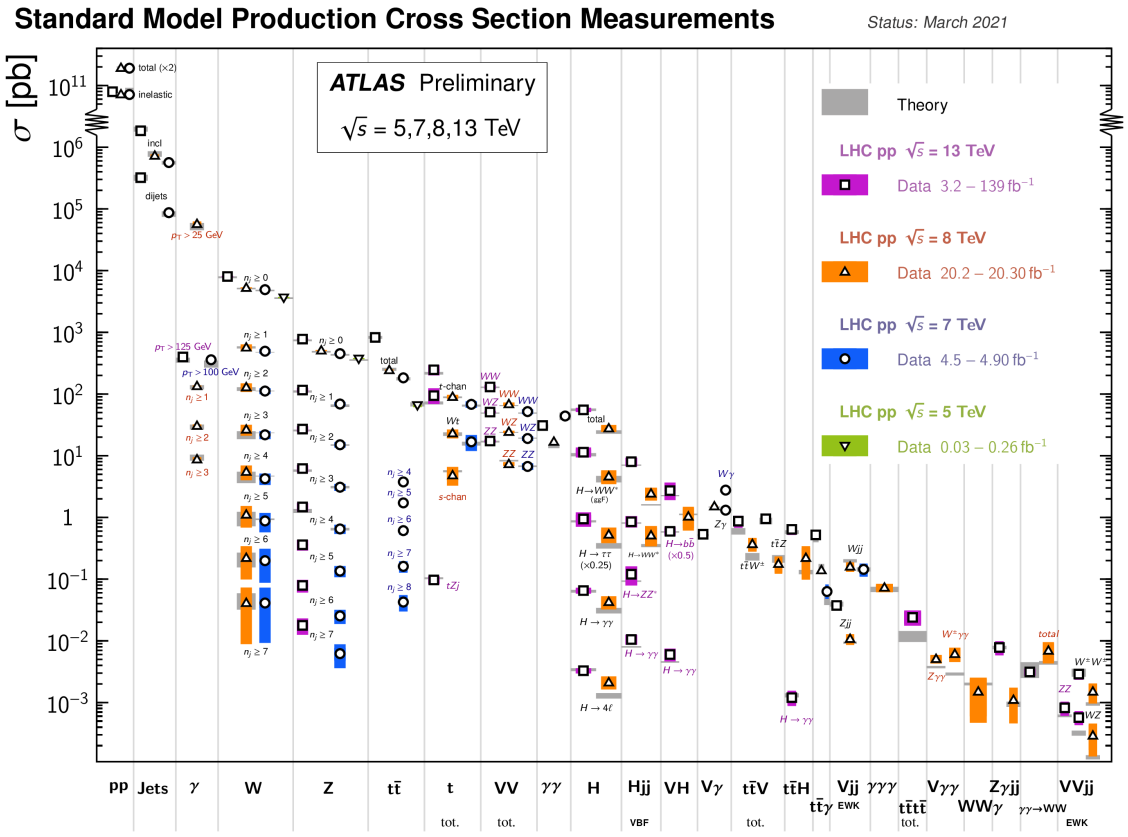

Figure 2.2: Summary of Standard Model production cross sections measured by the ATLAS Experiment. Reproduced from Ref. [11].

and an electrically neutral neutrino. For each particle in the Standard Model, there exists an antiparticle with opposite charge.

The Standard Model describes three of the four fundamental forces as exchanges of four spin-1 bosons:

- The *electromagnetic* force is experienced by all particles with electric charge, including all quarks and charged leptons; it is mediated by the electrically-neutral and massless photon.

- The *strong* force is responsible for binding together the proton, neutron, and atom. It is experienced by particles with colour: quarks can take on one of three

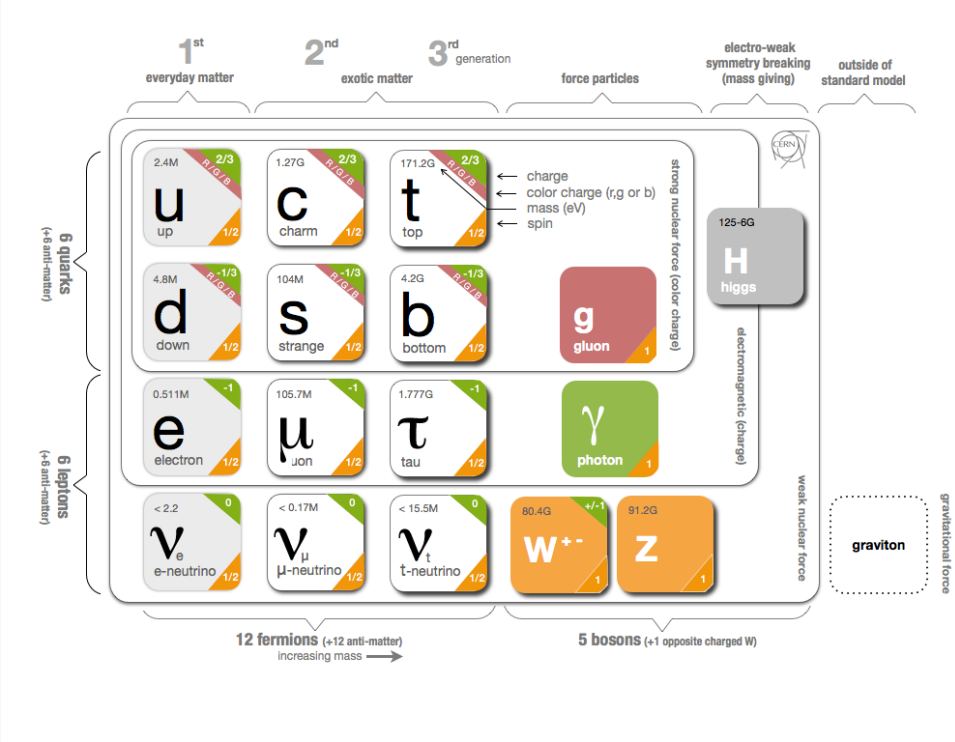

Figure 2.3: The particle content of the Standard Model. Particles' masses, charges, and spins are listed. Taken from Ref. [15].

colours, anti-quarks take on one of three anti-colours. It is mediated by the electrically-neutral and massless gluon, which can take on one of eight colours.

- The *weak* force is responsible for nuclear decay. The charged weak current is experienced by left-chiral particles and right-chiral anti-particles, while the neutral weak current is experienced by all fermions. It is mediated by the charged $W^{\pm}$ bosons and neutral and Z bosons; the weak bosons are massive.

The *gravitational* force is not described in the Standard Model, and is insignificant at the distance and energy scales concerned in this thesis.[1] There exist theories of quantum gravity; they hypothesise gravity is mediated by a massless spin-2 boson known as the *graviton* [16]. See Ref. [17] for further discussion.

[1] As an example, the electric force between two stationary electrons is $\sim 10^{43}$ times stronger than their gravitational attraction.

Finally, the spin-0 Higgs boson is the excitation of the Higgs field. The Higgs field is responsible for mixing the electromagnetic and weak forces into one — the electroweak force. It is also responsible for giving fermions (except perhaps neutrinos) non-zero masses [18–21].

2.2.2 Formalism

The Standard Model is a quantum field theory which combines Poincaré symmetry and symmetry under the Standard Model gauge group $SU(3)_c \times SU(2)_L \times U(1)_Y$, along with the Higgs mechanism to explain the structure of forces and matter. The Standard Model Lagrangian is assembled from the terms

$$\mathcal{L} = \mathcal{L}_{\text{Dirac,kinetic}} + \mathcal{L}_{\text{Yang-Mills}} + \mathcal{L}_{\text{Higgs}} + \mathcal{L}_{\text{Yukawa}}, \tag{2.6}$$

which are explained below.

Poincaré symmetry and admissible field representations The Poincaré group enforces symmetries under Lorentz boosts, rotations in space, and translations in spacetime. As a result, vector fields can be written as $A_\mu(x)$, and scalar fields as $\phi(x)$. Fermion fields are written as spinors $\psi(x)$ and $\overline{\psi} = \psi^\dagger\gamma^0$, which are solutions to the Dirac equation given by

$$\mathcal{L}_{\text{Dirac,free}} = \overline{\psi}(i\gamma^\mu\partial_\mu - m)\psi \tag{2.7}$$

The four Dirac gamma matrices γ^μ enforce Lorentz symmetry. They are defined by $\{\gamma^\mu, \gamma^\mu\} = 2\eta^{\mu\nu}$, where $\eta^{\mu\nu}$ is the Minkowski metric.

Gauge symmetries and forces The requirement of gauge symmetry allows for the descriptions of forces [22]. To illustrate, consider the electromagnetic interaction: it is described by requiring the Dirac equation to obey a $U(1)_{\text{EM}}$ symmetry, which has a vector field A_μ associated to it. For a local transformation by phase $\chi =$

$\chi(x)$, $\psi \to \psi' = e^{-iq\chi}\psi$ and $A_\mu \to A'_\mu = A_\mu - \partial_\mu\chi$. Invariance of the kinetic term in the Dirac equation is maintained by replacing the derivative with the covariant derivative $\partial_\mu \to D_\mu = \partial_\mu - iqA_\mu$:

$$\mathcal{L}_{\text{Dirac,kinetic}} = i\overline{\psi}\gamma^\mu D_\mu\psi \qquad \text{for a general } D_\mu, \tag{2.8}$$

$$= i\overline{\psi}\gamma^\mu(\partial_\mu - iqA_\mu)\psi \qquad \text{for } U(1)_{EM} \text{ symmetry.} \tag{2.9}$$

Applying the $U(1)$ gauge transformation we have

$$\begin{aligned}\mathcal{L}_{\text{Dirac,kinetic}} \to \mathcal{L}'_{\text{Dirac,kinetic}} &= i\overline{(e^{-iq\chi}\psi)}\gamma^\mu(\partial_\mu - iq(A_\mu - \partial_\mu\chi))(e^{-iq\chi}\psi) \\ &= i\overline{\psi}\gamma^\mu e^{iq\chi}e^{-iq\chi}(-iq\partial_\mu\chi + \partial_\mu - iq(A_\mu - \partial_\mu\chi))\psi \\ &= i\overline{\psi}\gamma^\mu(\partial_\mu - iqA_\mu)\psi = \mathcal{L}_{\text{Dirac,kinetic}}.\end{aligned} \tag{2.10}$$

The new term proportional to $q\overline{\psi}A_\mu\psi$ corresponds to fermion interactions with the photon (Figure 2.1), and q is the electric charge of the fermion.

This technique is generalised to the Standard Model gauge group $SU(3)_c \times SU(2)_L \times U(1)_Y$: the strong force is described by the $SU(3)_c$ group, and the electroweak interactions are unified under the $SU(2)_L \times U(1)_Y$ group. The strong force has charges known as *colour* (hence the subscript c) and is mediated by 8 massless vector fields $G_\mu^{i\in\{1\ldots8\}}$. The charges of the electroweak interactions are weak isospin I_W and weak hypercharge Y. The $SU(2)$ fields $W_\mu^{(1)}, W_\mu^{(2)}, W_\mu^{(3)}$ and the $U(1)_Y$ field B_μ are mixed into the physical mediators of charged current $W_\mu^\pm$ and neutral current Z_μ and A_μ by:

$$\begin{aligned} W_\mu^\pm &= \frac{1}{\sqrt{2}}(W_\mu^{(1)} \mp iW_\mu^{(2)}) \\ \begin{pmatrix} A_\mu \\ Z_\mu \end{pmatrix} &= \begin{pmatrix} \cos\theta_W & \sin\theta_W \\ -\sin\theta_W & \cos\theta_W \end{pmatrix} \begin{pmatrix} B_\mu \\ W_\mu^{(3)} \end{pmatrix}, \end{aligned} \tag{2.11}$$

where θ_W is the weak mixing angle. Since the weak charged current is only experienced by left-handed particles (hence the subscript L), fields are organised into the weak isospin representation: the left-handed fields have $I_W = \frac{1}{2}$ and are written as weak isospin doublets [the upper (lower) components have third component of weak isospin $I_W^{(3)} = +\frac{1}{2}(-\frac{1}{2})$], and the right-handed fields, with $I_W = 0$, are written as singlets. The

electric charge is recovered from the weak hypercharge and the third component of weak isospin by

$$Q = \frac{1}{2}Y + I_W^{(3)}. \tag{2.12}$$

We can now write the full covariant derivative:

$$D_\mu = \partial_\mu - \frac{i}{2}g'YB_\mu - \frac{i}{2}g_W I_W \sigma^i W_\mu^i - \frac{i}{2}g_s S\lambda^a G_\mu^a, \tag{2.13}$$

where g', g_W, and g_s are the coupling constants of the $U(1)_Y$, $SU(2)_L$ and $SU(3)_c$ groups; $\frac{1}{2}$-times the Pauli matrices σ^i are the generators of the $SU(2)_L$ group, $\frac{1}{2}$-times the Gell-Mann matrices λ^a are the generators of the $SU(3)_c$ group, and $S = 1(0)$ for quarks (leptons). We can also write the kinetic terms of the vector fields:

$$\mathcal{L}_{\text{Yang-Mills}} = -\frac{1}{4}F^{\mu\nu}F_{\mu\nu}, \text{ where } iF^{\mu\nu} = [D^\mu, D^\nu]. \tag{2.14}$$

These terms describe the propagation of the vector bosons. For the non-Abelian groups $SU(3)$ and $SU(2)$, they also includes terms which describe interactions between bosons.

The fermion and vector fields in the Standard Model are summarised in Tables 2.1 and 2.2 respectively.

The Higgs mechanism The W and Z bosons are observed to have masses, but their explicit mass terms are not gauge invariant (Eq. 2.15). Additionally the fermion mass term requires the mixing of left-chiral doublet fields and right-chiral singlet fields (Eq. 2.16).

$$\mathcal{L} \supset \frac{1}{2}m_A^2 A^\mu A_\mu \qquad \text{is not invariant under } SU(2)_L \times U(1)_Y \tag{2.15}$$

$$\mathcal{L} \supset m_f\overline{\psi}\psi = m_f(\overline{\psi}_L\psi_R + \overline{\psi}_R\psi_L) \quad \text{mixes weak-isospin doublets and singlets} \tag{2.16}$$

Moreover, an explanation is needed for why the $SU(2)_L \times U(1)_Y$ symmetry is broken into the weak force and the $U(1)_{EM}$ symmetry which describes the electromagnetic forces. These are all accomplished by the *Higgs mechanism*.

Particles	Fields	Y	$I_W^{(3)}$
Leptons	$\begin{pmatrix}\nu_e\\e^-\end{pmatrix}_L, \begin{pmatrix}\nu_\mu\\\mu^-\end{pmatrix}_L, \begin{pmatrix}\nu_\tau\\\tau^-\end{pmatrix}_L$	-1	$\begin{pmatrix}+\frac{1}{2}\\-\frac{1}{2}\end{pmatrix}$
	e_R^-, μ_R^-, τ_R^-	-2	0
Quarks (×3 colours)	$\begin{pmatrix}u\\d'\end{pmatrix}_L, \begin{pmatrix}c\\s'\end{pmatrix}_L, \begin{pmatrix}t\\b'\end{pmatrix}_L$	$+\frac{1}{3}$	$\begin{pmatrix}+\frac{1}{2}\\-\frac{1}{2}\end{pmatrix}$
	u_R, c_R, t_R	$+\frac{4}{3}$	0
	d_R, s_R, b_R	$-\frac{2}{3}$	0

Table 2.1: The Standard Model fermion fields in the weak isospin representation. The left-handed fields have weak isospin $I_W = \frac{1}{2}$ and are written as doublets; the right-handed fields have $I_W = 0$ and are written as singlets. Quarks can take on a superposition of three colours; the colour quantum number is not expressed in the table. The left-handed down-quark type fields are written as flavour eigenstates (d'_L, s'_L, b'_L), which are mixed to the mass eigenstates (d_L, s_L, b_L) by the Cabbibo-Kobayashi-Maskawa matrix.

Interaction	Symmetry	Fields
Strong	$SU(3)$	Gluons $G_\mu^{i\in\{1\ldots8\}}$
Electroweak	$SU(2)_L \times U(1)_Y$	Weak bosons $W_\mu^{(1),(2),(3)}$ Hypercharge boson B_μ

Table 2.2: The Standard Model vector fields. The electroweak bosons are mixed into the physical $W^\pm$, Z bosons and the photon by Eq. 2.11.

The Higgs mechanism gives masses to vector bosons and fermions, and explains electroweak symmetry breaking by introducing new scalar fields. The scalar fields are required to have a non-zero vacuum energy and to interact with the fermion and vector fields. This allows the terms above to appear in the vacuum state while the Lagrangian remains invariant under $SU(2)_L \times U(1)_Y$.

In the Standard Model, the Higgs mechanism involves a weak isospin doublet complex scalar field

$$\phi = \begin{pmatrix}\phi^+\\\phi^0\end{pmatrix} \tag{2.17}$$

which is subject to the potential $V(\phi) = \mu^2\phi^\dagger\phi + \lambda(\phi^\dagger\phi)^2$ with $\mu^2 < 0$ and $\lambda > 0$. Expanding ϕ about the minimum of the potential and writing in the gauge $\phi^+ = \mathrm{Im}(\phi^0) = 0$ gives

$$\phi(x) = \frac{1}{\sqrt{2}}\begin{pmatrix} 0 \\ v + h(x) \end{pmatrix}, \tag{2.18}$$

where v is the non-zero vacuum expectation value (vev) of the ϕ^0 field and the h field corresponds to the physical $m \simeq 125\,\mathrm{GeV}$ Higgs boson. In the kinetic term $|D_\mu\phi|^2$, interaction of the $SU(2)_L \times U(1)_Y$ bosons with the Higgs vev gives masses to the $W^\pm$ and Z bosons while leaving the photon massless. The Lagrangian containing the potential and kinetic Higgs terms is

$$\mathcal{L}_{\mathrm{Higgs}} = |D_\mu\phi|^2 - \mu^2\phi^\dagger\phi - \lambda(\phi^\dagger\phi)^2. \tag{2.19}$$

Finally, the strength of the interaction between the fermion fields and the Higgs field is parametrised by the Yukawa couplings y_f, giving Lagrangian terms of the form:

$$\mathcal{L}_{\mathrm{Yukawa}} \supset y_f\overline{\psi}_f\phi\psi_f, \tag{2.20}$$

which is related to the fermion masses by

$$y_f = \sqrt{2}\frac{m_f}{v}. \tag{2.21}$$

We note that flavour mixing in the quark sector occurs because the flavour eigenstates differ from the mass eigenstates. This is described by the Cabbibo-Kobayashi-Maskawa matrix, which corresponds to a non-diagonal mass matrix in the flavour basis [14, 23–25].

Summing together all the components above, the Standard Model Lagrangian (with generational, Lorentz, colour, and flavour indicies suppressed for clarity) reads:

$$\mathcal{L} = -\frac{1}{4}F^2 + \overline{\psi}\gamma D\psi + |D\phi|^2 - V(\phi) + y\overline{\psi}\phi\psi. \tag{2.22}$$

2.2.3 Open problems

While the Standard Model has been successful in describing most particle phenomena to date, there still exist gaps in the Standard Model. A few of them are outlined below.

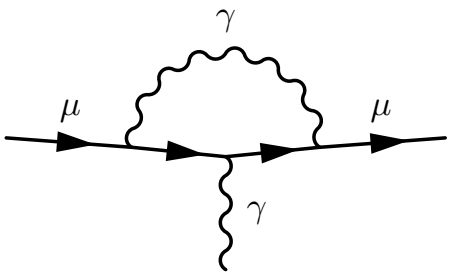

Figure 2.4: A basic Feynman diagram which contributes to the muon anomalous magnetic moment. In practice one has to account for more complicated diagrams with higher-order interactions.

Dark matter The observed amount and distribution of luminous matter in galaxies is insufficient to explain various astronomical observations, such as the gravitational lensing of distant sources [26], the dynamics of galactic collisions [27], and the behaviour of galactic rotation curves [28, 29]. These observations may be explained by the existence of *dark matter*, which may be composed of some massive particle with no electric charge [30], and which accounts for 26.4% of the critical density of the universe according to the ΛCDM cosmological model [25]. Dark matter is not described at all by the Standard Model. It must at least interact via gravity, but otherwise should rarely interact with Standard Model particles [30, 31].

Muon anomalous magnetic moment The muon magnetic moment g_μ is predicted by the Dirac equation to be $g_\mu = 2$. However when considering quantum loop effects (like one shown in Figure 2.4), a slight deviation from 2 is expected; this is parametrised by the muon's anomalous magnetic moment a_μ [25], defined

$$a_\mu = \frac{g_\mu - 2}{2}. \tag{2.23}$$

Currently the world-leading theoretical calculations [25] and the latest experimental result [32] are in 3.3σ tension (uncertainties have been summed in quadrature

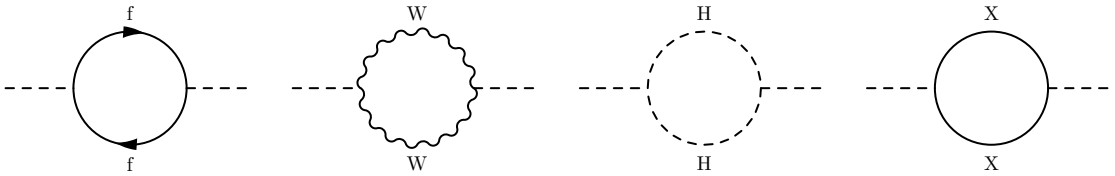

Figure 2.5: Feynman diagrams for loop corrections to the Higgs boson self-energy. The incoming and outgoing dashed lines are the Higgs boson, X is a new massive particle. Reproduced from Ref. [8].

for simplicity) [25]:

$$\begin{aligned} a_\mu^{\text{obs}} &= \quad 116\ 592\ 091\ (63) \quad \times 10^{-11} \\ a_\mu^{\text{SM}} &= \quad 116\ 591\ 830\ (48) \quad \times 10^{-11} \\ \Delta a_\mu &= \qquad\quad 261\ (79) \quad \times 10^{-11} \end{aligned} \tag{2.24}$$

This tension may suggest the existence of particles outside the Standard Model which contribute to the a_μ value.

Unification of forces In the Standard Model, the electromagnetic force and weak force mix into a single $SU(2) \times U(1)$ symmetry at the electroweak scale $\Lambda_{\text{EWK}} \sim 100\,\text{GeV}$. It may be possible to unify the electroweak and strong interactions under some larger symmetry with a single coupling constant at a higher energy [33].

Hierarchy problem The Higgs boson is observed to have $m_H \simeq 125\,\text{GeV}$ [25], and is influenced by virtual corrections from particles which couple directly or indirectly to its field. Loop calculations (Figure 2.5) show that the Higgs mass-squared is quadratically or logarithmically divergent at high energies, depending on the particle(s) in the loop. If the Higgs boson is a fundamental particle (so far it seems to be so), and the Standard Model is valid up to the Planck scale ($\Lambda_P \sim 10^{19}\,\text{GeV}$), then corrections to the Higgs mass-squared need to cancelled to a high precision [9]. Noting that the corrections from a spin-$\frac{1}{2}$ particle are equal in magnitude but opposite in sign to those from two scalar particles with the same Yukawa coupling, a new fermion-boson symmetry could be proposed in order to solve this problem.

Names		spin 0	spin 1/2	$SU(3)_c, SU(2)_L, U(1)_Y$
squarks, quarks (x3 generations, x3 colours)	Q	$\begin{pmatrix}\widetilde{u}_L & \widetilde{d}_L\end{pmatrix}$	$\begin{pmatrix}u_L & d_L\end{pmatrix}$	$(\mathbf{3}, \mathbf{2}, +\frac{1}{6})$
	$\overline{U}$	$\widetilde{u}_R^*$	$u_R^\dagger$	$(\overline{\mathbf{3}}, \mathbf{1}, -\frac{2}{3})$
	$\overline{D}$	$\widetilde{d}_R^*$	$d_R^\dagger$	$(\overline{\mathbf{3}}, \mathbf{1}, +\frac{1}{3})$
sleptons, leptons (x3 generations)	L	$\begin{pmatrix}\widetilde{\nu}_L & \widetilde{e}_L\end{pmatrix}$	$\begin{pmatrix}\nu_L & e_L\end{pmatrix}$	$(\mathbf{1}, \mathbf{2}, -\frac{1}{2})$
	$\overline{E}$	$\widetilde{e}_R^*$	$e_R^\dagger$	$(\mathbf{1}, \mathbf{1}, +1)$
Higgs, higgsinos	H_u	$\begin{pmatrix}H_u^+ & H_u^0\end{pmatrix}$	$\begin{pmatrix}\widetilde{H}_u^+ & \widetilde{H}_u^0\end{pmatrix}$	$(\mathbf{1}, \mathbf{2}, +\frac{1}{2})$
	H_d	$\begin{pmatrix}H_d^0 & H_d^-\end{pmatrix}$	$\begin{pmatrix}\widetilde{H}_d^0 & \widetilde{H}_d^-\end{pmatrix}$	$(\mathbf{1}, \mathbf{2}, -\frac{1}{2})$

Table 2.3: Chiral supermultiplets in the Minimal Supersymmetric Standard Model. Reproduced from Ref. [9].

2.3 Supersymmetry

Supersymmetry (SUSY) is a class of extensions to the Standard Model which posit a new symmetry between fermions and bosons. Using abstract notation:

$$\begin{aligned} Q|\text{fermion}\rangle &= |\text{boson}\rangle \\ Q|\text{boson}\rangle &= |\text{fermion}\rangle, \end{aligned} \tag{2.25}$$

where Q is the generator of supersymmetry. In such models, every Standard Model particle has a supersymmetric parter (spartner) which differs from it in spin by $\frac{1}{2}$; Standard Model fermions have bosonic superpartners and Standard Model bosons have fermionic superpartners. This section is heavily based on Ref. [9]. See Ref. [34, 35] for further discussion.

2.3.1 Particle content

In order to construct a Langrangian that is invariant under supersymmetry, SM particles and their superpartners are organised into *supermultiplets* which contain both the fermion and boson states. The SM fermions, Higgs bosons, and their superpartners reside in chiral supermultiplets (Table 2.3); the gauge bosons and their superpartners reside in gauge multiplets (Table 2.4).

Names	spin 1/2	spin 1	$SU(3)_c \times SU(2)_L \times U(1)_Y$
gluino, gluon	$\widetilde{g}$	g	$(\mathbf{8}, \mathbf{1}, 0)$
winos, W bosons	$\widetilde{W}^{\pm}, \widetilde{W}^0$	$W^{\pm}, W^0$	$(\mathbf{1}, \mathbf{3}, 0)$
bino, B boson	$\widetilde{B}^0$	B^0	$(\mathbf{1}, \mathbf{1}, 0)$

Table 2.4: Gauge supermultiplets in the Minimal Supersymmetric Standard Model. Reproduced from Ref. [9].

In the Minimal Supersymmetric Standard Model (MSSM), every SM fermion is superpartnered with two *sfermions* ("scalar-fermions"), one for each chiral state. In this thesis, sfermions are given subscripts $_L$ or $_R$ to indicate the chirality of their partner fermion. Note that the sfermions themselves, being scalar, have no chirality.

The Standard Model Higgs mechanism is modified to involve two Higgs doublets, rather than just one: a $Y = +\frac{1}{2}$ doublet H_u gives Yukawa couplings to up-type quarks, while a $Y = -\frac{1}{2}$ doublet H_d gives Yukawa couplings to down-type quarks and charged leptons. Their vacuum expectation values are related to that of the Standard Model Higgs $\langle v \rangle \simeq 174\,\text{GeV}$ by a new parameter $\tan\beta$: $\langle H_u \rangle = v_u = v \sin\beta$ and $\langle H_d \rangle = v_d = v\cos\beta$. Consequently, after electroweak symmetry breaking, there will be five Higgs mass eigenstates: two CP-even neutral (h^0 and H^0), one CP-odd neutral (A^0), and two charged $Q = \pm 1$ ($H^{\pm}$). The observed Higgs boson is consistent with h^0 [36, 37]. The two Higgs doublets are partnered with supersymmetric *higgsino* doublets $\widetilde{H}_u$ and $\widetilde{H}_d$.

The SM gauge bosons are superpartnered with spin-$\frac{1}{2}$ *gauginos*. Due to electroweak symmetry breaking, the SM bosons $W^{i\in\{1,2,3\}}$ and B are mixed into the mass eigenstates $W^{\pm}$, Z, and A. Similarly, the gauginos and the higgsinos are mixed into four electrically neutral mass eigenstates called neutralinos $\widetilde{\chi}^0_{j\in\{1,2,3,4\}}$ and two pairs of electrically charged mass eigenstates called charginos $\widetilde{\chi}^{\pm}_{j\in\{1,2\}}$, with the index j running in ascending order of mass.

In general the SUSY Lagrangian can be written [9]

$$\mathcal{L}_{\text{SUSY}} = -\partial^\mu \phi^{*i} \partial_\mu \phi_i + i\psi^{\dagger i}\bar{\sigma}^\mu \partial_\mu \psi_i - \frac{1}{2}(\mathcal{W}^{ij}\psi_i\psi_j)(\mathcal{W}^*_{ij}\psi^{\dagger i}\psi^{\dagger j}) - \mathcal{W}^i\mathcal{W}^*_i, \qquad (2.26)$$

where the index i runs over all gauges and flavours, the fields ϕ_i and ψ_i are the complex scalar and left-handed Weyl fermion in the same supermultiplet i, the matrices $\bar{\sigma}$ are related to the Pauli matrices by $\bar{\sigma}^0 = \sigma^0 = \mathbb{I}_2$, $\bar{\sigma}^k = -\sigma^k$, the object $\mathcal{W}$ is the *superpotential*, and $\mathcal{W}^i = \frac{\delta}{\delta\phi_i}\mathcal{W}$, $\mathcal{W}^{ij} = \frac{\delta^2}{\delta\phi_i\delta\phi_j}\mathcal{W}$. For the MSSM, the superpotential is

$$\mathcal{W} = \overline{u}\mathbf{y_u}QH_u - \overline{d}\mathbf{y_d}QH_d - \overline{e}\mathbf{y_e}LH_d + \mu H_u H_d. \tag{2.27}$$

Each term couples the supermultiplets from Tables 2.3 and 2.4 with some coupling strength. The Yukawa couplings are in the matrices $\mathbf{y_u}, \mathbf{y_d}, \mathbf{y_e}$ which are each 3×3 in generation space. Note that gauge and generational indices are suppressed for brevity.

2.3.2 Supersymmetry breaking

If supersymmetry were exact, SM particles and their superpartners would have the same mass. If this were so, such particle states would have been observed by now at experiments. However since this is not the case, supersymmetry must be broken [9].

One such mechanism, tested by the analysis described in Chapter 5, is called gauge-mediated supersymmetry breaking (GMSB) or general gauge mediation (GGM). In these models, the gauge interactions are responsible for soft SUSY breaking in the MSSM. In the limit that the MSSM couplings tend to 0, the theory decouples into the MSSM and a separate hidden sector that breaks SUSY. Among the predictions of these models is that the gravitino $\widetilde{G}$, superpartner of the graviton, would be the lightest supersymmetric particle [9, 38].

2.3.3 R-parity

The multiplicative quantum number R-parity is defined

$$R = (-1)^{3(B-L)+2s}, \tag{2.28}$$

where the baryon number $B = +1(B = -1)$ for (anti-)quarks, the lepton number $L = +1(L = -1)$ for (anti-)leptons, and s is the spin. Supersymmetric particles

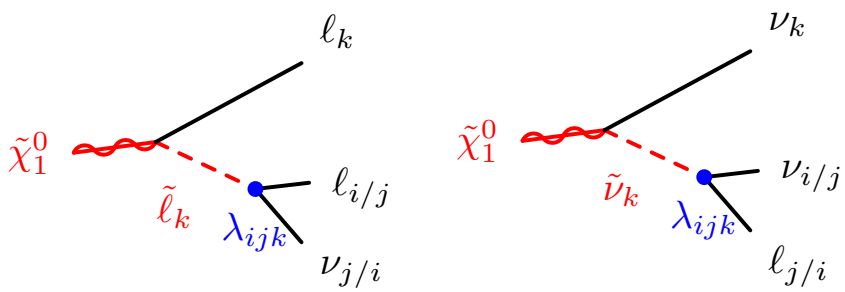

Figure 2.6: R-parity violating decays of the lightest neutralino allowed by a non-zero λ_{ijk} coupling. Lepton flavours i, j, k depend on which of the λ_{ijk} couplings are non-zero.

have $R = -1$, while Standard Model particles have $R = +1$. R-parity is assumed to be conserved in the MSSM [9].

The assumption of R-parity conservation (RPC) gives three phenomenological features exploited at collider searches for SUSY: SUSY particles are pair produced at colliders, they will always decay to the lightest supersymmetric particle (LSP), and if the LSP is electrically neutral and interacts weakly with SM particles, then it is a viable candidate for dark matter [9]. Additionally, R-parity conservation forbids SUSY processes that would otherwise lead to proton decay [9], a process with half-life $t_{\frac{1}{2}} > 10^{30}$ years [25].

Although R-parity conservation is phenomenologically favoured, R-parity violation (RPV) is neither experimentally nor theoretically excluded. If R-parity violation were allowed, baryon number violating terms ($\mathcal{W}_{\Delta B}$) and lepton number violating terms ($\mathcal{W}_{\Delta L}$) could appear in the superpotential $\mathcal{W}$ of the SUSY Lagrangian:

$$\mathcal{W} \supset \mathcal{W}_{\Delta L} + \mathcal{W}_{\Delta B} \tag{2.29}$$

$$\mathcal{W}_{\Delta L} = \frac{1}{2}\lambda_{ijk} L_i L_j \overline{E}_k + \lambda'_{ijk} L_i Q_j \overline{D}_k + \kappa_i L_i H_u \tag{2.30}$$

$$\mathcal{W}_{\Delta B} = \frac{1}{2}\lambda''_{ijk} \overline{U}_i \overline{D}_j \overline{D}_k. \tag{2.31}$$

Here the indices $i, j, k \in \{1, 2, 3\}$ run over the three fermion generations. Proton decay can still be suppressed provided that certain λ' or λ'' couplings are sufficiently small [9].

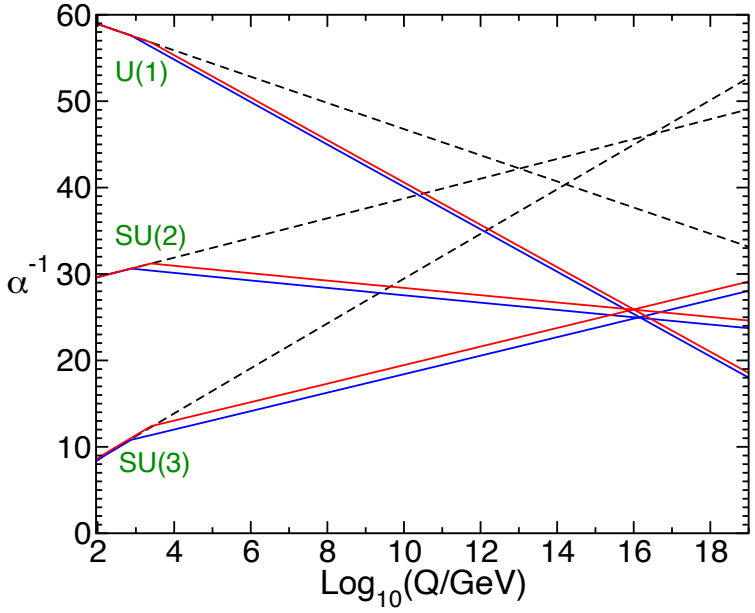

Figure 2.7: The inverse coupling constants $(1/\alpha)$ of the strong $(SU(3))$, weak $(SU(2))$, and electromagnetic forces $(U(1))$ as a function of the energy scale Q. The scenario without SUSY is shown in dashed lines, while representative SUSY scenarios are shown in solid coloured lines. Reproduced from [9].

Chapter 5 describes an analysis searching for R-parity violating SUSY where it is assumed either λ_{12k} or $\lambda_{i33} \neq 0$ for $i, k \in \{1, 2\}$ and all other RPV couplings are zero. These scenarios admit lepton-number and lepton-flavour violating decays of the lightest neutralino into SM leptons and a neutrino (Figure 2.6 left).

2.3.4 Solutions to Standard Model problems

Hierarchy problem Fermionic and bosonic corrections to the Higgs mass are of equal magnitude but opposite signs. Thus, supersymmetry gives the cancellations necessary to explain the stability of the Higgs mass [9, 35].

Unification of forces Currently, the electromagnetic and weak interactions can be mixed into one symmetry, but it is not possible to unify them with the strong force. With the addition of supersymmetry, the running strong, electromagnetic, and weak coupling constants are seen to converge at an energy scale below the Planck scale

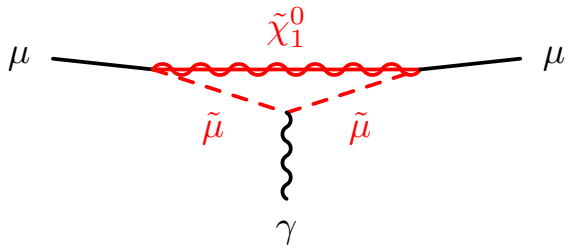

Figure 2.8: Diagram of an example smuon contribution to the $(g-2)_\mu$ calculation.

(Figure 2.7). This hints at the possibility that the three forces could be unified by some mechanism after the imposition of supersymmetry [33, 39, 40].

Dark matter candidates Assuming R-parity conservation, the lightest supersymmetric particle cannot decay. Sparticles in the early universe would have decayed into the LSP as the universe cooled and expanded, and if the LSP were electrically neutral and massive, then it could be a dark matter candidate. There are three possible LSP DM candidates: the sneutrino, the gravitino, and the neutralino. Of these, the sneutrino has been excluded by direct searches [9].

Explains $(g-2)_\mu$ anomaly SUSY is a possible, but not unique, solution to the 3.3σ tension on the value of a_μ. It could provide an additional correction [41]

$$a_\mu^{\text{SUSY}} \simeq \pm 130 \times 10^{-11} \cdot \left(\frac{100\,\text{GeV}}{m_{\text{SUSY}}}\right) \tan\beta. \tag{2.32}$$

The $\pm$ sign is dependent on the sign of the μ parameter in the SUSY superpotential, and it is likely that $\tan\beta \simeq 3-40$. Therefore SUSY particles in the range m_{SUSY} =100 to 500 GeV could give the required corrections [25, 42]. An example diagram showing the SUSY contribution to the muon magnetic moment is shown in Figure 2.8.

2.3.5 Current limits

Both ATLAS and CMS have set limits on the minimum masses of some supersymmetric particles in simplified models (Figure 2.9 shows the ATLAS limits as of March 2021).

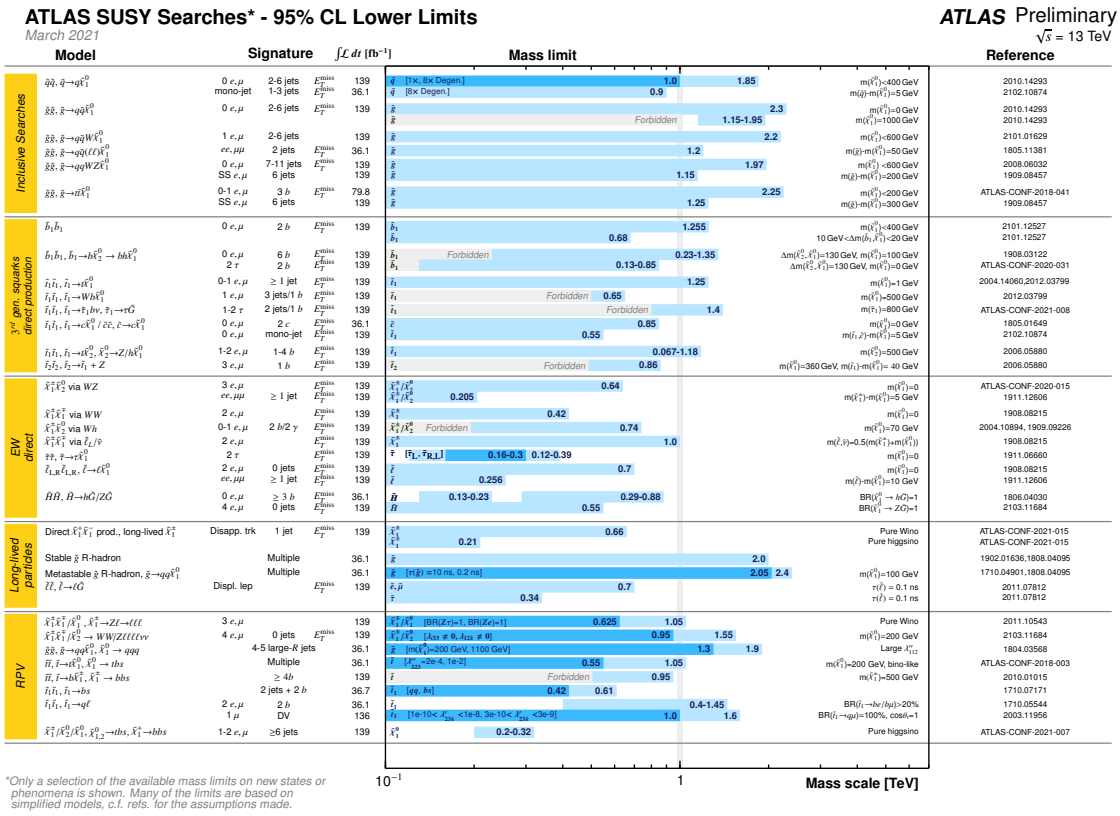

Figure 2.9: Limits on SUSY particle masses set by ATLAS under different simplified models and event signatures. The assumptions made in order to project the multidimensional limits from all these analyses onto a single graph are listed towards the right of the graph. Chapter 5 describes the analysis which set one of the limits shown in the "EW direct" category, that of the $\tilde{H}\tilde{H}, \tilde{H} \to h\tilde{G}/Z\tilde{G}$ model with the 4 e, μ signature. The same analysis also sets a limit in the "RPV" category, that of the $\tilde{\chi}_1^{\pm}\tilde{\chi}_1^{\mp}/\tilde{\chi}_2^0 \to W/ZZ\ell\ell\ell\ell\nu\nu$ model. Reproduced from Ref. [43].

These analyses are interpreted under simplified models which typically assume all SUSY couplings other than those considered are zero, and the masses of all SUSY particles other than those considered are out of reach of the experiment.

There also exist analyses [44, 45] which use the combined results of multiple SUSY searches to scan the parameter space of the MSSM. These analyses reveal underexplored regions in the space and therefore motivate more targeted searches in these regions in future.

2.4 Summary

The Standard Model of particle physics describes most observed subatomic phenomena with extraordinary success. Supersymmetry, a new fermion-boson symmetry, has been proposed as an extension to the Standard Model to address the model's limitations. Following a description of the ATLAS experiment in the next chapter, Chapter 4 discusses an ATLAS system key to the testing of the Standard Model and supersymmetry. After that, two searches for supersymmetry are described in Chapters 5 and 6.

3
Experiment

Particle physics is built on a long history of experiments. The earliest of these include Geiger and Marsden's experiment [46] which offered initial clues to the structure of the atom. In the 21st Century, a wide range of particle physics experiments are in operation; they are all designed to measure the Standard Model to ever increasing precision, or are optimised for the discovery of beyond-the-Standard-Model (BSM) physics, or both. Active experiments include the LUX-ZEPLIN dark matter detection experiment [47] and the IceCube Neutrino Observatory in Antarctica [48].

This thesis tests the predictions of the Standard Model at high-energy collider experiments. Such interactions can range from simple elastic scattering to the production of the Higgs boson. Due to proton structure, larger cross sections follow from higher beam energies, allowing for the probing of rare Standard Model processes and, potentially, the discovery of BSM processes — if they exist and are accessible at the given energy scale.

Recent particle colliders include:

- The **Large Electron-Positron Collider** (LEP), hosted by CERN, which had centre-of-mass energy of up to $\sqrt{s} \leq 209\,\text{GeV}$ [49]. Major results from LEP include studies of the Z boson and W^+W^- production. Famously, it excluded the

Standard Model Higgs boson at masses $\leq 114.4\,\text{GeV}$ [50], just below its currently known mass of $(125.10 \pm 0.14)\,\text{GeV}$ [25]. This thesis presents work which extends one of the limits on supersymmetry set by LEP (cf. Chapter 6).

- The **Tevatron**, hosted by Fermilab, was a proton-antiproton collider which reached $\sqrt{s} = 1.96\,\text{TeV}$, giving the collider its name. The top quark was first discovered at the Tevatron experiments D0 [51] and CDF [52].

- The **Large Hadron Collider** (LHC) at CERN, which is capable of colliding protons at up to $\sqrt{s} = 13\,\text{TeV}$. Constructed in the tunnel that formerly housed LEP, it is the highest energy particle accelerator to date. Among its goals is the probing of electroweak SUSY at the $\mathcal{O}(100\,\text{GeV})$ scale, a goal to which work in this thesis contributes. A more detailed description of the LHC is given in Section 3.1.

Particle debris from the collisions of such colliders need to be recorded by a detector with high resolution in momentum, position, and time. Such a detector also needs to have powerful particle discrimination capability. New physics at or near collision energy is expected to be produced with only small boosts along the beam, therefore the detector needs to be particularly well-instrumented at angles close to the orthogonal of the beamline.

The ATLAS experiment was designed and built with the aforementioned requirements in mind. An overview of ATLAS is presented in Section 3.2.

3.1 The Large Hadron Collider

The Large Hadron Collider is the world's largest machine [54]. It is roughly 27 km in circumference, and located about 100 m below the French-Swiss border near Geneva (Figure 3.1). It is capable of accelerating hadrons, usually lead ions or protons, to near

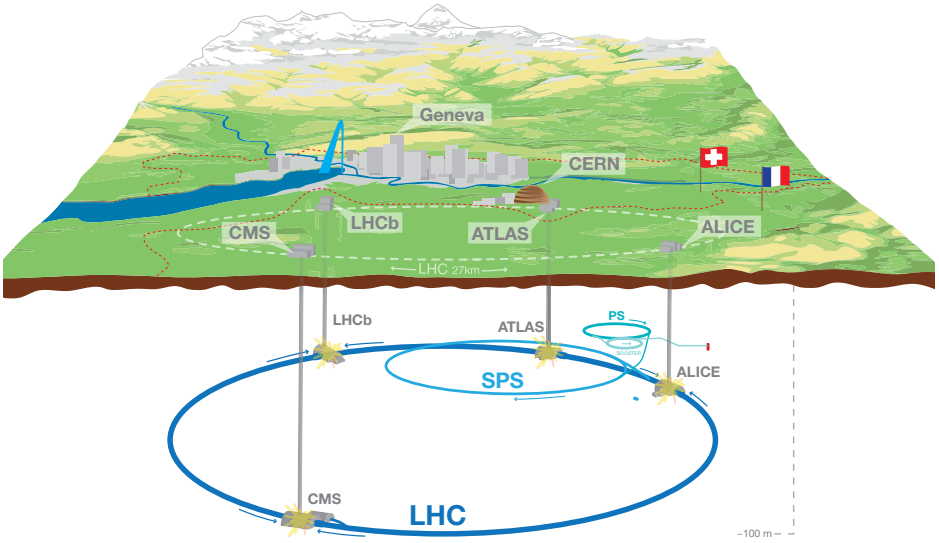

Figure 3.1: Cartoon showing the approximate location of the LHC, its experiments, and selected supporting facilities relative to the French-Swiss border and Genevan landmarks. Reproduced from Ref. [53].

light speed, and then bringing them to collision [55]. Work presented in this thesis studies the proton-proton collisions delivered by the LHC.

In the years 2008–2012, known as Run-1, the LHC provided pp collisions at $\sqrt{s} = 7$ or 8 TeV. Following a scheduled 2.5-year shutdown for upgrades, the pp collision energy was increased to $\sqrt{s}$ =13 TeV for Run-2, which lasted from 2015 to 2018 [56]. At the time of writing, the collider is once again undergoing a scheduled years-long period of shutdown and upgrades. Run-3 is expected to commence in spring 2022 at the earliest, with collision energy $\sqrt{s} = 13,\ 13.5$, or perhaps even 14 TeV.

When delivering pp collisions in Run-2, the LHC held two beams circulating in opposite directions. Each beam had up to 2556 bunches of $\sim 10^{11}$ protons per bunch. Bunch crossings occurred at four points around the LHC ring, where lie the four main experiments: ALICE, LHCb, CMS, and ATLAS [56]. When the bunches crossed, up to about 60 proton-proton interactions or *collisions* occurred. The experiments recorded the results of these collisions. ALICE is designed to probe heavy-ion collisions [57], LHCb is designed for precision CP and B-hadron physics [58], while CMS [59] and

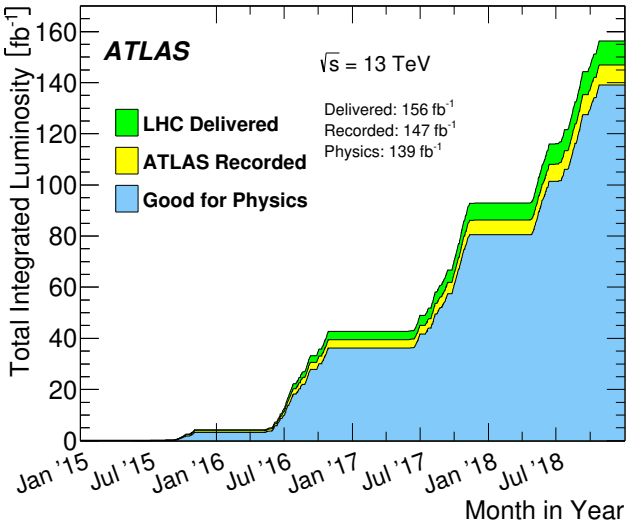

Figure 3.2: Integrated luminosity in Run-2 delivered by the LHC (in green), recorded by ATLAS (in yellow), and deemed "good for physics" (in blue). Reproduced from Ref. [60].

ATLAS are general purpose detectors.

The *instantaneous luminosity*, or simply *luminosity*, L is the rate at which collision events are delivered, measured in units of $\mathrm{cm}^{-2}\,\mathrm{s}^{-1}$. The rate of events $\frac{dN}{dt}$ for a process given its cross section σ can be written as

$$\frac{dN}{dt} = L\sigma.$$

In Run-2 the LHC delivered between about 0.5×10^{34} to $2 \times 10^{34}\,\mathrm{cm}^{-2}\,\mathrm{s}^{-1}$ of luminosity, the upper range being twice the design luminosity of the LHC – a remarkable technical achievement [56].

The *integrated luminosity* is a measure of the total number of collision events delivered: $\mathcal{L} = \int L dt$. Over the course of Run-2, ATLAS collected $138.9\,\mathrm{fb}^{-1} \pm 1.7\%$ of pp collision data (Figure 3.2) [60, 61], where $1\,\mathrm{fb}^{-1} = 1 \times 10^{-39}\,\mathrm{cm}^{-2}$. Following above, the total number of events N for a process with cross section σ is

$$N = \int \frac{dN}{dt}\, dt = \sigma \int L\, dt = \sigma\mathcal{L}.$$

In order to achieve high luminosities at the LHC, bunches are made to cross such that typically more than one pair of protons interact in any given bunch crossing. This

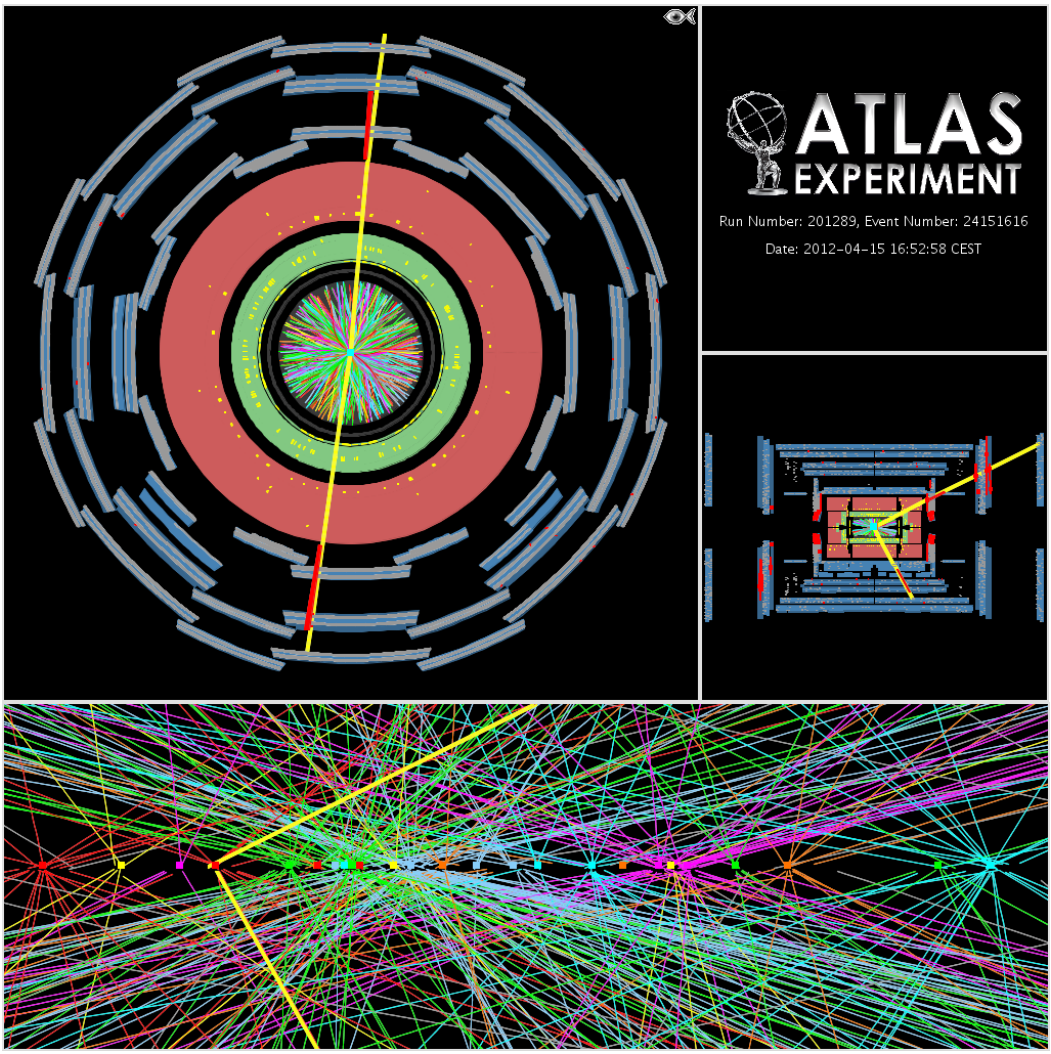

Figure 3.3: Display of a high-pileup event recorded by ATLAS in 2012. The bottom panel shows 25 reconstructed vertices and the charged particle tracks associated to them. The bold yellow lines emanating from the centre of the detector in the top panels (and the corresponding lines in the bottom panel) represent a muon pair whose invariant mass is consistent with the Z boson mass. Reproduced from Ref. [62].

gives rise to *pileup*, low-energy interactions that occur within the same bunch crossing as the hard-scatter interaction that interests the experimentalist. Pileup activity that is concurrent with a candidate $Z \to \mu\mu$ event is visualised in Figure 3.3. For the purposes of their measurements, it is critical that the experiments are capable of distinguishing between different interactions within the same bunch crossing

3.2 The ATLAS Experiment

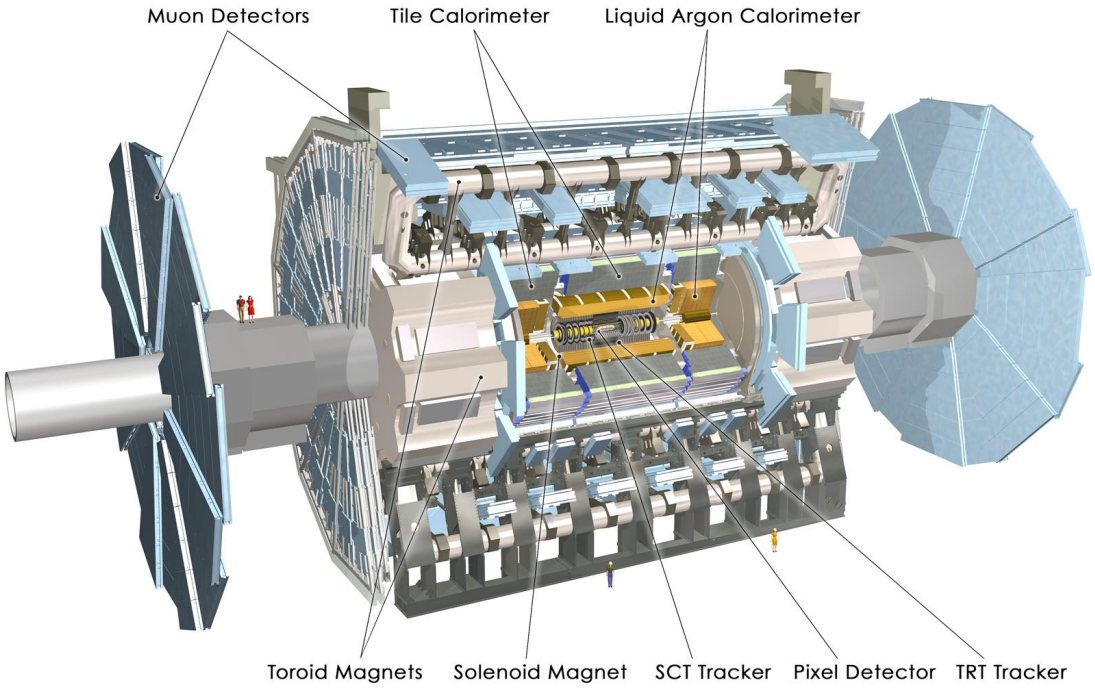

Figure 3.4: A schematic of the ATLAS detector, which is about 25 m in height, 40 m in length, and 7000 tonnes in weight. Reproduced from Ref. [63, 64].

3.2.1 Overview

ATLAS is a barrel-shaped, nearly fully-hermetic detector, providing close to 4π solid angle coverage of particle collisions which occur at the centre of the detector. It is designed for the physics goals of Standard Model measurement, Higgs boson discovery and measurement, and discovery of high-energy beyond-the-Standard-Model physics [64]; the latter being the focus of this thesis.

ATLAS uses a right-handed coordinate system where the positive x-axis is defined as pointing inwards to the centre of the LHC ring, the positive y-axis points upwards, and the z-axis is defined by the direction of the beamline. The origin is taken to be the centre of the detector, which is the nominal interaction point. The azimuthal angle

ϕ is measured around the beam axis, the polar angle θ is defined as the angle from the positive z-axis, and pseudorapidity is defined as $\eta = -\ln\tan(\frac{\theta}{2})$. It is sometimes also useful to define the Lorentz-invariant coordinate rapidity $y = \frac{1}{2}\ln[(E+p_z)/(E-p_z)]$, which has properties that $y = \eta$ for massless particles, and $\Delta y = y_1 - y_2$ is invariant for Lorentz boosts along the beamline. The *transverse* plane is defined as the projected $r - \phi$ plane, i.e. the direction transverse to the beamline.

The detector consists of these four main components, in order of increasing distance from the beamline: the inner detector, electromagnetic calorimeters, hadronic calorimeters, and the muon spectrometer. Details of detector construction are deferred to Section 3.2.2.

Particles which interact via the electromagnetic force or strong force leave energy deposits in the detector that can be recorded (Figure 3.5). *Physics objects* are constructed from the recorded detector responses. These objects include electrons, photons, muons, taus, and jets (collimated hadronic particles). The reconstruction of these objects is described in Section 3.2.4.

Some Standard Model particles, such as the Z boson, decay before reaching the detector or within the detector volume. They can be reconstructed from the characteristics of their decay, such as by the invariant mass of a same-flavour opposite-sign lepton pair.

Particles which do not interact with the detector can be indirectly detected by missing momentum, the non-zero sum of the momenta of visible particles. Invisible particles include neutrinos, which interact only through the weak force. Supersymmetric particles are also generally not detectable, as they rarely interact with Standard Model particles. Missing momentum reconstruction is also described in Section 3.2.4.

During data-taking, the *trigger* filters events such that the recorded event rate does not exceed limitations of readout, storage, and processing capacity. This is possible because the processes in which ATLAS is interested are many orders of magnitude rarer than that of proton-proton scattering [67]. The trigger is further discussed in

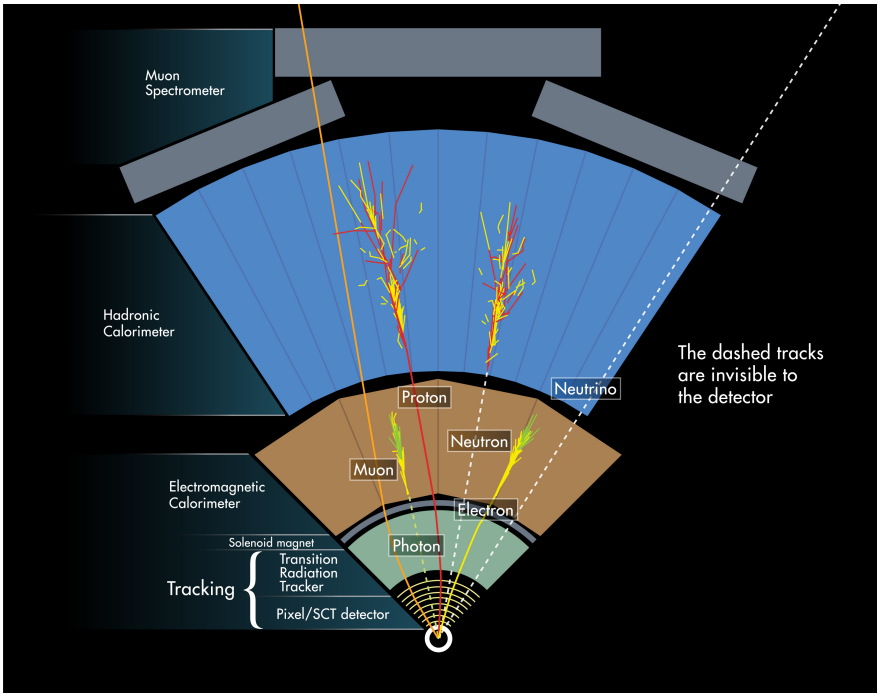

Figure 3.5: A schematic of the signatures left in the ATLAS detector by different particles. Reproduced from Ref. [65, 66].

Section 3.2.3. Events which pass the trigger are saved to disk for *offline* processing via the data acquisition system, while events which fail the trigger are discarded.

3.2.2 The detector

The four main components of the ATLAS detector, built to the requirements listed in Table 3.1 to facilitate ATLAS physics goals, are briefly described in this section.

Inner detector The inner detector (Figure 3.6) provides precision tracking within $|\eta| < 2.5$ for the reconstruction of the trajectories, momenta, and charges of charged particles. It consists of three different types of detectors with complementary technologies, all enclosed in a solenoid magnet which provides a uniform 2 T field along the beamline [64]. Charged particles are bent in the magnetic field and leave small energy deposits known as *hits* in the detectors; particle tracks and properties are reconstructed from these hits. Interaction vertices are reconstructed from the extrapolation of particle

Detector component	Required resolution	η coverage	
		Measurement	Trigger
Tracking	$\sigma_{p_T}/p_T = 0.05\% p_T \oplus 1\%$	± 2.5	
EM calorimetry	$\sigma_E/E = 10\%/\sqrt{E} \oplus 0.7\%$	± 3.2	± 2.5
Hadronic calorimetry			
barrel and end-cap	$\sigma_E/E = 50\%/\sqrt{E} \oplus 3\%$	± 3.2	± 3.2
forward	$\sigma_E/E = 100\%/\sqrt{E} \oplus 10\%$	$3.1 < \lvert\eta\rvert < 4.9$	$3.1 < \lvert\eta\rvert < 4.9$
Muon spectrometer	$\sigma_{p_T}/p_T = 10\%$ at p_T =1 TeV	± 2.7	± 2.4

Table 3.1: Performance goals of the ATLAS detector. Units for energy E and transverse momentum p_T are in GeV. Reproduced from Ref. [64].

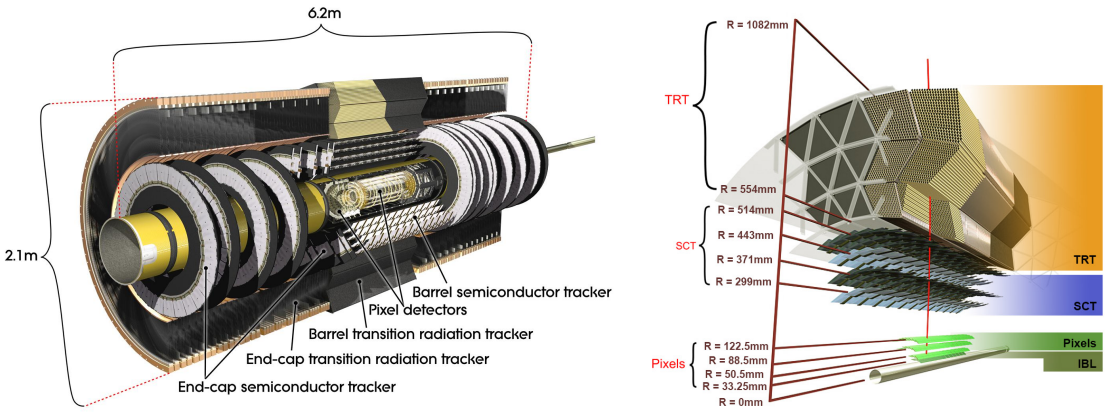

(a) Schematic of the inner detector. Reproduced from Ref. [64]

(b) The radii of inner detector layers from the beamline. A particle track traversing the inner detector is shown in red. Reproduced from Ref. [68].

Figure 3.6: Schematics of the inner detector.

trajectories to the beamline. The *hard-scatter vertex* is identified as the vertex which has the largest sum-square of transverse momenta of tracks associated with it [68].

Closest to the beamline at $33 < r < 122$ mm lies the pixel detector. It consists of 2024 identical pixel modules; these are arranged in four layers around the beamline and three disks in each of the two endcaps [64]. Its high position resolution enables high precision vertexing. At $299 < r < 514$ mm lies the Semiconductor Tracker (SCT), which consists of 4088 silicon strip modules in four barrel layers and two endcaps with

nine disks each. In each layer or disk, strips are mounted back-to-back at a small angle (40 mrad) to measure in two coordinates [64]. The combined hits of the pixel and SCT detectors (4 hits + 8 hits) are used in track reconstruction.

Finally at $554 < r < 1082$ mm lies the Transition Radiation Tracker (TRT), which consists of 350,848 straw tubes of 4 mm diameter. The tubes are arranged in 32 modules per layer for 3 layers along the barrel and 40 disks for each of the two endcaps. They are filled with a xenon- or argon-based gas mixture [69]. After tracks are found in the pixel and SCT detectors, tracks within $|\eta| < 2$ are extended into the TRT [70]. The TRT also allows for discrimination of electrons and pions of up to ~ 100 GeV in momentum [69], by exploiting transition radiation emitted by ultra-relativistic particles at the boundary between media of different dielectric constants [71].

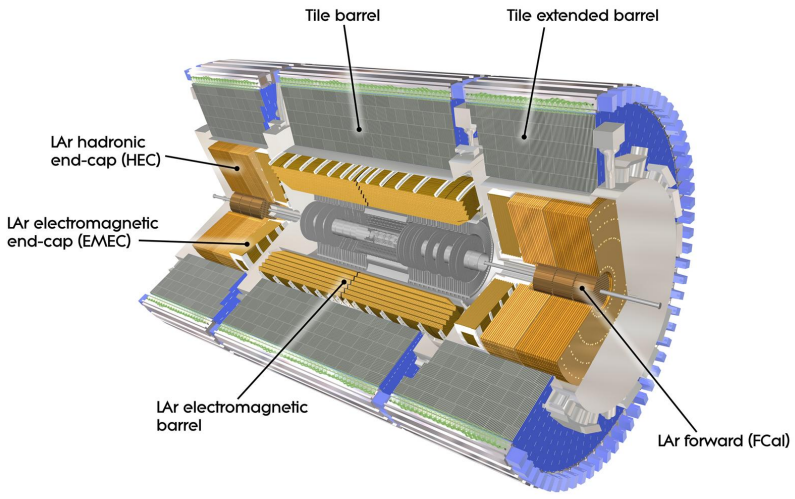

Figure 3.7: Schematic of the calorimeters. Reproduced from [64, 72].

Calorimeters The calorimeters (Figure 3.7) are designed to contain and measure the energies of particles with high energy and spatial resolution. They are also designed with sufficient depth to minimize punch-through into the muon spectrometer; this aids particle identification. In total, the calorimeter system consists of approximately

188,000 cells with $\Delta\eta \times \Delta\phi$ granularity of up to $0.025 \times \pi/128$ ($0.1 \times \pi/32$) in the electromagnetic (hadronic) calorimeter [73].

ATLAS calorimeters consist of alternating layers of absorbers and active material. The absorbers interact with traversing particles to induce particle showers. The active material responds measurably to passing particles, such as by the emission of light in a scintillator or the flowing of current in an ionised noble liquid. These responses induced by particles in the shower can be measured to give the energy of the original particle. Depth is typically measured in radiation lengths (interaction lengths) for electromagnetic (hadronic) calorimeters.

The electromagnetic calorimeters envelop the inner detector and its solenoid magnet. It provides coverage within $|\eta| < 3.2$, with the region $|\eta| < 2.5$ additionally instrumented for precision physics. The calorimeter is accordion-shaped, with alternating layers of lead absorber and liquid argon active material. It is arranged into 2 to 4 layers with a total depth of 22 to 24 radiation lengths, depending on $|\eta|$. A pre-sampler is installed in $|\eta| < 1.8$ to correct for energy losses [64].

Directly outside the electromagnetic calorimeter lie the hadronic calorimeters: the tile calorimeter along the barrel, and the endcap LAr calorimeter. The tile calorimeter uses steel as its absorber and scintillating tiles for its active material. It is divided into 64 modules and lies between $2.28 < r < 4.25$ m. Its total depth is equivalent to approximately 7.4 interaction lengths, sufficient to stop all but the most energetic hadronic particles. The LAr hadronic endcap calorimeter, with copper as its absorber, provides coverage of $1.5 < |\eta| < 3.2$ [64].

Two additional LAr calorimeters are placed in the forward region, $3.1 < |\eta| < 4.9$, one on each side of ATLAS. Each of these forward calorimeters (FCAL) consists of three layers: one layer with copper absorbers optimised for electromagnetic calorimetry, and two layers with tungsten absorbers to measure hadronic energy. Its depth is approximately 10 interaction lengths [64].

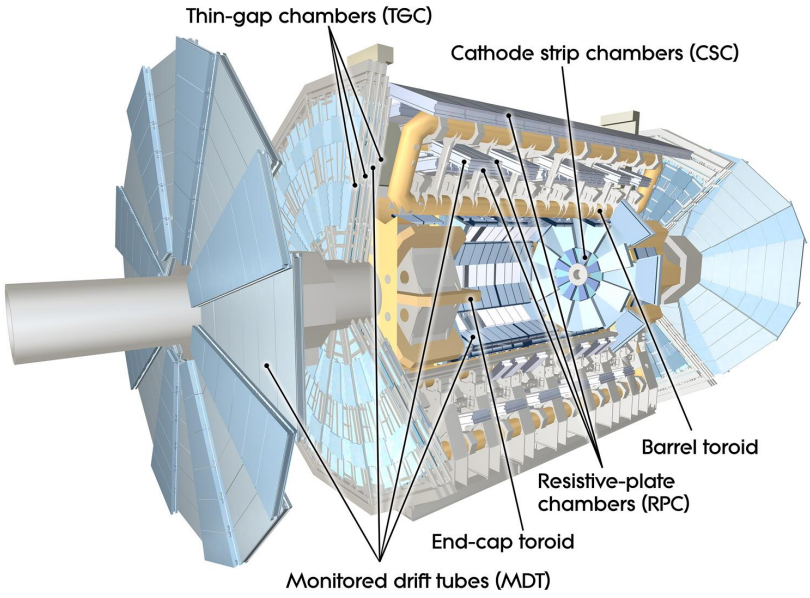

Figure 3.8: Schematic of the muon spectrometer. Reproduced from Ref. [64, 74].

Muon spectrometer The muon spectrometer is placed outside the calorimeters. Air-core toroids provide the spectrometer with a magnetic field integral in the range of $\int B\ dl = 2.0$ to $6.0\,\mathrm{T\,m}$. Tracks are reconstructed from hits left by traversing charged particles in the spectrometer, similar to the inner detector. Momentum and charge can be measured from the curvature of the tracks. These particles are mostly muons since electrons, photons, and most hadronic particles will have been stopped by the calorimeters. The spectrometer also enables the rejection of events containing cosmic rays.

The spectrometer has separate systems for triggering and precision tracking. For precision tracking, higher resolution is required. A combination of monitored drift tubes (MDT) and cathode strip chambers (CSC) provide momentum resolution of better than 3% over a wide range of muon transverse momenta p_T and up to 10% for muons with transverse momenta $p_\mathrm{T} \approx 1\,\mathrm{TeV}$. Triggering requires detectors with fast response times, which are provided by resistive plate chambers ($|\eta| < 1.05$) and thin-gap chambers ($1.0 < |\eta| < 2.4$). Additionally, the trigger chambers measure the coordinate orthogonal

to that measured by the precision tracking chambers [64, 75, 76].

3.2.3 The trigger

ATLAS receives 40 MHz of proton-proton bunch crossings from the Large Hadron Collider. However only a small subset of these events – about $\mathcal{O}(1\,\text{kHz})$ – are saved for further analysis due to constraints on disk space, bandwidth, and processing power.

The *trigger* system decides which events to keep and which to discard. In Run-2, ATLAS operated a two-level trigger, consisting of the L1 trigger and the high-level trigger (HLT) [77].

The L1 trigger, designed for low latency event selection, is implemented in custom hardware. It processes raw signals from the calorimeters and muon trigger chambers to perform basic event reconstruction, and then it selects events based on their reconstructed properties. Examples of the variables considered include event level quantities (such as missing energy, cf. Chapter 4), or the multiplicity of objects above thresholds (such as the number of electron candidates above a specified energy). The L1 trigger reduces the event rate to $\leq 100\,\text{kHz}$ within a latency of 2.5 µs [78].

The HLT is software based. It performs reconstruction and selection on events accepted by the L1 trigger. In reconstruction, fast algorithms are used first to provide early rejection, then more CPU-intensive algorithms perform more precise reconstruction. Reconstruction and event selection generally occurrs within a few hundred milliseconds. In Run-2, the HLT accepted events at 1.2 kHz on average, corresponding to an average throughput of 1.2 GB/s to the Tier-0 facility at the CERN computing centre [78].

$E_{\text{T}}^{\text{miss}}$-triggering is the main focus of Chapter 4. The algorithms used are discussed within that chapter.

Electron- and muon-triggered events are used in the analyses described in Chapters 5 and 6. An electron candidate at L1 is a small calorimeter cluster with high energy. A muon candidate at L1 is provided by tracks in the triggering muon chambers, with some false-positives rejected based on tile calorimeter information. Reconstruction of

electrons and muons in the HLT is then performed by simplified versions of offline algorithms [79, 80].

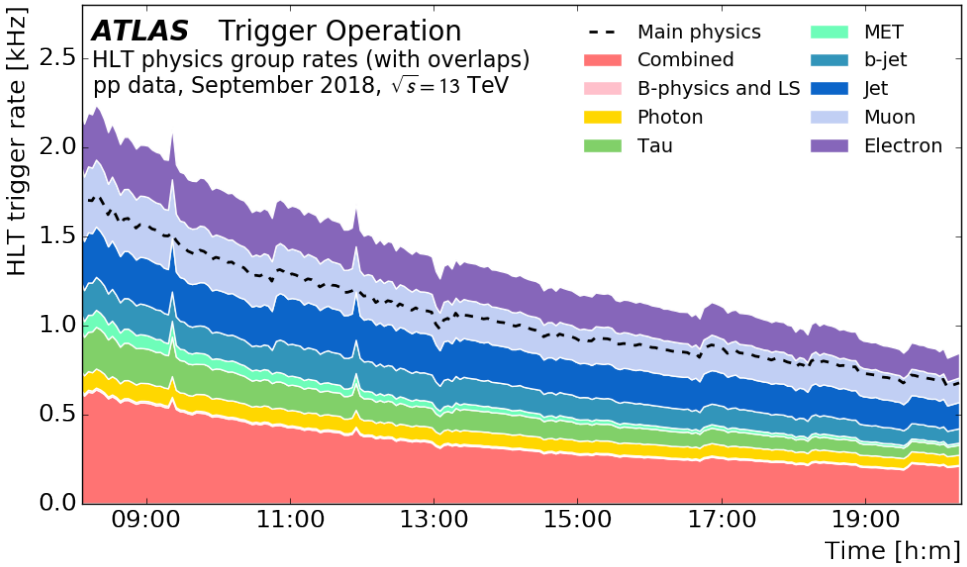

Figure 3.9: Trigger rates for different trigger signatures as a function of time during one run of *pp* data-taking. Missing transverse energy is labelled as "MET". "Combined" triggers are those which trigger on more than one type of object (e.g. a trigger that required one electron and one muon). There exists some overlap in events selected by each of the trigger signatures; the total rate of events accepted by the HLT is shown by the dashed line labelled "Main physics". Reproduced from Ref. [81].

The $\mathcal{O}(1\,\text{kHz})$ trigger output rate budget was shared between different *signatures*, where a trigger signature is defined by the triggering object considered (Figure 3.9). It is important that each signature abides by its individual rate budget. Exceeding the allotted rate can result in the trigger accepting more events than is affordable to write to disk.

3.2.4 Offline event reconstruction

Offline object and event reconstruction is performed for events accepted by the trigger and saved to disk. Object reconstruction is based on knowledge of the detector layout and the expected behaviour of particles in the detector. A description of the reconstruction of objects relevant to this thesis follows:

Tracks Inner detector tracks are reconstructed from a series of energy deposits, or *hits*. Tracks typically consist of 4 hits from the pixel detector and 8 hits from the SCT. If the track is within $|\eta| < 2.0$, it can be extended into the TRT where about 35 hits are expected [82]. The ATLAS Global χ^2 Track Fitter [83] is used to fit tracks to the hits. Muon spectrometer tracks are reconstructed by a similar procedure. Each track has two impact parameters associated with it: the transverse impact parameter d_0, which is the shortest distance between a track and the beamline in the transverse plane, and the longitudinal impact parameter z_0, which is the z displacement from the primary vertex (defined below) to the point on the track used to evaluate d_0.

Primary vertex Primary vertices are reconstructed using at least two inner-detector tracks with $p_{\mathrm{T}} > 500\,\mathrm{MeV}$ [84]. The hard-scatter vertex is the primary vertex with the largest sum-square of transverse momenta ($\sum_{\mathrm{tracks}} p_T^2$) associated with it.

Clusters Cells in the calorimeter are often grouped into *topoclusters*. A topocluster consists of close-by high-energy calorimeter cells grouped together based on the expected RMS noise threshold σ. Cells with energy $E > 4\sigma$ seed a topocluster, then all $E > 2\sigma$ cells neighbouring the topocluster are iteratively added to it, and finally a perimeter of $E > 0\sigma$ cells are added. The final step excludes negative calorimeter cell signals which are due to noise and pileup. [73].

Particle flow objects Particle flow (PFlow) objects are charged particle tracks matched to the hard-scatter vertex and to topoclusters. The topoclusters used need to have passed a pileup subtraction procedure which subtracts energy from energy deposits matched to vertices that were not the hard-scatter vertex [85].

Electrons and photons Electron candidates are reconstructed from inner detector tracks matched with calorimeter clusters. Likelihood-based identification is used to select electrons from these candidates. Inputs to the likelihood include track quality

variables (e.g. on the number of hits or impact parameter), cluster shape variables (e.g. cluster width and energy distribution across the calorimeter layers), and transition radiation from the TRT . The experimentalist can select from a variety of different electron identification working points such as `LooseAndBLayer`, `Medium`, and `Tight`. Typically a tighter working point has lower electron identification efficiency but a higher rejection of other objects misidentified as electrons. Different electron isolation working points are also available, with a similar trade-off of either having better electron efficiency or better isolation from other objects. In this thesis, the points `FCLoose` and `FCTight` are used [82].

Photons are reconstructed in parallel with electrons since they have similar signatures in the detector. Photons are seeded by calorimeter clusters. They are required either to not have a matching track, or to be matched with tracks that can be traced to a $\gamma \to e^+e^-$ conversion vertex in the inner-detector. Like for electrons, photon identification and isolation working points are available to the experimentalist. In this thesis, photons are identified using the `Tight` working point and isolated using the `FixedCutTight` working point [86].

Muons Muon candidates are reconstructed from a combination of inner detector tracks, muon spectrometer tracks, and energy deposits in the calorimeter consistent with a minimum ionising particle. Muons are identified from among these candidates based on several considerations including the number of hits in the MDT and CSC detectors, and the consistency of momentum measurements from the inner detector, muon spectrometer, and the calorimeter. Muon identification working points (such as `Loose`, `Medium`, and `Tight`) and isolation working points (such as `FCLoose` and `FCTight`) are defined [75].

Jets When a quark or gluon is produced in the collision, it hadronises to form hadrons, creating a shower of particles. Jets are the collimated tracks and clusters recorded by

the detector due to such activity. Reconstruction of jets is performed by the anti-k_t algorithm [87] with radius parameter $R = 0.4$ [88]. Inputs to the jet reconstruction were topoclusters [88] or particle-flow objects [85]. Topocluster jets were used in the $E_{\mathrm{T}}^{\mathrm{miss}}$ trigger studies of Chapter 4 and in the 4-lepton analysis described in Chapter 5. PFlow jets were used in the 2-lepton analysis described in Chapter 6.

Tau-leptons Tau-leptons decay via the weak force, with 65% probability of a hadronic final state ($\tau \to \nu_\tau q\bar{q}'$), and 35% probability of a leptonic final state ($\tau \to \nu_\tau \nu_\ell \ell$) [25]. In both cases there is some amount of undetectable energy carried away by the neutrino(s) in the decay. Leptonically decaying taus are not reconstructed, but the contributions of such decays have been considered in events with electrons and muons. Hadronically decaying taus — labelled τ_{had} and conventionally referred to simply as *taus* — are identified by the following procedure. Reconstruction is seeded by jets formed from topoclusters by the anti-k_t algorithm with radius parameter $R = 0.4$ [89]. From them, τ_{had} candidates are identified by a recurrent neural network (RNN) which considers track and cluster variables [90].

Overlap removal It is often the case that clusters or tracks are associated to more than one object. For example, an electron could be reconstructed as a jet from its energy clusters, or a muon could be reconstructed as an electron from its ID track and small energy deposits in the calorimeter. Therefore analyses usually employ an *overlap removal* procedure which removes the double counting of these objects.

Missing transverse energy Missing transverse momentum $\vec{p}_T^{\,\mathrm{miss}}$ is defined as the negative vector sum of the transverse momenta of all identified objects after overlap removal:

$$\vec{p}_T^{\,\mathrm{miss}} = -\left(\sum_{\text{electrons}} \vec{p}_T + \sum_{\text{photons}} \vec{p}_T + \sum_{\text{muons}} \vec{p}_T + \sum_{\text{jets}} \vec{p}_T + \sum_{\text{taus}} \vec{p}_T + \sum_{\text{soft tracks}} \vec{p}_T \right), \quad (3.1)$$

where the last term is the contribution of tracks from the hard-scatter vertex which are not matched to any other object [91]. Conventionally, the quantity *missing transverse energy* is defined as

$$E_{\mathrm{T}}^{\mathrm{miss}} = |\vec{p}_T^{\,\mathrm{miss}}|. \tag{3.2}$$

Particles such as neutrinos and dark matter candidates are not directly detectable because their interaction cross sections by the electromagnetic or strong forces are small or zero. Analyses searching for these particles often rely on the presence of missing transverse energy.

3.3 Summary

The ATLAS experiment records $\sqrt{s}$ =13 TeV pp collisions delivered by the Large Hadron Collider at 40 MHz. Its 25 m × 25 m × 40 m, 7000 tonne detector is instrumented with various technologies so that the collision events recorded can be reconstructed with high precision, which enables the study of the Standard Model and the potential discovery of BSM physics at high energies.

4

$E_{\mathrm{T}}^{\mathrm{miss}}$ Trigger

4.1 Introduction

As discussed in Section 3.2.3, the ATLAS trigger system selects events with interesting signatures to save to disk for later analysis. Events which do not pass the trigger are not recorded.

One such interesting signature is *missing transverse momentum* $\vec{p}_T^{\,\mathrm{miss}}$, which is the negative vector sum of the momenta of all detectable particles. This signature can often be observed when at least one undetectable particle is present in the final state of a pp collision.

Particles escape detection if they do not carry electric or colour charge, or if they do not decay within the detector volume into particles that do; such particles include neutrinos and some beyond-the-Standard-Model (BSM) particles. The presence of these particles can be inferred, using the conservation of momentum, from a large, non-zero vector sum of the momenta of detectable particles.

In pp collisions, it is the partons (quarks and gluons) within the protons that interact. These partons each carry a probabilistic fraction of the proton's momentum. Because

of this, the initial momentum along the collision axis is unknown. Therefore typically only the momentum in the transverse direction, which is zero initially, is considered.

Conventionally, and in the remainder of this chapter, we consider the quantity *missing transverse energy*, $E_{\mathrm{T}}^{\mathrm{miss}} = |\vec{p}_T^{\,\mathrm{miss}}|$. It is equivalent to missing transverse momentum when there is only one invisible particle and it is massless.

The $E_{\mathrm{T}}^{\mathrm{miss}}$ trigger has been critical to searches for supersymmetry [6, 92], vector-like quarks [93], leptoquarks [94], and dark matter [95]. It has also been used recently in the ATLAS observation of ZH and WH production in the $H \to b\bar{b}$ decay channel [96], and the search for Higgs decays to invisible particles [97] which set limits on the coupling of the Standard Model Higgs boson to BSM physics.

There are two levels of $E_{\mathrm{T}}^{\mathrm{miss}}$ triggering: the hardware-based `L1` $E_{\mathrm{T}}^{\mathrm{miss}}$ trigger processes events delivered by the LHC at 40 MHz, and accepts 5 to 10 kHz of them. The accepted events are then processed by the software-based HLT $E_{\mathrm{T}}^{\mathrm{miss}}$ trigger. For both levels of triggering, only information from the calorimeters is considered. In this thesis, only the HLT $E_{\mathrm{T}}^{\mathrm{miss}}$ trigger is studied in detail.

This chapter will be organised as follows. First I outline the key challenges faced by the $E_{\mathrm{T}}^{\mathrm{miss}}$ trigger in Section 4.1.1, then I describe the algorithms used in the trigger in Section 4.1.2. In Section 4.2, I list the data samples used for studies described in this chapter. In Section 4.3, I document performance studies of the $E_{\mathrm{T}}^{\mathrm{miss}}$ trigger which form part of a publication in the *Journal of High Energy Physics* [1]. As software manager of the $E_{\mathrm{T}}^{\mathrm{miss}}$ trigger from August 2018 to July 2020, I redesigned the trigger software, which is described in Section 4.4. I also attempted to develop a new trigger algorithm, which is documented in Section 4.5.

4.1.1 Key challenges

The key challenges to the HLT $E_{\mathrm{T}}^{\mathrm{miss}}$ trigger are the following.

Processing time constraints Given the rate of events received by the triggers and the computing power available in the HLT computing farm, on average events are processed within about 100 ms [1]. If events cannot be processed within several minutes, they are saved to disk and reconstructed again without the time limit [78].

Efficiency to events with high $E_{\mathbf{T}}^{\mathbf{miss}}$ The trigger needs to be highly efficient to events with high $E_{\mathrm{T}}^{\mathrm{miss}}$. In this chapter it will be shown that over the course of Run-2, the trigger was close to 100% efficient for events with $E_{\mathrm{T}}^{\mathrm{miss}} > 200\,\mathrm{GeV}$. The efficiency decreases at lower values of $E_{\mathrm{T}}^{\mathrm{miss}}$.

Rejection of events with little to no $E_{\mathbf{T}}^{\mathbf{miss}}$ The majority of collision events, including those accepted by the `L1` trigger, have little to no $E_{\mathrm{T}}^{\mathrm{miss}}$. While these events could be accepted by other triggers if they satisfy their selections, these events should be rejected by the $E_{\mathrm{T}}^{\mathrm{miss}}$ trigger. This rejection becomes challenging when the number of simultaneous interactions is high, as it becomes difficult to distinguish calorimeter responses due to *hard-scatter* from those due to *pileup*. Pileup in this chapter is parametrised by $\langle\mu\rangle$, the average number of interactions per bunch crossing. The high pileup in Run-2 and expected higher pileup in future runs motivated the development and use of pileup mitigation techniques.

4.1.2 Trigger algorithms

The rate of the $E_{\mathrm{T}}^{\mathrm{miss}}$ trigger increases approximately exponentially with pileup $\langle\mu\rangle$, due to an increased probability for the mis-measurement of $E_{\mathrm{T}}^{\mathrm{miss}}$ [98], resulting in a large number of events with little to no $E_{\mathrm{T}}^{\mathrm{miss}}$ being measured as having large $E_{\mathrm{T}}^{\mathrm{miss}}$. Therefore as pileup increased throughout Run-2, techniques were developed to mitigate this rate increase while maintaining the efficiency of the trigger to events with large real $E_{\mathrm{T}}^{\mathrm{miss}}$.

The trigger accepts events with measured $E_{\mathrm{T}}^{\mathrm{miss}}$ greater than some defined threshold value. The magnitude of $E_{\mathrm{T}}^{\mathrm{miss}}$ is calculated from

$$\begin{aligned} E_x^{\mathrm{miss}} &= -\sum_{i=1}^{|\mathrm{elements}|} E_i \sin\theta_i \cos\phi_i \\ E_y^{\mathrm{miss}} &= -\sum_{i=1}^{|\mathrm{elements}|} E_i \sin\theta_i \sin\phi_i \\ E_{\mathrm{T}}^{\mathrm{miss}} &= \sqrt{(E_x^{\mathrm{miss}})^2 + (E_y^{\mathrm{miss}})^2}, \end{aligned} \tag{4.1}$$

where *elements* are groups of geometrically contained energy depositions within the calorimeter, |elements| is the number of elements, and θ_i and ϕ_i are the polar and azimuthal angles of element i. Each technique had its own particular definition of "element", and elements have similar definitions as offline objects (cf. Sec. 3.2.4). The techniques are described below. The reader may also refer to Ref. [1].

Note that all the algorithms discussed here used calorimeter information only. The addition of tracking information would aid in distinguishing between energy deposits from the hard-scatter vertex and those from pileup; deposits matched to a pileup vertex can be ignored. However, tracking within the time scale required for making trigger decisions was not possible in Run-3. New techniques and hardware developed for Run-3 and beyond will make this possible in future. These improvements are outside the scope of this thesis.

`cell` In the `cell` algorithm, $E_{\mathrm{T}}^{\mathrm{miss}}$ is calculated from the energies of calorimeter cells which pass pileup-dependent noise thresholds. The noise thresholds were adjusted throughout data-taking to account for changing data-taking conditions [73].

`mht` In the `mht` algorithm, $E_{\mathrm{T}}^{\mathrm{miss}}$ is calculated from the energies of *jets*. Jets are formed using the anti-k_t clustering algorithm [87] implemented in the `FastJet` toolkit [99], with radius parameter $R = 0.4$ using *topoclusters* as inputs. A topocluster consists of close-by high-energy calorimeter cells grouped together based on the expected RMS noise threshold σ. Cells with energy $E > 4\sigma$ seed a topocluster, then all $E > 2\sigma$

cells neighbouring the topocluster are iteratively added to it, finally a perimeter of $E > 0\sigma$ cells are added [73].

Jets group close-by topoclusters into one single object which can typically be associated to some particle produced in the hard-scatter interaction, such as a gluon, quark, electron, or photon. This is particularly important for coloured final state particles (gluons and quarks), as they shower and hadronise into multiple close-by hadrons.

Jets are corrected for pileup and are well calibrated against simulation [88] since they are frequently used in physics analysis.

`pufit` The `pufit` algorithm takes topoclusters as input, and corrects for pileup contributions to $E_{\mathrm{T}}^{\mathrm{miss}}$ by computing a χ^2 fit based on two assumptions: (i) the vector sum of pileup transverse energy is zero, and (ii) pileup energy is evenly distributed across η and ϕ. The steps in the algorithm are as follows.

1. The $\eta \times \phi$ space of the calorimeters is separated into 112 patches such that there are 14 divisions in $\eta \in (-5, 5)$ and 8 divisions in $\phi \in [0, 2\pi)$, therefore each patch has size $\eta \times \phi = 0.714 \times 0.785$. The transverse energy $E_{T,j}$ for any patch j is the sum of the transverse energies of all topoclusters within the patch:

$$E_{T,j} = \sum_{i \in \text{topoclusters within patch } j} E_{T,i}. \tag{4.2}$$

2. For each event, a trimmed mean $\langle E_T \rangle_{\text{patch}}$ is calculated over the middle 90% (ordered by transverse energy E_T) of all $N = 112$ calorimeter patches:

$$\langle E_T \rangle_{\text{patch}} = \frac{1}{N} \sum_{j=0.05N}^{0.95N} E_{T,j} \tag{4.3}$$

The 5% tails are discarded in this calculation to exclude the lowest energy contributions, which are likely from soft pileup, and the highest energy contributions

to avoid biasing the mean to extreme energies of hard-scatter jets. The variance of the trimmed mean $\langle E_T \rangle_{\text{patch}}$ is estimated by

$$V_{\text{patch}} = \frac{1}{N} \left\{ \sum_{j=1}^{0.95N} (E_{T,j} - \langle E_T \rangle_{\text{patch}})^2 + \sum_{j=1}^{0.05N} (E_{T,j} - \langle E_T \rangle_{\text{patch}})^2 \right\}, \tag{4.4}$$

where the lowest 5% of patches is used to estimate the contribution to the variance from the highest 5%, this is done because the variance of E_T of hard-scatter jets is significantly larger than that of pileup jets.

3. Patches with transverse energy greater than a certain threshold are assumed to be from the hard-scatter interaction, while the remaining patches are associated with pileup. The threshold, based on $\langle E_T \rangle_{\text{patch}}$ and V_{patch}, is given by

$$E_T^{\text{threshold}} = \langle E_T \rangle_{\text{patch}} + n_\sigma \sqrt{V_{\text{patch}}}, \tag{4.5}$$

where n_σ is a parameter of the algorithm which has been tuned to $n_\sigma = 5$ to manage rate while maintaining efficiency.

4. The χ^2 function is built based on the previously stated assumptions. Its input includes the coordinates and areas of all patches, and the measured E_T in low energy patches. The explicit form of the χ^2 for n high-energy patches is $\chi^2 = \Delta^T V^{-1} \Delta$, where

$$\Delta = \begin{pmatrix} \sum_i E_{T,i} \cos\phi_i + \sum_k \varepsilon_{T,k} \cos\phi_k \\ \sum_i E_{T,i} \sin\phi_i + \sum_k \varepsilon_{T,k} \sin\phi_k \\ A_1 \times \langle \rho \rangle - \varepsilon_{T,1} \\ \vdots \\ A_n \times \langle \rho \rangle - \varepsilon_{T,n} \end{pmatrix}, \tag{4.6}$$

and

$$
\begin{aligned}
i &\in \text{low-energy patches} \\
k &\in \text{high-energy patches}, 1 \leq k \leq n \\
E_{T,i} &= \text{Measured transverse energy in patch } i \\
\varepsilon_{T,k} &= \text{Fitted transverse pileup energy in patch } k \\
\langle\rho\rangle &= \textstyle\sum_i E_i/A_0 = \text{Pileup energy density} \\
A_0 &= \text{Total area of low-energy patches} \\
A_k &= \text{Area of high-energy patch } k.
\end{aligned}
$$

The covariance matrix V is defined by

$$
V = \sum_i \sigma_i^2 \begin{pmatrix} \cos^2\phi_i & \cos\phi_i \sin\phi_i \\ \cos\phi_i \sin\phi_i & \sin^2\phi_i \end{pmatrix} \oplus sV_{\text{patch}}\mathcal{I}_n, \tag{4.7}
$$

where σ_i is the variance of the low-energy patch i, $\mathcal{I}_n$ is the n-dimensional identity matrix. The first two elements of Δ and the 2×2 matrix in V correspond to the first assumption of the `pufit` algorithm, while the remaining n elements of Δ and the matrix $sV_{\text{patch}}\mathcal{I}_n$ correspond to the second. The parameter s controls the relative strength of these two constraints and has been optimised to $s = 1$.

5. The χ^2 is minimised to find the pileup contribution to high-energy patches $\{\vec{\varepsilon}_{T,k}\}$.

6. $E_{\text{T}}^{\text{miss}}$ is estimated by a vector sum of the pileup-subtracted transverse energies of high-energy patches:

$$
\vec{E}_T^{\text{miss}} = -\sum_{k \in \text{high-energy patches}} (\vec{E}_{T,k} - \vec{\varepsilon}_{T,k}) \tag{4.8}
$$

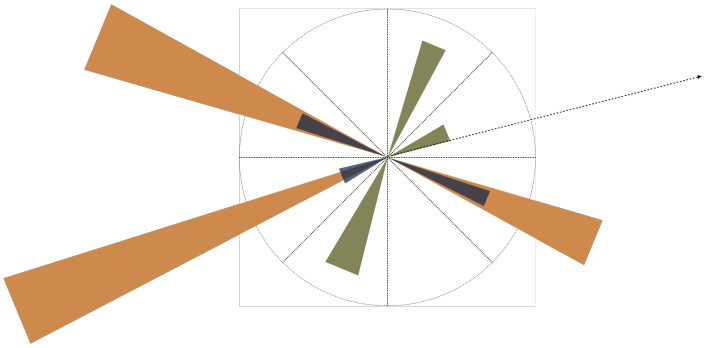

Figure 4.1: A cross-sectional cartoon of `pufit`. In the diagram, 8 divisions are taken over the ϕ coordinate; in `pufit`, an additional 14 divisions are taken over the η coordinate, giving 14×8 patches in $\eta \times \phi$. The orange triangles represent the magnitude of E_T in hard-scatter `pufit` patches, while the green triangles represent the same for pileup `pufit` patches. The length of the triangles represents the magnitude of the patch E_{T}, and the dotted circle represents the threshold between hard-scatter and pileup patches. This threshold is dependent on the mean and variance of E_T in the event. The blue triangles represent the fitted pileup energy within the hard-scatter patches. In the fit it is assumed pileup energy is evenly distributed in $\eta \times \phi$ and that its vector sum is zero. $E_{\mathrm{T}}^{\mathrm{miss}}$, shown as the dotted arrow, is estimated by the vector sum of the pileup-subtracted E_T of hard-scatter patches.

4.1.3 Trigger menu and naming conventions

Table 4.1 shows the primary $E_{\mathrm{T}}^{\mathrm{miss}}$ triggers used during Run-2. Listed are the HLT algorithms used, and the thresholds on L1 and HLT $E_{\mathrm{T}}^{\mathrm{miss}}$.

The naming convention used is as follows. Each trigger name is prefixed by "`HLT`" denoting that trigger was a software-based high-level trigger. The postfix "`L1XE50(55)`" indicates this trigger has been seeded by the `L1` trigger which requires $E_{\mathrm{T}}^{\mathrm{miss}} > 50(55)$ GeV. In between the prefix and the postfix, there are one or more tags `xe`xx indicating the requirement $E_{\mathrm{T}}^{\mathrm{miss}} > xx$ GeV as calculated by a trigger algorithm. The trigger algorithm used was `cell` unless otherwise indicated by the label after the `xe`xx tag. In 2017 a requirement of `cell` $E_{\mathrm{T}}^{\mathrm{miss}} > 50\,\mathrm{GeV}$ was imposed which is not explicit in the name.

As an example, the `HLT_xe110_pufit_xe65_L1XE50` trigger used in 2018 was seeded by the `L1` trigger requiring `L1` $E_{\mathrm{T}}^{\mathrm{miss}} > 50\,\mathrm{GeV}$. In the high-level trigger, `cell` $E_{\mathrm{T}}^{\mathrm{miss}} > 65\,\mathrm{GeV}$ and `pufit` $E_{\mathrm{T}}^{\mathrm{miss}} > 110\,\mathrm{GeV}$ were required.

Year	Trigger name	HLT algorithm [GeV]	L1 threshold [GeV]	HLT threshold [GeV]	$\int \mathcal{L}\,dt$ [fb^{-1}]
2015	HLT_xe70_mht_L1XE50	mht	50	70	3.5
2016	HLT_xe90_mht_L1XE50	mht	50	90	12.7
2016	HLT_xe110_mht_L1XE50	mht	50	110	30.0
2017	HLT_xe90_pufit_L1XE50	pufit, cell	50	90, 50	21.8
2017	HLT_xe100_pufit_L1XE50	pufit, cell	50	100, 50	33.0
2017	HLT_xe110_pufit_L1XE50(55)	pufit, cell	50 (55)	110, 50	47.7
2018	HLT_xe110_pufit_xe65_L1XE50	pufit, cell	50	110, 65	57.0
2018	HLT_xe110_pufit_xe70_L1XE50	pufit, cell	50	110, 70	62.6

Table 4.1: The primary $E_{\mathrm{T}}^{\mathrm{miss}}$ triggers used in Run-2. The L1 $E_{\mathrm{T}}^{\mathrm{miss}}$ threshold, HLT algorithm, and HLT $E_{\mathrm{T}}^{\mathrm{miss}}$ thresholds for every trigger is listed. Where more than one HLT algorithm was used, the first threshold was applied to the first algorithm, and the second threshold to the second algorithm. In 2017 a requirement on `cell` $E_{\mathrm{T}}^{\mathrm{miss}} > 50\,\mathrm{GeV}$ was applied that is not specified in the trigger name. The integrated luminosity for which each trigger was active is listed; some triggers were used concurrently, and therefore the integrated luminosities cannot be directly summed. Reproduced from Ref. [1].

4.2 Samples used and event selection

The samples used for performance studies in this chapter are described in this section.

As the $E_{\mathrm{T}}^{\mathrm{miss}}$ trigger is dependent on pileup, it is important to note the pileup distributions of the samples used. Figure 4.2 shows the distribution of average interactions per bunch crossing $\langle\mu\rangle$ for each data-taking year in Run-2. The distributions are scaled such that the area under each curve is unity. In 2017 and 2018 data, the distribution tends towards higher values of $\langle\mu\rangle$, and therefore is more suitable than 2015 and 2016 data for studies concerning trigger algorithm development for high pileup data-taking.

Samples of $\sqrt{s} = 13\,\mathrm{TeV}$ pp data collected by ATLAS were used for the studies in this chapter. They underwent the following reconstruction and overlap removal procedures (cf. Section 3.2.4).

Electrons and muons are required to have $p_{\mathrm{T}} > 25\,\mathrm{GeV}$, $|\eta| < 2.47$, impact parameter $|z_0 \sin\theta| < 0.5\,\mathrm{mm}$, and to pass `Medium` identification and `FCTight` isolation [75, 82]. Electrons additionally need to have impact parameter $|d_0/\sigma(d_0)| < 5$. For muons

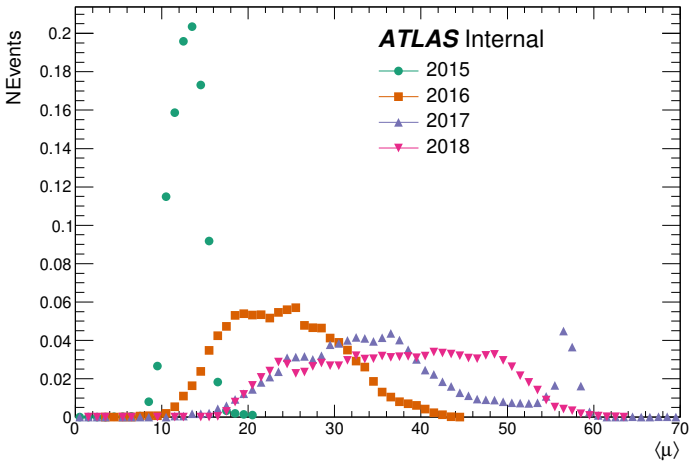

Figure 4.2: Pileup distribution in data collected by ATLAS in Run-2.

the requirement is $|d_0/\sigma(d_0)| < 3$.

Jets are reconstructed from topoclusters with the anti-k_t algorithm [87] with radius parameter $R = 0.4$. They are required to have $p_{\mathrm{T}} > 20\,\mathrm{GeV}$ and $|\eta| < 4.5$. Jets within $|\eta| < 2.5$ are required to pass the Jet Vertex Tagger [100], which determines the likelihood of a jet originating from the hard-scatter vertex.

Overlap removal is then performed sequentially as follows. Any jet within $\Delta R = \sqrt{\Delta\eta^2 + \Delta\phi^2} = 0.2$ of an electron is removed. Any electron within $\Delta R = 0.4$ of a remaining jet is removed. Any muon within $\Delta R = 0.4$ of a jet is removed if the jet has a least three charged tracks with $p_{\mathrm{T}} > 500\,\mathrm{MeV}$; otherwise the jet is removed.

Two different kinds of samples were used: $Z \to \mu\mu$, and `HLT_noalg`; the former sample consists of muon-triggered events which appear to the $E_{\mathrm{T}}^{\mathrm{miss}}$ trigger as events with $E_{\mathrm{T}}^{\mathrm{miss}}$, the latter sample is representative of the events accepted by the L1 trigger that are then processed by the HLT.

$\mathbf{Z \to \mu\mu}$ $Z \to \mu\mu$ events are selected from data with small ($\lesssim 1\%$) contamination from other processes by requiring a single- or di-muon trigger, exactly two muons, and no electrons. The muons must have opposite charge, and have dimuon invariant

mass consistent with the Z boson mass ($66.6\,\text{GeV} < m_{\mu\mu} < 116.6\,\text{GeV}$). These events are useful for measuring the performance of the trigger as a function of $E_{\text{T}}^{\text{miss}}$. Muons leave very little energy ($\sim$1 to 3 GeV) in the calorimeters; since the $E_{\text{T}}^{\text{miss}}$ trigger takes information only from the calorimeters, muons appear as missing momentum to the trigger. The p_{T} of the $Z \to \mu\mu$ system is used as a proxy for real $E_{\text{T}}^{\text{miss}}$. Additional reconstruction details can be found in Section 3.2.4 and Ref. [1].

`HLT_noalg` During data-taking, a small fraction of events which pass the `L1` $E_{\text{T}}^{\text{miss}}$ trigger are saved at random to comprise the `HLT_noalg` sample. No additional requirement is made at the HLT. This sample is representative of the environment faced by the HLT $E_{\text{T}}^{\text{miss}}$ trigger, and is used for studies concerning the event rate and rejection rate of the HLT. The fraction of high $E_{\text{T}}^{\text{miss}}$ events in this sample is negligible.

4.3 Performance studies

Performance of the $E_{\text{T}}^{\text{miss}}$ trigger is assessed by how well it accepts events with high $E_{\text{T}}^{\text{miss}}$, and whether its rate can be kept within its budget. Informed by trigger performance assessments, trigger thresholds are set as low as possible given the available rate budget to maximise efficiency to high $E_{\text{T}}^{\text{miss}}$ events.

Over the course of Run-2, the ATLAS experiment operated at unprecedented instantaneous luminosities of 0.5×10^{34} cm^{-2}s^{-1} to 2.0×10^{34} cm^{-2}s^{-1} [1], corresponding to on average 10 to 50 simultaneous pp interactions every 25 ns. Calculating $E_{\text{T}}^{\text{miss}}$ in the trigger in this environment proved to be challenging due to detector responses to non-hard-scatter interactions; different combinations of algorithms from Section 4.1.2 were used at different thresholds depending on the data-taking conditions. Overall the trigger accepted close to 100% of events with $E_{\text{T}}^{\text{miss}} > 200\,\text{GeV}$ across all values of pileup.

Performance and optimisation of the $E_{\text{T}}^{\text{miss}}$ trigger in the first two-years of Run-2 was documented in Ref. [98]. In this section, I present an assessment of the trigger performance using the whole Run-2 dataset. The work documented here forms a

significant part of the $E_{\mathrm{T}}^{\mathrm{miss}}$ trigger performance paper which has been published in the *Journal of High-Energy Physics* [1].

The measures of trigger performance are introduced in Section 4.3.1. The overall performance of the trigger in Run-2 is overviewed in Section 4.3.2, while the performance of individual algorithms and their combinations are described in Sections 4.3.3 and 4.3.4 respectively.

4.3.1 Measures of trigger performance

In this section, the performance of the trigger is measured by the following three metrics:

Rate Rate measures the number of events accepted by the $E_{\mathrm{T}}^{\mathrm{miss}}$ trigger per second. It is imperative that the rate of the trigger remains within its budget to prevent the rejection of events due to insufficient computing power.

Acceptance Acceptance measures how many events out of those presented to the trigger are accepted by the trigger. This can be converted to give an event rate (and vice versa). It is measured from the $E_{\mathrm{T}}^{\mathrm{miss}}$ distribution of an `HLT_noalg` sample, where $E_{\mathrm{T}}^{\mathrm{miss}}$ is calculated by emulations of the online trigger algorithms.

Efficiency Efficiency is defined as the fraction of events passing the trigger as a function of $E_{\mathrm{T,offline}}^{\mathrm{miss}}$:

$$\text{Efficiency}(E_{\mathrm{T,offline}}^{\mathrm{miss}}, \langle\mu\rangle) = \frac{N(\text{passed trigger}|E_{\mathrm{T,offline}}^{\mathrm{miss}}, \langle\mu\rangle)}{N(E_{\mathrm{T,offline}}^{\mathrm{miss}}, \langle\mu\rangle)}. \tag{4.9}$$

In this calculation, $E_{\mathrm{T,offline}}^{\mathrm{miss}}$ is defined with respect to some offline measure, rather than the value of $E_{\mathrm{T}}^{\mathrm{miss}}$ as calculated in the trigger. The behaviour of the efficiency of the ideal $E_{\mathrm{T}}^{\mathrm{miss}}$ trigger is that of a step function: zero efficiency below a threshold $E_{\mathrm{T,offline}}^{\mathrm{miss}}$ value, and 100% efficiency immediately above the threshold. In practice the efficiency increases gradually from 0% to 100%, subject to the $E_{\mathrm{T}}^{\mathrm{miss}}$ resolution, which is the difference between $E_{\mathrm{T,offline}}^{\mathrm{miss}}$ and trigger $E_{\mathrm{T}}^{\mathrm{miss}}$.

Pileup significantly degrades the $E_{\mathrm{T}}^{\mathrm{miss}}$ resolution [1, 98], and therefore the efficiency of the trigger can also be measured in bins of pileup.

For studies shown in this thesis, efficiency is measured with $Z \to \mu\mu$ events in data. The transverse momentum of the $\mu\mu$ system $p_{\mathrm{T}}(\mu\mu)$ can be used as a proxy for $E_{\mathrm{T,offline}}^{\mathrm{miss}}$ as muons are invisible to the calorimeter and therefore appear as $E_{\mathrm{T}}^{\mathrm{miss}}$ to the trigger.

Stability

$$\mathrm{Stability}(\langle\mu\rangle) = \frac{N(\text{passed trigger}|E_{\mathrm{T,offline}}^{\mathrm{miss}} > x, \langle\mu\rangle)}{N(E_{\mathrm{T,offline}}^{\mathrm{miss}} > x, \langle\mu\rangle)}. \tag{4.10}$$

Stability is a measure of the trigger efficiency dependence on pile-up $\langle\mu\rangle$ for some fixed selection $E_{\mathrm{T,offline}}^{\mathrm{miss}} > x$. As $E_{\mathrm{T}}^{\mathrm{miss}}$ resolution worsens with $\langle\mu\rangle$, it is important to evaluate whether the trigger efficiency is also dependent on $\langle\mu\rangle$. In the ideal case, the dependence should be negligible.

4.3.2 Overall performance

First the performance of the trigger in the whole of Run-2 is summarised.

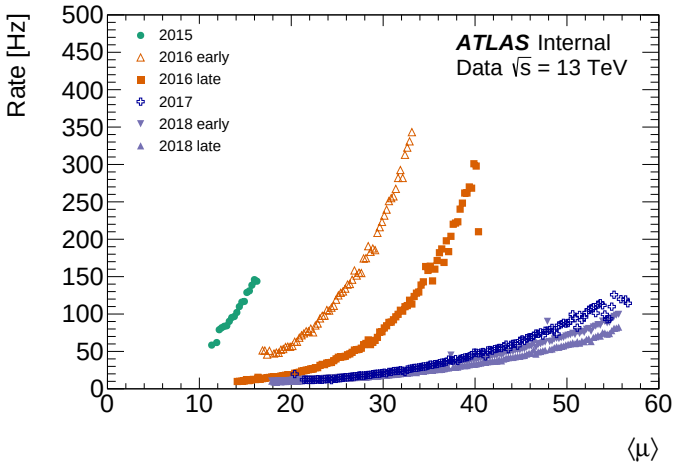

Figure 4.3: The rate of the $E_{\mathrm{T}}^{\mathrm{miss}}$ trigger as a function of pileup over various data-taking periods. This Figure was produced by the $E_{\mathrm{T}}^{\mathrm{miss}}$ trigger group.

Figure 4.3 shows the rate of the $E_{\mathrm{T}}^{\mathrm{miss}}$ trigger as a function of pileup over various data-taking periods. In 2015 and 2016, the rate of the trigger rose rapidly with pileup.

The rate curve for early 2016 is translated to the right compared to 2015, and covers a wider range of pileup. A similar translation and widening of pileup range is observed for the curve of late 2016. The `mht` trigger was used at this time, as shown in Table 4.1. Its threshold was adjusted between these periods to mitigate the increase in rate due to increased pileup. In early 2015 the trigger rate was approximately 50 Hz at $\langle\mu\rangle = 12$, but was reduced to about 10 Hz at $\langle\mu\rangle = 14$ in late 2016. It is clear, however, that the trigger rate rose drastically with increasing $\langle\mu\rangle$, peaking in early 2016 at 350 Hz when $\langle\mu\rangle = 32$ and in late 2016 at 300 Hz when $\langle\mu\rangle = 40$.

In 2017 and 2018, the increase in rate was much less dramatic due to the use of triggers with thresholds on both `cell` $E_{\mathrm{T}}^{\mathrm{miss}}$ and `pufit` $E_{\mathrm{T}}^{\mathrm{miss}}$. The rate of the trigger was reduced from 300 Hz at $\langle\mu\rangle = 40$ in late 2016 to 80 Hz at $\langle\mu\rangle = 56$ in late 2018. This allowed the trigger to operate even at $\langle\mu\rangle > 50$ with rates below 150 Hz. Similar to 2015 and 2016, the thresholds were adjusted periodically to reduce rate, giving the flatter rate curves in 2018 compared to 2017.

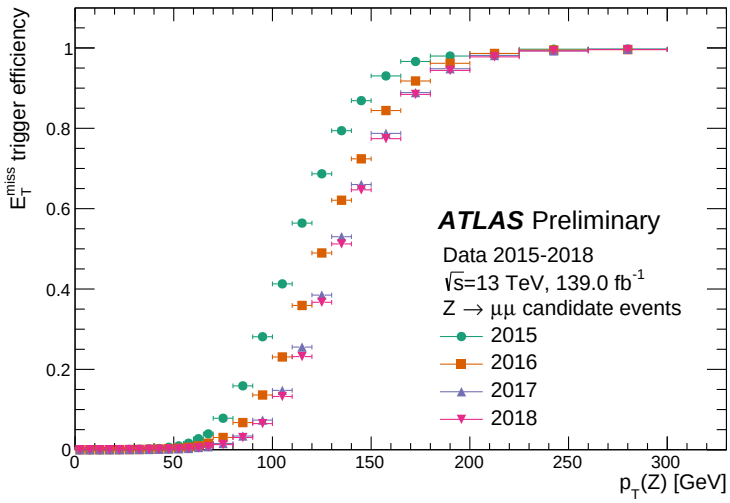

Figure 4.4: The efficiency of the $E_{\mathrm{T}}^{\mathrm{miss}}$ trigger to $Z \to \mu\mu$ events in data as a function of $p_{\mathrm{T}}(Z \to \mu\mu)$ over various data-taking years. The value of $p_{\mathrm{T}}(Z)$ in these events is used as a proxy for $E_{\mathrm{T}}^{\mathrm{miss}}$.

Figure 4.4 shows the efficiency of the $E_{\mathrm{T}}^{\mathrm{miss}}$ trigger to $Z \to \mu\mu$ events in data as

a function of $p_{\mathrm{T}}(Z \to \mu\mu)$ over the four years of Run-2. The value of $p_{\mathrm{T}}(Z)$ in these events is used as a proxy for $E_{\mathrm{T}}^{\mathrm{miss}}$. Owing to the different trigger algorithms used and adjustment of trigger thresholds each year, the corresponding efficiency curves are slightly different. In later data-taking years, the efficiency to events with intermediate $p_{\mathrm{T}}(Z)$ is reduced, corresponding to the decrease in rate seen in Figure 4.3. However, the efficiency at $p_{\mathrm{T}}(Z) > 200\,\mathrm{GeV}$ remained constant.

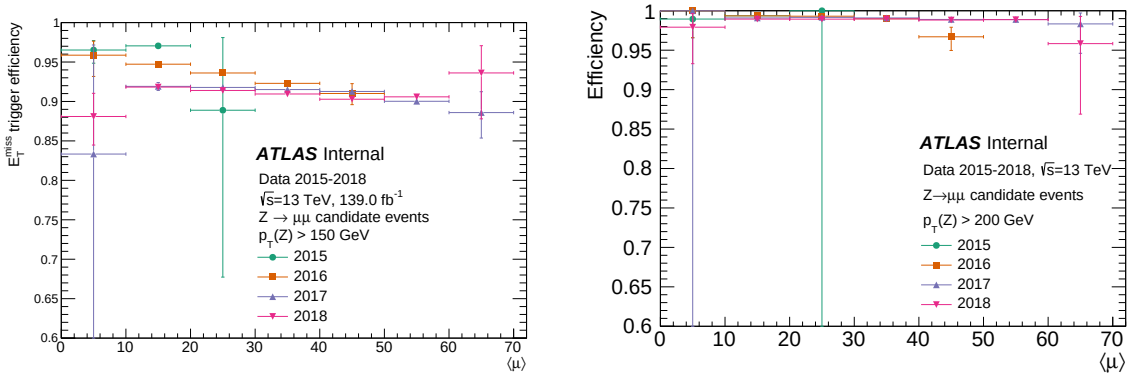

(a) **(b)**

Figure 4.5: The stability of the $E_{\mathrm{T}}^{\mathrm{miss}}$ trigger as a function of to $Z \to \mu^+\mu^-$ events with (a) $p_{\mathrm{T}}(Z) > 150$ GeV and (b) $p_{\mathrm{T}}(Z) > 200$ GeV as a function of average pileup over various data-taking years.

Figure 4.5 shows the stability of the $E_{\mathrm{T}}^{\mathrm{miss}}$ trigger to $Z \to \mu\mu$ events in data as a function of average pileup over the four years of Run-2. For the case when $p_{\mathrm{T}}(Z) > 150\,\mathrm{GeV}$, a dependence on the data-taking year and pileup is observed. In 2015, the stability was about 96%. In 2016, the stability shows a slight pileup dependence, decreasing from about 95% in $\langle\mu\rangle \in [0, 10)$ to about 90% in $\langle\mu\rangle \in [40, 50)$. In 2017 and 2018, when the `cell+pufit` combination was used, the stability remained largely stable at about 90% across all values of pileup. When evaluating stability on events with $p_{\mathrm{T}}(Z) > 200\,\mathrm{GeV}$, where the trigger efficiency plateaus, the stability of the trigger is roughly constant across pileup at $> 98\%$ for all years.

4.3.3 Algorithm performance

The performance of the three main $E_{\mathrm{T}}^{\mathrm{miss}}$ trigger algorithms — `cell`, `pufit`, and `mht` — are evaluated.

The acceptance rate of each trigger as a function of the algorithm $E_{\mathrm{T}}^{\mathrm{miss}}$ was measured in a `HLT_noalg` sample (Figure 4.6 left). For `cell`, the acceptance rate does not depend greatly on $\langle\mu\rangle$; for `pufit`, around the threshold value of `pufit` $E_{\mathrm{T}}^{\mathrm{miss}} \sim 100\,\mathrm{GeV}$, the acceptance rate increases slightly with $\langle\mu\rangle$. The `mht` acceptance rate is generally higher than for other algorithms, and it varies greatly with $\langle\mu\rangle$: at `mht` $E_{\mathrm{T}}^{\mathrm{miss}} \sim 100\,\mathrm{GeV}$, the acceptance rate increases by a factor of three across the the pileup range — from 0.7×10^{-1} to 2×10^{-1}. The great variance of the `mht` acceptance curve with pileup echoes the dramatic increase in rate of the `mht` trigger seen in Figure 4.3. Considering that most of the events in the `HLT_noalg` sample have little to no $E_{\mathrm{T}}^{\mathrm{miss}}$, the high acceptance of `mht` implies that, when using `mht`, the $E_{\mathrm{T}}^{\mathrm{miss}}$ trigger rate is being spent on events that ought to be rejected.

We now evaluate the same-rate efficiency of the algorithms. As before, efficiency is measured as a function of $p_{\mathrm{T}}(Z)$ in $Z \to \mu\mu$ events, where $p_{\mathrm{T}}(Z)$ is a proxy for real $E_{\mathrm{T}}^{\mathrm{miss}}$. The thresholds on the algorithms were set such that, in each bin of $\langle\mu\rangle$, the acceptance rate is 3×10^{-2}. This represents a case where the trigger thresholds are adjusted based on data-taking conditions in order to maintain the same rate. The threshold for `cell` was constant over pileup, while the thresholds for `mht` and `pufit` were pileup dependent — increasing from 95 GeV to 110 GeV for `pufit`, and from 110 GeV to 150 GeV for `mht`.

Figure 4.6 right shows that, the efficiency curves for `cell` and `pufit` have a slight pileup dependence, but those for `mht` greatly depend on pileup. In the region $p_{\mathrm{T}}(Z) > 200\,\mathrm{GeV}$, it is seen that the efficiencies of `cell` and `pufit` reach $> 95\%$ across all values of pileup, while for `mht` at high pileup the efficiency is only 80%. Not only, then, does `mht` tend to accept events which ought to be rejected, but it also fails to be efficient to events that should be accepted.

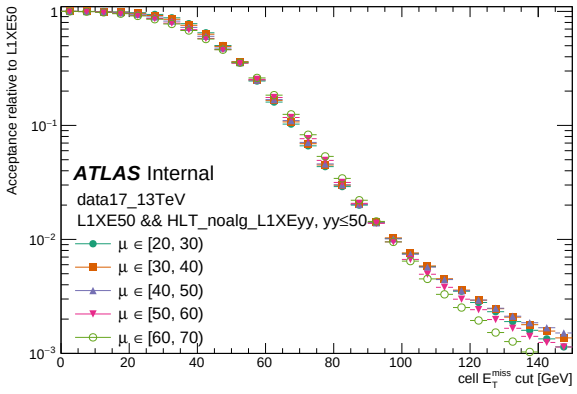

(a) `cell` acceptance

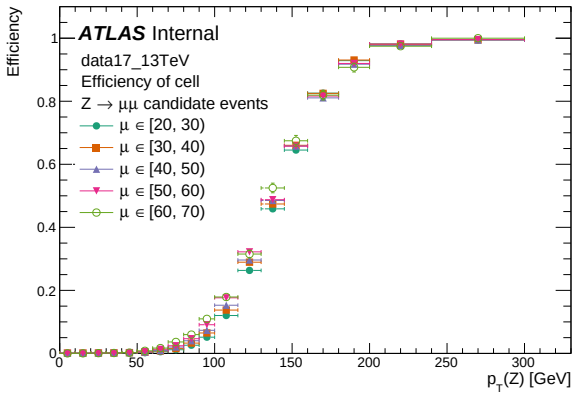

(b) `cell` same-rate efficiencies

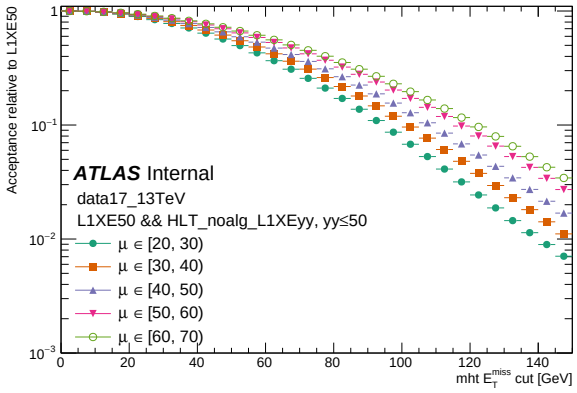

(c) `mht` acceptance

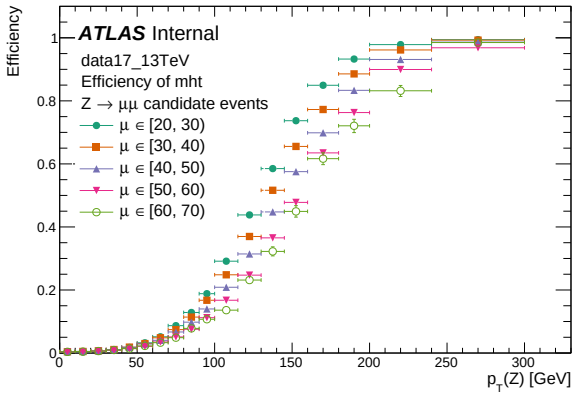

(d) `mht` same-rate efficiencies

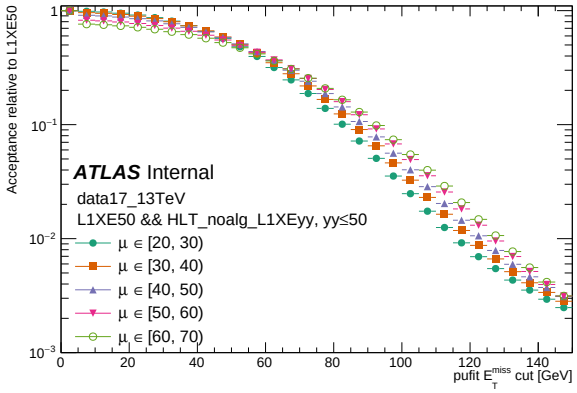

(e) `pufit` acceptance

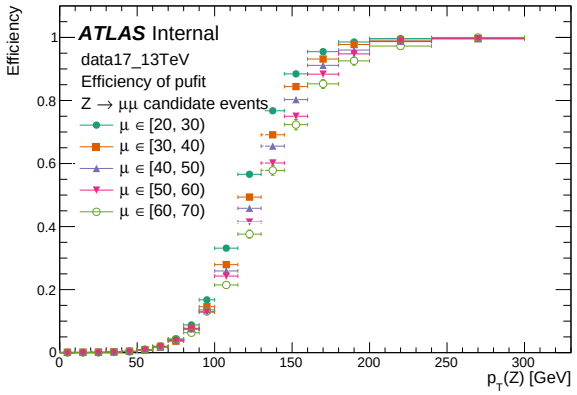

(f) `pufit` same-rate efficiencies

Figure 4.6: Left: The acceptance of `cell`, `mht`, and `pufit` as a function of the algorithm $E_{\mathrm{T}}^{\mathrm{miss}}$ and pileup as measured in an `HLT_noalg` sample of 2017 data. Right: The same-rate efficiencies of `cell`, `mht`, and `pufit` in bins of pileup are compared. The algorithm thresholds are set such that the acceptance is 3×10^{-2} for every algorithm in every pileup bin.

Therefore we see that the performance with respect to pileup of `mht` is significantly worse than that of `cell` and `pufit`. For `mht` to maintain high efficiency, it would have needed a significantly larger rate budget; given that in 2017 and 2018 the pileup increased up to $\langle\mu\rangle \sim 70$, the $E_{\mathrm{T}}^{\mathrm{miss}}$ trigger rate would likely have been in excess of 500 Hz (cf. Figure 4.3), which is infeasibly high. Beginning 2017, a combination of `cell` and `pufit`, which are much more efficient at lower rates, allowed the $E_{\mathrm{T}}^{\mathrm{miss}}$ trigger to maintain a reasonable rate at high pileup.

4.3.4 Combination performance

In 2016, the effectiveness of having requirements on both `mht` $E_{\mathrm{T}}^{\mathrm{miss}}$ and `cell` $E_{\mathrm{T}}^{\mathrm{miss}}$ was investigated. It was found that mismeasured $E_{\mathrm{T}}^{\mathrm{miss}}$ was uncorrelated across both algorithms while real $E_{\mathrm{T}}^{\mathrm{miss}}$ was highly correlated. Therefore operating a trigger with thresholds on both algorithms could be highly effective for rejecting events with little to no $E_{\mathrm{T}}^{\mathrm{miss}}$, while being highly efficient for events with high $E_{\mathrm{T}}^{\mathrm{miss}}$ [98].

As demonstrated in the previous section, `pufit` is much more stable against pileup than `mht`. Therefore a combination of `cell` $E_{\mathrm{T}}^{\mathrm{miss}}$ and `pufit` $E_{\mathrm{T}}^{\mathrm{miss}}$ was taken instead. An evaluation of the performance of this combination is presented below.

Figure 4.7 shows the correlations of `cell` $E_{\mathrm{T}}^{\mathrm{miss}}$ and `pufit` $E_{\mathrm{T}}^{\mathrm{miss}}$ in two samples of 2017-2018 data: an `HLT_noalg` sample and a $Z \to \mu\mu$ sample where $p_{\mathrm{T}}(Z) > 175\,\mathrm{GeV}$. Events in the former sample mostly have no real $E_{\mathrm{T}}^{\mathrm{miss}}$ and should be rejected by the trigger, while events in the latter sample should be accepted. It can be seen that the trigger $E_{\mathrm{T}}^{\mathrm{miss}}$ for non-$E_{\mathrm{T}}^{\mathrm{miss}}$ events is concentrated at low values, but a large number of these events still have either high `pufit` $E_{\mathrm{T}}^{\mathrm{miss}}$ or high `cell` $E_{\mathrm{T}}^{\mathrm{miss}}$. By comparison, $E_{\mathrm{T}}^{\mathrm{miss}}$ events typically have both high `pufit` $E_{\mathrm{T}}^{\mathrm{miss}}$ and high `cell` $E_{\mathrm{T}}^{\mathrm{miss}}$. Therefore the rejection of unwanted events is enhanced by requirements on both algorithms rather than on just one. Acceptance of high $E_{\mathrm{T}}^{\mathrm{miss}}$ events, however, is relatively unaffected as most events pass both requirements.

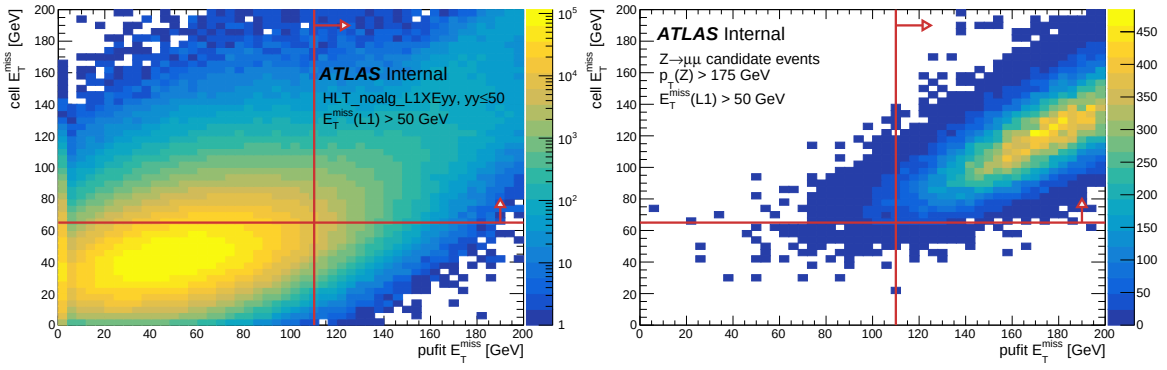

(a) (b)

Figure 4.7: The distribution in 2017 and 2018 data of `cell` $E_{\mathrm{T}}^{\mathrm{miss}}$ and `pufit` $E_{\mathrm{T}}^{\mathrm{miss}}$ in (a) an `HLT_noalg` sample and (b) a $Z \to \mu\mu$ sample where $p_{\mathrm{T}}(Z) > 175\,\mathrm{GeV}$. Lines are drawn representing the requirements of a trigger requiring `cell` $E_{\mathrm{T}}^{\mathrm{miss}} > 65\,\mathrm{GeV}$ and `pufit` $E_{\mathrm{T}}^{\mathrm{miss}} > 110\,\mathrm{GeV}$, which was active in late 2018. Events in the upper right hand quadrant would be accepted, while the remaining would be rejected.

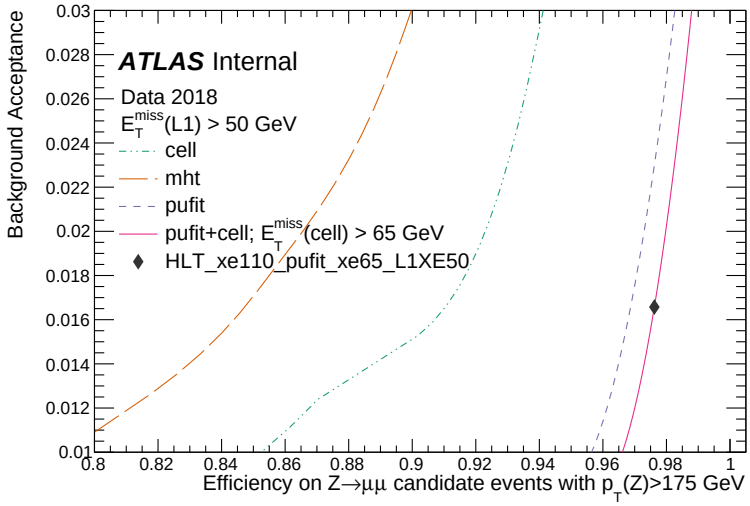

Figure 4.8: ROC curves comparing the performance of `cell`, `mht`, `pufit`, and a combined `cell+pufit` trigger. Efficiency to $Z \to \mu\mu$ events with $p_{\mathrm{T}}(Z) > 175\,\mathrm{GeV}$ is plotted against the fraction of `L1XE50`-passing events accepted by the HLT. A point corresponding to one of the implemented triggers is shown.

The effect of the combination is shown in Figure 4.8, where the acceptances and efficiencies of `cell`, `mht`, `pufit`, and a combined `cell+pufit` trigger are compared. Using 2018 data, the background acceptance was evaluated on an `HLT_noalg` sample, while the efficiencies were measured to $Z \to \mu\mu$ events with $p_{\mathrm{T}}(Z) > 175$ GeV. The performance of `mht` is significantly worse than `cell` and `pufit`. It is also seen that, despite the great pileup-stability of `cell`, `pufit` is seen to give greater efficiency at lower rate. However, combining `pufit` with `cell` still gives better performance: at the same efficiency, the background acceptance drops from $\sim 2.25 \times 10^{-2}$ to $\sim 1.65 \times 10^{-2}$, corresponding to a $\sim 26\%$ reduction in rate; alternatively a percentage point can be gained in efficiency while holding the background acceptance (i.e. trigger rate) constant.

4.3.5 Summary

Despite the factor 4 increase in instantaneous luminosity of Run-2 compared to Run-1, the $E_{\mathrm{T}}^{\mathrm{miss}}$ trigger remained fully efficient with manageable data rates. Its outstanding performance is owed to the adoption of pileup mitigating strategies, in particular applying requirements on both `cell` $E_{\mathrm{T}}^{\mathrm{miss}}$ and `pufit` $E_{\mathrm{T}}^{\mathrm{miss}}$ was shown to be highly effective.

4.4 Software migration

During my tenure as software manager of the $E_{\mathrm{T}}^{\mathrm{miss}}$ trigger from Aug 2018 to Jul 2020, I migrated the $E_{\mathrm{T}}^{\mathrm{miss}}$ trigger software to a new software framework in preparation for data-taking in Run-3.

The ATLAS software framework *Athena* is responsible for handling object reconstruction and most physics analysis within the experiment. There is an experiment-wide effort in ATLAS to migrate Athena to a multi-threaded version, *AthenaMT*. Memory consumption is lower with multi-threading [101].

This migration is particularly significant for the trigger. In Run-1 and Run-2, the HLT had been using its own steering software, separate from Athena, which implemented trigger-specific designs such as trigger menus and chains. Offline reconstruction algorithms needed to be wrapped in a special interface layer to be used in the HLT. However, beginning with Run-3, the trigger-specific designs will be implemented in AthenaMT, allowing the trigger to use Athena instead of its custom steering software. This means offline algorithms can be easily used in the trigger without the previously needed intermediate layer (and with some parameters adjusted such that they can run with low latency). This is projected to reduce the differences between offline and online reconstruction, giving the trigger sharper efficiency curves. For the $E_{\mathrm{T}}^{\mathrm{miss}}$ trigger, the use of offline $E_{\mathrm{T}}^{\mathrm{miss}}$ reconstruction algorithms will not be possible because the calibrations available for offline physics objects will not all be available in the trigger. However, $E_{\mathrm{T}}^{\mathrm{miss}}$ trigger algorithms will be able to make use of jets or particle flow objects reconstructed with offline algorithms.

Concurrent with the AthenaMT migration, it had become clear that the $E_{\mathrm{T}}^{\mathrm{miss}}$ trigger software itself was in need of a redesign. When it was written initially, the $E_{\mathrm{T}}^{\mathrm{miss}}$ trigger software was designed to support only one trigger algorithm (`cell`), but had since been extended poorly to support multiple algorithms. It had become fairly difficult to track down bugs or add new algorithms. Therefore it was necessary to improve the legibility of the code to allow for the easy addition and modification of trigger algorithms to support the trigger's development, maintenance, and operation in Run-3 and beyond.

The $E_{\mathrm{T}}^{\mathrm{miss}}$ trigger software was redesigned to allow for easy algorithm development, and to be compliant with AthenaMT and its new trigger steering software.

Three different components of the $E_{\mathrm{T}}^{\mathrm{miss}}$ trigger code were rewritten: reconstruction, hypothesis, and configuration. Continuous integration and nightly tests were written and deployed to detect unexpected changes in behaviour. The code logic along with dummy examples of how the code could be used were documented in the code's git repository for the benefit of other developers, particularly future students [102].

The reconstruction code is where the $E_{\mathrm{T}}^{\mathrm{miss}}$ algorithms (`cell`, `pufit`, `mht`) are implemented. This was the most convoluted and the most difficult to rewrite. As an example, the original class which contained the logic for the `cell` algorithm was 764 lines long. Its many duplicate methods were consolidated. Iterations over indices (which were difficult to keep track of) were replaced with iterations over enums (which were given easily understandable names). The new class was simplified to be only 161 lines long while preserving all useful functionality.

Data flow within the reconstruction code was improved. A simplified diagram of my planned design change is shown in Figure 4.9. In the original design, the $E_{\mathrm{T}}^{\mathrm{miss}}$ trigger algorithms (`cell`, `mht` etc) were written in `C++` classes with names `EFMissingETFrom`$\cdots$, where $\cdots$ was the name of the algorithm. `EFMissingETFrom`$\cdots$ would return a vector of `TrigEFMissingETComponent`s. Each component contained the variables for some component of the detector. The components would then be summed in the class `EFMissingETFromHelper`, which would then output a final `TrigEFMissingET` object. The `TrigEFMissingET` object contained the $E_{\mathrm{T}}^{\mathrm{miss}}$ value considered by the hypothesis code, which made the trigger decisions. The classes `EFMissingETHelper` and `EFMissingETFromHelper` were originally intended to aid in debugging the `cell` algorithm by grouping variables according to different components of the detector. However, not only were these intermediate steps not useful, but the circuitous design of the data flow made it unnecessarily difficult to implement new algorithms and find bugs.

In the new design, it was intended for the `TrigEFMissingET` object to be created directly by the `EFMissingETFrom`$\cdots$ algorithm, thereby removing the intermediate `EFMissingETHelper` and `EFMissingETFromHelper` classes. At the point this rewrite was handed over to a collaborator, the extraneous `EFMissingETFromHelper` class had successfully been removed. The `EFMissingETHelper` object was being used by the `EFMissingETFrom`$\cdots$ algorithms to directly output the `TrigEFMissingET` object.

The hypothesis and configuration code was written from scratch to be compatible with the new trigger steering software in AthenaMT. The hypothesis itself simply

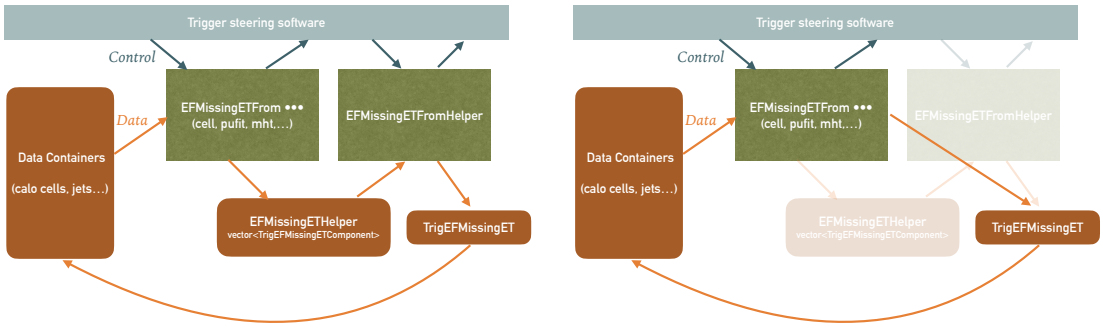

(a) Run-2 software design **(b)** My software design

Figure 4.9: Diagrams of the $E_{\mathrm{T}}^{\mathrm{miss}}$ trigger reconstruction software before my rewrite and my planned redesign. The blue and orange arrows represent control and data flows respectively. The $E_{\mathrm{T}}^{\mathrm{miss}}$ trigger algorithms took calorimeter cells, topoclusters, jets as input, and output a `TrigEFMissingET` object which contained the reconstructed $E_{\mathrm{T}}^{\mathrm{miss}}$ value. In Run-2 the trigger had dedicated steering software, while in Run-3 the trigger will use AthenaMT.

implemented the boolean decision of whether the calculated $E_{\mathrm{T}}^{\mathrm{miss}}$ of an event was greater than a certain threshold (cf. Table 4.1). The configuration code set up the control and data flows needed to execute the reconstruction and hypothesis within AthenaMT.

During migration, unit tests were written to be executed automatically every night and for every merge request which affected the $E_{\mathrm{T}}^{\mathrm{miss}}$ trigger code. These tests ensured that, as the development of the trigger software continued, any changes that impacted the $E_{\mathrm{T}}^{\mathrm{miss}}$ trigger were known. Moreover, in the reconstruction and hypothesis code, interesting variables such as E_{T}, ΣE_{T}, and the execution time were saved into monitoring histograms which were regularly reviewed. With tests and monitoring in place, unexpected behaviour could be noticed and rectified early, well before the start of data-taking.

The migration of the $E_{\mathrm{T}}^{\mathrm{miss}}$ trigger software was completed in summer 2019, earlier than other trigger signatures, and two years before the then-expected start date of Run-3 data-taking. This work paved the way for other collaborators to further improve the software design of the $E_{\mathrm{T}}^{\mathrm{miss}}$ trigger with greater modularisation, less duplicated code, and improved readability.

4.5 Trigger algorithm development – pufitjet

While the rate of the $E_{\mathrm{T}}^{\mathrm{miss}}$ trigger has been relatively stable in the high pileup environments of 2017 and 2018, it is expected that pileup may increase up to $\langle\mu\rangle \sim 140$ in Runs-3 and 4. Given the $E_{\mathrm{T}}^{\mathrm{miss}}$ trigger rate is expected to increase exponentially with pileup [1], it is desirable to seek out algorithms which have weaker pileup dependence.

As part of this effort, I developed and studied the performance of `pufitjet`, where the `pufit` algorithm is modified to use jets instead of topoclusters as its input objects. A jet consists of a group of pileup-corrected [88] topoclusters. `pufitjet` then attempts to take advantage of this pileup correction in addition to the `pufit` χ^2 fit.

4.5.1 Description of the `pufitjet` algorithm

The steps of the `pufitjet` algorithm, based on the original `pufit` algorithm (c.f. Section 4.1.2), are as follows:

1. In an event, divide the jets into high-energy jets and low-energy jets. High-energy jets are assumed to be from the hard-scatter interaction, and low-energy jets from pileup. The energy threshold which divided them was subject to optimisation.

2. Divide the $\eta \times \phi$ space into 112 patches with size $\eta \times \phi = 0.714 \times 0.785$ as before. The transverse energy of each patch j which does not overlap in $\eta \times \phi$ with a high-energy jet is the sum of transverse energies of topoclusters within the patch not clustered to the high-energy jets.

$$E_{T,j} = \sum_{i \in \text{topoclusters within patch } j} E_{T,i} \tag{4.11}$$

3. Construct and minimise the χ^2 as before (Eq. 4.6 and 4.7) to find the energy corrections to patches which overlap with high-energy jets.

4. $E_{\mathrm{T}}^{\mathrm{miss}}$ is calculated from the sum of energies of high-energy jets and the pileup corrections to high-energy patches.

$$\vec{E}_T^{\mathrm{miss}} = -\Big[\sum_{m\in\text{high-energy jets}} \vec{E}_{T,m} - \sum_{k\in\text{high-energy patches}} \vec{\varepsilon}_{T,k}\Big] \tag{4.12}$$

4.5.2 Optimisation of the jet threshold

Different thresholds on jet p_{T} were tested to differentiate between jets from hard-scatter and jets from pileup.

Fixed threshold A fixed threshold on $p_T^{\mathrm{jet}} \in \{20, 30, 40, 50, 60\}$ GeV was tested. The threshold for *forward* ($|\eta| > 2.4$) jets was optimised separately from that for *central* ($|\eta| < 2.4$) jets as there tends to be more pileup energy in the forward region.

Dynamic threshold A dynamic threshold based on that of the existing `pufit` algorithm (Eq. 4.5) was also tested. It has been shown in internal studies that the dynamic threshold of `pufit` is a major contributor to its pileup-robustness.

$$\begin{aligned} \langle E_T\rangle_{\text{patch}} &= \frac{1}{N}\sum\nolimits_{j=1}^{0.90N} E_{T,j} \\ V_{\text{patch}} &= \langle E_T^2\rangle_{\text{patch}} - \langle E_T\rangle_{\text{patch}}^2 \\ E_T^{\text{thres}} &= \langle E_T\rangle_{\text{patch}} + n_\sigma\sqrt{V_{\text{patch}}} \end{aligned} \tag{4.13}$$

Here N = number of jets. Since jets are required to have $E > 15\,\mathrm{GeV}$, most soft contributions have already been removed, therefore the sample mean and variance are taken over the lowest energy 90% of jets instead of the middle 90%.

4.5.3 Results

Trigger algorithm performance was measured, as before, by the algorithm's efficiency to events with high $E_{\mathrm{T}}^{\mathrm{miss}}$ and rejection of events with little-or-no $E_{\mathrm{T}}^{\mathrm{miss}}$. Signal events are taken to be $Z \to \mu\mu$ events from 2017. Only every fifth run was considered in this

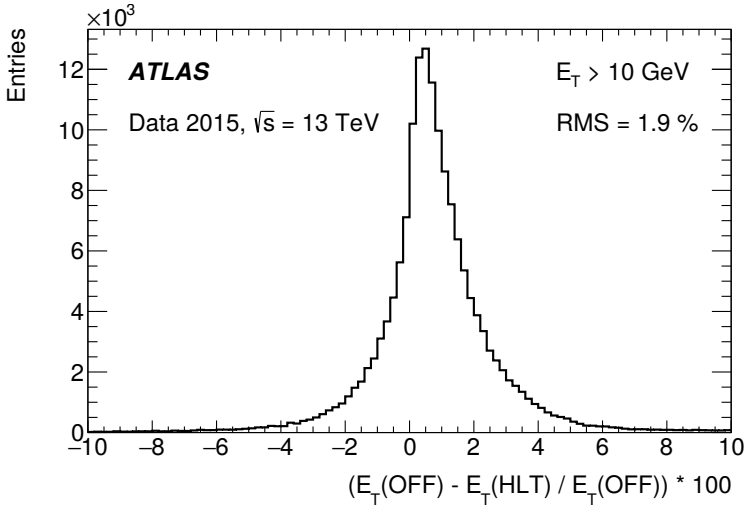

Figure 4.10: The relative difference in E_T of HLT topoclusters compared to offline topoclusters for data collected in 2015. Reproduced from Ref. [77].

selection, as this already provided sufficient event yields for the study. Background events are taken from an `HLT_noalg` sample of all 2017 data.

The performance of emulations of the `pufitjet` variants are compared to an emulation of the `pufit` algorithm, and to the existing online `pufit` algorithm. Emulated algorithms were implemented in offline analysis software, while the online algorithms were implemented in the HLT. The main difference between two was the use of HLT topoclusters online and offline topoclusters offline. HLT and offline topoclusters differ mainly in energy calibration (Figure 4.10); the resolution is about 2% for clusters above 10 GeV [77].

In Figure 4.11 the fixed threshold variants of `pufitjet` are compared against `pufit` $E_{\mathrm{T}}^{\mathrm{miss}}$. The performance of `pufitjet` depends strongly on the central jet threshold and weakly on the forward jet threshold. `pufitjet` is comparable to `pufit` when requiring central jet $p_T > 30$ GeV, but is worse when requiring $p_{\mathrm{T}} > 40$ GeV.

In Figure 4.12 the performance of the dynamic threshold variants of `pufitjet` is shown. The parameter n_σ is varied from 0 to 1. The traditional `pufit` algorithm performs better than these variants.

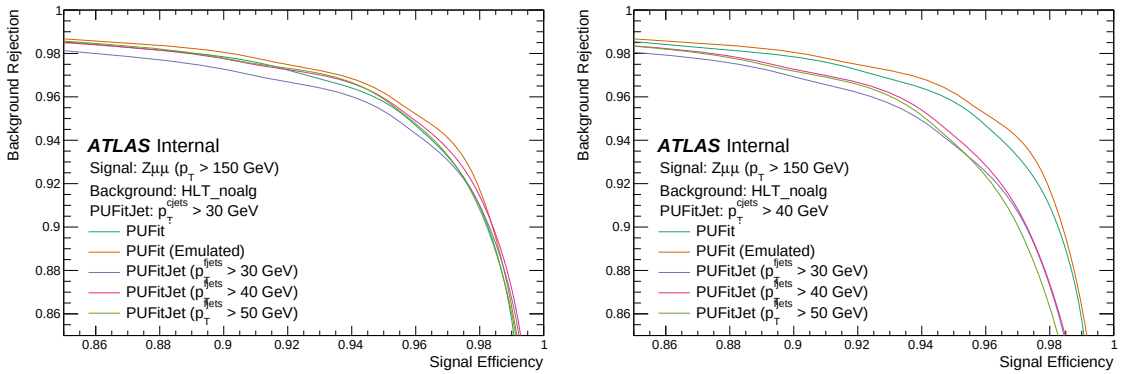

(a) Central jets $p_T > 30$ GeV **(b)** Central jets $p_T > 40$ GeV

Figure 4.11: ROC curves comparing the performance of the `pufit` algorithm with those of the fixed threshold `pufitjet` algorithms. In each plot, the forward jet p_T threshold ($p_{\mathrm{T}}^{\mathrm{fjets}}$) in GeV is selected from $\{30, 40, 50\}$.

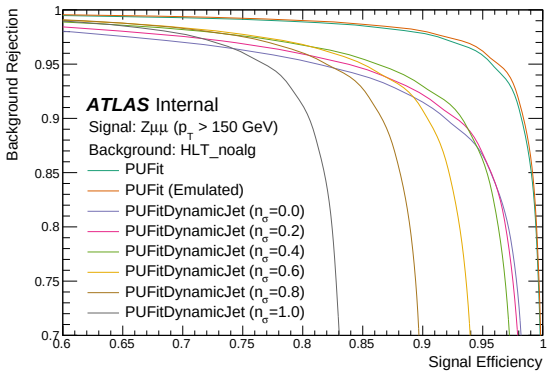

Figure 4.12: ROC curves comparing the performance of the `pufit` algorithm with those of the dynamic threshold `pufitjet` algorithms. The parameter n_σ is adjusted for the dynamic threshold.

4.5.4 Discussion

The `pufitjet` algorithm was developed with the aim of being a pileup-resistant, efficient, low-rate $E_{\mathrm{T}}^{\mathrm{miss}}$ trigger algorithm to supersede `pufit`. However, none of the `pufitjet` variants attempted were shown to outperform `pufit` in 2017 data. This study could be extended in future by measuring the performance of `pufitjet` in simulated or real samples of data with pileup $\langle\mu\rangle \sim 100$ to 140, the values expected in Runs-3

and -4. However given the poor performance at low pileup, improvement at high pileup seems unlikely. Morever, although a dynamic threshold was key to `pufit`, implementing one in `pufitjet` gave worse performance than when using a fixed threshold. The physics motivation of calculating $E_{\mathrm{T}}^{\mathrm{miss}}$ from jets rather than patches and topoclusters is still solid, therefore further optimisation may still yield good results. For example, alternate functional forms of dynamic threshold and patch variance could be tested. The combination of `pufitjet` with other algorithms such as `cell` could also be tested. In the meantime, other algorithms, such as those which take advantage of tracking or particle flow objects, are being developed and considered by the $E_{\mathrm{T}}^{\mathrm{miss}}$ trigger group for use in the high-pileup environments of Run-3 and beyond.

4.6 Conclusion

The performance of the ATLAS $E_{\mathrm{T}}^{\mathrm{miss}}$ trigger in Run-2, and some of its preparations for Run-3 and beyond, were discussed. In Run-2, the trigger maintained a high acceptance of $E_{\mathrm{T}}^{\mathrm{miss}}$ events by introducing new algorithms and tuning those algorithms to cope with the increase in pileup. The $E_{\mathrm{T}}^{\mathrm{miss}}$ trigger enabled key Standard Model measurements and searches for beyond-the-Standard-Model physics. In preparation for future runs, the high-level trigger software was upgraded to a multi-threaded framework for better memory scaling, and rewritten to be easier to develop and maintain. Development of new algorithms even less sensitive to pileup, like `pufitjet`, will be key to its continued excellent performance in Run-3 and beyond.

5

Searching for new physics in final states with four or more leptons

5.1 Introduction

This chapter presents a search for beyond-the-Standard-Model physics in events with four or more leptons in $139\,\text{fb}^{-1}$ of $\sqrt{s} = 13\,\text{TeV}$ ATLAS data.

In a hadronic collider such as the LHC, the cross section of QCD-mediated processes is much higher than that of electroweak-mediated processes. As leptons can only be produced through electroweak processes or decays, leptonic events are relatively rare in comparison to all-hadronic events. Generally, the more leptons required in the final state, the lower the Standard Model cross-section. Therefore, if there existed any beyond-the-Standard-Model processes which produced four or more leptons in the final state, their contributions may be easily observed as an excess over the small expected contribution from the Standard Model.

Standard Model measurements and beyond-the-Standard-Model searches in events with four or more leptons conducted by ATLAS [103–106] and CMS [107–111] so far have observed no significant deviation from Standard Model expectations. Searches for

SUSY in four-or-more lepton events at ATLAS [112–114] and CMS [115–118] have set strong limits on the range of possible SUSY particle masses and branching ratios.

This analysis is designed to be sensitive to a wide range of beyond-the-Standard-Model processes with four or more leptons in the final state. Additionally, the analysis is optimised for and interpreted in several SUSY models, discussed in Section 5.1.1. The analysis strategy closely follows those of previous four-or-more lepton ATLAS searches with $\sqrt{s} = 7\,\text{TeV}$ data [112], $\sqrt{s} = 8\,\text{TeV}$ data [113], and with $36.1\,\text{fb}^{-1}$ of $\sqrt{s} = 13\,\text{TeV}$ data [114].

The analysis was conducted with collaborators from the University of Cambridge and the Max Planck Institute [119]. Figures and tables presented in this chapter that were made by the analysis team are noted as such in their respective captions. This analysis was presented at the 2020 International Conference on High Energy Physics [2], and in a poster by the author at the 2020 International Conference on Particle Physics and Astrophysics [3]. A paper documenting these efforts has been submitted to the *Journal of High Energy Physics* [4].

5.1.1 SUSY models considered

The analysis is designed to be sensitive to a wide range of models, but is also optimised for and interpreted in various SUSY models as follows. The SUSY models considered are classified according to whether R-parity is conserved or violated.

R-parity conserving models The first class of SUSY models considered fall under the R-parity conserving (RPC) general gauge-mediated (GGM) scenarios [38], which were previously discussed in Section 2.3.2. Simplified models [120–122] are considered where the only particles within reach of the LHC are the gravitino $\tilde{G}$ and the gauginos $\tilde{\chi}_1^{\pm}\tilde{\chi}_2^0\tilde{\chi}_1^0$. The lightest supersymmetric particle is assumed to be the $\tilde{G}$ with mass 1 MeV, while the gauginos $\tilde{\chi}_1^{\pm}\tilde{\chi}_2^0\tilde{\chi}_1^0$ are mostly higgsino and are nearly mass degenerate. The available production modes are $pp \to \tilde{\chi}_1^{\pm}\tilde{\chi}_2^0, \tilde{\chi}_1^{\pm}\tilde{\chi}_1^{\mp}, \tilde{\chi}_1^0\tilde{\chi}_2^0, \tilde{\chi}_1^0\tilde{\chi}_1^{\pm}$. The $\tilde{\chi}_1^{\pm}$ ($\tilde{\chi}_2^0$) is assumed

to decay with 100% branching ratio to the $\tilde{\chi}_1^0$ and a virtual W (Z) boson whose final states are not reconstructed due their low energies. To ensure these decays are prompt (i.e. that there is no intermediate state and the decay time is short), the masses of the $\tilde{\chi}_1^\pm$ and the $\tilde{\chi}_2^0$ are set to 1 GeV above the mass of the $\tilde{\chi}_1^0$. The $\tilde{\chi}_1^0$ then decays to the gravitino and either the Z boson or Standard Model Higgs boson h. The mass of the $\tilde{\chi}_1^0$ ($m(\tilde{h})$) and the branching ratio to the Z boson ($\mathcal{B}(\tilde{\chi}_1^0 \to Z\tilde{G})$) are free parameters. Representative Feynman diagrams of these processes are shown in Figure 5.1.

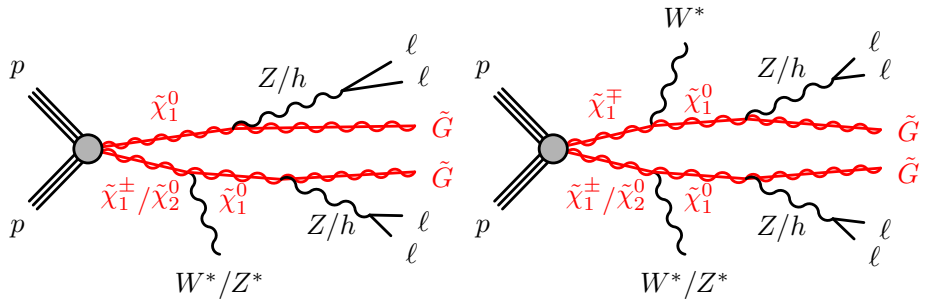

(a) Production of $\tilde{\chi}_1^\pm$ $\tilde{\chi}_1^0$ or $\tilde{\chi}_2^0$ $\tilde{\chi}_1^0$ **(b)** Production of $\tilde{\chi}_1^\pm$ $\tilde{\chi}_1^\mp$ or $\tilde{\chi}_2^0$ $\tilde{\chi}_1^\mp$

Figure 5.1: Feynman diagrams for general gauge-mediated (GGM) models considered. The particles $\tilde{\chi}_1^\pm$ $\tilde{\chi}_2^0$ $\tilde{\chi}_1^0$ are assumed to be nearly mass degenerate, with $m(\tilde{\chi}_1^\pm, \tilde{\chi}_2^0) - m(\tilde{\chi}_1^0) = 1\,\text{GeV}$, therefore the decay products of the virtual W^*/Z^* bosons are low in energy and not reconstructed. The gravitino $\tilde{G}$ does not decay.

This analysis targets the $\tilde{\chi}_1^0 \to Z\tilde{G}$ decay; the complimentary decay, $\tilde{\chi}_1^0 \to h\tilde{G}$, is covered by analyses which search for final states consistent with the decay of two Higgs bosons [123–125].

R-parity violating models The second class of SUSY models considered is R-parity violating (RPV) due to a non-zero coupling λ_{ijk} in a term of the SUSY superpotential $\mathcal{W}$ (cf. Eq. 2.30):

$$\mathcal{W} \supset \frac{1}{2}\lambda_{ijk} L_i L_j \overline{E}_k, \tag{5.1}$$

which couples the lepton SU(2)-doublet superfields L_i, L_j to a lepton singlet superfield $\overline{E}_k$. This allows the lightest neutralino to decay via a virtual slepton to two charged

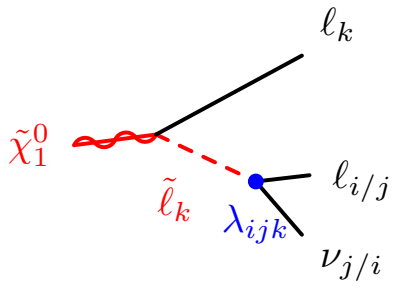

Figure 5.2: Feynman diagram of the decay of the lightest neutralino to two charged leptons and one neutrino via a virtual slepton.

leptons and one neutrino (Figure 5.2). This decay violates not only R-parity, but also lepton number conservation. The lightest supersymmetric particle (LSP) is assumed to be the $\tilde{\chi}_1^0$.

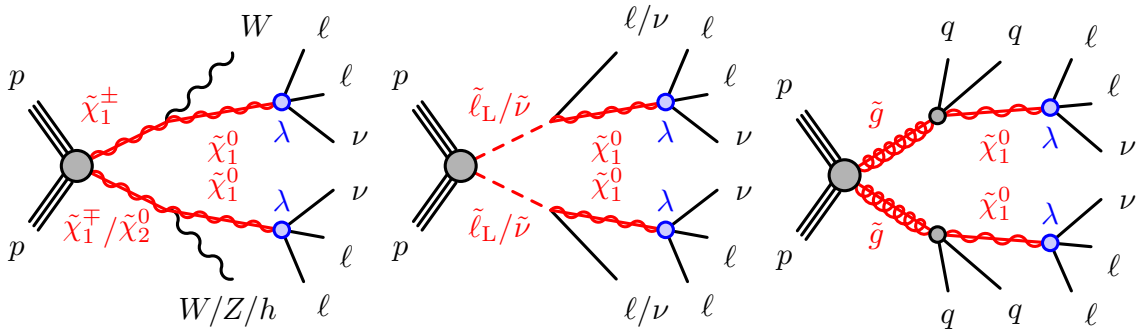

(a) Wino NLSP **(b)** $\tilde{\ell}_L/\tilde{\nu}$ NLSP **(c)** $\tilde{g}$ NLSP

Figure 5.3: Feynman diagrams of the R-parity violating SUSY models considered. The production and decay of the NLSP (wino (a), slepton/sneutrino (b), or gluino (c)) conserve R-parity, while the decay of the $\tilde{\chi}_1^0$ violates R-parity. The branching ratio of the LSP decay $\tilde{\chi}_1^0 \to \ell\ell\nu$ is assumed to be 100%.

The direct production of $\tilde{\chi}_1^0\tilde{\chi}_1^0$ is not considered due to its low cross section, instead the production of the next-to-lightest supersymmetric particle (NLSP) is considered. Three NLSP candidates were considered:

- **Wino NLSP**: Mass-degenerate wino charginos and neutralinos are produced in association ($\tilde{\chi}_1^+\tilde{\chi}_1^-$ or $\tilde{\chi}_1^\pm\tilde{\chi}_2^0$). The charginos decay via $\tilde{\chi}_1^\pm \to W^{(*)}\tilde{\chi}_1^0$ with 100%

branching fraction, while the neutralinos decay via $\tilde{\chi}_2^0 \to Z^{(*)}\tilde{\chi}_1^0$ or $h\tilde{\chi}_1^0$ with 50% branching fraction each, as shown in Figure 5.3(a).

- **Slepton/sneutrino NLSP**: Mass-degenerate sleptons and sneutrinos of all three generations are produced in association ($\tilde{\ell}_\mathrm{L}\tilde{\ell}_\mathrm{L}$, $\tilde{\nu}\tilde{\nu}$, $\tilde{\ell}_\mathrm{L}\tilde{\nu}$, where the subscript L refers to the chirality of the partner lepton). The sleptons decay via $\tilde{\ell}_\mathrm{L} \to \ell\tilde{\chi}_1^0$ and sneutrinos decay via $\tilde{\nu} \to \nu\tilde{\chi}_1^0$, both with 100% branching fraction, as seen in Figure 5.3(b).

- **Gluino NLSP**: Gluinos are pair-produced, then the gluino decays with 100% branching fraction via $\tilde{g} \to q\bar{q}\tilde{\chi}_1^0$ ($q = u, d, s, c, b$ only, with equal branching fractions), as seen in Figure 5.3(c).

The LSP mass is restricted to the range $10\,\mathrm{GeV} \leq m(\mathrm{LSP}) \leq m(\mathrm{NLSP}) - 10\,\mathrm{GeV}$ to ensure that the decays into and of the LSP are both prompt.

Scenario	$\tilde{\chi}_1^0$ branching ratios		
$LL\bar{E}12k$	$e^+e^-\nu$ (1/4)	$e^\pm\mu^\mp\nu$ (1/2)	$\mu^+\mu^-\nu$ (1/4)
$LL\bar{E}i33$	$e^\pm\tau^\mp\nu$ (1/4)	$\tau^+\tau^-\nu$ (1/2)	$\mu^\pm\tau^\mp\nu$ (1/4)

Table 5.1: Decay modes and branching ratios for the $\tilde{\chi}_1^0$ particle in the R-parity violating models, where ν denotes neutrinos or antineutrinos of any lepton generation.

Two scenarios for the coupling constant λ_{ijk} are considered, their final states differ in the flavour of charged leptons expected: (i) $LL\bar{E}12k$ ($k \in \{1, 2\}$), where $\lambda_{12k} \neq 0$ and only decays to electrons and muons are included, and (ii) $LL\bar{E}i33$ ($i \in \{1, 2\}$), where $\lambda_{i33} \neq 0$ and only decays to taus in association with electrons or muons are included. In each case it is assumed that $\lambda_{ijk} = 0$ for all other combinations of $i, j, k \in \{1, 2, 3\}$. The other R-parity violating coupling constants λ', λ'', and κ (cf Eqs. 2.30 and 2.31) are also assumed to be zero. The final states of each considered scenario and their respective branching ratios are listed in Table 5.1.

The expected signature of these events is that of four prompt charged leptons originating from the R-parity violating decays, and some amount of $E_{\mathrm{T}}^{\mathrm{miss}}$ from the neutrinos. For the $LL\bar{E}12k$ case the four charged leptons would be either e or μ. For the $LL\bar{E}i33$ case at least two of the four charged leptons will be τ.

Additional particles may be expected in the final state depending on the choice of NLSP. For the $\tilde{g}$ NLSP case, jets may be expected from the $\tilde{g} \to qq\tilde{\chi}_1^0$ decay. For the wino NLSP case, the W in the $\tilde{\chi}_1^\pm \to W^\pm\tilde{\chi}_1^0$ decay may decay hadronically or leptonically, giving either jets or additional leptons. For the $\tilde{\ell}_{\mathrm{L}}/\tilde{\nu}$ NLSP case, $\tilde{\ell}_{\mathrm{L}} \to \tilde{\chi}_1^0\ell$ gives an additional lepton while $\tilde{\nu} \to \tilde{\chi}_1^0\nu$ gives a neutrino which contributes to missing energy. It is possible that b-jets are produced in the $\tilde{g}$ (or $\tilde{\chi}_1^\pm$) decay if $\Delta m(\tilde{g}, \tilde{\chi}_1^0)$ (or $\Delta m(\tilde{\chi}_1^\pm, \tilde{\chi}_1^0)$) is sufficiently large.

In order to be sensitive to all the cases outlined above, this analysis defines regions with various requirements on the number of light leptons (e or μ) and the number of τs. A veto or requirement of b-jets is applied depending on the targeted mass splitting of the $\tilde{g}$ and Wino NLSP models. As low NLSP masses have been excluded by previous searches and because SM processes tend to be at a lower mass scale, a requirement is made on the overall mass scale of the event in order to gain sensitivity to higher NLSP masses.

5.2 Analysis strategy

The analysis strategy follows closely that of the previous paper [114]. Three sets of signal regions were designed to optimise for three different types of decay:

- Four light leptons (e or μ) in two same-flavour opposite-sign (SFOS) pairs from ZZ-like decays targeting the GGM models,
- Four light leptons from R-parity violating decays targeting the $LL\bar{E}12k$ scenario, and

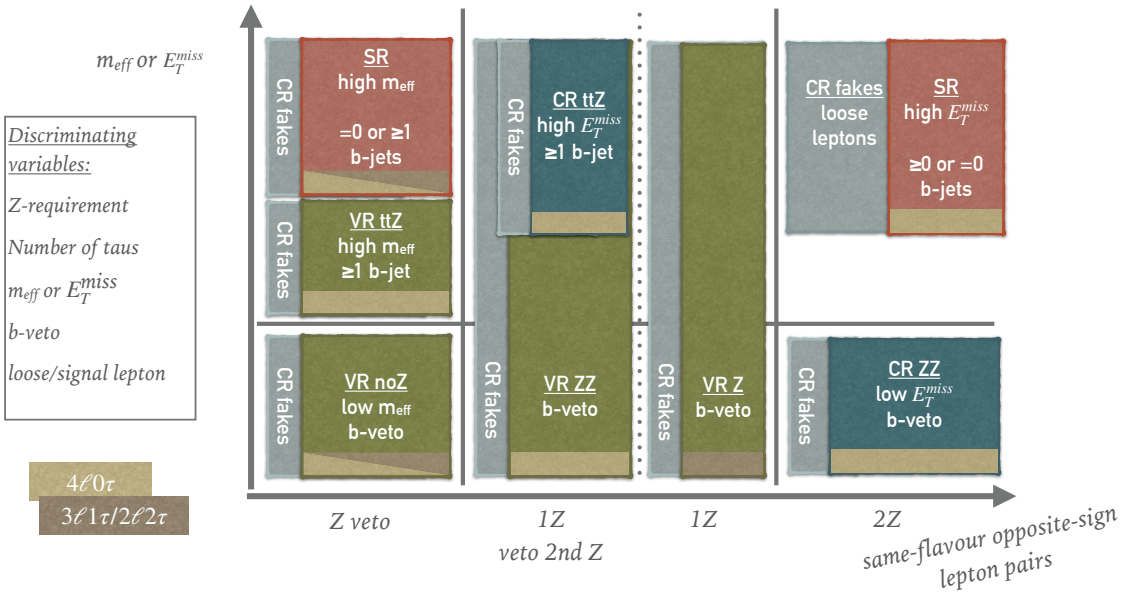

Figure 5.4: A graphical overview of the signal, control, and validation regions. Along the x-axis, regions are grouped by their Z selection. Along the y-axis, requirements may be made on m_{eff} or $E_{\text{T}}^{\text{miss}}$, depending on the region. The labels "$4\ell0\tau/3\ell1\tau/2\ell2\tau$" indicate the number of light leptons (ℓ) or hadronically-decaying taus (τ) required in a region. An additional requirement may be made on the number of b-jets. Signal regions (SR) are shown in red, validation regions (VR) are shown in green, and control regions (CR ZZ and CR ttZ) for the normalisation of simulated backgrounds in dark blue. Control regions in grey (CR fakes) require loose leptons in place of tight leptons, but otherwise share the same definitions as their parallel signal, control, and validation regions; these regions are used for the estimation of reducible "fake" backgrounds. See Table 5.6 for the full definitions.

- Four leptons (including one or two hadronically decaying taus) from R-parity violating decays targeting the $LL\bar{E}i33$ scenario.

Standard Model contributions to the signal regions are constrained and validated in dedicated control and validation regions. An overview of the techniques used to estimate these contributions is deferred to later in this Section.

A graphical overview of the signal, control, and validation regions used in this analysis is shown in Figure 5.4.

Figure of merit The sensitivity of the signal regions to the considered signal models was measured in *significance* following the definition in Ref. [126]:

$$Z = \sqrt{2\left(n\ln\left[\frac{n(b+\sigma^2)}{b^2+n\sigma^2}\right] - \frac{b^2}{\sigma^2}\ln\left[1+\frac{\sigma^2(n-b)}{b(b+\sigma^2)}\right]\right)}, \tag{5.2}$$

where b is the number of background events, σ is the uncertainty on the background, and n is the total number of background and signal events. A signal model can be excluded at the 95% confidence level if its significance $Z > 1.64$, assuming $n = b$. The previous analysis [114] had uncertainties of 20% to 30%, so a conservative 30% uncertainty is assumed in the optimisation of this analysis unless otherwise stated. In the plots to follow, binned and "cumulative" distributions are often considered. The cumulative distributions show the number of events which satisfy a minimum requirement on the variable plotted on the x-axis. The significance plots found under the binned distributions show the significance per bin, while those under the cumulative distributions show the significance for a given requirement.

Key variables The key discriminating variables used in defining the signal, control, and validation regions are described below.

The missing transverse energy $E_{\mathrm{T}}^{\mathrm{miss}}$ is defined as $E_{\mathrm{T}}^{\mathrm{miss}} = |\vec{p}_{\mathrm{T}}^{\,\mathrm{miss}}|$, where

$$\vec{p}_{\mathrm{T}}^{\,\mathrm{miss}} = -\sum_{i\in\{e,\mu,\gamma,\text{jets,soft tracks}\}} \vec{p_{\mathrm{T}}}(i), \tag{5.3}$$

i.e. the negative vector sum of the transverse momenta of calibrated objects (electrons, photons, muons, jets) and soft tracks measured in the inner detector. Hadronic taus enter the $E_{\mathrm{T}}^{\mathrm{miss}}$ calculation as jets. This variable was used to define the GGM-targeting signal regions.

The effective mass m_{eff} is defined as the scalar sum

$$m_{\mathrm{eff}} = \sum_{\ell=e,\mu,\tau} p_T(\ell) + \sum_{j\in\text{jets},p_T(j)>40\,\mathrm{GeV}} p_T(j) + E_{\mathrm{T}}^{\mathrm{miss}}. \tag{5.4}$$

The effective mass is sensitive to the overall mass scale of an event, which is typically larger for SUSY events than those of the Standard Model. This variable was used to define the $LL\bar{E}$-targeting regions.

Regions with stringent requirements on $E_{\mathrm{T}}^{\mathrm{miss}}$ or m_{eff} provided high sensitivity to the signal models discussed in the previous sections, while regions with less stringent $E_{\mathrm{T}}^{\mathrm{miss}}$ or m_{eff} requirements were retained to provide sensitivity to a wider range of models.

As most of the main background processes in four-lepton events contain a Z boson (for example ZZ, $t\bar{t}Z$), events were selected based on whether a Z boson candidate is present among combinations of light leptons ($\ell \in \{e, \mu\}$). A first Z requirement is satisfied if any same-flavor opposite-sign lepton pair satisfies $|m(\ell^+\ell^-) - m_Z| < 10\,\mathrm{GeV}$. A second Z requirement is satisfied if a second same-flavor opposite-sign pair satisfies $61.2 < m(\ell^+\ell^-) < 101.2\,\mathrm{GeV}$. In regions where a Z veto is applied, events which satisfy any of the following conditions are rejected (ℓ' may or may not have the same flavour as ℓ):

$$\begin{aligned} |m(\ell^+\ell^-) - m_Z| &< 10\,\mathrm{GeV}, \\ |m(\ell^+\ell^-\ell'^{\pm}) - m_Z| &< 10\,\mathrm{GeV}, \\ |m(\ell^+\ell^-\ell'^+\ell'^-) - m_Z| &< 10\,\mathrm{GeV}. \end{aligned} \tag{5.5}$$

A small number of four-lepton events will pass the Z veto but satisfy none of the Z selection requirements. These events are typically from rare $Z \to 4\ell$ or $Z \to \ell^+\ell^-\gamma(\gamma \to \ell'^+\ell'^-)$ events and are not considered in this analysis as they are not signal-like.

In most signal regions, either vetoing or requiring b-jets was employed in order to extend sensitivity to the gluino (wino) scenarios across $\Delta m(\tilde{g}, \tilde{\chi}_1^0)$ $\left[\text{or } \Delta m(\tilde{W}, \tilde{\chi}_1^0)\right]$. Regions with a b-requirement were sensitive to larger Δm, while regions with a b-veto were sensitive to smaller Δm.

Background estimation Backgrounds are classified into two categories: "irreducible" and "reducible". [1] The former are from Standard Model processes with signatures similar to the signal processes, while the latter are due to detector and mis-measurement effects. Irreducible backgrounds include four-lepton decays of ZZ, $t\bar{t}Z$, VVV (where $V = W, Z$), and various Higgs processes. Of these simulations, those of the major contributions ($t\bar{t}Z$ and ZZ) were normalised to data in dedicated control regions high in purity of the relevant process. Reducible backgrounds, i.e. contributions from events containing fake and non-prompt leptons, were estimated using a fake-factor method [114, 127]. All background estimates were validated in regions similar to but orthogonal to the signal region. The techniques used for background estimation are described in detail in Section 5.5.

5.3 Samples used and event selection

5.3.1 Samples used

This analysis makes use of data recorded by ATLAS of pp collisions delivered by the LHC. Events simulated by the Monte Carlo method are used in the estimation of backgrounds.

Data Data used in this analysis were pp collisions recorded by the ATLAS detector between 2015 and 2018, corresponding to $139\,\text{fb}^{-1}$ of integrated luminosity. Events were required to pass the single-lepton, dilepton, or trilepton triggers [79, 80] listed in Table 5.2.

MC Simulation Simulated Standard Model and SUSY events were produced by Monte Carlo generators. Standard Model processes considered were those which produce the signal signature of at least four reconstructed leptons. These include processes such

[1] The author speculates the rationale behind this choice of jargon is because the contribution of reducible backgrounds could theoretically be reduced by improving techniques in reconstruction, isolation, detector design, and others. Irreducible backgrounds, however, are irreducible because they share the same signature as that expected from BSM events.

Trigger	Offline p_{T} threshold [GeV]		
	2015	2016	2017–2018
Single e (isolated)	25	27	27
Single e	61	61	61
Single μ (isolated)	21	25 or 27	27
Single μ	41	41 or 51	51
Double e	13, 13	18, 18	(18, 18) or (25, 25)
Double μ (symmetric)	11, 11	(11, 11) or (15, 15)	15, 15
(asymmetric)	19, 9	(21, 9) or (23, 9)	23, 9
Double $e\mu$	8(e), 25(μ)	8(e), 25(μ)	8(e), 25(μ)
	18(e), 15(μ)	18(e), 15(μ)	18(e), 15(μ)
		27(e), 9(μ)	27(e), 9(μ)
Triple $e\mu\mu$, $ee\mu$	13(e), 11(2μ)	13(e), 11(2μ)	13(e), 11(2μ)
	13(2e), 11(μ)	13(2e), 11(μ)	13(2e), 11(μ)

Table 5.2: The triggers used in the analysis. The offline p_{T} thresholds are required only for reconstructed charged leptons which match to the trigger signatures. Trigger thresholds increase across the years due to the increase in beam luminosity, and "or" denotes a move to a higher-threshold trigger during data-taking.

as ZZ and ttZ which produce four real leptons, and processes such as $t\bar{t}$ and Z+jets where one or more objects are mis-reconstructed as leptons. Simulation details are given in Table 5.3. Additionally, simulated pileup events were generated by Pythia8. All simulated events were weighted to match the pileup distribution in data. After event generation, the detector response was simulated by `GEANT4` [128].

5.3.2 Object and event selection

Real and simulated events are reconstructed by the algorithms described previously in Section 3.2.4, after which selections are made on objects in the events for use in the analysis. Reconstructed objects are categorised as follows, and the categories are shown graphically in Figure 5.5.

- **Preselected**: Objects which pass initial selection, before overlap removal;

Process	Generator(s)	Cross-section calculation	Tune	PDF set
ZZ, WZ, WW	Sherpa 2.2.2 [129]	NLO [130]	Sherpa default	NNPDF30NNLO [131]
VVV	Sherpa 2.2.1	NLO [130]	Sherpa default	NNPDF30NNLO
H via ggF, VBF, VH	Powheg-Box v2 [132–134] + Pythia 8.212 [135]	NNNLO+NNLL [136–142]	AZNLO [143]	CTEQ6L1 [144]
$t\bar{t}H$	Powheg-Box v2 + Pythia 8.230	NLO [136]	A14 [145]	NNPDF23LO [146]
$t\bar{t}Z$	MadGraph5_aMC@NLO 2.3.3 [147] + Pythia 8.210	NLO [148]	A14	NNPDF23LO
$t\bar{t}WW$	MadGraph5_aMC@NLO 2.2.2 + Pythia 8.186	NLO [148]	A14	NNPDF23LO
$t\bar{t}WZ$, tWZ	MadGraph5_aMC@NLO 2.3.3 + Pythia 8.212	NLO [148]	A14	NNPDF23LO
$t\bar{t}ZZ$, $t\bar{t}WH$, $t\bar{t}HH$	MadGraph5_aMC@NLO 2.6.7 + Pythia 8.240	NLO [148]	A14	NNPDF23LO
$t\bar{t}tW$, $t\bar{t}t\bar{t}$	MadGraph5_aMC@NLO 2.2.2 + Pythia 8.186	NLO [147]	A14	NNPDF23LO
$t\bar{t}$	Powheg-Box v2 + Pythia 8.230	NNLO+NNLL [149–155]	A14	NNPDF23LO
Z+jets, W+jets	Powheg-Box v1 + Pythia 8.186	NNLO [156]	AZNLO	CTEQ6L1
SUSY signal	MadGraph5_aMC@NLO 2.2.2 + Pythia 8.230	NLO+NLL [157–164]	A14	NNPDF23LO

Table 5.3: Summary of the simulated SM background and SUSY signal samples used in this analysis, where $V = W, Z$, and off-shell contributions are included. "Tune" refers to the set of tuned parameters used by the generator.

- **Baseline**: Preselected objects which pass overlap removal;
- **Signal**: Objects that pass all selection criteria;
- **Loose**: Baseline objects which fail certain selection criteria, used for the estimation of reducible backgrounds.

Preselection Electrons are required to have $p_{\mathrm{T}} > 4.5$ GeV, $|\eta| < 2.47$, and pass the `LooseAndBLayer` identification criteria [82]. Muons are required to have $p_{\mathrm{T}} > 3$ GeV, $|\eta| < 2.7$, and pass the `Medium` identification criteria [75]. Both electrons and muons are required to have tracks which trace back to the primary vertex, with impact parameter $|z_0 \sin\theta| < 0.5\,\mathrm{mm}$.

Jets are reconstructed from topoclusters with the anti-k_t algorithm [87], with radius parameter $R = 0.4$. They are required to have $p_{\mathrm{T}} > 20\,\mathrm{GeV}$ and $|\eta| < 2.8$. At this point, a jet can additionally be labelled as a hadronically-decaying tau τ_{had}, or as a pile-up jet. To be labelled τ_{had}, the jet must have $|\eta| \in (0, 1.37) \cup (1.52, 2.47)$ which avoids a gap in electromagnetic calorimetry, and 1 or 3 tracks to reconstruct tau decays to either one or three charged pions. TRT and calorimeter information is used to suppress electrons misidentified as τ_{had}. Pileup-jets are identified as those which fail to satisfy quality criteria described in Ref. [165].

Figure 5.5: Diagram showing the relationships between and uses of preselected, baseline, signal, and loose object selections

Overlap removal To avoid the double counting of objects, the following objects are removed successively from events:

1. The electron with lower p_{T} of two electrons which share the same track,
2. Any τ_{had} within $\Delta R = 0.2$ of an electron or muon,
3. Any electron which shares the same ID track as a muon,
4. Any jet within $\Delta R = 0.2$ of an electron,
5. Any electron within $\Delta R = 0.4$ of a jet,
6. Any jet with fewer than three associated tracks if it is within $\Delta R = 0.2$ of a muon or if a muon can be matched to a track associated with the jet,
7. Any muon within $\Delta R = 0.4$ of a jet,
8. Any jet within $\Delta R = 0.4$ of a τ_{had} passing the `Medium` working point of a recurrent-neural-network-based τ_{had} identifier [90];

where $\Delta R = \sqrt{(\Delta\eta)^2 + (\Delta\phi)^2}$.

Also, the following lepton pairs consistent with low-mass processes are removed:

- an opposite sign e^+e^-, $e^\pm\mu^\mp$ or $\mu^+\mu^-$ pair if its invariant mass is small, $m_{\ell\ell} < 4\,\text{GeV}$;
- an e^+e^- or $\mu^+\mu^-$ pair, if it has $8.4\,\text{GeV} < m_{\ell\ell} < 10.4\,\text{GeV}$, which is consistent with the decay of an Υ meson.
- a lepton pair with $\Delta R(\ell_1, \ell_2) < 0.6$ where either lepton has $p_\text{T} < 30\,\text{GeV}$

The last rejection suppresses leptons from decay chains where multiple heavy flavour quarks undergo leptonic decay. These decays can often result in at least two close-by leptons. Since these events are not signal-like, and their contributions are difficult to estimate, such events are rejected.

Signal object selection Following overlap removal, the objects used for signal event selection are defined. Electrons are required to have $p_\text{T} > 7\,\text{GeV}$, pass `Medium` identification criteria [82], and have impact parameter $|d_0/\sigma(d_0)| < 5$. Muons are required to have $p_\text{T} > 5\,\text{GeV}$ and $|d_0/\sigma(d_0)| < 3$. Both electrons and muons are required to pass `FCLoose` isolation [75, 82].

Signal τ_had objects need to pass the `Medium` neural-network based identification criteria [90]. Pile-up jets are removed. Of the remaining jets within $|\eta| < 2.5$, those from the decay and hadronisation of b-quarks are labelled as b-jets according to a b-tagging algorithm [166] which has 85% tagging efficiency and a light-flavour jets rejection factor of 25.

Loose object selection Loose leptons are defined as baseline leptons which fail the following signal selection criteria. They are used for the estimation of reducible backgrounds (cf. Section 5.5.2). Loose electrons are baseline electrons which fail signal identification, impact parameter or isolation criteria. Loose muons are baseline muons

which fail signal impact parameter or isolation criteria. Loose taus are baseline taus with identification neural-network score > 0.05 but fail the `Medium` requirement [90].

5.4 Signal region optimisation

In this section, I outline the procedure by which the signal regions in this analysis were optimised according to the analysis strategy (cf. Section 5.2). Following this optimisation procedure, I define the final, optimised signal regions.

Signal regions were optimised to provide sensitivity to a set of benchmark signal points. For the GGM scenarios, four benchmark points were chosen with reference to the previous analysis [114]: one within the previous exclusion $\left(m(\widetilde{h}) = 200\,\text{GeV}, \mathcal{B}(\tilde{\chi}_1^0 \to Z\tilde{G}) = 100\%\right)$, one that could not be excluded due to observed excesses $\left(m(\widetilde{h}) = 200\,\text{GeV}, \mathcal{B}(\tilde{\chi}_1^0 \to Z\tilde{G}) = 50\%\right)$, and two well outside the previous exclusion $\left(m(\widetilde{h}) = 400\,\text{GeV}, \mathcal{B}(\tilde{\chi}_1^0 \to Z\tilde{G}) = 50, 100\%\right)$. Note that $m(\widetilde{h}) = m(\tilde{\chi}_1^0)$ and $m(\tilde{\chi}_2^0), m(\tilde{\chi}_1^\pm) = m(\tilde{\chi}_1^0) + 1\,\text{GeV}$. For the RPV scenarios, benchmark signal points were chosen from the edge of the sensitivity of the previous analysis [114] (subject to sample availability at the time of signal region optimisation). They are listed in Table 5.4.

	RPV $LL\bar{E}12k$ benchmark points	RPV $LLEi33$ benchmark points
NLSP	m(NLSP,LSP) [GeV]	m(NLSP,LSP) [GeV]
$\widetilde{W}$	(1300,1290)	(1000,990)
	(1500,1490)	(800,790)
$\widetilde{g}$	(2200,10)	(1600,800)
	(2200,50)	(1600,1590)
$\tilde{\ell}_\text{L}/\tilde{\nu}$	(1100,600)	(700,100)
	(1200,600)	(800,400)

Table 5.4: Benchmark points used to optimise the RPV-targeting signal regions.

In general, requirements on variables such as E_T^miss, m_eff, and the number of b-jets

Notation	$N(e, \mu)$	$N(\tau_{\text{had}})$
$4\ell 0\tau$	≥ 4	≥ 0
$3\ell 1\tau$	$= 3$	≥ 1
$2\ell 2\tau$	$= 2$	≥ 2

Table 5.5: Number of electrons, muons, and τ_{had} required in different regions.

were tested in order to provide the greatest sensitivity to the benchmark points while maintaining a reasonable number of expected SM events in order to avoid large statistical and systematic uncertainties due to low event yields.

During optimisation, all reducible and irreducible backgrounds are taken from MC simulation. Later in the chapter, the methods for normalising irreducible backgrounds to data in control regions (cf. Section 5.5.1) and estimating reducible backgrounds from data (cf. Section 5.5.2) are described, but they are not used here.

The signal regions follow a naming convention `SRX`$*$, where the number `X` denotes the number of hadronically decaying taus required in the region, and $*$ are superscripts, subscripts, and postfixes which are indicative of the selection made. The notation $4\ell 0\tau, 3\ell 1\tau, 2\ell 2\tau$ is defined to indicate the number of leptons in a selection in Table 5.5.

In the publications on which this chapter is based [2, 4], a signal region with five or more light leptons is also defined. This region is not discussed in this thesis.

5.4.1 Signal regions targeting GGM models

The first class of regions is designed to be sensitive to decays via nearly on-shell Z bosons, and are optimised using the GGM models. Four regions of this class were defined. Two regions (`SR0-ZZ`$^{\text{loose}}$ and `SR0-ZZ`$^{\text{tight}}$) have been redefined with minimal changes from the previous analysis, where a 2.3σ excess was observed [114]. Two additional regions have been defined as a result of further optimisation based on the benchmark models.

For the GGM models, electronic and muonic decays from the two Z bosons are targeted. Therefore two same-flavor opposite-sign (SFOS) light-lepton (e or μ) pairs consistent with a Z boson decay are selected. Where multiple combinations exist for

the SFOS pairing, the combination giving the smallest $|m_{\text{pair1}} - m_Z| + |m_{\text{pair2}} - m_Z|$ is chosen. SFOS pair 1 is chosen as the pair closest to the Z mass. Events with additional light leptons were also accepted. No requirement is made on the number of hadronically decaying taus in the event.

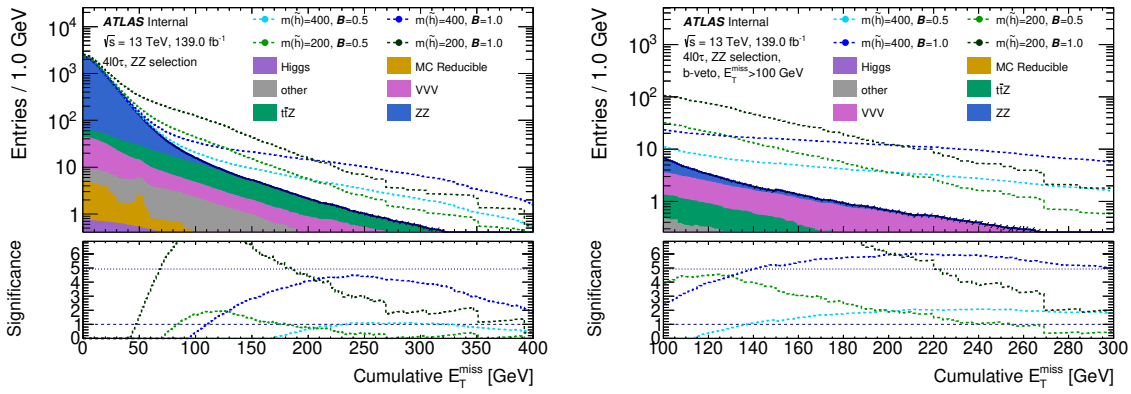

(a) No $E_{\text{T}}^{\text{miss}}$ floor nor b-veto **(b)** $E_{\text{T}}^{\text{miss}} > 100\,\text{GeV}$ and b-veto

Figure 5.6: Cumulative $E_{\text{T}}^{\text{miss}}$ distributions of simulated signal and background events in $4\ell 0\tau$ regions with two Z candidate SFOS lepton pairs. The upper pad shows the number of events in a region with $E_{\text{T}}^{\text{miss}}$ greater than the value on the x-axis, while the lower pad shows the significance of the same region. $m(\tilde{h})$ is the mass of the LSP in GeV, while $\mathbf{B} = \mathcal{B}(\tilde{\chi}_1^0 \to Z\tilde{G})$. The regions SR0-ZZ$^{\text{loose}}$ and SR0-ZZ$^{\text{tight}}$ are defined with the requirements $E_{\text{T}}^{\text{miss}} > 50,\ 100$ GeV on the left plot, while SR0-ZZ$^{\text{loose}}_{\text{bveto}}$ and SR0-ZZ$^{\text{tight}}_{\text{bveto}}$ are defined with the requirements $E_{\text{T}}^{\text{miss}} > 100,\ 200$ GeV on the right plot. Note that the increase in number of MC Reducible events in Figure 5.6(a) around $E_{\text{T}}^{\text{miss}} = 50\,\text{GeV}$ is due to the presence of simulated events with negative weights, the contribution of such events is not significant.

The cumulative $E_{\text{T}}^{\text{miss}}$ distribution for events with four leptons and two Z candidates is shown in Figure 5.6(a). The SM background is dominated by ZZ production, and is concentrated at low values of $E_{\text{T}}^{\text{miss}}$. The signal regions where an excess was observed in the $36.1\,\text{fb}^{-1}$ analysis are mimicked by SR0-ZZ$^{\text{loose}}$ and SR0-ZZ$^{\text{tight}}$, which have requirements of $E_{\text{T}}^{\text{miss}} > 50\,\text{GeV}$ and $E_{\text{T}}^{\text{miss}} > 100\,\text{GeV}$ respectively. Note that lepton identification and other reconstruction and identification techniques in ATLAS have changed since the publication of the last analysis, therefore these new signal regions do not reproduce those from the previous analysis entirely. However internal

studies have shown that the excess still persists in the same dataset even with current reconstruction techniques and identification criteria, therefore whether the excess persists significantly in the full Run-2 dataset must be investigated as it could hint at contributions from BSM physics.

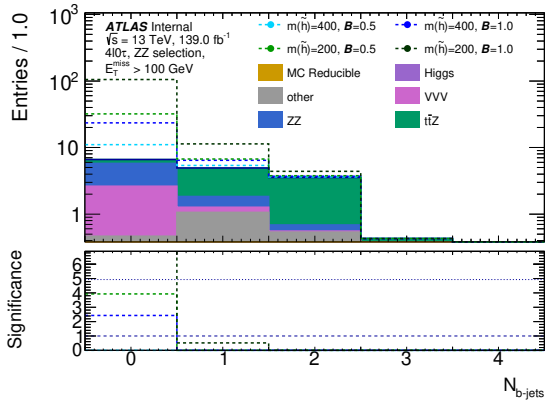

Figure 5.7: b-jet multiplicity of simulated signal and background events in $\texttt{SR0-ZZ}^{\text{tight}}$, which requires $4\ell 0\tau$, 2 Z candidates, and $E_{\text{T}}^{\text{miss}} > 100\,\text{GeV}$. The significance of each bin in b-jet multiplicity is shown in the lower pad. The region $\texttt{SR0-ZZ}^{\text{loose}}_{\text{bveto}}$ is the bin with 0 b-jets. $m(\tilde{h})$ is the mass of the LSP in GeV, while $\mathbf{B} = \mathcal{B}(\tilde{\chi}_1^0 \to Z\tilde{G})$.

After reproducing the signal regions above, further optimisation was attempted. As few events with b-jets are expected from the signal processes, a b-veto is required to further suppress $t\bar{t}Z$ and $t\bar{t}WW$ backgrounds. Figure 5.7 shows that this veto is effective at doing so, and that the greatest sensitivity is achieved when b-jets are vetoed. Additionally, increasing the $E_{\text{T}}^{\text{miss}}$ floor up to 200 GeV increases the significance of signal points with higher $m(\tilde{h})$ (Figure 5.6(b)). Therefore two additional signal regions are defined: $\texttt{SR0-ZZ}^{\text{loose}}_{\text{bveto}}$, which requires a b-veto and $E_{\text{T}}^{\text{miss}} > 100\,\text{GeV}$, and $\texttt{SR0-ZZ}^{\text{tight}}_{\text{bveto}}$, which additionally requires $E_{\text{T}}^{\text{miss}} > 200\,\text{GeV}$. Of these two regions, $\texttt{SR0-ZZ}^{\text{loose}}_{\text{bveto}}$ is more sensitive to intermediate $\tilde{h}$ masses, while $\texttt{SR0-ZZ}^{\text{tight}}_{\text{bveto}}$ is more sensitive to high $\tilde{h}$ masses.

5.4.2 Signal regions targeting RPV models with decays to light leptons only

The second class of signal regions targets both general 4-lepton signatures and the $LL\bar{E}12k$ R-parity violating signatures. Events with at least four light leptons and no hadronically decaying taus were required. As the signals targeted do not contain on-shell Z-bosons, a Z-veto is applied to reduce the otherwise overwhelming ZZ background.

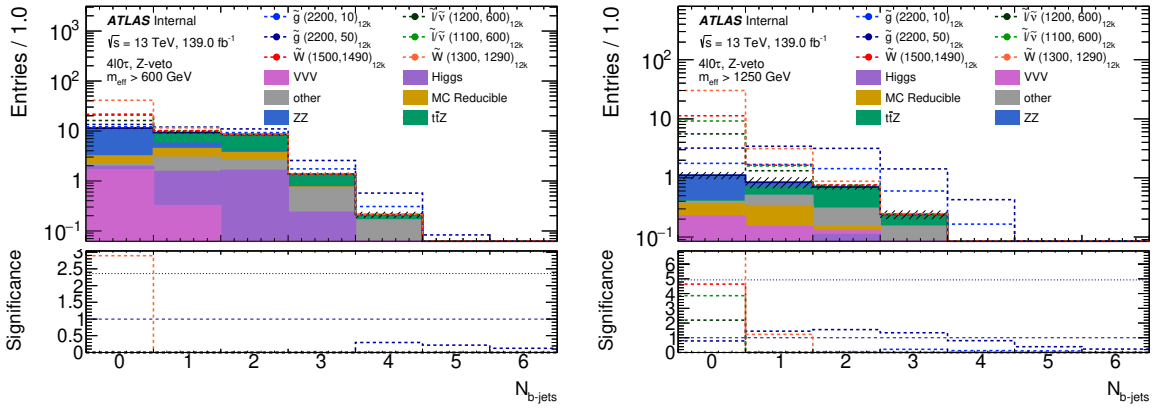

(a) $m_{\text{eff}} > 600\,\text{GeV}$ **(b)** $m_{\text{eff}} > 1250\,\text{GeV}$

Figure 5.8: b-jet multiplicities of simulated signal and background events in $4\ell 0\tau$ Z-veto regions with (a) $m_{\text{eff}} > 600\,\text{GeV}$ or (b) $m_{\text{eff}} > 1250\,\text{GeV}$. The significance of each bin in b-jet multiplicity is shown in the lower pad. The signal region $\texttt{SR0}^{\text{loose}}_{\text{bveto}}$ is the first bin of the left plot, and $\texttt{SR0}^{\text{tight}}_{\text{bveto}}$ is the first bin of the right plot. The labels for the signal points show the NLSP candidate considered, and $(m_{\text{NLSP}}, m_{\text{LSP}})$ in GeV.

A requirement on the number of b-jets is applied to further increase sensitivity. Figure 5.8 shows that when b-jets are vetoed, most $t\bar{t}Z$ background contributions are removed and there is high sensitivity to models with a high-mass wino or gluino NLSP. When b-jets are required, most ZZ contributions are removed and there is high sensitivity to models with an intermediate-mass wino or gluino NLSP.

The "general" signal region was optimised as follows. Figure 5.10 shows the number of events for a given minimum requirement on m_{eff} in a $4\ell 0\tau$ region with a Z-veto and b-veto. A modest requirement on m_{eff} was desired to eliminate most background events

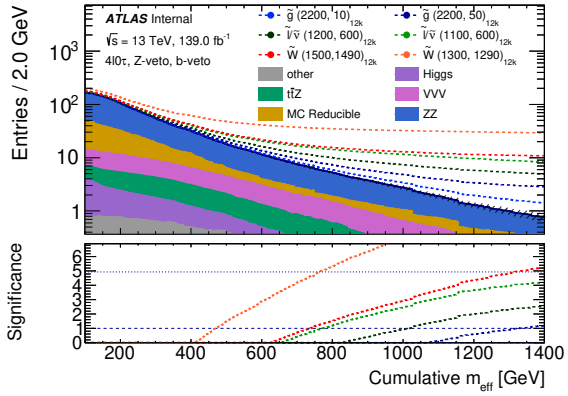

Figure 5.9: Cumulative m_{eff} distribution for simulated signal and background events in a $4\ell 0\tau$ region with Z-veto and b-veto. The upper pad shows the number of events in a region with m_{eff} greater than the value on the x-axis, while the lower pad shows the significance of the same region. The region $\texttt{SR0}^{\text{loose}}_{\text{bveto}}$ is defined by $m_{\text{eff}} > 600\,\text{GeV}$. The region $\texttt{SR0}^{\text{tight}}_{\text{bveto}}$ is defined by $m_{\text{eff}} > 1250\,\text{GeV}$. The labels for the signal points show the NLSP candidate considered, and $(m_{\text{NLSP}}, m_{\text{LSP}})$ in GeV.

while retaining sensitivity to a general range of models. The resulting region, $\texttt{SR0}^{\text{loose}}_{\text{bveto}}$, is defined with $m_{\text{eff}} > 600\,\text{GeV}$, a selection which reduces the number of expected background events from about 200 to about 10.

A region targeting the $LL\bar{E}12k$ R-parity violating models is defined next. It is observed that increasing the m_{eff} floor further increases significance. A limit of ≥ 1 background event in MC was required in the optimisation of the signal regions in order to avoid large uncertainties in the reducible background estimate. With this consideration $m_{\text{eff}} > 1250\,\text{GeV}$ was chosen to define $\texttt{SR0}^{\text{tight}}_{\text{bveto}}$.

A third region, requiring b-jets, is defined to target the intermediate $\Delta m(\text{NLSP}, \text{LSP})$ region for the gluino and wino NLSP cases. Similar to the $\texttt{SR0}^{\text{tight}}_{\text{bveto}}$ definition, a m_{eff} requirement is placed such that significance is maximised while preserving ≥ 1 background event in MC (Figure 5.10). Therefore the requirements of ≥ 1 b-jet and $m_{\text{eff}} > 1300\,\text{GeV}$ define $\texttt{SR0}_{\text{breq}}$.

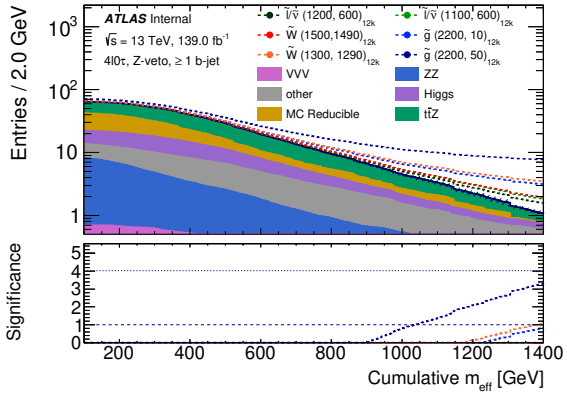

Figure 5.10: Cumulative m_{eff} distribution for simulated signal and background events in a $4\ell 0\tau$ region with Z-veto and b-requirement. The upper pad shows the number of events in a region with m_{eff} greater than the value on the x-axis, while the lower pad shows the significance of the same region. The region $\texttt{SR0}_{\text{breq}}$ is defined by $m_{\text{eff}} > 1300\,\text{GeV}$. The labels for the signal points show the NLSP candidate considered, and $(m_{\text{NLSP}}, m_{\text{LSP}})$ in GeV.

5.4.3 Signal regions targeting RPV models with decays to tau-leptons and light leptons

The third class of regions require both light leptons and hadronically-decaying taus in the final state. These target the $LL\bar{E}i33$ R-parity violating models. Regions with prefix `SR1` require at least 1 tau and exactly 3 light leptons, while those with the prefix `SR2` require at least 2 taus and exactly 2 light leptons. The Z-veto was applied to reduce contributions from Standard Model processes with Z decays.

As with the $4\ell 0\tau$ regions, a requirement on the number of b-jets was considered. Figure 5.11 shows that a b-veto is effective against eliminating $t\bar{t}Z$ and $t\bar{t}WW$ backgrounds at the expense of sensitivity to the intermediate mass gluino NLSP models. Therefore both b-vetoing and b-requiring signal regions are again defined to provide good sensitivity to each of the models considered.

General signal regions $\texttt{SR1}^{\text{loose}}_{\text{bveto}}$ and $\texttt{SR2}^{\text{loose}}_{\text{bveto}}$ are defined to mirror $\texttt{SR0}^{\text{loose}}_{\text{bveto}}$ and have $m_{\text{eff}} > 600\,\text{GeV}$ and a b-veto. These general regions are defined in order to have sensitivity to a wide range of models.

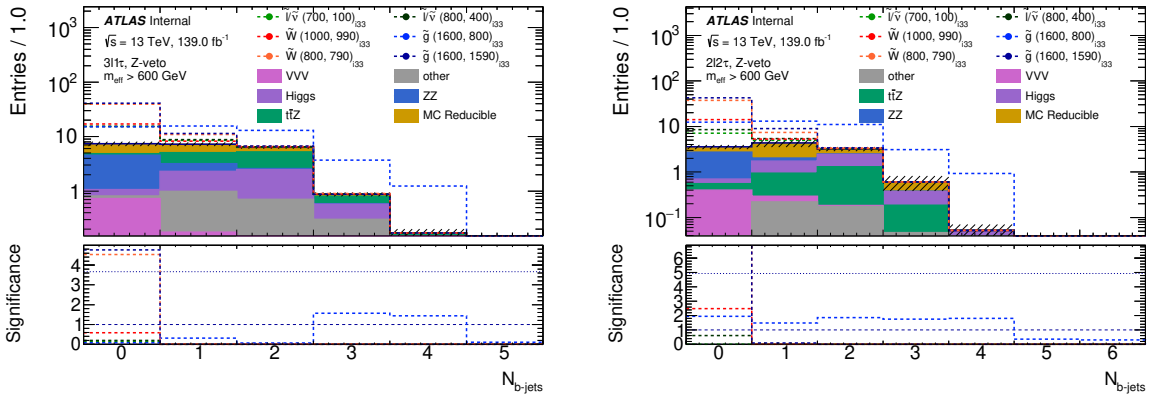

(a) b-jet multiplicity in $3\ell 1\tau$ events **(b)** b-jet multiplicity in $2\ell 2\tau$ events

Figure 5.11: b-jet multiplicities of simulated signal and background events in regions with hadronically-decaying taus, a Z-veto and $m_{\text{eff}} > 600\,\text{GeV}$. The signal region $\texttt{SR1}^{\text{loose}}_{\text{bveto}}$ is the first bin of the left plot, and $\texttt{SR2}^{\text{loose}}_{\text{bveto}}$ is the first bin of the right plot. The significance of each bin in b-jet multiplicity is shown in the lower pad. The labels for the signal points show the NLSP candidate considered, and $(m_{\text{NLSP}}, m_{\text{LSP}})$ in GeV.

For the regions specifically targeting the $LL\bar{E}i33$ models, at least 1 MC background event was kept in the signal region (as observed in Figure 5.12), and sufficient data statistics were ensured in the control regions for the fake lepton estimation. The b-vetoing signal regions $\texttt{SR1}^{\text{tight}}_{\text{bveto}}$ and $\texttt{SR2}^{\text{tight}}_{\text{bveto}}$ are defined requiring $m_{\text{eff}} > 1000\,\text{GeV}$. Two b-requiring signal regions are defined in order to have sensitivity to the gluino models: $\texttt{SR1}_{\text{breq}}$ requires $m_{\text{eff}} > 1300\,\text{GeV}$, while $\texttt{SR2}_{\text{breq}}$ requires $m_{\text{eff}} > 1100\,\text{GeV}$.

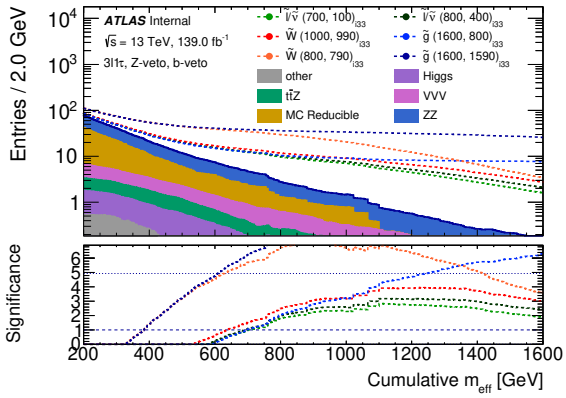

(a) Region requiring $3\ell 1\tau$ and vetoing b-jets. $\texttt{SR1}^{\text{loose}}_{\text{bveto}}$ requires $m_{\text{eff}} > 600\,\text{GeV}$ while $\texttt{SR1}^{\text{tight}}_{\text{bveto}}$ requires $m_{\text{eff}} > 1000\,\text{GeV}$.

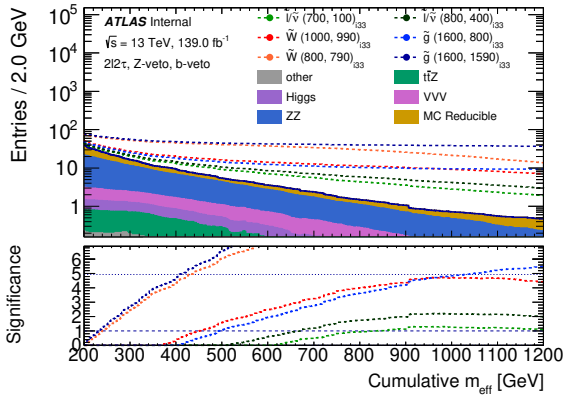

(b) Region requiring $2\ell 2\tau$ and vetoing b-jets. $\texttt{SR2}^{\text{loose}}_{\text{bveto}}$ requires $m_{\text{eff}} > 600\,\text{GeV}$ while $\texttt{SR2}^{\text{tight}}_{\text{bveto}}$ requires $m_{\text{eff}} > 1000\,\text{GeV}$.

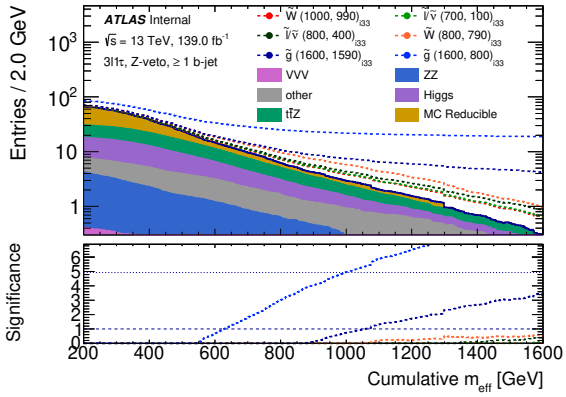

(c) Region requiring $3\ell 1\tau$ and b-jets. $\texttt{SR1}_{\text{breq}}$ requires $m_{\text{eff}} > 1300\,\text{GeV}$.

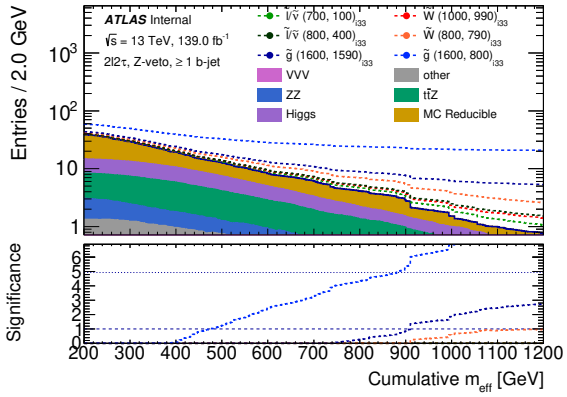

(d) Region requiring $2\ell 2\tau$ and b-jets. $\texttt{SR2}_{\text{breq}}$ requires $m_{\text{eff}} > 1100\,\text{GeV}$.

Figure 5.12: Cumulative m_{eff} distributions of simulated signal and background events in $3\ell 1\tau$ (left) and $2\ell 2\tau$ (right) Z-vetoing signal regions which either veto (upper) or require (lower) b-jets. The upper pad shows the number of events in a region with m_{eff} greater than the value on the x-axis, while the lower pad shows the significance of the same region. The labels for the signal points show the NLSP candidate considered, and $(m_{\text{NLSP}}, m_{\text{LSP}})$ in GeV.

5.4.4 Summary of signal regions

The optimised signal regions are summarised in Table 5.6. In the naming convention, the number denotes the number of hadronically decaying taus required in the region.

Each of the four SR0-ZZ requires two same-flavour opposite-sign light-lepton pairs with invariant masses close to the Z boson mass. These target the GGM models where

Region	$N(e,\mu)$	$N(\tau_{\text{had}})$	Z boson	Selection	b-jets	Target
SR0-ZZ$^{\text{loose}}$ [2]	≥ 4	≥ 0	require 1st and 2nd	$E_{\text{T}}^{\text{miss}} > 50$ GeV		GGM low mass
SR0-ZZ$^{\text{tight}}$ [2]				$E_{\text{T}}^{\text{miss}} > 100$ GeV		GGM intermediate mass
SR0-ZZ$^{\text{loose}}_{\text{bveto}}$				$E_{\text{T}}^{\text{miss}} > 100$ GeV	veto	GGM intermediate mass
SR0-ZZ$^{\text{tight}}_{\text{bveto}}$				$E_{\text{T}}^{\text{miss}} > 200$ GeV		GGM high mass
SR0$^{\text{loose}}_{\text{bveto}}$	≥ 4	≥ 0	veto	$m_{\text{eff}} > 600$ GeV	veto	General 4ℓ
SR0$^{\text{tight}}_{\text{bveto}}$				$m_{\text{eff}} > 1250$ GeV		RPV $LL\bar{E}12k$
SR0$_{\text{breq}}$				$m_{\text{eff}} > 1300$ GeV	required	
SR1$^{\text{loose}}_{\text{bveto}}$	$= 3$	≥ 1	veto	$m_{\text{eff}} > 600$ GeV	veto	General $3\ell 1\tau$
SR1$^{\text{tight}}_{\text{bveto}}$				$m_{\text{eff}} > 1000$ GeV		RPV $LL\bar{E}i33$
SR1$_{\text{breq}}$				$m_{\text{eff}} > 1300$ GeV	required	
SR2$^{\text{loose}}_{\text{bveto}}$	$= 2$	≥ 2	veto	$m_{\text{eff}} > 600$ GeV	veto	General $2\ell 2\tau$
SR2$^{\text{tight}}_{\text{bveto}}$				$m_{\text{eff}} > 1000$ GeV		RPV $LL\bar{E}i33$
SR2$_{\text{breq}}$				$m_{\text{eff}} > 1100$ GeV	required	

Table 5.6: Summary of signal regions.

a decay via the Z boson is expected. For these regions, the requirements on $E_{\text{T}}^{\text{miss}}$ reduce background contributions from Standard Model ZZ production while the b-veto reduces $t\bar{t}Z$ contributions. Two regions (SR0-ZZ$^{\text{loose}}$ and SR0-ZZ$^{\text{tight}}$) where excesses were observed in the previous analysis [114] have been replicated.

All of the remaining regions veto same-flavour opposite-sign light-lepton pairs with invariant masses close to the Z boson mass to reduce contributions to the background from Z boson decays. High m_{eff} regions are optimised to be sensitive to the R-parity violating $LL\bar{E}$ models, while low m_{eff} b-vetoing regions are defined to provide sensitivity to a wider range of models.

5.5 Background estimation

Backgrounds to this search are events with the same signature – at least 4 reconstructed leptons – as the SUSY signal. These leptons can either be "real" or "fake". Real leptons are those which are prompt and isolated, while "fake" leptons include non-prompt leptons, non-isolated leptons, and other objects mis-identified as prompt, isolated leptons.

[2] These signal regions have been frozen from the previous iteration of this analysis [114].

This distinction between real and fake leptons allows for the classification of backgrounds into "irreducible" and "reducible" backgrounds. Irreducible backgrounds are due to Standard Model processes with at least 4 real leptons in the final state, while reducible backgrounds are due to processes which give at least 1 fake lepton.

The main irreducible backgrounds are ZZ, $t\bar{t}Z$, and VVV (where $V = W, Z$). These contributions are estimated from MC simulation and are normalised to data where possible. This is described in Section 5.5.1. Reducible backgrounds are modelled by a fake factor method [114, 127], and its implementation in this analysis is described in Section 5.5.2. The validation of these estimates is described in Section 5.5.3. The effect of systematic uncertainties relevant to this analysis is discussed in Section 5.5.4.

5.5.1 Irreducible backgrounds

Irreducible backgrounds are due to Standard Model processes which have the same physics signature as that expected from the signal models, i.e. events with four real leptons and high $E_{\mathrm{T}}^{\mathrm{miss}}$ or high m_{eff}. These backgrounds are dominated by ZZ, $t\bar{t}Z$, VVV contributions, with additional contributions from $t\bar{t}WW$, $tt\bar{t}$, $t\bar{t}t\bar{t}$, and various production and decays modes of the Higgs. The ZZ and $t\bar{t}Z$ contributions are taken from simulation and normalised to data, while the remaining contributions were taken from simulation.

Region	$N(e,\mu)$	$N(\tau_{\mathrm{had}})$	$N(b-\mathrm{jets})$	Z boson	Selection
`CRZZ`	≥ 4	≥ 0	$= 0$	require 1st & 2nd	$E_{\mathrm{T}}^{\mathrm{miss}} < 50$ GeV
`CRttZ`	≥ 4	≥ 0	≥ 1	require 1st & veto 2nd	$E_{\mathrm{T}}^{\mathrm{miss}} > 100$ GeV

Table 5.7: Definitions of control regions for irreducible background estimate.

The contributions from ZZ and $t\bar{t}Z$ were normalised to data in control regions enriched in the corresponding process. The definitions of these control regions are listed in Table 5.7. From simulation, the control region `CRZZ` is expected to have about 2200 events, of which about 95% are expected from ZZ; while the region `CRttZ` is expected

to have about 50 events, of which about 60% are expected from $t\bar{t}Z$. Normalising the simulations in the control regions improves the modelling of backgrounds in the signal regions. The normalisation factors, obtained through the HistFitter framework [167] were fitted such that the expected number of events in simulation agreed with the number of events observed in data. The shape of the kinematic distributions was not modified. The number of events expected from simulation and that observed in the control regions are shown in Table 5.8. The resulting normalisation factors were 1.15 ± 0.10 for ZZ and 0.95 ± 0.27 for $t\bar{t}Z$.

The VVV simulation was not normalised to data even though the expected VVV contribution is comparable to or greater than those from ZZ and $t\bar{t}Z$ in some regions. This was because it was not possible to define a control region with sufficient event yields in this analysis. However this can be considered in a future analysis. By the end of Run-3 in 2025, the ATLAS is expected to have collected $\sim 300\,\text{fb}^{-1}$ of $\sqrt{s} =$ 13 TeV to 14 TeV data. With the doubling of the present dataset, and following the recent 5σ discovery of VVV production by CMS [108], defining a VVV normalisation control region may be possible.

The data/MC agreement in the m_{eff} and $E_{\text{T}}^{\text{miss}}$ distributions before and after the fit are shown for `CRZZ` in Figure 5.13, and for `CRttZ` in Figure 5.14. The pre- and post-fit yields in these regions are shown in Table 5.8. The simulation alone is found to model the shape of the distributions well; after the data-derived normalisation factors are applied, the agreement between data and simulation improves especially in the bulk of the distributions.

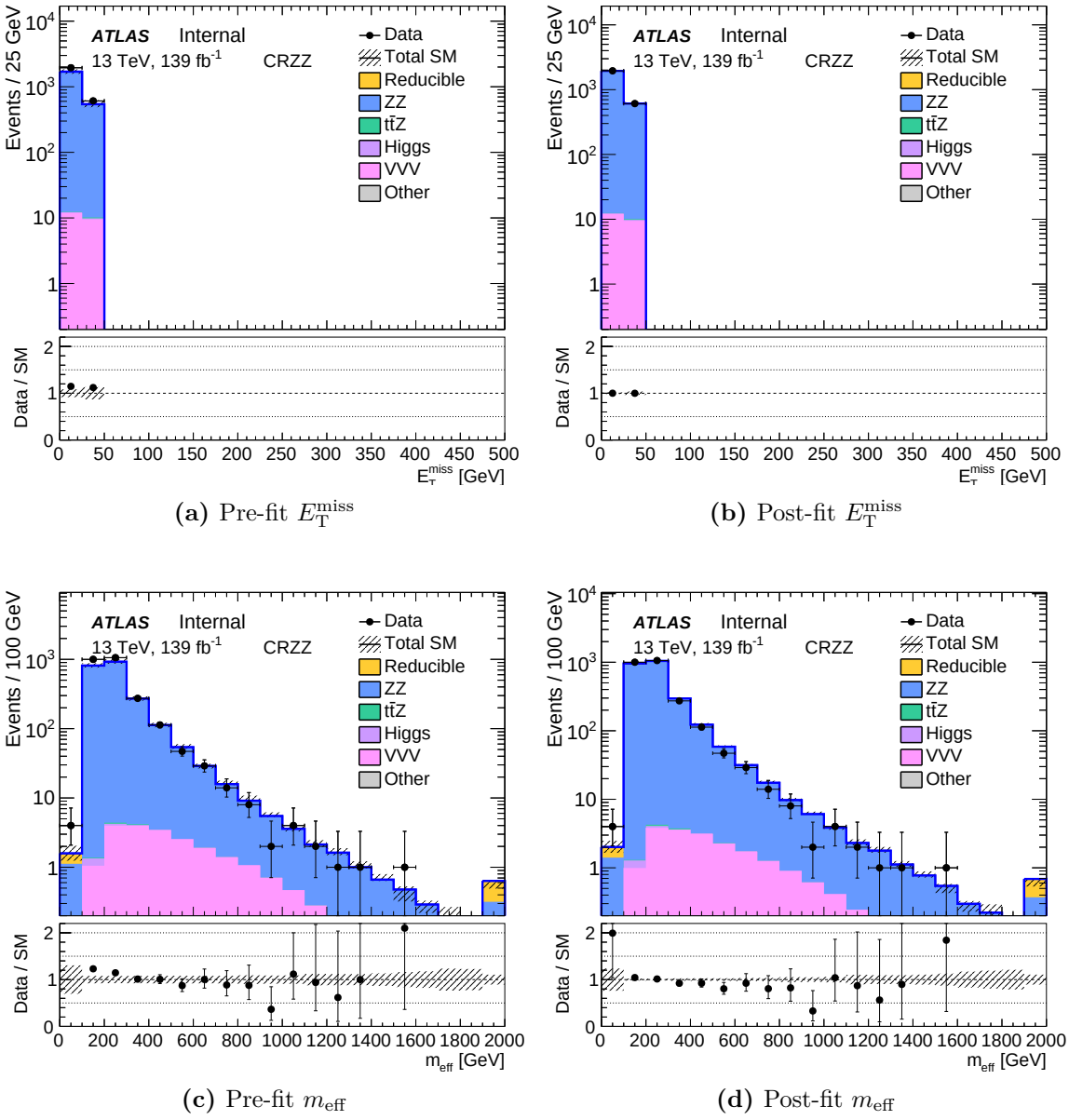

(a) Pre-fit $E_{\mathrm{T}}^{\mathrm{miss}}$ **(b)** Post-fit $E_{\mathrm{T}}^{\mathrm{miss}}$

(c) Pre-fit m_{eff} **(d)** Post-fit m_{eff}

Figure 5.13: The distributions of events in $E_{\mathrm{T}}^{\mathrm{miss}}$ (upper) and m_{eff} (lower) in CRZZ before (left) and after (right) fitting the background to data. Both the statistical and systematic uncertainties in the SM background are included in the uncertainties, shown as the shaded bands. Irreducible backgrounds are taken from MC and normalised to data where possible. Reducible backgrounds are estimated from the fake factor method. "Other" is the sum of the tWZ, $t\bar{t}WW$, $t\bar{t}ZZ$, $t\bar{t}WH$, $t\bar{t}HH$, $t\bar{t}tW$, and $t\bar{t}t\bar{t}$ backgrounds. Note that the region $E_{\mathrm{T}}^{\mathrm{miss}} > 50\,\mathrm{GeV}$ is not part of the control region. This figure was produced by collaborators in the analysis team.

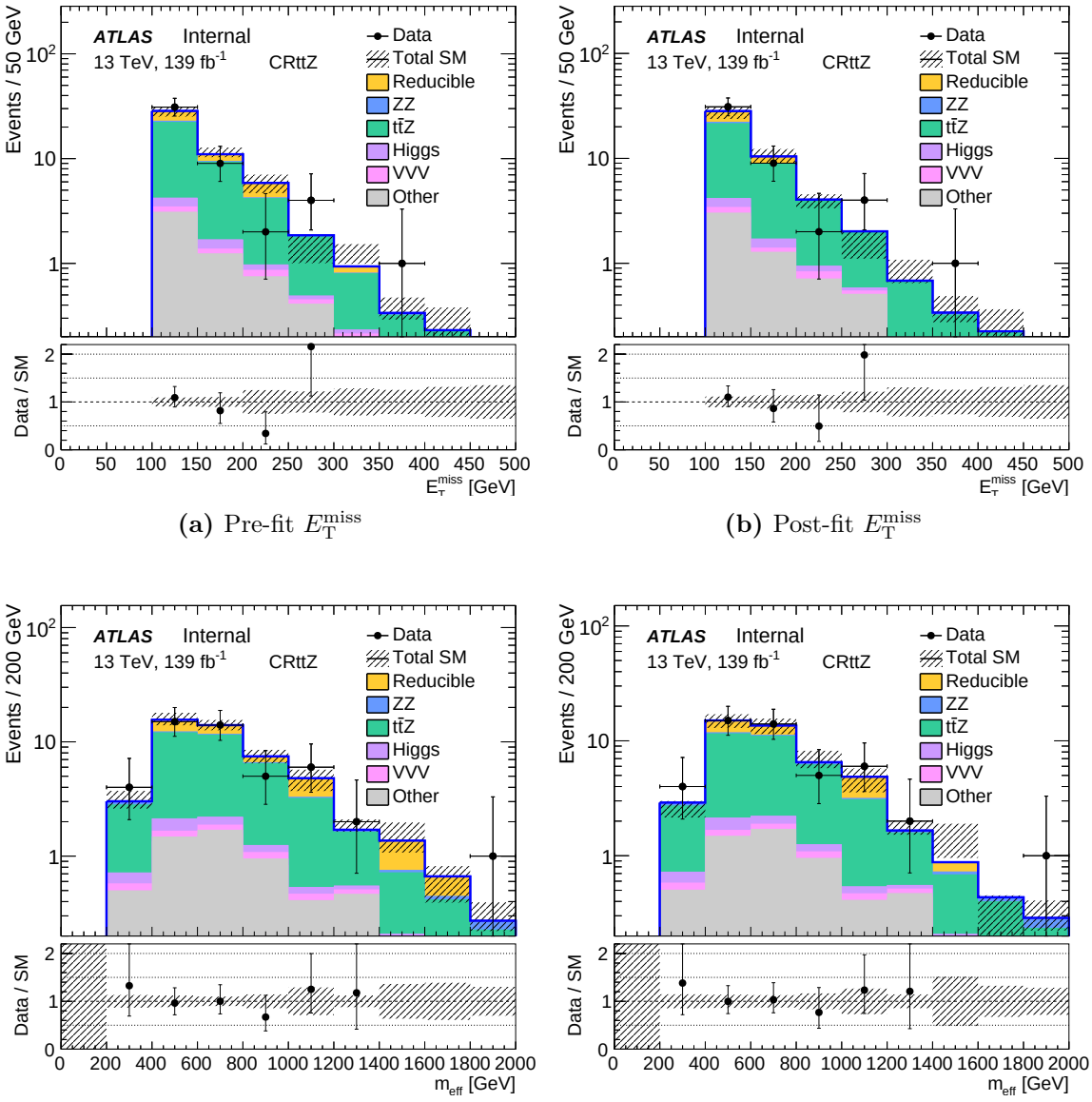

(a) Pre-fit $E_{\mathrm{T}}^{\mathrm{miss}}$ **(b)** Post-fit $E_{\mathrm{T}}^{\mathrm{miss}}$

(c) Pre-fit m_{eff} **(d)** Post-fit m_{eff}

Figure 5.14: The distributions of events in $E_{\mathrm{T}}^{\mathrm{miss}}$ (upper) and m_{eff} (lower) in `CRttZ` before (left) and after (right) fitting the background to data. Both the statistical and systematic uncertainties in the SM background are included in the uncertainties, shown as the shaded bands. Irreducible backgrounds are taken from MC and normalised to data where possible. Reducible backgrounds are estimated from the fake factor method. "Other" is the sum of the tWZ, $t\bar{t}WW$, $t\bar{t}ZZ$, $t\bar{t}WH$, $t\bar{t}HH$, $t\bar{t}tW$, and $t\bar{t}t\bar{t}$ backgrounds. Note that the region $E_{\mathrm{T}}^{\mathrm{miss}} < 100\,\mathrm{GeV}$ is not part of the control region. This figure was produced by collaborators in the analysis team.

Sample	CRZZ	CRttZ
Observed events	2555	47
Fitted bkg events	2555^{+63}_{-62}	47 ± 8
Fitted ZZ	2482^{+64}_{-63}	$0.97^{+0.34}_{-0.51}$
Fitted ttZ	0.43 ± 0.15	29 ± 8
Fitted Higgs	0.61 ± 0.12	1.23 ± 0.19
Fitted VVV	21^{+4}_{-5}	$0.77^{+0.2}_{-0.22}$
Fitted Other	0.17 ± 0.07	5.9 ± 1.1
Fitted fakes	51^{+11}_{-23}	$8.7^{+2.5}_{-2.7}$
MC exp. SM events	2239^{+150}_{-191}	49^{+6}_{-5}
MC exp. ZZ	2165^{+150}_{-189}	$0.84^{+0.32}_{-0.5}$
MC exp. ttZ	0.46 ± 0.12	31^{+5}_{-4}
MC exp. Higgs	0.61 ± 0.12	1.23 ± 0.19
MC exp. VVV	21 ± 5	$0.77^{+0.2}_{-0.22}$
MC exp. Other	0.17 ± 0.07	5.9 ± 1.1
Exp. fakes	51^{+11}_{-23}	$8.7^{+2.5}_{-2.7}$

Table 5.8: Pre- and post-fit yields of events from background processes in `CRZZ` and `CRttZ`. Both the statistical and systematic uncertainties in the SM background are included in the uncertainties shown. Irreducible backgrounds are taken from MC and normalised to data where possible. Reducible backgrounds are estimated from the fake factor method. "Other" is the sum of the tWZ, $t\bar{t}WW$, $t\bar{t}ZZ$, $t\bar{t}WH$, $t\bar{t}HH$, $t\bar{t}tW$, and $t\bar{t}t\bar{t}$ backgrounds. This table was produced by collaborators in the analysis team.

5.5.2 Reducible backgrounds

Reducible backgrounds are due to events with at least four reconstructed leptons where at least one of the reconstructed leptons is an object mis-identified as a prompt, isolated lepton. Such objects are known as "fake" leptons. This contribution is estimated from data by the fake factor method, used previously in Refs. [114, 127]. Its implementation in this analysis is described below. Further details can be found in Refs. [4, 119].

The fake factor is defined as the ratio of the number of fake leptons which satisfy "signal" criteria to that which satisfy "loose" criteria in some control region enriched in fake leptons:

$$f = \frac{\text{Number of signal, fake leptons}}{\text{Number of loose, fake leptons}}. \tag{5.6}$$

The definitions of signal and loose leptons were described previously in Section 5.3.2.

When considering only one possible fake lepton, the reducible contribution to the signal region $N_{\text{SR}}^{\text{reducible}}$ is estimated by multiplying the fake factor by the number of reducible events in a control region $N_{\text{CR}}^{\text{reducible}}$, where the control region requires a loose lepton in place of a signal lepton: $N_{\text{SR}}^{\text{reducible}} = f \times N_{\text{CR}}^{\text{reducible}}$.

As signal regions in this analysis require at least four leptons, the fake factor method can be generalised to account for up to four fake leptons. However it was found that the number of events with three or four fakes is $< 1\%$ of the total SM background so their contributions are neglected. The systematic uncertainty of the reducible estimate is increased to account for these neglected backgrounds (cf. Section 5.5.4). Therefore the number of reducible events in a signal region $N_{\text{SR}}^{\text{reducible}}$ is estimated by accounting for up to two possible fakes:

$$N_{\text{SR}}^{\text{reducible}} = N_{\text{CR1}}^{\text{reducible}} \times f_1 - N_{\text{CR2}}^{\text{reducible}} \times f_1 \times f_2. \tag{5.7}$$

The negative sign of the second term removes doubly counted events from the first term. The control region `CR1` (`CR2`) is defined with the exact same requirements as the signal regions except that it requires one loose lepton (two loose leptons) in place of one (two) of the signal leptons.

The number of reducible events in a control region is estimated by subtracting the contribution of irreducible backgrounds from the number of events observed in data:

$$N_{\text{CR}}^{\text{reducible}} = N_{\text{CR,data}} - N_{\text{CR,MC}}^{\text{irreducible}}. \tag{5.8}$$

The irreducible backgrounds are estimated from MC simulation as previously described in Section 5.5.1.

For this analysis, the dominant processes contributing to the reducible background are $t\bar{t}$ and Z+jets decays which give two fake leptons. Fakes can arise from several sources: light-flavour jets or heavy-flavour jets for all leptons, gluon-jets for τ, or photon conversions for e and τ.

The fake factor was found to depend on lepton flavour, the contributing process, and the source of fakes. Per-process i, per-source j fake factors $f_{i,j}$ are measured in MC simulation for each lepton flavour. The fractional contribution of fakes to the signal region from different processes and sources $R_{i,j}$ is measured in MC simulation in `CR2`. In this region, the composition of fakes is similar to that in the signal region, but `CR2` has significantly more events and therefore smaller statistical uncertainties. Per-source scale factors s_j are used to correct the fake factors measured in MC simulation to data. These were measured in dedicated control regions for lepton flavour and fake source combinations when such a control region with sufficient event yields could be defined, otherwise the scale factor was assumed to be unity.

The total fake rate f_w for a given lepton flavour is computed from a weighted sum. MC fake rates $f_{i,j}$ of a given process i and source j are corrected to data by scale factors s_j and weighted by the fractional contribution of the process and source $R_{i,j}$. The corrected and weighted fake rates are summed over all the processes and sources considered:

$$f_w = \sum_{\substack{i\in\{t\bar{t},Z\text{+jets}\} \\ j\in\{\text{LF,HF,QJ,GJ},\gamma\}}} f_{i,j} \times s_j \times R_{i,j}. \tag{5.9}$$

Signal contamination in control regions

The ratio of expected signal events to the total number of expected events $\frac{N_{\text{MC,signal}}}{N_{\text{MC,SM}}+N_{\text{MC,signal}}}$ was measured in MC simulation for all fake control regions `CR1` and `CR2`. This quantifies the signal contamination expected. It was found that this fraction was as high as 80% for some mass points of certain models. Examples are shown in Figure 5.15.

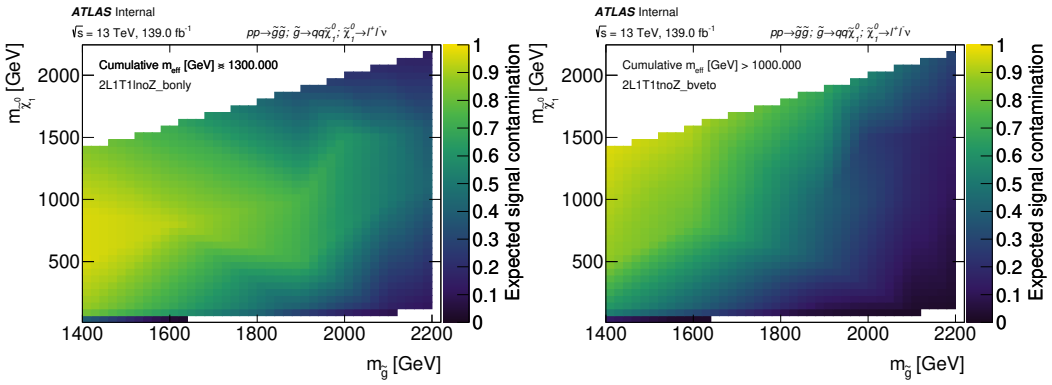

(a) CR1 for $\texttt{SR1}_{\text{breq}}$, where one loose light-lepton is required

(b) CR1 for $\texttt{SR2}^{\text{tight}}_{\text{bveto}}$, where one loose tau is required

Figure 5.15: Examples of high contamination of SUSY events in some fake control regions, assuming the $LL\bar{E}i33$ scenario with a gluino NLSP. The contamination was measured in MC simulation as a function of the masses of the LSP and NLSP.

The effect of high signal contamination was studied for a few signal points by including their contributions in the $N^{\text{irreducible}}_{\text{CR,MC}}$ term of Eq. 5.8, thereby subtracting the potential signal contamination from the fake control regions. This resulted in a smaller reducible estimate in the signal region. It was decided to ignore the signal contamination in favour of a larger, more conservative reducible estimate.

5.5.3 Validation

The background estimates from the methods described in sections 5.5.1 and 5.5.2 were compared to data in validation regions. These regions are designed to be low in signal contamination, and kinematically similar to but statistically orthogonal to the signal regions. The region definitions and their targeted backgrounds are listed in Table 5.9.

The data yields and the background estimates before and after fitting to the irreducible backgrounds are shown in Table 5.10. The yields and background estimates are compatible within 2σ, giving confidence to the background predictions.

The distributions in the validation regions of the variables $E_{\text{T}}^{\text{miss}}$ and m_{eff} are shown in Figures 5.16 and 5.17 respectively. Overall the modelled distributions agree with

Validation Region	$N(e,\mu)$	$N(\tau_{\text{had}})$	$N(b-\text{jets})$	Z boson	Selection	Target
VRZZ	≥ 4	$= 0$	$= 0$	require 1st & veto 2nd	–	ZZ
VRttZ	≥ 4	$= 0$	≥ 0	veto	$400 < m_{\text{eff}} < 1300$ GeV	$t\bar{t}Z$
VR0-noZ	≥ 4	$= 0$	$= 0$	veto	$m_{\text{eff}} < 600$ GeV	$t\bar{t}$, Z+jets, ZZ
VR1-noZ	$= 3$	≥ 1	$= 0$	veto	$m_{\text{eff}} < 600$ GeV	$t\bar{t}$, Z+jets
VR2-noZ	$= 2$	≥ 2	$= 0$	veto	$m_{\text{eff}} < 600$ GeV	$t\bar{t}$, Z+jets
VR1-Z	$= 3$	≥ 1	$= 0$	require 1st	–	Z+jets
VR2-Z	$= 2$	≥ 2	$= 0$	require 1st	–	Z+jets

Table 5.9: Definitions of validation regions.

those observed in data within uncertainties.

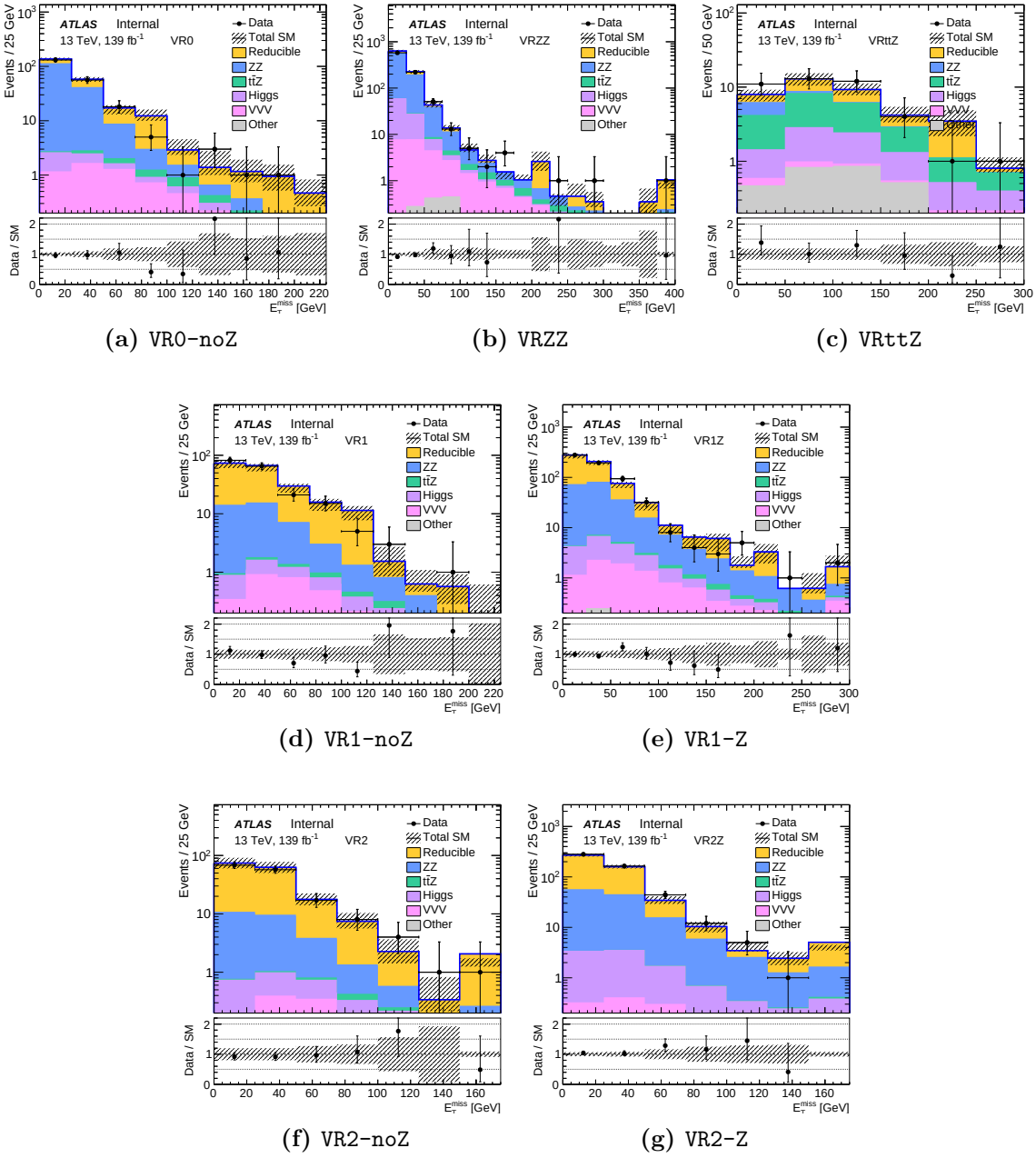

(a) VR0-noZ (b) VRZZ (c) VRttZ

(d) VR1-noZ (e) VR1-Z

(f) VR2-noZ (g) VR2-Z

Figure 5.16: The distributions of events in $E_{\mathrm{T}}^{\mathrm{miss}}$ in the validation regions. Both the statistical and systematic uncertainties in the SM background are included in the uncertainties, shown as the shaded bands. Irreducible backgrounds are taken from MC and normalised to data where possible. Reducible backgrounds are estimated from the fake factor method. "Other" is the sum of the tWZ, $t\bar{t}WW$, $t\bar{t}ZZ$, $t\bar{t}WH$, $t\bar{t}HH$, $t\bar{t}tW$, and $t\bar{t}t\bar{t}$ backgrounds. This figure was produced by collaborators in the analysis team.

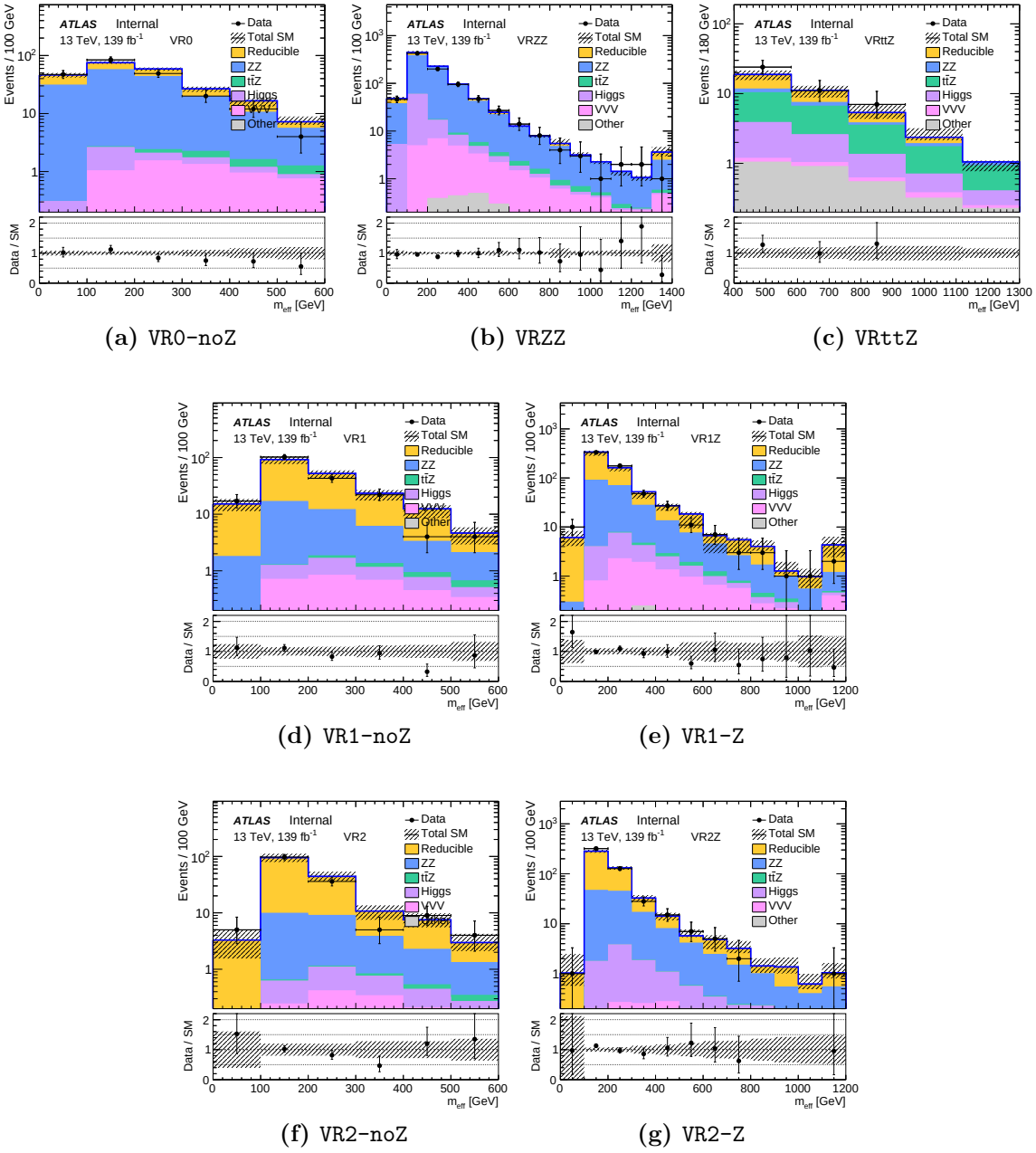

(a) VR0-noZ (b) VRZZ (c) VRttZ

(d) VR1-noZ (e) VR1-Z

(f) VR2-noZ (g) VR2-Z

Figure 5.17: The distributions of events in m_{eff} in the validation regions. Both the statistical and systematic uncertainties in the SM background are included in the uncertainties, shown as the shaded bands. Irreducible backgrounds are taken from MC and normalised to data where possible. Reducible backgrounds are estimated from the fake factor method. "Other" is the sum of the tWZ, $t\bar{t}WW$, $t\bar{t}ZZ$, $t\bar{t}WH$, $t\bar{t}HH$, $t\bar{t}tW$, and $t\bar{t}t\bar{t}$ backgrounds. This figure was produced by collaborators in the analysis team.

Sample	VRZZ	VRttZ	VR0	VR1	VR1Z	VR2	VR2Z
Observed events	874	42	216	192	620	156	505
Fitted bkg events	924^{+43}_{-34}	38 ± 5	230 ± 12	199 ± 25	624^{+57}_{-58}	164 ± 29	480 ± 26
Fitted ZZ	738 ± 20	$2.7^{+1.0}_{-1.1}$	160 ± 7	$36.8^{+2.3}_{-2.2}$	200^{+9}_{-11}	$23.3^{+1.2}_{-1.3}$	119 ± 7
Fitted ttZ	$4.6^{+1.3}_{-1.4}$	15 ± 4	1.7 ± 0.5	0.75 ± 0.34	$2.1^{+1.1}_{-1.0}$	0.31 ± 0.1	0.12 ± 0.04
Fitted Higgs	77^{+36}_{-26}	5.5 ± 0.8	$3.1^{+1.0}_{-0.7}$	2.4 ± 0.5	13.6 ± 3.0	1.87 ± 0.31	8.8 ± 1.8
Fitted VVV	26 ± 5	$0.43^{+0.1}_{-0.11}$	5.4 ± 1.1	2.8 ± 0.8	$8.7^{+2.1}_{-2.2}$	1.23 ± 0.26	1.52 ± 0.33
Fitted Other	$2.2^{+0.4}_{-0.5}$	3.1 ± 0.4	$0.45^{+0.1}_{-0.11}$	$0.24^{+0.19}_{-0.2}$	0.9 ± 0.5	0.15 ± 0.04	$0.082^{+0.025}_{-0.028}$
Fitted fakes	77 ± 10	$12.2^{+3.5}_{-3.6}$	59 ± 9	156 ± 24	398 ± 56	137 ± 29	350 ± 25
MC exp. SM events	830^{+63}_{-64}	39 ± 4	210^{+12}_{-14}	195 ± 25	599^{+58}_{-59}	161 ± 29	464 ± 27
MC exp. ZZ	644^{+51}_{-57}	$2.4^{+1.0}_{-1.1}$	140^{+8}_{-10}	$32.1^{+2.7}_{-3.2}$	175^{+14}_{-16}	$20.3^{+1.8}_{-2.1}$	104^{+9}_{-10}
MC exp. ttZ	4.9 ± 0.9	$15.5^{+2.4}_{-2.1}$	$1.84^{+0.36}_{-0.35}$	$0.8^{+0.32}_{-0.31}$	2.2 ± 1.0	0.33 ± 0.07	$0.128^{+0.029}_{-0.026}$
MC exp. Higgs	77^{+36}_{-26}	5.5 ± 0.8	$3.1^{+1.0}_{-0.7}$	2.4 ± 0.5	$13.6^{+3.1}_{-3.0}$	1.87 ± 0.31	8.8 ± 1.8
MC exp. VVV	26 ± 5	0.43 ± 0.11	5.4 ± 1.1	2.8 ± 0.8	8.7 ± 2.2	1.23 ± 0.26	1.52 ± 0.33
MC exp. Other	2.2 ± 0.5	3.1 ± 0.4	$0.45^{+0.1}_{-0.12}$	$0.24^{+0.19}_{-0.2}$	0.9 ± 0.5	0.15 ± 0.04	$0.082^{+0.025}_{-0.028}$
Exp. fakes	77 ± 10	$12.2^{+3.5}_{-3.6}$	59 ± 9	156 ± 24	398 ± 56	137 ± 29	350 ± 25

Table 5.10: The yields in data, and pre- and post-fit background estimates in the validation regions. Both the statistical and systematic uncertainties in the SM background are included in the uncertainties shown. Irreducible backgrounds are taken from MC and normalised to data where possible. Reducible backgrounds are estimated from the fake factor method. "Other" is the sum of the tWZ, $t\bar{t}WW$, $t\bar{t}ZZ$, $t\bar{t}WH$, $t\bar{t}HH$, $t\bar{t}tW$, and $t\bar{t}t\bar{t}$ backgrounds. This table was produced by collaborators in the analysis team.

5.5.4 Systematic uncertainties

The systematic uncertainties affecting the estimates of Standard Model and SUSY signal events arise from three sources: (1) experimental uncertainties in event reconstruction, (2) theoretical uncertainties, and (3) statistical uncertainty of MC simulation. Uncertainties on the reducible backgrounds are also considered. Figure 5.18 shows a breakdown of the systematic uncertainties.

Uncertainty on reducible backgrounds The dominant uncertainty in most regions is that of the reducible background. In the 4-light-lepton regions, the reducible

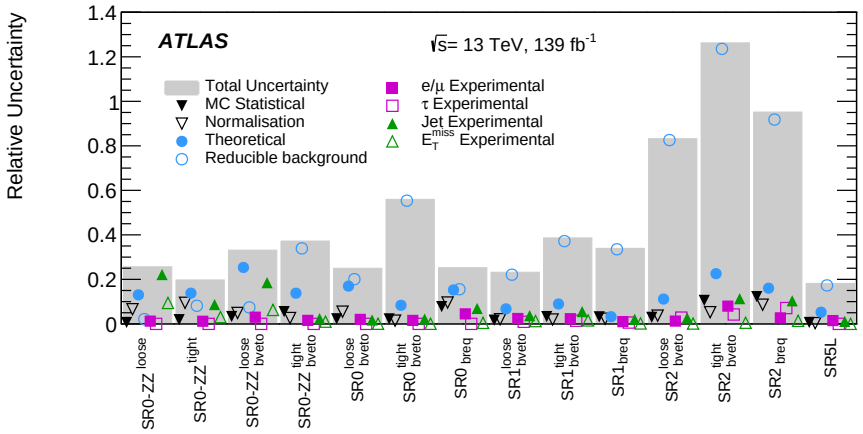

Figure 5.18: A breakdown of the uncertainties in all the signal regions. Note that this figure, created by collaborators in the analysis team and reproduced from Ref. [4], includes a five-lepton region, SR5L, not described in this thesis.

background uncertainty is the greatest in $\texttt{SR0-ZZ}^{\text{tight}}_{\text{bveto}}$and $\texttt{SR0}_{\text{breq}}$, reaching 40% and 60% respectively; in these regions only one event is observed in data. In the regions requiring $2\tau_{\text{had}}$, the reducible uncertainty is as high as 120% due to low event yields in the associated control regions.

The reducible uncertainty is dominated by the statistical uncertainty of the data events in the corresponding CR1 and CR2. There is a small contribution from the uncertainty on the weighted fake factor, propagated from statistical uncertainties of the per-source, per-process fake factors, the data/MC scale-factors, and the process fractions.

The contribution of events with three or four fake leptons to the reducible estimate is considered as part of the reducible background uncertainty. An upper limit on this contribution was obtained by applying the fake factors to control regions with three loose leptons and one signal lepton. This upper limit added to its 1σ statistical uncertainty was subsequently added to the reducible background uncertainty.

Theoretical uncertainties on irreducible backgrounds The next largest uncertainty in most regions is the theoretical uncertainty. This includes uncertainties on the cross-section, and uncertainties on acceptance. The former uncertainty was

estimated by calculating the cross-section to a higher order in perturbation theory than that in the Monte Carlo program (cf. Table 5.3). Its effect was considered for processes taken from MC simulation without normalisation to data; the magnitudes of uncertainties were taken to be 20% for VVV [130], 10% for $t\bar{t}H$ [168], 5% for H via gluon-gluon fusion [168], and 20% for all other processes.

The uncertainties on acceptance arise from differences in event yields when holding the event selection constant while varying underlying parameters of the Monte Carlo generator or of the theory. For ZZ, $t\bar{t}Z$, VVV, $t\bar{t}H$, and Higgs samples, the effects of varying the renormalisation and factorisation scales by factors of 1/2 and 2 were considered. For ZZ, VVV, $t\bar{t}H$, and Higgs samples, the impact of varying the strong coupling constant $\alpha_S \pm 0.001$ was studied. For the ZZ samples, uncertainties were considered that arose from resummation and merging scale variations, as well as from using an alternate recoil scheme for single particle emission in Sherpa.

Uncertainties in the SUSY signal yields were also evaluated. Conservatively, 5 to 20% variations were considered in the factorisation, renomalisation, and merging scales, while 10 to 25% variations were considered in parton shower tuning. Larger variations were considered in regions with smaller expected yields. The theoretical uncertainties in SUSY signal yields were found to be from about 5% in the 4 light-lepton regions to about 20% in the regions with 2 τ_{had}.

Experimental uncertainties Experimental uncertainties were considered for all physics objects. For electrons, muons, and τ_{had}, these included uncertainties on triggering, reconstruction, identification, isolation, and lepton energy scale and resolution; these uncertainties were less than 5% of the expected background yields. Uncertainties on jets include those on the jet energy scale, jet energy resolution, jet vertex tagging, and b-tagging. Uncertainty on $E_{\text{T}}^{\text{miss}}$ was propagated from all other physics objects. Jet and $E_{\text{T}}^{\text{miss}}$ uncertainties were generally about a few percent in most regions, but they approach 20% in the `SR0-ZZ` regions where requirements on $E_{\text{T}}^{\text{miss}}$ are made.

For SUSY signals, the experimental uncertainties were typically about 10%.

5.6 Results and interpretation

The expected and observed yields in the signal regions are listed in Table 5.11 and shown in Figure 5.19. We note that no excess was observed in the signal regions SR0-ZZ$^{\text{loose}}$ and SR0-ZZ$^{\text{tight}}$, where excesses were observed in the previous analysis [114].

The $E_{\text{T}}^{\text{miss}}$ and m_{eff} distributions in the signal regions of data, expected backgrounds, and example SUSY models are shown in Figures 5.20 and 5.21. The expected SM distributions are seen to model the observed distributions in data excellently.

Visualisations of selected events within the signal regions are shown in Figures 5.22 and 5.23.

	SR0-ZZ$^{\text{loose}}$	SR0-ZZ$^{\text{tight}}$	SR0-ZZ$^{\text{loose}}_{\text{bveto}}$	SR0-ZZ$^{\text{tight}}_{\text{bveto}}$	SR0$^{\text{loose}}_{\text{bveto}}$	SR0$^{\text{tight}}_{\text{bveto}}$	SR0$_{\text{breq}}$
Observed	157	17	5	1	11	1	3
Total SM	161^{+41}_{-43}	$18.4^{+3.6}_{-3.3}$	$7.3^{+2.4}_{-1.9}$	1.1 ± 0.4	$11.5^{+2.9}_{-2.2}$	$3.5^{+2.0}_{-2.2}$	$1.19^{+0.30}_{-0.28}$
ZZ	125^{+40}_{-42}	$4.5^{+2.6}_{-2.1}$	$3.7^{+2.2}_{-1.7}$	$0.05^{+0.11}_{-0.04}$	$7.6^{+1.6}_{-1.7}$	$0.64^{+0.28}_{-0.29}$	$0.19^{+0.15}_{-0.19}$
$t\bar{t}Z$	15 ± 4	7.4 ± 1.8	0.87 ± 0.24	$0.12^{+0.05}_{-0.04}$	$0.7^{+0.18}_{-0.19}$	$0.02^{+0.014}_{-0.015}$	0.49 ± 0.13
Higgs	0.79 ± 0.1	0.29 ± 0.05	$0.09^{+0.028}_{-0.027}$	$0.0046^{+0.0019}_{-0.0018}$	0.24 ± 0.04	$0.02^{+0.007}_{-0.006}$	$0.16^{+0.05}_{-0.06}$
VVV	$7.9^{+1.9}_{-2.0}$	2.4 ± 0.6	2.2 ± 0.5	0.44 ± 0.12	1.6 ± 0.4	0.21 ± 0.06	$0.083^{+0.027}_{-0.029}$
Other	3.3 ± 0.7	1.7 ± 0.4	0.32 ± 0.09	$0.04^{+0.013}_{-0.014}$	$0.142^{+0.029}_{-0.032}$	$0.032^{+0.019}_{-0.022}$	$0.27^{+0.06}_{-0.05}$
Reducible	$9.1^{+3.4}_{-4.4}$	$2.0^{+1.5}_{-1.7}$	$0.15^{+0.54}_{-0.15}$	0.4 ± 0.4	$1.2^{+2.3}_{-1.2}$	$2.6^{+1.9}_{-2.2}$	$0.00^{+0.19}_{-0.00}$

	SR1$^{\text{loose}}_{\text{bveto}}$	SR1$^{\text{tight}}_{\text{bveto}}$	SR1$_{\text{breq}}$	SR2$^{\text{loose}}_{\text{bveto}}$	SR2$^{\text{tight}}_{\text{bveto}}$	SR2$_{\text{breq}}$
Observed	7	2	2	5	2	1
Total SM	$7.7^{+1.8}_{-1.9}$	$1.6^{+0.6}_{-0.7}$	2.2 ± 0.7	$3.4^{+2.8}_{-1.6}$	$0.35^{+0.44}_{-0.13}$	$0.52^{+0.50}_{-0.13}$
ZZ	$2.0^{+0.4}_{-0.6}$	$0.39^{+0.13}_{-0.19}$	0.04 ± 0.04	$1.54^{+0.3}_{-0.4}$	$0.23^{+0.08}_{-0.13}$	0.06 ± 0.06
$t\bar{t}Z$	0.19 ± 0.1	$0.029^{+0.047}_{-0.029}$	0.22 ± 0.06	$0.058^{+0.024}_{-0.025}$	0.0 ± 0.0	0.19 ± 0.07
Higgs	0.24 ± 0.07	$0.033^{+0.019}_{-0.020}$	$0.14^{+0.05}_{-0.06}$	0.2 ± 0.04	$0.033^{+0.010}_{-0.011}$	0.2 ± 0.07
VVV	$0.66^{+0.16}_{-0.17}$	$0.16^{+0.04}_{-0.05}$	0.021 ± 0.008	$0.38^{+0.09}_{-0.10}$	$0.084^{+0.025}_{-0.027}$	$0.024^{+0.009}_{-0.010}$
Other	0.009 ± 0.005	$0.02^{+0.013}_{-0.018}$	$0.183^{+0.039}_{-0.034}$	0.005 ± 0.005	0.0014 ± 0.0012	$0.054^{+0.019}_{-0.015}$
Reducible	4.7 ± 1.7	1.0 ± 0.6	1.6 ± 0.7	$1.2^{+2.8}_{-1.2}$	$0.0^{+0.4}_{-0.0}$	$0.0^{+0.5}_{-0.0}$

Table 5.11: Expected and observed yields for 139 fb^{-1} in the signal regions after the background-only fit. "Other" is the sum of the tWZ, $t\bar{t}WW$, $t\bar{t}ZZ$, $t\bar{t}WH$, $t\bar{t}HH$, $t\bar{t}tW$, and $t\bar{t}t\bar{t}$ backgrounds. Both the statistical and systematic uncertainties in the SM background are included in the uncertainties shown. This table was produced by collaborators in the analysis team, and is reproduced from Ref. [4].

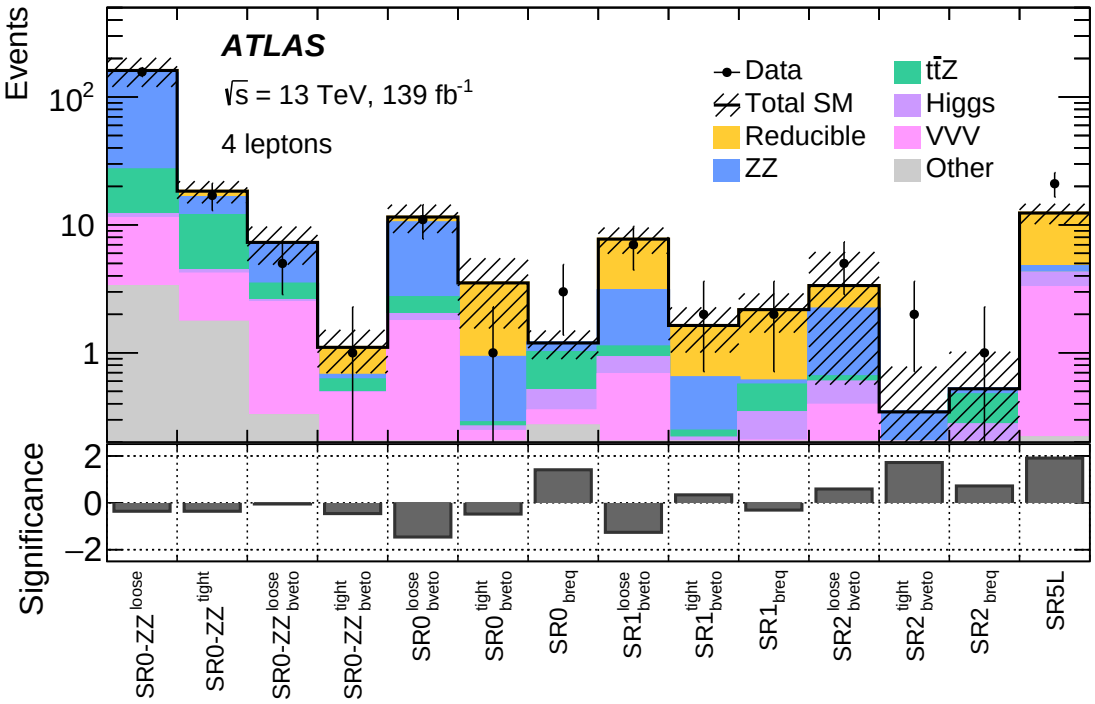

Figure 5.19: The observed and expected yields in the signal regions. "Other" is the sum of the tWZ, $t\bar{t}WW$, $t\bar{t}ZZ$, $t\bar{t}WH$, $t\bar{t}HH$, $t\bar{t}tW$, and $t\bar{t}t\bar{t}$ backgrounds. Both the statistical and systematic uncertainties in the SM background are included in the uncertainties, shown as the shaded bands. The statistical significance of differences between the observed and expected yields are shown in the bottom panel, as calculated by the profile likelihood method in Ref. [169]. This figure was produced by collaborators in the analysis team and is reproduced from Ref. [4]. Note that the figure reports the results of a five-or-more lepton signal region `SR5L`, which is not described in this thesis, and where a 1.9σ excess was observed.

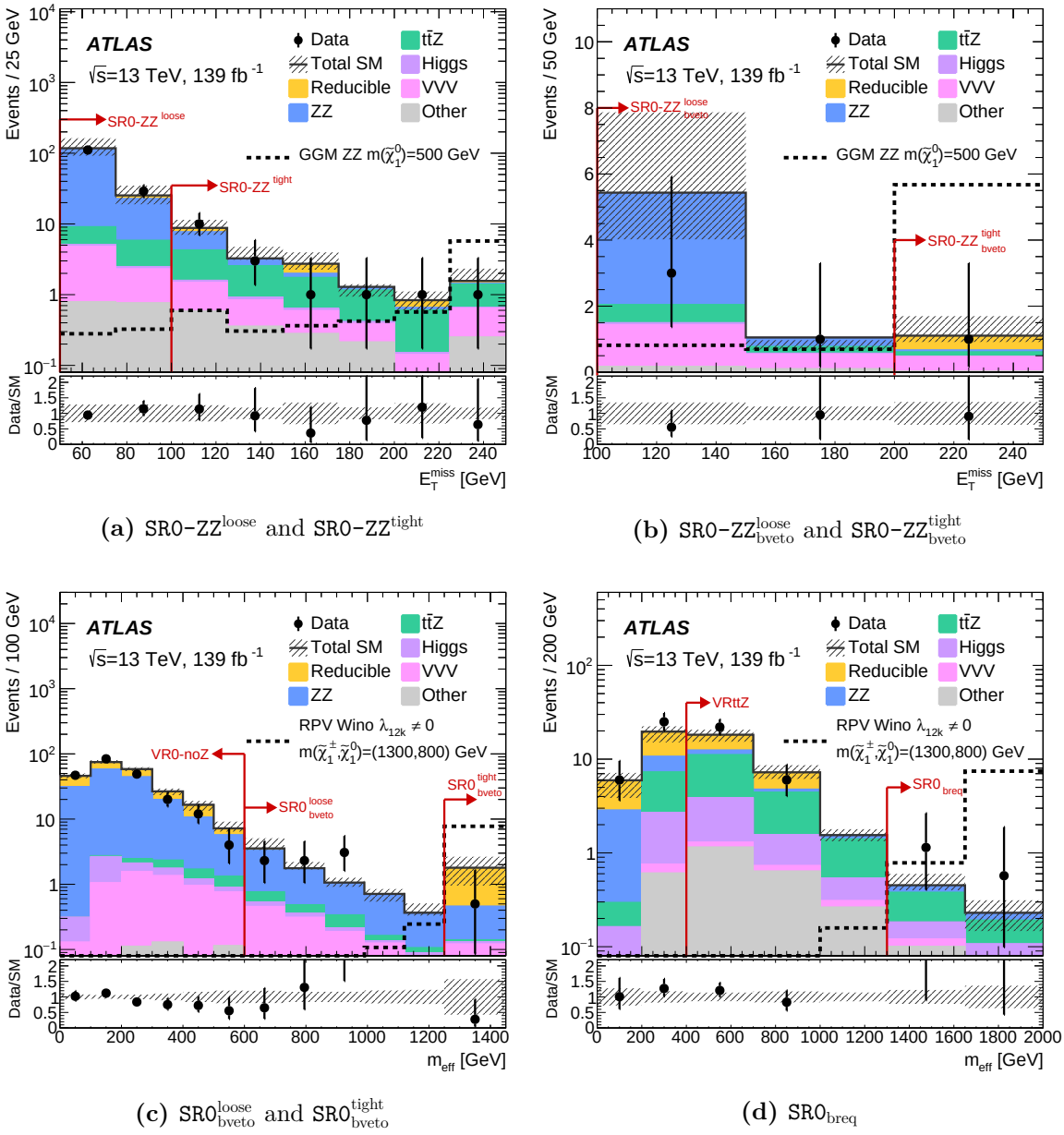

(a) SR0-ZZ$^{\text{loose}}$ and SR0-ZZ$^{\text{tight}}$

(b) SR0-ZZ$^{\text{loose}}_{\text{bveto}}$ and SR0-ZZ$^{\text{tight}}_{\text{bveto}}$

(c) SR0$^{\text{loose}}_{\text{bveto}}$ and SR0$^{\text{tight}}_{\text{bveto}}$

(d) SR0$_{\text{breq}}$

Figure 5.20: The distributions of (a,b) $E_{\text{T}}^{\text{miss}}$ in the GGM-targeting signal regions and (c,d) m_{eff} in the RPV-targeting signal regions with four light leptons. Distributions from the data, the expected SM contribution from the background-only fit, and an example SUSY scenario are shown. "Other" is the sum of the tWZ, $t\bar{t}WW$, $t\bar{t}ZZ$, $t\bar{t}WH$, $t\bar{t}HH$, $t\bar{t}tW$, and $t\bar{t}t\bar{t}$ backgrounds. Both the statistical and systematic uncertainties in the SM background are included in the uncertainties, shown as the shaded area. The final bin in each histogram is an overflow bin. The arrows indicate the requirements on $E_{\text{T}}^{\text{miss}}$ or m_{eff} defining the labelled regions. This figure was produced by collaborators in the analysis team, and is reproduced from Ref. [4].

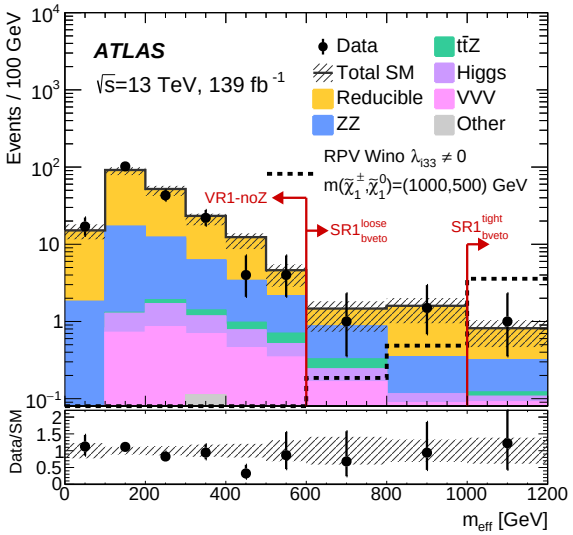

(a) $\texttt{SR1}^{\text{loose}}_{\text{bveto}}$ and $\texttt{SR1}^{\text{tight}}_{\text{bveto}}$

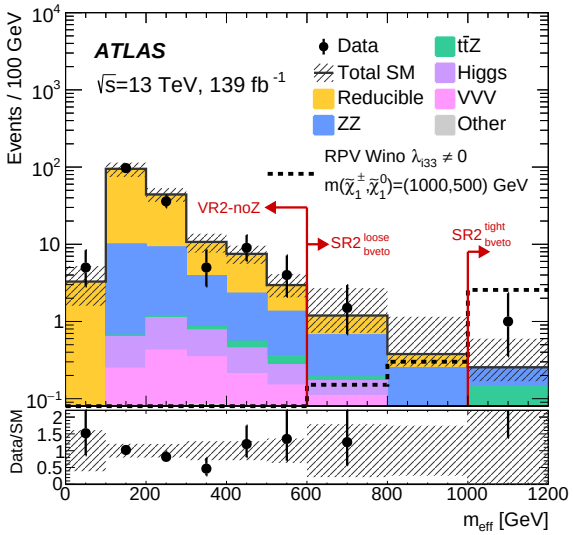

(b) $\texttt{SR2}^{\text{loose}}_{\text{bveto}}$ and $\texttt{SR2}^{\text{tight}}_{\text{bveto}}$

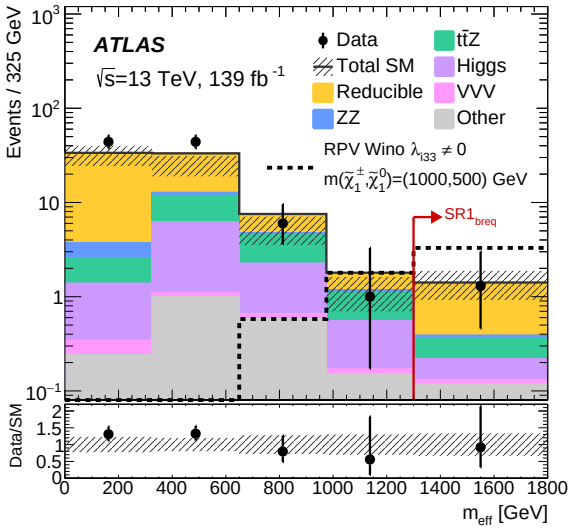

(c) $\texttt{SR1}_{\text{breq}}$

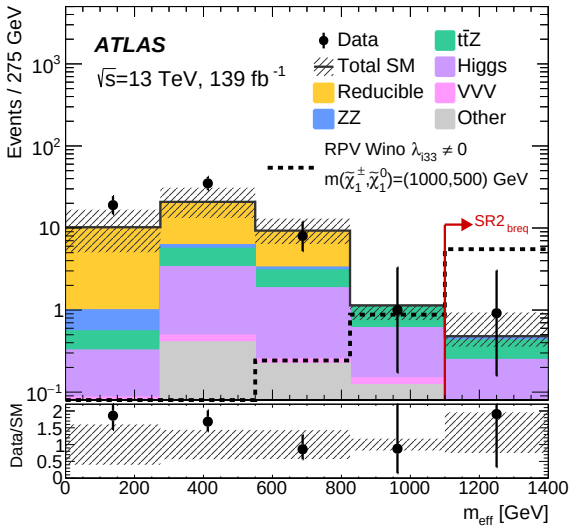

(d) $\texttt{SR2}_{\text{breq}}$

Figure 5.21: The distributions in m_{eff} in the RPV-targeting signal regions with hadronically-decaying taus. Distributions from the data, the expected SM contribution from the background-only fit, and an example SUSY scenario are shown. "Other" is the sum of the tWZ, $t\bar{t}WW$, $t\bar{t}ZZ$, $t\bar{t}WH$, $t\bar{t}HH$, $t\bar{t}tW$, and $t\bar{t}t\bar{t}$ backgrounds. Both the statistical and systematic uncertainties in the SM background are included in the uncertainties, shown as the shaded area. The final bin is an overflow bin. The arrows indicate the requirements on m_{eff} defining the labelled regions. This figure was produced by collaborators in the analysis team, and is reproduced from Ref. [4].

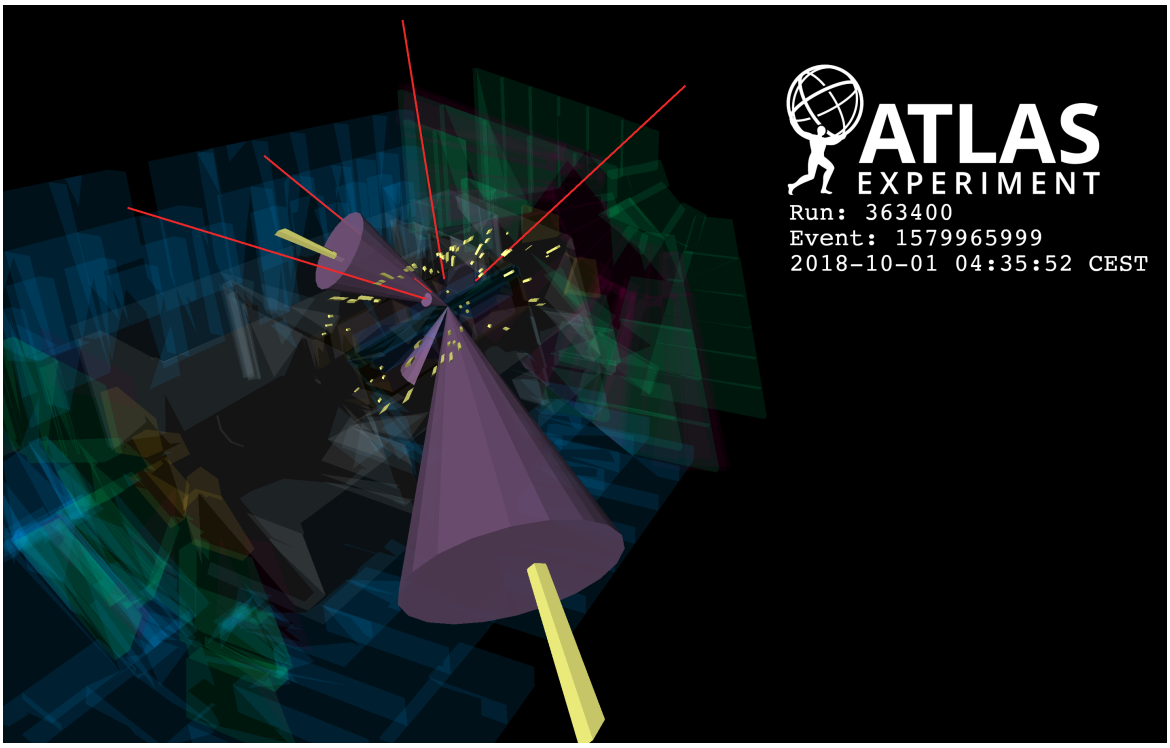

Figure 5.22: Visualisation of a 4-muon event which falls within $\texttt{SR0}_{\text{breq}}$. The event was recorded by ATLAS on 1 October 2018. The muons are represented by the red tracks. Jets are represented by the purple cones and energies in calorimeter clusters are represented by yellow blocks. The highest energy jet has transverse momentum of 595 GeV, while the next highest energy jet has transverse momentum of 262 GeV and is b-tagged.

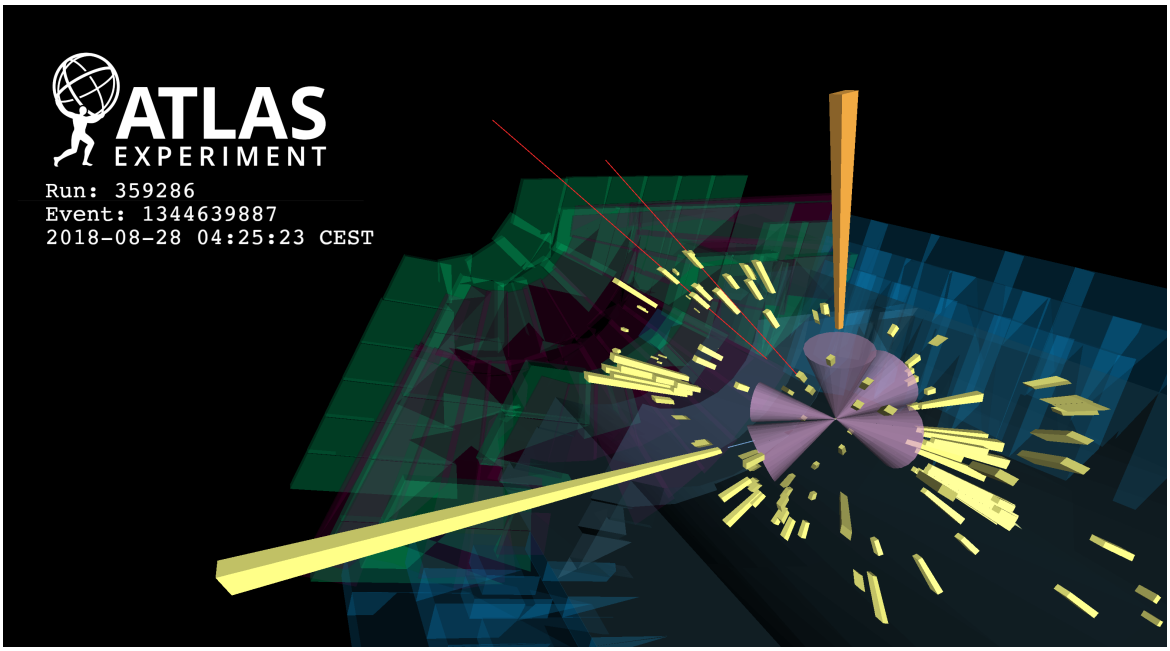

Figure 5.23: Visualisation of a $2\mu 1e1\tau_{\text{had}}$ event which falls within $\texttt{SR1}_{\text{breq}}$. The event was recorded by ATLAS on 28 August 2018. The muons are represented by the red tracks, and the electron by the blue track. Jets are represented by the purple cones and energies in calorimeter clusters are represented by yellow and orange blocks. The orange clusters are those associated with a hadronically-decaying tau.

The statistical interpretation of results was implemented by analysis collaborators in the HistFitter [167] software framework. The probabilities for the observed event counts under the background-only and signal-plus-background hypotheses, with consideration for statistical and systematic uncertainties, were calculated using pseudo-experiments and quantified as one-sided p-values, where the profile likelihood ratio is used as a test statistic [170].

The significances in all signal regions are within 2σ, indicating good agreement between the observed event counts and the expectation from the Standard Model. The largest deviations were observed in $\texttt{SR2}^{\text{tight}}_{\text{bveto}}$, which has a 1.72σ excess, and in $\texttt{SR0}^{\text{loose}}_{\text{bveto}}$, which has a -1.46σ deficit.

The CL_{s} [171] is constructed from the p-values; a signal point is considered excluded at the 95% confidence level if it has $CL_{\text{s}} < 0.05$. Table 5.12 shows, for each signal region, the expected and observed upper limits on the number of BSM events at 95% confidence level (S^{95}_{exp} and S^{95}_{obs}), and the 95% confidence level upper limit on the cross-section-times-efficiency ($\langle\epsilon\sigma\rangle^{95}_{\text{obs}}$) of new physics. These limits can be used to exclude a wide range of BSM models with four-lepton final states.

Figure 5.24 shows the expected and observed exclusions for the models considered in this analysis. The exclusions of all signal regions are combined: for cases when more than one region excludes a given signal point, the region with the best exclusion is considered. The plots show the impact of systematic and statistical uncertainties ($\pm1\sigma_{\text{exp}}$), and the impact of the uncertainty on the cross section of SUSY processes ($\pm1\sigma^{\text{SUSY}}_{\text{theory}}$).

Limits set for the GGM scenario are greatly improved compared to the previous analysis [114], owing to the b-veto and high $E^{\text{miss}}_{\text{T}}$ requirements in the signal regions. Higgsino masses of up to 540 GeV are excluded at the 95% confidence level when the branching fraction of the $\tilde{\chi}^0_1$ to the Z boson $\mathcal{B}(\tilde{\chi}^0_1 \to Z\tilde{G}) = 100\%$, which extends the previous limit by 240 GeV. At higgsino masses of 200 GeV, sensitivity to $\mathcal{B}(\tilde{\chi}^0_1 \to Z\tilde{G})$ was extended from 60% to 22%. The regions close to $\mathcal{B}(\tilde{\chi}^0_1 \to Z\tilde{G}) = 0\%$ are better covered by analyses such as Ref. [123] which target the Higgs decay. The combined

	$\langle\epsilon\sigma\rangle^{95}_{\text{obs}}$ [fb]	S^{95}_{obs}	S^{95}_{exp}
SR0-ZZ$^{\text{loose}}$	0.481	66.86	$67.43^{+20.43}_{-15.71}$
SR0-ZZ$^{\text{tight}}$	0.081	11.28	$11.52^{+4.81}_{-3.34}$
SR0-ZZ$^{\text{loose}}_{\text{bveto}}$	0.043	6.01	$7.10^{+2.82}_{-1.90}$
SR0-ZZ$^{\text{tight}}_{\text{bveto}}$	0.028	3.87	$3.63^{+1.44}_{-0.63}$
SR0$^{\text{loose}}_{\text{bveto}}$	0.070	9.79	$8.28^{+3.58}_{-2.30}$
SR0$^{\text{tight}}_{\text{bveto}}$	0.028	3.87	$4.29^{+1.56}_{-0.86}$
SR0$_{\text{breq}}$	0.046	6.33	$3.78^{+1.59}_{-0.66}$
SR1$^{\text{loose}}_{\text{bveto}}$	0.046	6.37	$7.46^{+2.92}_{-2.04}$
SR1$^{\text{tight}}_{\text{bveto}}$	0.032	4.47	$4.22^{+1.63}_{-1.04}$
SR1$_{\text{breq}}$	0.033	4.56	$4.59^{+1.77}_{-1.22}$
SR2$^{\text{loose}}_{\text{bveto}}$	0.061	8.45	$7.45^{+2.36}_{-1.24}$
SR2$^{\text{tight}}_{\text{bveto}}$	0.041	5.63	$3.53^{+1.06}_{-0.15}$
SR2$_{\text{breq}}$	0.030	4.17	$3.16^{+1.20}_{-0.16}$
SR5L	0.129	17.88	$9.88^{+4.08}_{-2.44}$

Table 5.12: The model-independent limits calculated from the signal region observations; the 95% confidence level upper limits on the cross-section-times-efficiency ($\langle\epsilon\sigma\rangle^{95}_{\text{obs}}$) of BSM physics, the observed number of BSM events (S^{95}_{obs}), and the expected number of BSM events given the expected number of background events (S^{95}_{exp}, $\pm1\sigma$ variations of the expected number) were calculated with pseudo-experiments in each signal region. This table was produced by collaborators in the analysis team, and is reproduced from Ref. [4].

exclusion of Ref. [123] and this analysis is shown in Figure 5.25, where it is seen that the two analyses are complimentary along the $\mathcal{B}(\tilde{\chi}^0_1 \to h\tilde{G})$ axis[3].

For the R-parity violating scenarios, the exclusion of higher NLSP masses is driven by the stringent requirements on m_{eff} in the signal regions, which reject most background contributions but are high in efficiency to events from the targeted SUSY scenarios. Requiring or vetoing b-jets provided sensitivity across the $\Delta m = m(\text{NLSP}) - m(\tilde{\chi}^0_1)$ range. In the case when $\lambda_{12k} \neq 0$, wino, slepton/sneutrino, and gluino masses of up to 1.65 TeV, 1.22 TeV, and 2.5 TeV respectively have been excluded at the 95% confidence level. In the case when $\lambda_{i33} \neq 0$, the corresponding NLSP masses of up to 1.11 TeV,

[3]For this model, $\mathcal{B}(\tilde{\chi}^0_1 \to h\tilde{G}) + \mathcal{B}(\tilde{\chi}^0_1 \to Z\tilde{G}) = 1$.

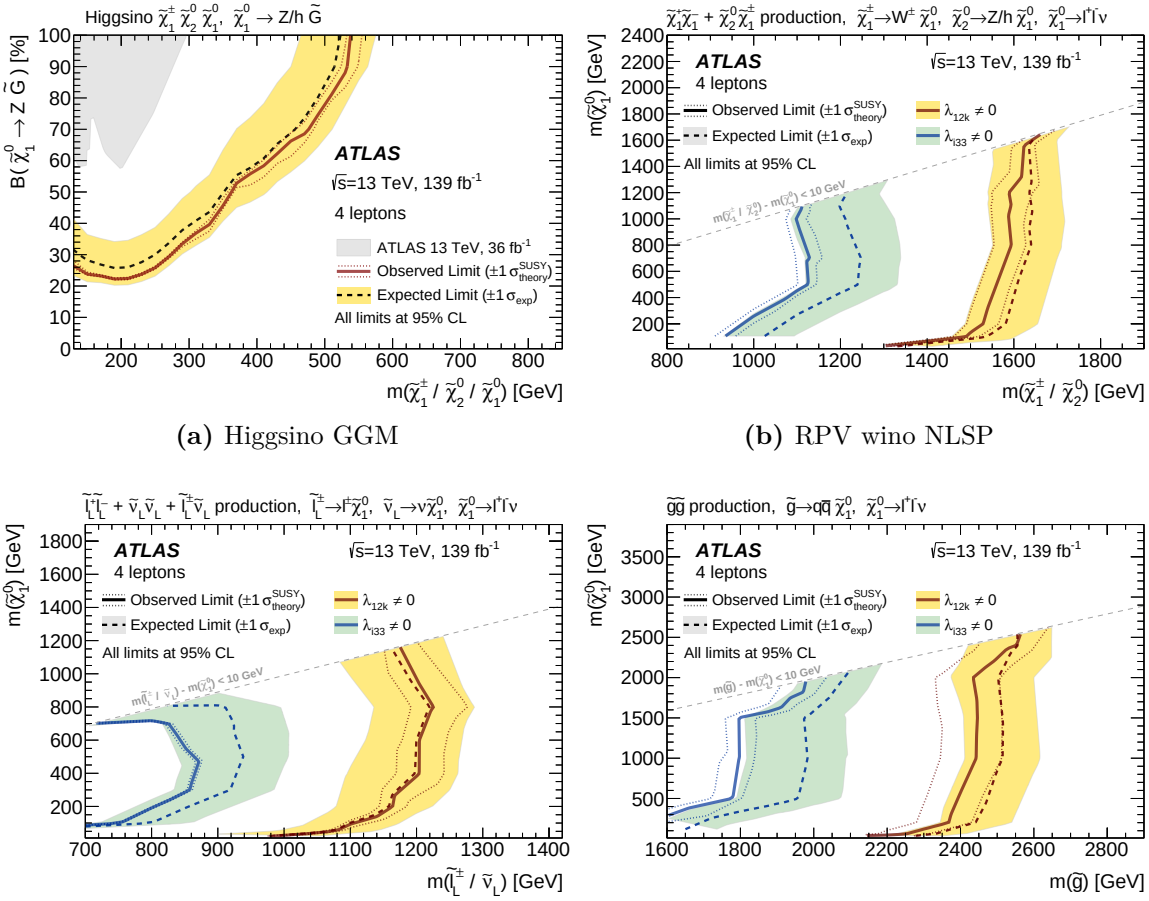

(a) Higgsino GGM **(b)** RPV wino NLSP

(c) $\tilde{\ell}_L/\tilde{\nu}$ NLSP **(d)** $\tilde{g}$ NLSP

Figure 5.24: Expected and observed exclusions for the models considered in this analysis. For the GGM model, the current limits are shown alongside the limits from the previous analysis [114]. For each NLSP candidate in the RPV scenarios, the current limits for $LL\bar{E}12k$ and $LL\bar{E}i33$ scenarios are shown in the same plots. This figure was produced by collaborators in the analysis team and is reproduced from Ref. [4].

860 GeV, and 1.95 TeV respectively are excluded. These exclusions have been expanded by 150 to 200 GeV along the mass of the NLSP compared to the previous analysis [114].

5.7 Conclusion

A search for supersymmetry in events with four or more leptons at the ATLAS experiment was presented. The search was optimised for general gauge mediated SUSY

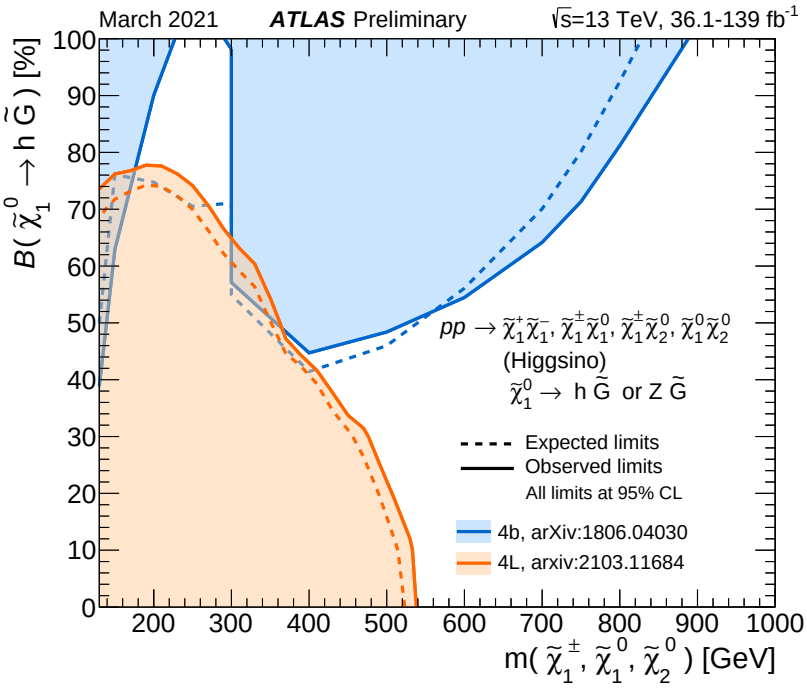

Figure 5.25: Expected and observed exclusion limits from this analysis (orange) and Ref. [123] (blue). Reproduced from Ref. [43].

models and R-parity violating SUSY models which both produce at least four leptons in the final state. No significant excess above the Standard Model expectation was observed, from which limits on the cross-section-times-branching-fraction of new physics were set. The results were interpreted to give limits on the SUSY model parameters. In the general gauge mediated SUSY models, higgsino masses of up to 540 GeV were excluded, which extends the previous limit by about 250 GeV. For the R-parity violating SUSY models, wino, slepton/sneutrino, and gluino masses of up to 1.6 TeV, 1.2 TeV, and 2.5 TeV respectively were excluded, extending the previous limits by 150 to 200 GeV.

6

Searching for SUSY in final states with two leptons

6.1 Introduction

This chapter presents a search for supersymmetry in events with two leptons in 139 fb^{-1} of $\sqrt{s} = 13\,\text{TeV}$ ATLAS data.

Two previous $\sqrt{s} = 13\,\text{TeV}$ ATLAS searches targeted direct slepton production (Figure 6.1), both searching in two-lepton (e^+e^-, $\mu^+\mu^-$) final states. They differ by the space in $\Delta m \equiv m_{\tilde{\ell}} - m_{\tilde{\chi}_1^0}$ to which they are sensitive (Figure 6.2). The "soft 2ℓ"

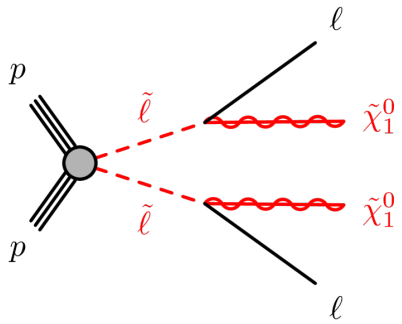

Figure 6.1: Feynman diagram for direct slepton production and decay to SM leptons and $\tilde{\chi}_1^0$.

analysis [6] is sensitive to $\Delta m \in (1.5, 15)\,\text{GeV}$, while the general 2ℓ analysis [5] is sensitive to $\Delta m > 80\,\text{GeV}$, leaving a large gap in between the two. This gap region is favored by the $(g-2)_\mu$ anomaly [42] and dark matter relic constraints [172], so is of particular interest.

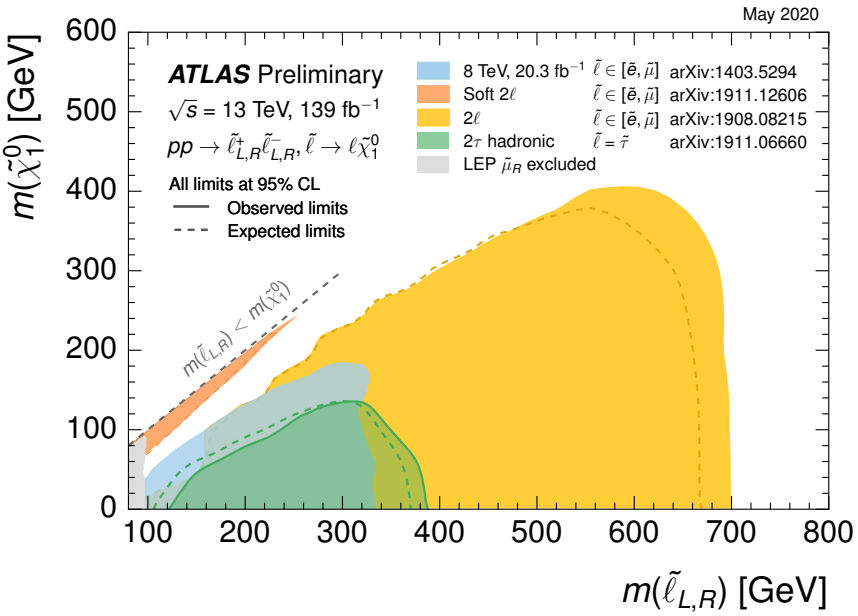

Figure 6.2: Summary of slepton exclusions from ATLAS [5, 6, 173, 174] and LEP searches. Reproduced from Ref. [43].

This gap region has been difficult to probe because the Standard Model process $WW \to \ell\nu\ell\nu$ ($\ell \in \{e, \mu\}$) has a nearly identical signature (two leptons and $E_{\text{T}}^{\text{miss}}$) but a large cross section. However, WW and $\tilde{\ell}\tilde{\ell}$ have different spin structures: in $W \to \ell\nu$ a spin-1 particle decays to two spin-$\frac{1}{2}$ particles, while in $\tilde{\ell} \to \ell\tilde{\chi}^{0}_{1}$ a spin-0 particle decays to two spin-$\frac{1}{2}$ particles. This could give rise to different features in angular distributions that can be exploited for event selection.

This chapter presents a proposal to probe the gap in Figure 6.2. The model considered is the same, that of direct slepton production. Only decays to electrons and muons are considered, and their superpartners are assumed to be mass degenerate

$m(\tilde{e}_L) = m(\tilde{e}_R) = m(\tilde{\mu}_L) = m(\tilde{\mu}_R)$. Each slepton decays with a 100% branching ratio to its corresponding Standard Model lepton and the lightest neutralino.

It is proposed to employ a machine-learning classifier which could learn the feature differences between Standard Model events and SUSY signal events, and thus discriminate between them. Using the classifier could provide sensitivity to this challenging and previously unprobed region.

In parallel, a cut-and-count analysis with "traditional" kinematic variables was developed to target this same region. Its sensitivity is compared with the machine-learning approach.

This analysis was conducted with collaborators from Cambridge, Lecce, Oslo, Milan, and DESY. The author was responsible for studying the viability of a machine-learning-based analysis. Other collaborators were responsible for developing the traditional cut-and-count analysis. Their work has been replicated by the author in this thesis for the sake of completeness.

6.2 Analysis strategy

In the targeted physics model of this analysis, the final state consists of a pair of same-flavour opposite-sign leptons (electrons or muons), and some amount of missing transverse energy. Event variables and selections were designed to target these events.

Two approaches In this thesis, two different approaches for targeting the slepton mass gap are presented.

The first approach, developed by the author, is machine-learning-based. Kinematic variables are used as inputs to machine-learning classifiers, the outputs of which are used to define signal regions. This approach is discussed in Section 6.4.

In the second approach, developed by analysis collaborators, a signal region was defined by placing optimised requirements on kinematic variables. This approach is discussed in Section 6.5.

For both cases, expected limits in the $(m_{\tilde{\ell}}, m_{\tilde{\chi}_1^0})$ plane are set based on the expected number of signal and background events in the signal region, and on hypotheses about the corresponding uncertainties.

Background estimation The backgrounds to this search are events with the same signature — two reconstructed leptons and missing transverse energy — as the SUSY signal. These leptons can either be "real" or "fake". Real leptons are those which are prompt and isolated, while "fake" leptons include non-prompt leptons, non-isolated leptons, and other objects mis-identified as prompt, isolated leptons.

As in the four-lepton analysis, the distinction between real and fake leptons allows for the classification of backgrounds into "reducible" and "irreducible" backgrounds. Reducible backgrounds are due to Standard Model processes which give at least one fake lepton, while irreducible backgrounds are due to processes with two real leptons in the final state. In this analysis, irreducible backgrounds are further subdivided into flavour-symmetric and flavour-asymmetric backgrounds.

Flavour-symmetric backgrounds are due to dileptonic decays of processes such as W^+W^-, $t\bar{t}$, Wt, and $Z \to \tau\tau$+jets. Due to lepton universality, the lepton pairs of these decays are equally probable to be different-flavour opposite-sign (DFOS) or same-flavour opposite-sign (SFOS). In order not to rely on simulation, data-driven methods in which DFOS events are weighted to obtain an estimate of the magnitude of this contribution to SFOS events are expected to be used. These methods, developed by collaborators, are discussed in Section 6.6.

Flavour-asymmetric backgrounds are due to processes such as $Z \to ee$, $Z \to \mu\mu$, and $WZ(\to qq\ell\ell)$ which produce, due to lepton flavour conservation in Z decays, SFOS lepton pairs but not DFOS pairs. These contributions are estimated by Monte Carlo simulation.

Reducible backgrounds are due to Standard Model processes with fewer than two leptons in the final state being reconstructed as having two leptons. This is

because jets or leptons from hadronic decays are occasionally mis-identified as prompt, isolated leptons. Contributing processes include $W \to \ell\nu$, $WW \to qq\ell\nu$ or single-leptonic decays of Wt, $t\bar{t}$, and $Z \to \tau\tau$. The reducible backgrounds are estimated by MC simulation in this chapter.

Figure of merit The *significance* [126] — previously used in the optimisation of the four-lepton analysis — is used as the figure of merit for optimisation and evaluation in this analysis:

$$Z = \sqrt{2\left(n \ln\left[\frac{n(b+\sigma^2)}{b^2+n\sigma^2}\right] - \frac{b^2}{\sigma^2}\ln\left[1+\frac{\sigma^2(n-b)}{b(b+\sigma^2)}\right]\right)}, \tag{6.1}$$

where b is the number of background events, σ is the uncertainty on the background, and n is the total number of background and signal events. A signal point is excluded at the 95% confidence level if $Z > 1.64$ assuming $n = b$. As the analyses which this study extends [5, 6] have uncertainties of about 10%, a flat systematic uncertainty of 10% was assumed in this study except where specified. In the plots to follow, binned and "cumulative" distributions are often considered. The cumulative distributions show the number of events which satisfy a requirement on the variable plotted on the x-axis. The significance plots found under the binned distributions show the significance per bin, while those under the cumulative distributions show the significance for a given requirement.

Key variables Key variables used include the missing transverse momentum $E_{\mathrm{T}}^{\mathrm{miss}}$, the transverse momenta of the two leptons, labelled in descending order $p_T^{\ell 1}$, $p_T^{\ell 2}$, the invariant mass of the lepton pair $m_{\ell\ell}$, and others described below.

The variable $E_{\mathrm{T}}^{\mathrm{miss}}$ significance, $S(E_{\mathrm{T}}^{\mathrm{miss}})$, is defined by the log-likelihood ratio [175]

$$[S(E_{\mathrm{T}}^{\mathrm{miss}})]^2 = 2\ln\left(\frac{\max_{\vec{p}_T^{\,\mathrm{inv}}\neq 0}\mathcal{L}(E_{\mathrm{T}}^{\mathrm{miss}}|\vec{p}_T^{\,\mathrm{inv}})}{\max_{\vec{p}_T^{\,\mathrm{inv}}=0}\mathcal{L}(E_{\mathrm{T}}^{\mathrm{miss}}|\vec{p}_T^{\,\mathrm{inv}})}\right), \tag{6.2}$$

where $\vec{p}_T^{\,\mathrm{inv}}$ is the assumed sum of the transverse momenta of invisible particles (if any) in the final state. $S(E_{\mathrm{T}}^{\mathrm{miss}})$ quantifies whether the measured value of $E_{\mathrm{T}}^{\mathrm{miss}}$ is likely to have arisen from invisible particles ($\vec{p}_T^{\,\mathrm{inv}} \neq 0$), or from resolution effects ($\vec{p}_T^{\,\mathrm{inv}} = 0$). Events with larger $E_{\mathrm{T}}^{\mathrm{miss}}$ or that are more likely to have non-zero $\vec{p}_T^{\,\mathrm{inv}}$ tend to have higher $S(E_{\mathrm{T}}^{\mathrm{miss}})$. Therefore signal-like events, which have large $E_{\mathrm{T}}^{\mathrm{miss}}$, are expected to have high $S(E_{\mathrm{T}}^{\mathrm{miss}})$ [175].

Certain angular variables were also shown to exhibit some separation power between signal and background events. The variable $\cos\theta^*_{\ell\ell}$ is defined by [176]

$$\cos\theta^*_{\ell\ell} = \tanh(\Delta\eta_{\ell^+\ell^-}/2). \tag{6.3}$$

The angle $\theta^*_{\ell\ell}$ can be interpreted as the angle between each lepton and the beam axis in the frame where $\eta_{\ell^+} = -\eta_{\ell^-}$. The decay the slepton pair will tend to produce leptons at small values of $|\cos\theta^*_{\ell\ell}|$ [176].

Simulation showed other angular variables possess strong separation power between Standard Model events and SUSY events. These variables, shown in Figure 6.3, include the difference in azimuthal angle between leptons $\Delta\phi_{\ell,\ell}$, between the lepton pair and the $E_{\mathrm{T}}^{\mathrm{miss}}$ vector $\Delta\phi_{E_{\mathrm{T}}^{\mathrm{miss}},\ell\ell}$, and between the leading lepton and $E_{\mathrm{T}}^{\mathrm{miss}}$ vector $\Delta\phi_{E_{\mathrm{T}}^{\mathrm{miss}},\ell 1}$.

The variable $p^{\ell\ell}_{\mathrm{T,b}}$ is the magnitude of the vector sum of the transverse momenta of the two leptons and the missing transverse momentum:

$$p^{\ell\ell}_{\mathrm{T,b}} = |\vec{p}^{\,\ell\ell}_{\mathrm{T,b}}| = |\vec{p}_T^{\,\ell 1} + \vec{p}_T^{\,\ell 2} + \vec{E}_T^{\mathrm{miss}}|. \tag{6.4}$$

In signal-like events, the two leptons and the missing energy are the only objects within the event. Therefore, by the conservation of momentum, the value of $p^{\ell\ell}_{\mathrm{T,b}}$ in these events is expected to be close to zero.

The stransverse mass[1] m_{T2} [177, 178] is defined by

$$m^{\chi}_{T2}\left(\vec{p}_T^{\,\ell 1}, \vec{p}_T^{\,\ell 2}, \vec{p}_{\mathrm{T}}^{\,\mathrm{miss}}\right) = \min_{\vec{q}_{\mathrm{T},1}+\vec{q}_{\mathrm{T},2}=\vec{p}_{\mathrm{T}}^{\,\mathrm{miss}}} \left\{ \max\left[\, m_{\mathrm{T}}(\vec{p}_T^{\,\ell 1}, \vec{q}_{\mathrm{T},1}|\chi), m_{\mathrm{T}}(\vec{p}_T^{\,\ell 2}, \vec{q}_{\mathrm{T},2}|\chi) \,\right] \right\}, \tag{6.5}$$

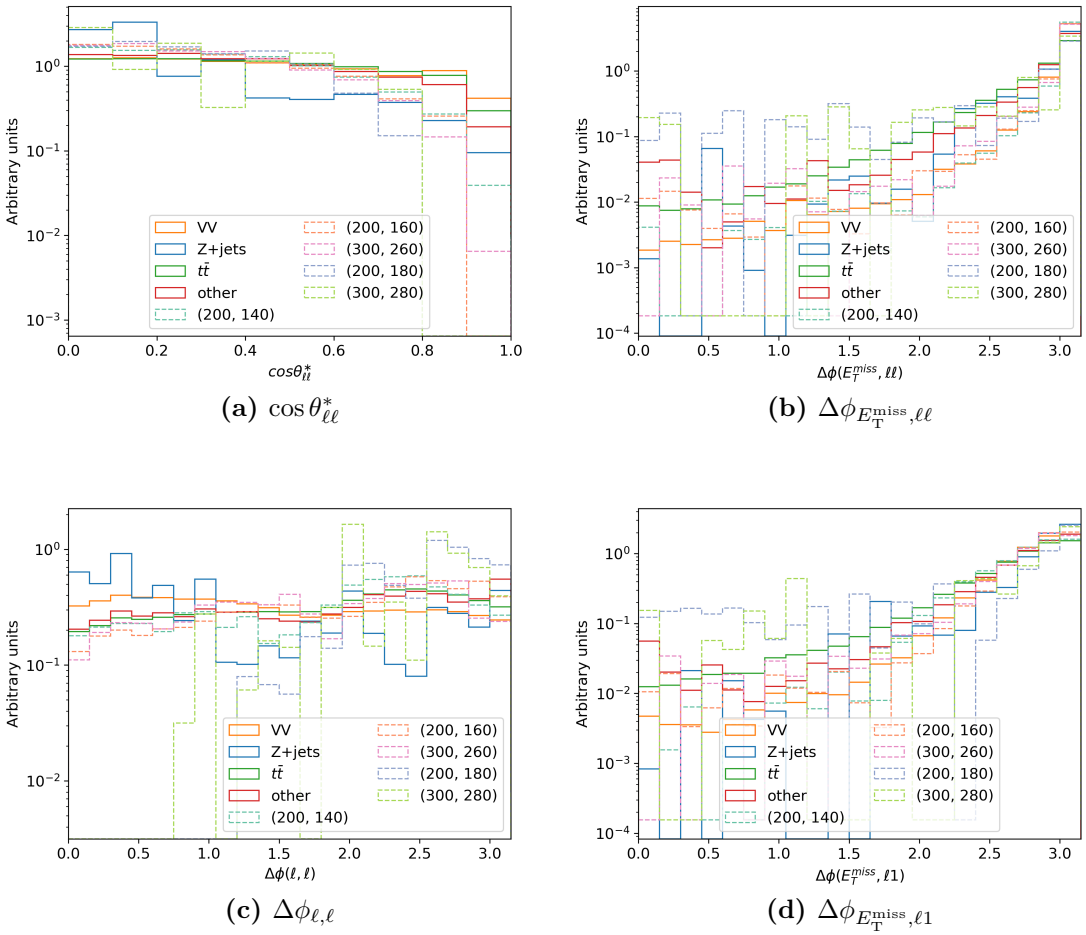

(a) $\cos\theta^*_{\ell\ell}$ **(b)** $\Delta\phi_{E_{\mathrm{T}}^{\mathrm{miss}},\ell\ell}$

(c) $\Delta\phi_{\ell,\ell}$ **(d)** $\Delta\phi_{E_{\mathrm{T}}^{\mathrm{miss}},\ell 1}$

Figure 6.3: Angular variable distributions of simulated signal and background events. Two different simulated samples are used as described in Section 6.3; background events are taken from Geant MC and signal events from smeared MC. Here $V = W, Z$, and simulated signals are labelled by their $(m_{\tilde{\ell}}, m_{\tilde{\chi}_1^0})$ in GeV. "other" includes $Z \to \tau\tau$, top processes, and VVV. The distributions are scaled to have unit area. Events were required to pass the "machine-learning" selection of Section 6.3. The difference in signal and background distribution shapes is most prominent in $\cos\theta^*_{\ell\ell}$ (Sub-figure (a): the signal distributions peak higher near 0 and have smaller tails compared to VV, $t\bar{t}$, and 'other'.

where transverse mass is defined by

$$m_T(\vec{p}_T^{\,\ell}, q_T|\chi) = \sqrt{m_\ell^2 + \chi^2 + 2\left(E_T^\ell E_T^q - \vec{p}_T \cdot \vec{q}_T\right)}, \tag{6.6}$$

$\vec{p}_T^{\,\ell 1}$ and $\vec{p}_T^{\,\ell 2}$ are the transverse-momentum vectors of the two leptons in the event, and χ and $\vec{q}_T$, are the assumed mass and transverse momentum of the neutralino to which the slepton decays. If $m_{\tilde{\chi}_1^0} = \chi$ then $m_T \leq m_{\tilde{\ell}}$, where the equality is satisfied if the trajectories of the visible lepton and the invisible neutralino lie entirely in the transverse plane. In the limit of a large sample, $\max_{\text{many events}} m_{T2} = m_{\tilde{\ell}}$. Studies by collaborators found that the sensitivity of m_{T2} to the targeted SUSY events had only a weak dependence on the assumed value of χ. In this analysis $\chi = 0$ is assumed.

6.3 Samples used and event selection

6.3.1 Samples used

This study uses simulated events of two different kinds; they are labelled *Geant MC* and *smeared MC* in this chapter. Additionally, *pp* data recorded by ATLAS is used for the data-driven flavour-symmetric background estimate.

Data Data used in this analysis were *pp* collisions recorded by the ATLAS detector between 2015 and 2018, corresponding to $139\,\text{fb}^{-1}$ of integrated luminosity. Events were required to pass an "or" of the single-lepton triggers listed in Table 6.1, and then they were reconstructed according to the techniques described in Section 3.2.4.

Geant MC Simulated events of signal and Standard Model processes were generated. The details of the generators and showering are listed in Table 6.2. Simulated signal events were generated across a grid of possible masses ($m_{\tilde{\ell}}$, $m_{\tilde{\chi}_1^0}$), and were required to have two leptons with $p_\text{T} > 8\,\text{GeV}$. Simulated pileup events were generated by

[1]This variable is known as "stransverse" mass because its definition is inspired by that of the transverse mass m_T and it is used to search for supersymmetric events [178].

	Single electron	Single muon
2015	HLT_e24_lhmedium_L1EM20VH HLT_e60_lhmedium HLT_e120_lhloose	HLT_mu20_iloose_L1MU15 HLT_mu60_0eta105_msonly HLT_mu40
2016	HLT_e24_lhtight_nod0_ivarloose HLT_e26_lhtight_nod0_ivarloose HLT_e60_lhmedium_nod0 HLT_e140_lhloose_nod0 HLT_e300_etcut	HLT_mu24_ivarloose HLT_mu24_ivarmedium HLT_mu26_ivarmedium HLT_mu50
2017-2018	HLT_e26_lhtight_nod0_ivarloose HLT_e60_lhmedium_nod0 HLT_e140_lhloose_nod0 HLT_e300_etcutP	HLT_mu26_ivarmedium HLT_mu50 HLT_mu60_0eta105_msonly

Table 6.1: List of single-lepton (electron or muon) triggers used in the analysis.

Process	Generator (PDF set)	Normalisation	Parton shower (PDF set)	Tune
$t\bar{t}$, $t\bar{t}H$	Powheg-Boxv2 [132–134] (NNPDF3.0NLO [131])	NLO [130]	Pythia 8 [135] (NNPDF2.3LO [146])	A14 [145]
Wt	Powheg-Boxv2 (NNPDF3.0NLO)	NLO	Pythia 8 (NNPDF2.3LO)	A14
$t\bar{t}V$, tWZ, tZq	MadGraph5_aMC@NLO v2.3.3 [147] (NNPDF3.0NLO)	NLO	Pythia 8.2 (NNPDF2.3LO)	A14
$t\bar{t}\gamma$	MadGraph5_aMC@NLO v2.3.3 (NNPDF2.3LO)	LO	Pythia 8.2 (NNPDF2.3LO)	A14
VV	Sherpa v2.2.1 or v2.2.2 [129] (NNPDF3.0NLO)	NLO	Sherpa (NNPDF3.0NLO)	Sherpa
$VVjj$	Sherpa v2.2.2 (NNPDF3.0NLO)	LO	Sherpa (NNPDF3.0NLO)	Sherpa
VVV	Sherpa v2.2.2 (NNPDF3.0NLO)	NLO	Sherpa (NNPDF3.0NLO)	Sherpa
W+jets, Z+jets	Sherpa v2.2.1 (NNPDF3.0NLO)	NLO, NNLO	Sherpa (NNPDF3.0NLO)	Sherpa
$\tilde{\ell}\,\tilde{\ell}$	MadGraph5_aMC@NLO v2.6.1 (NNPDF2.3LO)	LO	Pythia 8.2 (NNPDF2.3LO)	A14

Table 6.2: Summary of simulated samples for the Standard Model and signal processes.

Pythia 8. All Geant MC events were weighted to match the pileup distributions in data. After event generation, the detector response was simulated by `GEANT4` [128], then the events were reconstructed as described in Section 3.2.4.

Smeared MC A large number of simulated events were generated separately for the machine-learning study. After event generation, the events underwent a process known as *smearing* with the ATLAS `SimpleAnalysis` framework [7]. This was done in place of computationally expensive detector simulation and event reconstruction. In smearing, the energy and momentum distributions of the simulated events were smeared to model the detector simulation and event reconstruction. Samples for five mass points

outside the existing exclusion but within the targeted region of the $(m_{\tilde{\ell}}, m_{\tilde{\chi}_1^0})$ plane were generated. The kinematics of final state leptons are expected to vary with the energy available to produce them, which is determined by $\Delta m \equiv m_{\tilde{\ell}} - m_{\tilde{\chi}_1^0}$. Therefore points across a range of Δm are produced. These mass points are listed in Table 6.3.

Δm [GeV]	$(m_{\tilde{\ell}}, m_{\tilde{\chi}_1^0})$ [GeV]
60	(200, 140)
40	(200, 160)
	(300, 260)
20	(200, 180)
	(300, 280)

Table 6.3: Signal points for which smeared MC samples were generated.

6.3.2 Object and event selection

The physics objects used in this analysis undergo the following selection steps:

- **Baseline**: Objects which pass initial selection before overlap removal,
- **Signal**: Objects that pass overlap removal and signal selection criteria

Following this, event selection occurs in two steps: "preselected" and "machine-learning". The preselected sample is used to define the traditional signal region and control regions for the data-driven background estimation. The "machine-learning" sample is used in the machine-learning study.

Baseline object selection Electrons are required to have $p_{\mathrm{T}} > 9\,\mathrm{GeV}$, $|\eta| < 2.47$, and impact parameter $|z_0 \sin\theta| < 0.5\,\mathrm{mm}$. They are also required to pass `LooseAndBLayer` identification [82]. Muons are required to have $p_{\mathrm{T}} > 9\,\mathrm{GeV}$, $|\eta| < 2.4$, $|z_0 \sin\theta| < 0.5\,\mathrm{mm}$, and pass `Medium` identification [75]. Jets are reconstructed from particle flow objects clustered by the anti-k_t algorithm [87] with the radius parameter $R = 0.4$. They are required to have $p_{\mathrm{T}} > 20\,\mathrm{GeV}$ and $|\eta| < 2.8$.

Overlap removal Overlap removal is performed on baseline objects to avoid the cases when different objects are reconstructed from the same detector signals. Jets within $\Delta R = \sqrt{\Delta\eta^2 + \Delta\phi^2} = 0.2$ of an electron are removed. A jet is also removed if it has with fewer than three associated tracks and is $\Delta R = 0.4$ of a muon. Electrons and muons within $\Delta R = \min(0.4, 0.04 + \frac{10}{p_{\mathrm{T}}[\mathrm{GeV}]})$ of the remaining jets are discarded. A muon that has an ID track and is matched with a calorimeter deposit but does not have a matching muon spectrometer track is removed if it shares its ID track with an electron. Finally electrons sharing an ID track with any remaining muons are removed.

Signal object selection Additional object quality requirements are applied after overlap removal. Electrons are required to pass `Tight` identification and `FCLoose` isolation [82], and have impact parameter significance $|d_0/\sigma_{d_0}| < 5$. Muons are required to pass `FCLoose` isolation [75] and have $|d_0/\sigma_{d_0}| < 3$. Jets are required to be within $|\eta| < 2.4$. Jets with $p_{\mathrm{T}} \in (20, 60)$ GeV need to pass $JVT > 0.5$, where the Jet Vertex Tagger (JVT) [179] uses track information to suppress pileup jets.

The missing transverse momentum $E_{\mathrm{T}}^{\mathrm{miss}}$ is calculated from the transverse momenta of jets, muons, and electrons, as well as photons and all tracks matched to the primary vertex not associated with these objects (cf. Section 3.2.4).

Event selection Events used for the analysis were required to pass the "Preselected" requirements listed in Table 6.4. Thresholds on lepton p_{T} were set such that the single lepton triggers were maximally efficient: $p_T^{\ell 1} > 27\,\mathrm{GeV}$, $p_T^{\ell 2} > 9\,\mathrm{GeV}$. Events with lepton pairs of low invariant mass $m_{\ell\ell} < 11$ GeV were rejected to avoid resonances from the decay of J/ψ, Υ and other hadrons. Events with jets in the central region are vetoed; jets are not expected in signal events and this requirement is very effective at removing events from Z+jets and top processes. Due to the difficulty in distinguishing between hard-scatter jets and pileup jets in the forward region ($|\eta| > 2.4$), no requirements on these forward jets are made. Contributions from Z+jets are further suppressed by

Variable	Value
Preselected	
$N_{\text{OS leptons}}$	2
$p_T^{\ell 1}$	$> 27\,\text{GeV}$
$p_T^{\ell 2}$	$> 9\,\text{GeV}$
$m_{\ell\ell}$	$> 11\,\text{GeV}$
$n_{\text{jet},\lvert\eta\rvert<2.4}$	< 2
$S(E_{\text{T}}^{\text{miss}})$	> 3
$\lvert m_{\ell\ell} - m_Z\rvert$	$> 15\,\text{GeV}$ (SF only)
Machine-learning samples	
$S(E_{\text{T}}^{\text{miss}})$	> 7
$n_{\text{jet},\lvert\eta\rvert<2.4}$	$= 0$

Table 6.4: Event selection applied to samples

a requirement on the $E_{\text{T}}^{\text{miss}}$ significance $S(E_{\text{T}}^{\text{miss}}) > 3$, and requiring the lepton pair invariant mass to be inconsistent with the Z mass $|m_{\ell\ell} - m_Z| > 15$ GeV.

Additional requirements are applied to the events used in the machine-learning study and in the signal regions. The $E_{\text{T}}^{\text{miss}}$ significance requirement is increased to $S(E_{\text{T}}^{\text{miss}}) > 7$ for increased Z+jets rejection, and only events with zero jets are considered.

6.4 Machine-learning approach

In this approach, developed by the author, event kinematic variables are used as inputs to machine-learning classifiers which attempt to distinguish between Standard Model background and SUSY signal events. Three classifiers are used, one for each targeted value of $\Delta m \equiv m_{\tilde{\ell}} - m_{\tilde{\chi}_1^0} \in \{20, 40, 60\}$ GeV. Each classifier assigns to every event a signal score and a set of background scores, depending on how signal-like or individual background-like the event is. Signal regions based on requirements on these scores are defined.

6.4.1 Training, validation, and evaluation samples

Statistically independent training, validation, and evaluation samples were created from simulated events. Training samples are used the train the classifiers. The outputs of the classifier on the training and validation samples are compared to check for *overtraining*, when the classifier has overfitted to fluctuations or unique features in the training sample. The training samples are four times larger than their respective validation samples. This gives a large number of events for training while still keeping a sufficient number of events for statistically meaningful overtraining tests. The evaluation samples are used to optimise and estimate the yields in the signal regions. No overtraining was observed, so the absolute and relative sizes of the samples used was deemed suitable.

Simulated events passing the machine-learning sample selection criteria (cf. Table 6.4) were assigned to the training, validation, and evaluation samples by their event numbers according to Table 6.5 for Standard Model events and Table 6.6 for signal events. SUSY events and all Standard Model events in the evaluation sample were simulated by Geant MC, while SUSY events in the training and validation samples were simulated by smeared MC (cf. Section 6.3).

	Simulation	Selection
Training	Geant MC	`(EventNumber % 2 == 0) && (EventNumber % 5 != 0)`
Validation	Geant MC	`(EventNumber % 2 == 0) && (EventNumber % 5 == 0)`
Evaluation	Geant MC	`EventNumber % 2 == 1`

Table 6.5: Division of simulated Standard Model events into training, validation, and evaluation samples.

	Simulation	Selection	Grouping
Training	Smeared MC	`EventNumber % 5 != 0`	One sample for each $\Delta m = 20, 40, 60\,\text{GeV}$
Validation	Smeared MC	`EventNumber % 5 == 0`	One sample for each $\Delta m = 20, 40, 60\,\text{GeV}$
Evaluation	Geant MC	–	One sample for each $(m_{\tilde{\ell}}, m_{\tilde{\chi}_1^0})$ point

Table 6.6: Division of simulated signal events into training, validation, and evaluation samples.

For signal events, three training samples and three validation samples were considered — one training/validation sample pair for every targeted $\Delta m = 20, 40, 60\,\text{GeV}$. This is justified because variable behaviour is seen to depend heavily on Δm but only weakly on the absolute masses $m_{\tilde{\ell}}$ and $m_{\tilde{\chi}_1^0}$. In evaluation, each $(m_{\tilde{\ell}}, m_{\tilde{\chi}_1^0})$ mass point was considered to be its own sample.

Smeared MC signal events are used in training and validation. However Geant MC signal events are used in evaluation, so it is not essential that the event variables are modelled perfectly in smeared MC. Variable distributions of Geant MC and smeared MC signal events were compared visually (Figure 6.4). The consistency of modelling of $p_T^{\ell 1}$ and $p_T^{\ell 2}$ is fairly good; while that of variables $E_{\text{T}}^{\text{miss}}$ and $S(E_{\text{T}}^{\text{miss}})$ differs slightly at high values, but are still similar across samples. Variables for which the modelling is significantly inconsistent are not used in the classifier and are not shown here; these include $p_{\text{T,b}}^{\ell\ell}$ and $\Delta\phi(E_{\text{T}}^{\text{miss}}, \ell 1)$.

6.4.2 Classifier training

Classifier selection The machine-learning classifier used for this study was LightGBM [180], a classifier which has performed well in international machine-learning competitions. LightGBM is an implementation of a Gradient Boosting Decision Tree (GBDT). Brief descriptions of GBDT and LightGBM follow.

Consider a classification problem where one needs to distinguish between signal and background events. One decision tree, like that in Figure 6.5, can be trained to make requirements on event variables in order to maximise the purity of signal (background) events in its leaf nodes. When applying the tree, events in a leaf node where the majority of events are signal (background) events are classified as signal-like (background-like). When training a GBDT, an ensemble of decision trees is trained in sequence; each tree is trained to learn from the classification errors of the previous tree. When an event is evaluated by a GBDT, each tree in the ensemble votes on whether the event is signal-like or background-like; the final "signal scores" and "background

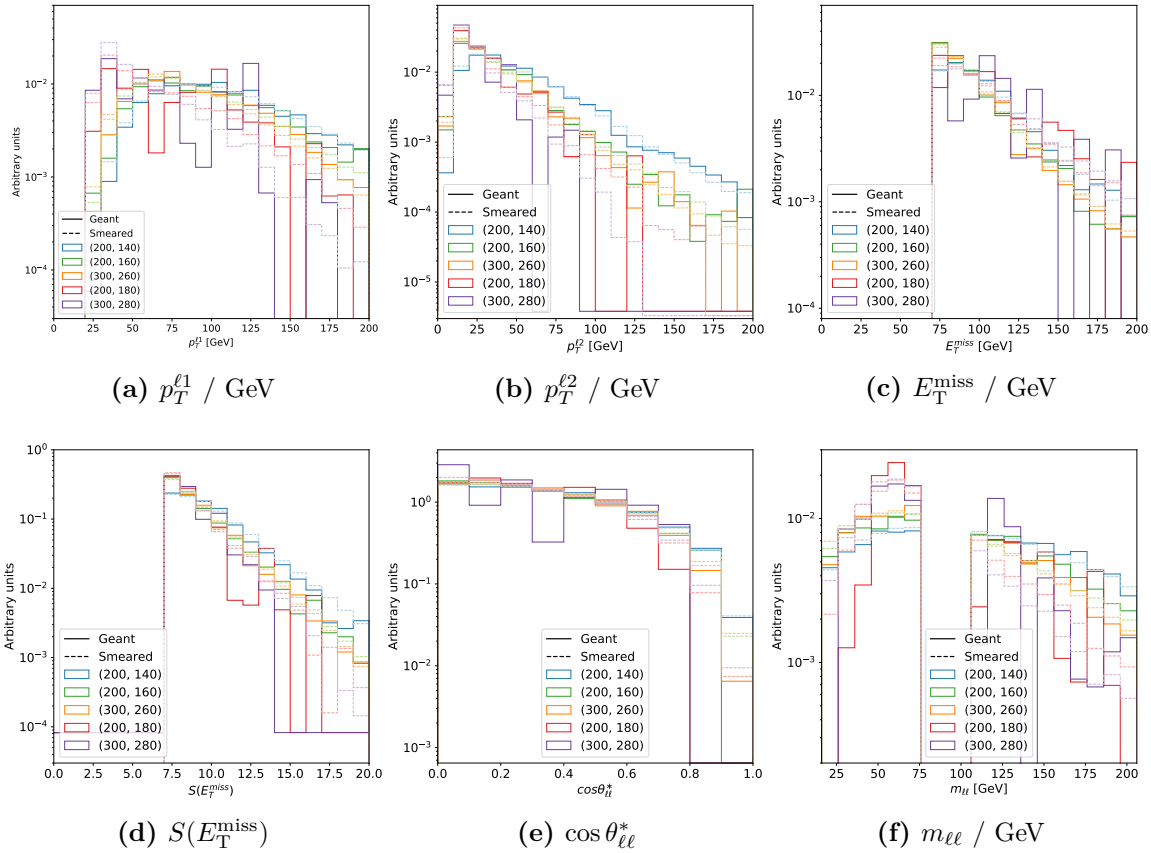

(a) $p_T^{\ell 1}$ / GeV **(b)** $p_T^{\ell 2}$ / GeV **(c)** $E_{\mathrm{T}}^{\mathrm{miss}}$ / GeV

(d) $S(E_{\mathrm{T}}^{\mathrm{miss}})$ **(e)** $\cos\theta_{\ell\ell}^*$ **(f)** $m_{\ell\ell}$ / GeV

Figure 6.4: Consistency of variable modelling of signal events in smeared MC and Geant MC samples. Events were required to pass "machine-learning" sample selection of Table 6.4. Distributions are coloured by signal point; the Geant MC distributions are drawn in solid lines, while the smeared MC are drawn in faded dashed lines. The Geant and smeared distributions are seen to mostly have the same shapes, save for $m_{\ell\ell}$.

scores" given to the events are the weighted averages of the votes by the trees, where the votes of the trees with stronger classification power are weighted more strongly.

LightGBM is an implementation of GBDT that reduces training time significantly. The complexity of GBDT training scales dominantly by $\mathcal{O}$(amount of data × number of variables). In LightGBM the amount of data considered in training is reduced significantly without compromising the classifier's efficiency. In the training of every tree, the training sample is created to consist of all events which are mis-classified but only a small number of correctly classified events. The correctly classified events are

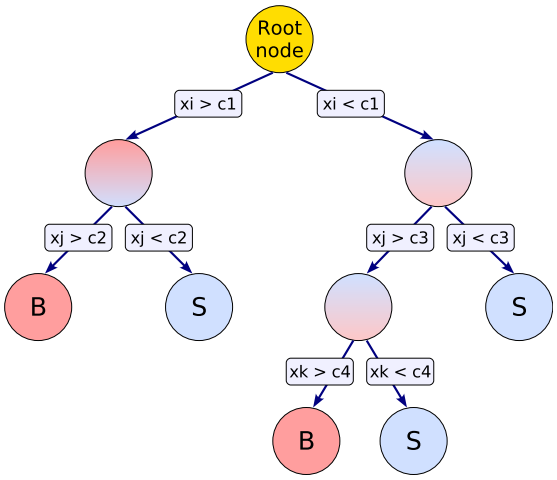

Figure 6.5: Schematic of one decision tree. A decision tree divides a sample into leaf nodes which are either background-like ("B", red) or signal-like ("S", blue). This is done by considering event variables $(xi, xj, xk...)$ and making requirements on them $(c1, c2, c3, c4...)$ to optimise signal efficiency. Techniques such as limiting the tree depth or limiting the minimum number of events in the leaf nodes prevent overtraining. Taken from Ref. [181].

then up-weighted to make up for their reduced number, therefore roughly reproducing the original distribution with a significantly smaller sample size. LightGBM trains 20 times faster than a traditional GBDT while achieving similar accuracy [180].

Other classifiers considered for this study include a single decision tree, a random forest, and a neural network. A random forest consists of a set of decision trees, where each tree is trained on a random subset of training data and considers a random subset of input variables. A neural network is a popular kind of classifier which consists of "layers" of linear matrix equations propagated through "nodes" of non-linear activation functions; the coefficients in the matrix equations are optimised to give the desired output. Initial testing considered a simple decision tree, a random forest of ten trees, and a neural network with two "hidden" layers of eleven and five nodes between the input and output layers. The random forest was seen to perform better than the single decision tree, but the performance of the neural network was worse than completely random classification.

A machine-learning approach was also adopted by collaborators searching a different

Hyper-parameter	Value	Hyper-parameter	Value	Hyper-parameter	Value
boosting_type	'gbdt'	class_weight	None	colsample_bytree	1.0
importance_type	'split'	learning_rate	0.01	max_depth	-1
min_child_samples	20	min_child_weight	0.001	min_split_gain	0.0
n_estimators	328	n_jobs	-1	num_leaves	31
num_threads	16	objective	None	random_state	None
reg_alpha	0.0	reg_lambda	0.0	silent	True
subsample	1.0	subsample_for_bin	200000	subsample_freq	0

Table 6.7: Hyper-parameters of the LightGBM trained for the slepton analysis

SUSY process with a similar final state — chargino pair-production $\tilde{\chi}_1^{\pm}\tilde{\chi}_1^{\mp}$ where each chargino decays to the LSP and a leptonically-decaying W boson $\tilde{\chi}_1^{\pm} \to \tilde{\chi}_1^0 W(W \to \ell\nu)$, resulting in a final state also of two leptons and $E_{\mathrm{T}}^{\mathrm{miss}}$. In the chargino search it was found that LightGBM offered good training speed and classification performance. This motivated the adoption of LightGBM in this analysis.

Input variables The input variables to the LightGBM were selected such that their shapes in Geant MC were well modelled by smeared MC. The variables chosen are $p_T^{\ell 1}$, $p_T^{\ell 2}$,$E_{\mathrm{T}}^{\mathrm{miss}}$, $S(E_{\mathrm{T}}^{\mathrm{miss}})$, $m_{\ell\ell}$, and $\cos\theta_{\ell\ell}^*$. These were defined and described previously in Section 6.2. Their distributions in Geant MC simulated samples of major backgrounds and selected signal points are shown in Figure 6.6.

Hyper-parameter optimisation Hyper-parameters of the LightGBM were optimised to give the largest possible area under the ROC curve of the signal scores. The hyper-parameters `min_child_weight, learning_rate, n_estimators, max_depth, num_leaves` were varied by hand in small increments from their default values. No major effect on signal discrimination power was observed. The hyper-parameter values used for the remainder of the study are listed in Table 6.7.

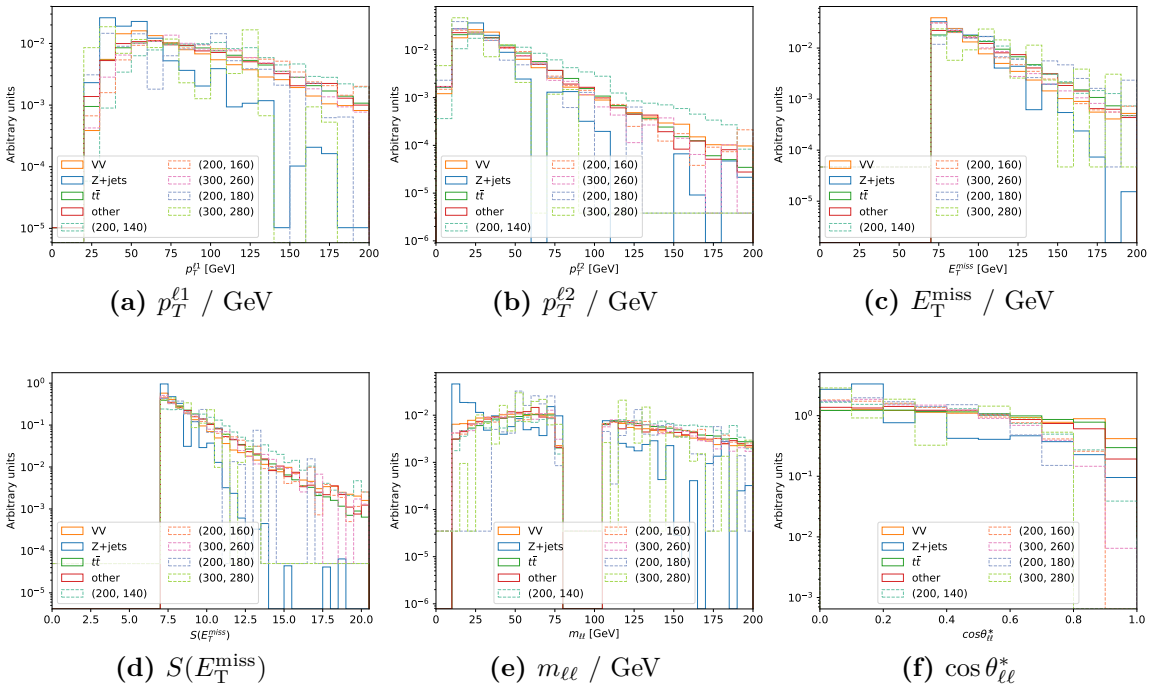

(a) $p_T^{\ell 1}$ / GeV **(b)** $p_T^{\ell 2}$ / GeV **(c)** $E_{\mathrm{T}}^{\mathrm{miss}}$ / GeV

(d) $S(E_{\mathrm{T}}^{\mathrm{miss}})$ **(e)** $m_{\ell\ell}$ / GeV **(f)** $\cos\theta_{\ell\ell}^*$

Figure 6.6: Classifier input variable distributions normalised to unit area. Geant MC SM events and smeared MC SUSY events are shown. Here, $V = W, Z$; "other" includes $Z \to \tau\tau$, top processes, and VVV; and the SUSY signals are labelled by their $(m_{\tilde{\ell}}, m_{\tilde{\chi}_1^0})$ in GeV. Standard Model distributions are drawn in solid lines, while SUSY distributions are drawn in faded dashed lines. Events are required to pass the machine-learning sample selection criteria in Table 6.4. The shape differences between Standard Model and SUSY distributions could be exploited by a classifier. In particular, Z+jets events have very different distributions from signals and other backgrounds. In $p_T^{\ell 1}$ (Sub-figure (a)), compared to VV, $t\bar{t}$, and 'other', the $\Delta m = 20\,\mathrm{GeV}$ signals peak at lower values, while the larger Δm signals have taller tails. Similar behaviour is seen in $p_T^{\ell 2}$ (Sub-figure (b)), where the $\Delta m = 20\,\mathrm{GeV}$ signals peak at also lower values, and the $\Delta m = 60\,\mathrm{GeV}$ point (200, 140) has a significantly taller tail. The variable $\cos\theta_{\ell\ell}^*$ (Sub-figure (f)) also has powerful discrimination potential, as the signals tend to peak higher near zero and have smaller tails.

Δm-specific classifiers Three classifiers were trained, one each for every targeted value of $\Delta m \in \{20, 40, 60\}$ GeV. These are labelled LGBM_{20}, LGBM_{40}, and LGBM_{60} respectively (Table 6.8). Each classifier was trained to discriminate between five different classes of events: signal, Z+jets, $t\bar{t}$, VV, and 'other'. The 'other' class includes all the remaining reducible and irreducible backgrounds. This five-way classification is employed to account for the differences in behaviour of each of the classes (cf. Figure 6.6), and was seen to perform better than simple two-way classification between signal and background.

Classifier	Δm target [GeV]	$(m_{\tilde{\ell}}, m_{\tilde{\chi}_1^0})$ points for training [GeV]	Background samples used
LGBM_{20}	20	$(200, 180), (300, 280)$	
LGBM_{40}	40	$(200, 160), (300, 260)$	VV, Z+jets, $t\bar{t}$, 'other'
LGBM_{60}	60	$(200, 140)$	

Table 6.8: List of classifiers trained, the Δm diagonals they target, and the smeared MC simulated signal and the Geant MC simulated backgrounds samples used to train them.

Each classifier assigns to each event five scores: a signal score, a Z+jets score, a $t\bar{t}$ score, a VV score, and an 'other' score. A high signal score means the event is deemed signal-like, a high Z+jets score means the event is deemed Z+jets-like, and so on. In total this gives $3 \times 5 = 15$ outputs with which signal regions can be defined.

6.4.3 Training results

The resulting signal score distributions in the training and validation samples from each of the three classifiers are shown in Figure 6.7. The distributions shown are normalised to unit area. In all three signal score distributions, background events are noticeably concentrated at low values; meanwhile signal events tend towards higher values. There are also noticeable shape differences between the signal samples and the background samples. These shape differences could themselves be exploited to define a signal region, though that approach is not used here.

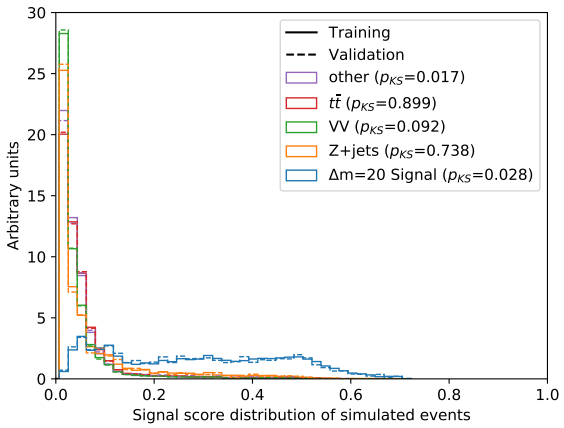

(a) LGBM$_{20}$

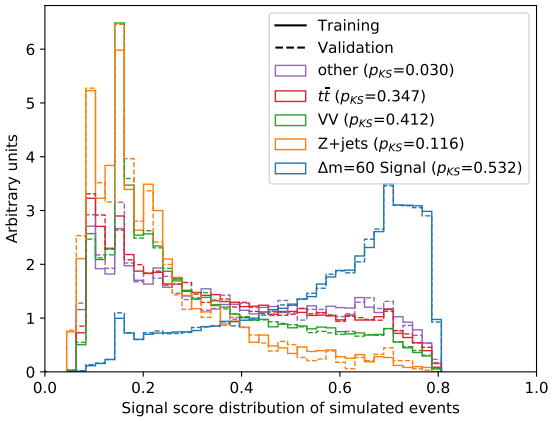

(b) LGBM$_{40}$

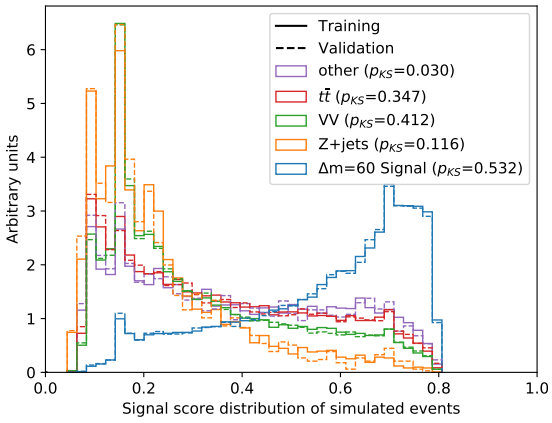

(c) LGBM$_{60}$

Figure 6.7: The signal score distributions for different signals and backgrounds in the training and validation samples. The distributions are normalised to unit area. Each plot shows the distributions given by the captioned classifier. The p-value of the Kolmogorov-Simirnov test p_{KS} quantifies the consistency between the training and testing distributions.

The background scores varied in their discrimination power, as shown in Figures 6.8, 6.9, and 6.10. In the normalised Z+jets score distributions, non-Z+jets events are concentrated towards low values, while the distribution of Z+jets events has a longer tail. The shapes of the $t\bar{t}$ and VV scores vary widely between the classifiers, but in general events targeted by each score tended towards high values. The 'other' score distribution is similar across all classes of events, and therefore has low discrimination power.

Overtraining was checked for by the two-sample Kolmogorov-Smirnov test, which tests the hypothesis that two given distributions are sampled from the same underlying distribution. When the p-value of the test $p_{KS} < 0.05$, the training and validation distributions may be inconsistent [182], indicating that there is some noticeable overtraining. In most cases the the training and validation distributions are consistent by the p_{KS} metric; for the few cases where $p_{KS} < 0.05$, a visual examination of the distributions show no concerning differences.

The performance of the three classifiers is summarised in the ROC curves shown in Figure 6.11. These curves plot the efficiency to the targeted event class against the false positive rate. In general, an effective classifier has a large area under its ROC curve. For signal discrimination, the classifier trained on the $\Delta m = 20$ GeV signal events was most powerful, achieving close to 100% efficiency with only 20% false positive rate. Out of the three signal scores, its ROC curve had the largest area.

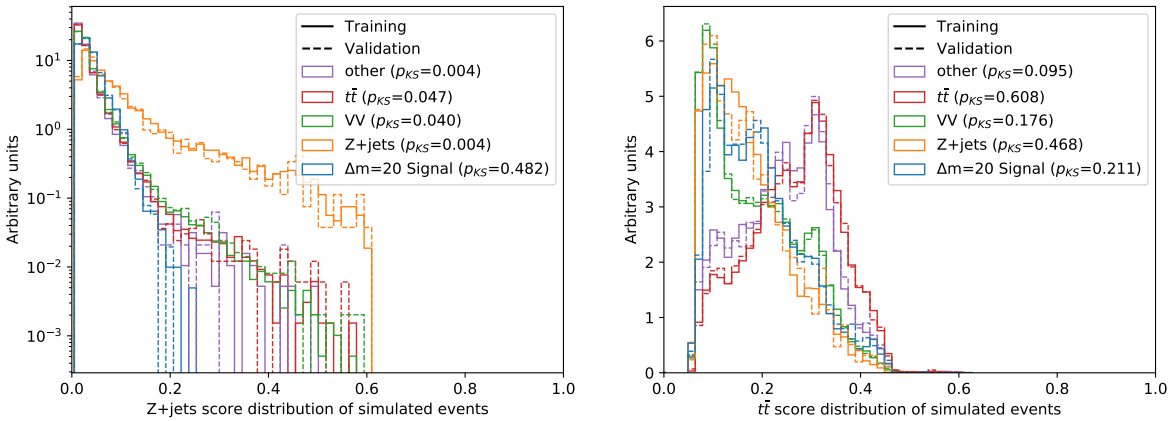

(a) LGBM$_{20}$ Z+jets score **(b)** LGBM$_{20}$ $t\bar{t}$ score

(c) LGBM$_{20}$ VV score **(d)** LGBM$_{20}$ 'other' score

Figure 6.8: The LGBM$_{20}$ Z+jets, $t\bar{t}$, VV, and 'other' score distributions for different signals and backgrounds in the training and validation samples. The distributions are normalised to unit area. Each plot shows the captioned distributions given by the captioned classifier on different simulated samples. The $p-$value of the Kolmogorov-Simirnov test p_{KS} quantifies the consistency between the training and testing distributions.

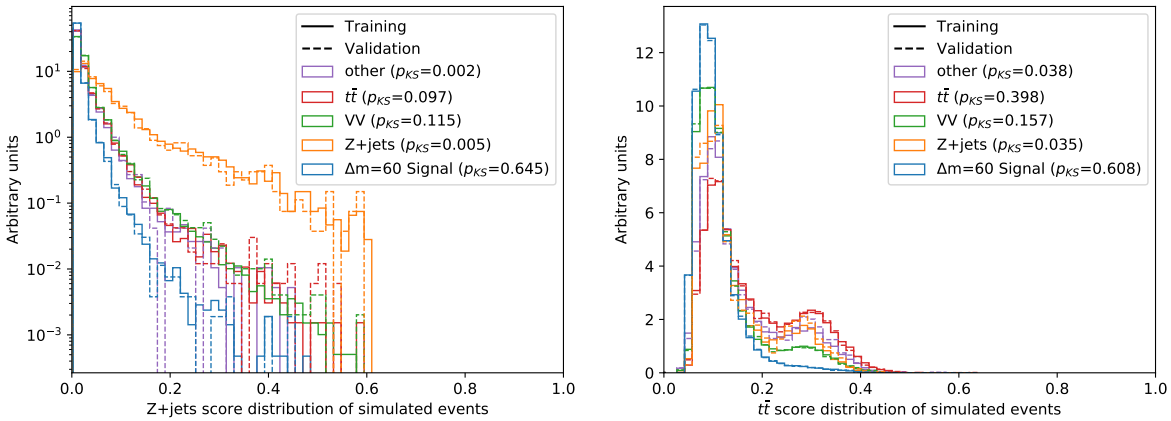

(a) LGBM$_{40}$ Z+jets score **(b)** LGBM$_{40}$ $t\bar{t}$ score

(c) LGBM$_{40}$ VV score **(d)** LGBM$_{40}$ 'other' score

Figure 6.9: The LGBM$_{40}$ Z+jets, $t\bar{t}$, VV, and 'other' score distributions for different signals and backgrounds in the training and validation samples. The distributions are normalised to unit area. Each plot shows the captioned distributions given by the captioned classifier on different simulated samples. The $p-$value of the Kolmogorov-Simirnov test p_{KS} quantifies the consistency between the training and testing distributions.

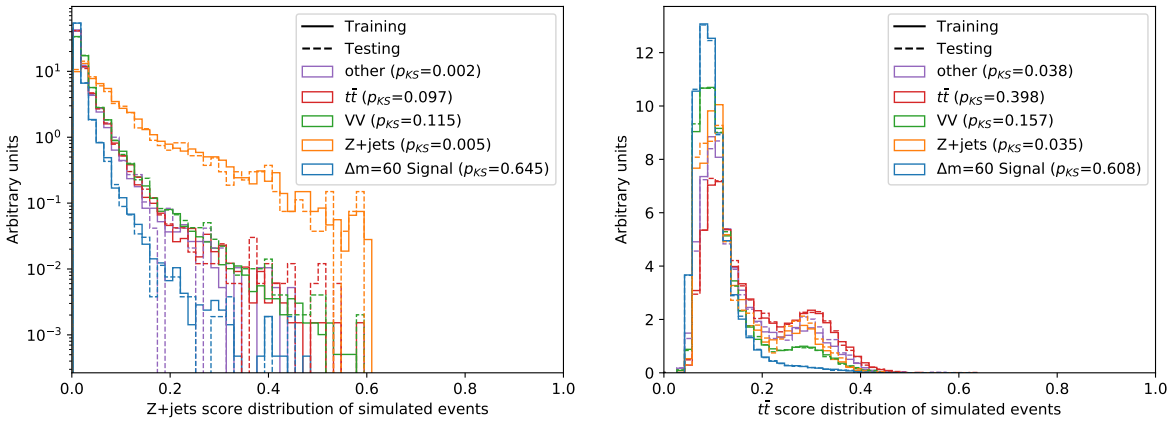

(a) LGBM$_{60}$ Z+jets score **(b)** LGBM$_{60}$ $t\bar{t}$ score

(c) LGBM$_{60}$ VV score **(d)** LGBM$_{60}$ 'other' score

Figure 6.10: The LGBM$_{60}$ Z+jets, $t\bar{t}$, VV, and 'other' score distributions for different signals and backgrounds in the training and validation samples. The distributions are normalised to unit area. Each plot shows the captioned distributions given by the captioned classifier on different simulated samples. The $p-$value of the Kolmogorov-Simirnov test p_{KS} quantifies the consistency between the training and testing distributions.

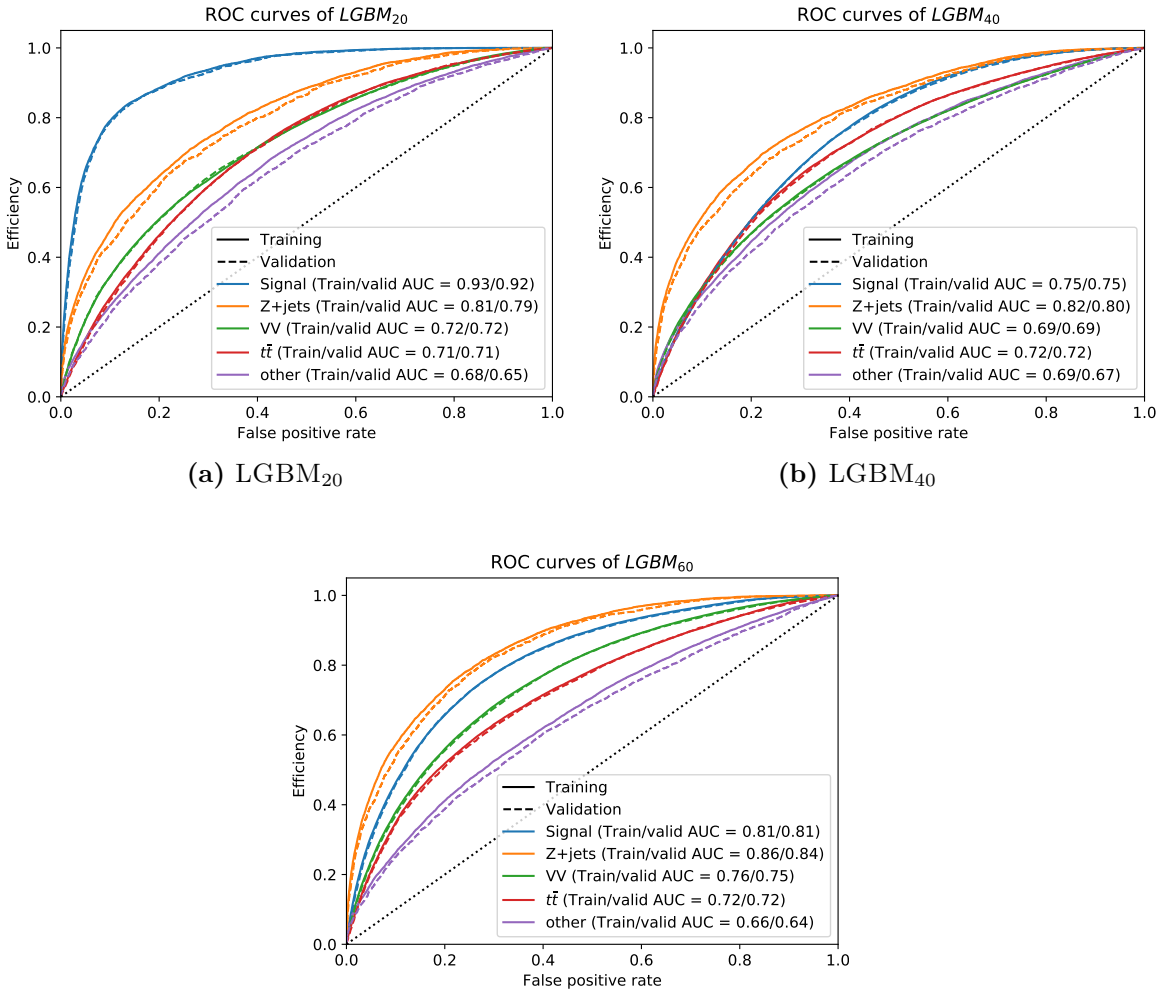

(a) LGBM_{20} **(b)** LGBM_{40}

(c) LGBM_{60}

Figure 6.11: The ROC curves plot the efficiency (true positive rate) of every classifier to targeted events against its false positive rate. A larger area under the curve (AUC) indicates greater discrimination power. Curves for training and the validation samples are shown. A large difference between the training and validation curves is a sign of overtraining. The dashed diagonal line shows the performance of a completely random classifier.

6.4.4 Signal region design

Simulated background and signal events from the evaluation samples were assigned scores by the LGBM_{20}, LGBM_{40}, and LGBM_{60} classifiers. In order to define signal regions, requirements on these scores were placed to obtain high sensitivity to selected benchmark signal points. Sensitivity is measured by the *significance* (cf. Section 6.2) for $\mathcal{L} = 139\,\text{fb}^{-1}$, and 10% uncertainty is assumed unless otherwise specified. In total, four signal regions were attempted: $\texttt{SR}_{20}$ is defined using LGBM_{20} scores, $\texttt{SR}_{40}$ is defined using LGBM_{40} scores, while $\texttt{SR}_{60}^{\texttt{high}}$ and $\texttt{SR}_{60}^{\texttt{low}}$ are defined with LGBM_{60} scores, where the two $\texttt{SR}_{60}$ regions are made orthogonal to each other by opposite requirements on m_{T2}.

Figure 6.12 shows the signal score distributions of simulated signal and background events. The significance of each bin is plotted below the score distributions. The signal points shown in these plots were those chosen for training. Behaviour suggested by the normalised distributions in Figure 6.7 is reflected here: in the LGBM_{20} signal score, the distribution of events from $\Delta m = 20\,\text{GeV}$ samples $(200, 180)$ and $(300, 280)$ is relatively flat compared to other events; for LGBM_{40} and LGBM_{60}, the distributions of their targeted signal events tend towards high signal scores; In all signal score distributions, the backgrounds fall with increasing signal score.

The sensitivity to the points on which the classifier was trained is limited, in part due to the low event yields for heavy sleptons. For the remainder of this section, the optimisation of signal regions will be conducted with benchmark signal points outside the existing exclusion but of lower masses; these points therefore have higher cross sections. These points are listed in Table 6.9. Figure 6.13 shows the signal score

Δm [GeV]	$(m_{\tilde{\ell}}, m_{\tilde{\chi}_1^0})$ [GeV]
20	(100, 80)
40	(150, 110)
60	(150, 90)

Table 6.9: List of benchmark signal points used in signal region optimisation.

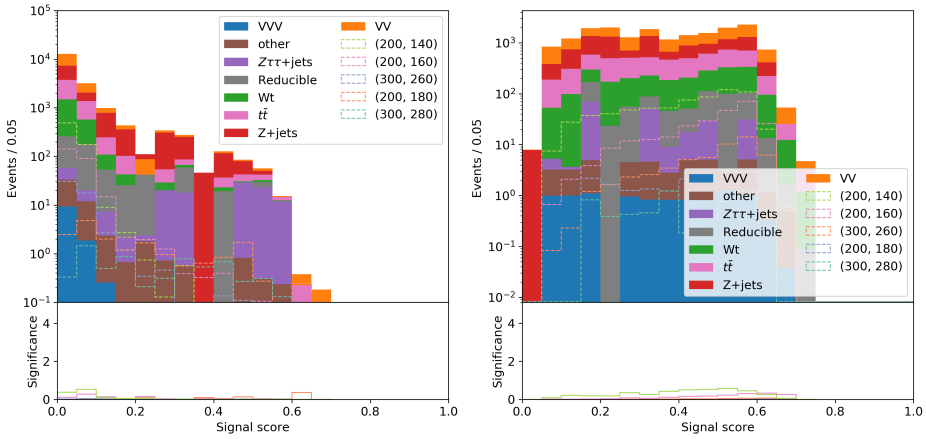

(a) LGBM$_{20}$ **(b)** LGBM$_{40}$

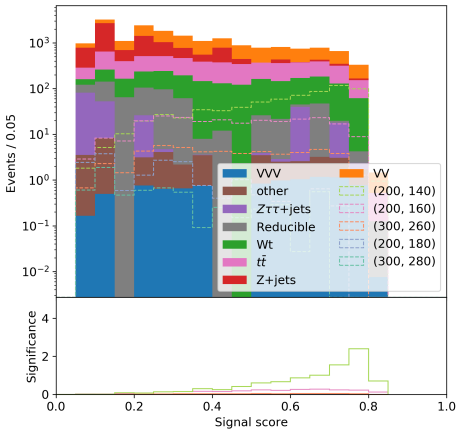

(c) LGBM$_{60}$

Figure 6.12: The signal score distributions of background and signal events in the evaluation samples. The scores are obtained from the captioned classifier. Here, $V = W, Z$; "other" includes other top processes, and the simulated signals are labelled by their $(m_{\tilde{\ell}}, m_{\tilde{\chi}_1^0})$ in GeV.

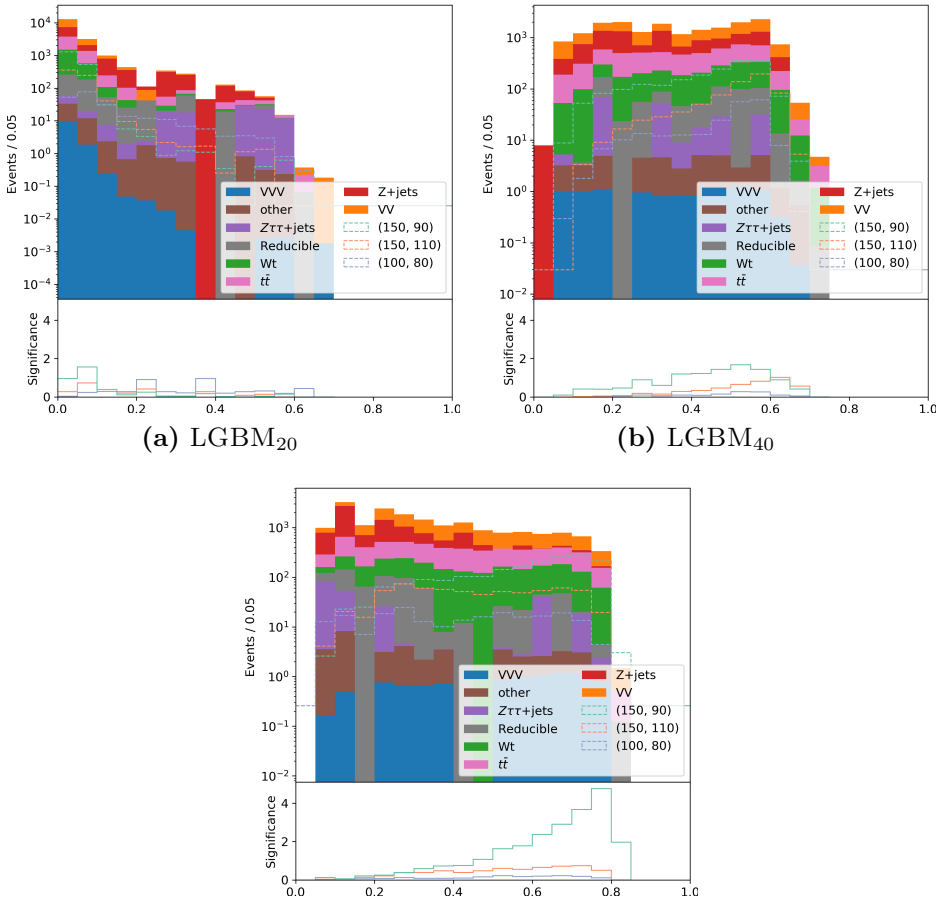

(a) LGBM$_{20}$ **(b)** LGBM$_{40}$

(c) LGBM$_{60}$

Figure 6.13: The signal score distributions of background and signal events in the evaluation samples. The scores are obtained from the captioned classifier. Here, $V = W, Z$; "other" includes other top processes, and the simulated signals are labelled by their $(m_{\tilde{\ell}}, m_{\tilde{\chi}_1^0})$ in GeV. Compared to Figure 6.12, the signal points of lower mass and higher cross section are shown here.

distributions with these signal points and the corresponding per-bin significances. Again it can be seen that the sensitivity to signal points is concentrated towards high values of LGBM$_{40}$ and LGBM$_{60}$ signal scores, but in low values of LGBM$_{20}$ signal scores. Moreover the LGBM$_{20}$ classifier is seen to be the least sensitive

For added sensitivity, requirements can be placed on the background scores as well as on the signal scores. Figures 6.14 to 6.16 show, for the LGBM$_{20}$, LGBM$_{40}$, and LGBM$_{60}$ classifiers respectively, the distributions in Z+jets score, $t\bar{t}$ score, VV score,

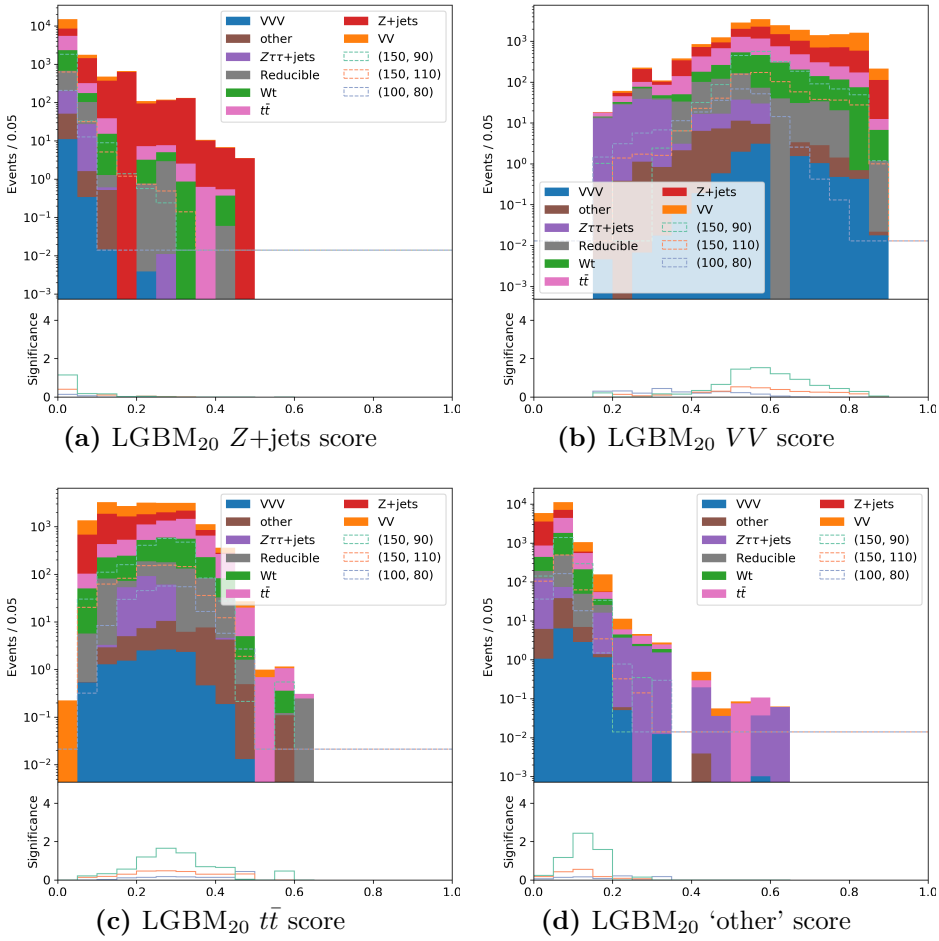

(a) LGBM$_{20}$ Z+jets score **(b)** LGBM$_{20}$ VV score

(c) LGBM$_{20}$ $t\bar{t}$ score **(d)** LGBM$_{20}$ 'other' score

Figure 6.14: The background score distributions of background and signal events in the evaluation samples. The scores are obtained from LGBM$_{20}$. Here, $V = W, Z$; "other" includes other top processes, and the simulated signals are labelled by their $(m_{\tilde{\ell}}, m_{\tilde{\chi}_1^0})$ in GeV.

and 'other' score. Placing maximum requirements on the LGBM$_{40}$ and LGBM$_{60}$ VV scores improves sensitivity to the benchmark models. Meanwhile for a LGBM$_{20}$-based signal region, requirements can be placed on all the scores in areas where significance peaks to achieve greater sensitivity.

It is seen in almost all signal and background score bins that sensitivity to the $\Delta m = 60\,\text{GeV}$ $(150, 90)$ point is the greatest, and sensitivity to the $\Delta m = 20\,\text{GeV}$ $(100, 80)$ point is the least. The author speculates this is likely due to the trigger strategy. Signal points with small Δm tend to have final states with low-energy ($p_{\text{T}} \sim 5$

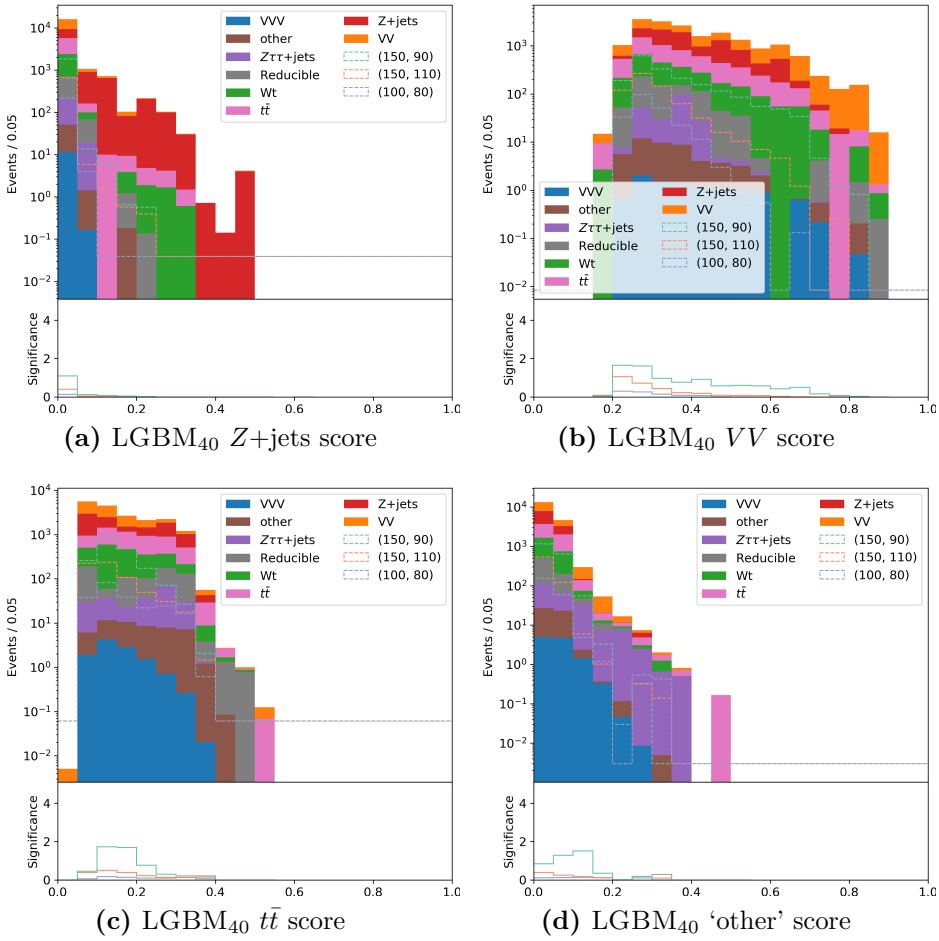

(a) LGBM$_{40}$ Z+jets score **(b)** LGBM$_{40}$ VV score

(c) LGBM$_{40}$ $t\bar{t}$ score **(d)** LGBM$_{40}$ 'other' score

Figure 6.15: The background score distributions of background and signal events in the evaluation samples. The scores are obtained from LGBM$_{40}$. Here, $V = W, Z$; "other" includes other top processes, and the simulated signals are labelled by their $(m_{\tilde{\ell}}, m_{\tilde{\chi}_1^0})$ in GeV.

to 20 GeV) leptons to which the single-lepton triggers used in this analysis are not efficient. Sensitivity to smaller Δm points could be provided by analyses such as Ref. [6] which trigger on the $E_{\mathrm{T}}^{\mathrm{miss}}$ of the neutralinos produced by a decaying slepton pair recoiling off high-energy initial state radiation.

Further insight into the kinematics of signal-like events can be found in the m_{T2} distributions of candidate signal regions, shown in Figure 6.17. One candidate region requires LGBM$_{20}$ scores Signal < 0.1, Z+jets < 0.05, $VV \in (0.5, 0.65)$, $t\bar{t} \in (0.2, 0.35)$, and 'other' $\in (0.05, 0.2)$. Another region requires LGBM$_{40}$ scores Signal > 0.55 and

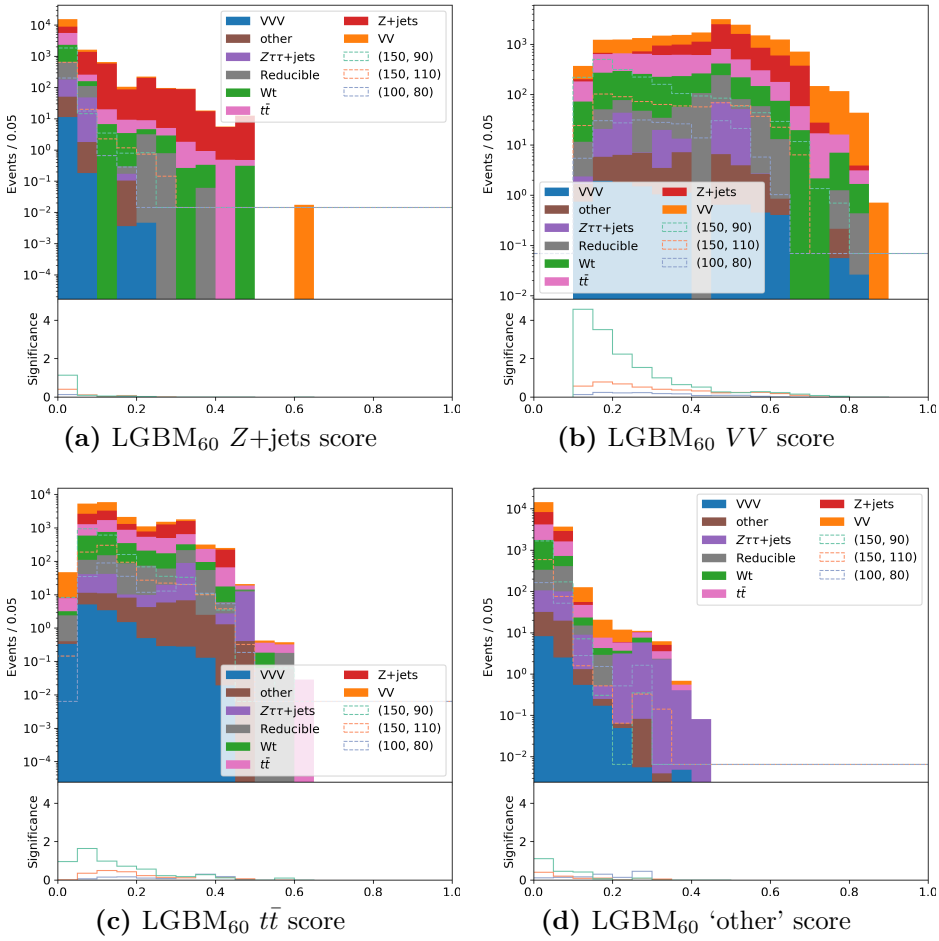

(a) LGBM$_{60}$ Z+jets score **(b)** LGBM$_{60}$ VV score

(c) LGBM$_{60}$ $t\bar{t}$ score **(d)** LGBM$_{60}$ 'other' score

Figure 6.16: The background score distributions of background and signal events in the evaluation samples. The scores are obtained from LGBM$_{60}$. Here, $V = W, Z$; "other" includes other top processes, and the simulated signals are labelled by their $(m_{\tilde{\ell}}, m_{\tilde{\chi}_1^0})$ in GeV.

$VV < 0.3$. A third region requires LGBM$_{60}$ scores Signal > 0.65 and $VV < 0.2$. It is observed that different ranges of m_{T2} are sensitive to different mass ranges. For the cases shown here, sensitivity to the large Δm $(150, 90)$ point is concentrated in $m_{T2} > 60\,\text{GeV}$, while sensitivity to the smaller Δm $(150, 110)$ and $(100, 80)$ points is concentrated at $m_{T2} < 60\,\text{GeV}$. This motivates defining regions according to high and low values of m_{T2}. As sensitivity of the LGBM$_{60}$-based candidate signal region is the most promising, this additional optimisation is done for it only. No additional requirements are made on the LGBM$_{20}$- and LGBM$_{40}$-based candidate signal regions.

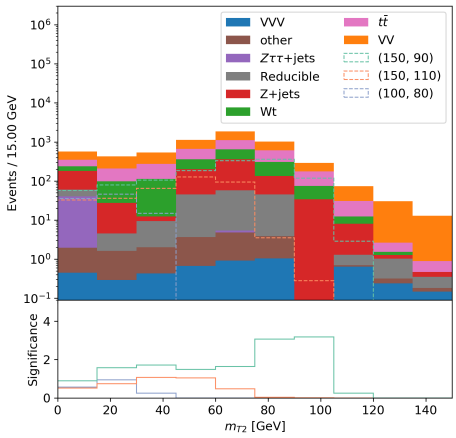

(a) Candidate signal region based on LGBM_{20} scores: Signal < 0.1, Z+jets < 0.05, $VV \in (0.5, 0.65)$, $t\bar{t} \in (0.2, 0.35)$, and 'other' $\in (0.05, 0.2)$.

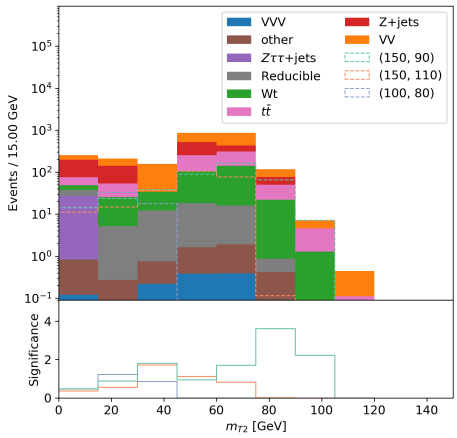

(b) Candidate signal region based on LGBM_{40} scores: Signal > 0.6 and $VV < 0.3$.

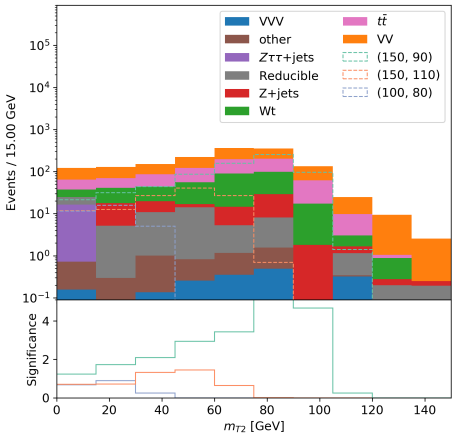

(c) Candidate signal region based on LGBM_{60} scores: Signal > 0.7 and $VV < 0.2$.

Figure 6.17: The m_{T2} distributions of background and signal events in the evaluation samples in candidate signal regions. Here, $V = W, Z$; "other" includes other top processes, and the simulated signals are labelled by their $(m_{\tilde{\ell}}, m_{\tilde{\chi}_1^0})$ in GeV.

Signal region	Classifier used	Signal score	Z+jets score	VV score	$t\bar{t}$ score	'other' score	m_{T2} [GeV]
SR_{20}	LGBM_{20}	< 0.1	< 0.05	$\in (0.5, 0.65)$	$\in (0.2, 0.35)$	$\in (0.05, 0.2)$	-
SR_{40}	LGBM_{40}	> 0.55	-	< 0.3	-	-	-
$\text{SR}_{60}^{\text{low}}$	LGBM_{60}	> 0.65	-	< 0.2	-	-	< 60
$\text{SR}_{60}^{\text{high}}$							> 60

Table 6.10: List of signal regions defined using LGBM scores and m_{T2}.

In summary, four signal regions are defined: $\texttt{SR}_{20}$ is optimised to target $\Delta m = 20\,\text{GeV}$; it requires LGBM_{20} scores Signal < 0.1, Z+jets < 0.05, $VV \in (0.5, 0.65)$, $t\bar{t} \in (0.2, 0.35)$, and 'other' $\in (0.05, 0.2)$. $\texttt{SR}_{40}$ is optimised to target $\Delta m = 40\,\text{GeV}$; it requires LGBM_{40} scores Signal > 0.55 and $VV < 0.3$. $\texttt{SR}_{60}^{\texttt{low}}$ and $\texttt{SR}_{60}^{\texttt{high}}$ are optimised to target $\Delta m = 60\,\text{GeV}$, but also have sensitivity to a wider range of Δm due to requirements on m_{T2}; both regions require LGBM_{60} scores Signal > 0.65, $VV < 0.2$; $\texttt{SR}_{60}^{\texttt{low}}$ additionally requires $m_{T2} < 60\,\text{GeV}$, while for $\texttt{SR}_{60}^{\texttt{high}}$, $m_{T2} > 60\,\text{GeV}$. These definitions are listed in Table 6.10.

6.5 Traditional approach

A traditional cut-based approach was developed by analysis collaborators. Requirements were placed on variables in order to increase signal significance to the benchmark points in Table 6.9. The requirements applied were informed by the distributions of the variables in signal and background events; this difference in distributions was previously described in the *key variables* paragraph of Section 6.2.

To target the required final state, the signal region requires events with exactly two leptons, and that the lepton pair be of the same flavour and with opposite sign.

Events were required to have zero jets with $p_{\text{T}} > 20\,\text{GeV}$ and $|\eta| < 2.4$; as before, no requirement was made on jets in the forward region ($|\eta| > 2.4$). The lepton p_{T} requirements were $p_T^{\ell 1} > 140\,\text{GeV}$ and $p_T^{\ell 2} > 20\,\text{GeV}$. The dilepton invariant mass was required to be $m_{\ell\ell} > 11\,\text{GeV}$ to reject low-mass resonances, and $|m_{\ell\ell} - 91.2\,\text{GeV}| > 15\,\text{GeV}$ to reject the Z boson resonance. $S(E_{\text{T}}^{\text{miss}}) > 7$ was required to suppress events with low or mis-measured $E_{\text{T}}^{\text{miss}}$, particularly events from Z+jets. A requirement of $p_{\text{T,b}}^{\ell\ell} < 5\,\text{GeV}$ constrains the lepton transverse momenta and $E_{\text{T}}^{\text{miss}}$ such that they are balanced against each other. Requirements on angular variables $\cos\theta_{\ell\ell}^{*} < 0.2$, $\Delta\phi(\ell, \ell) > 2.2$, and $\Delta(E_{\text{T}}^{\text{miss}}, \ell 1) > 2.2$ were seen to be effective. The definition of the signal region `SR-trad` is summarised in Table 6.11. The distributions of key variables in the signal

Variable	SR-trad
N(jets)	$= 0$
N(OS leptons)	$= 2$, SF
$p_T^{\ell 1}$ [GeV]	> 140
$p_T^{\ell 2}$ [GeV]	> 20
$S(E_{\mathrm{T}}^{\mathrm{miss}})$	> 7
$E_{\mathrm{T}}^{\mathrm{miss}}$ [GeV]	
$p_{\mathrm{T,b}}^{\ell\ell}$ [GeV]	< 5
$\cos\theta_{\ell\ell}^{*}$	< 0.2
$\Delta\phi(\ell,\ell)$	> 2.2
$\Delta\phi(E_{\mathrm{T}}^{\mathrm{miss}},\ell 1)$	> 2.2

Table 6.11: Definition of the traditional signal region.

region, in simulated SM and SUSY events are shown in Figures 6.18 and 6.19. The plots show that the significances to the benchmark points are high in the signal region.

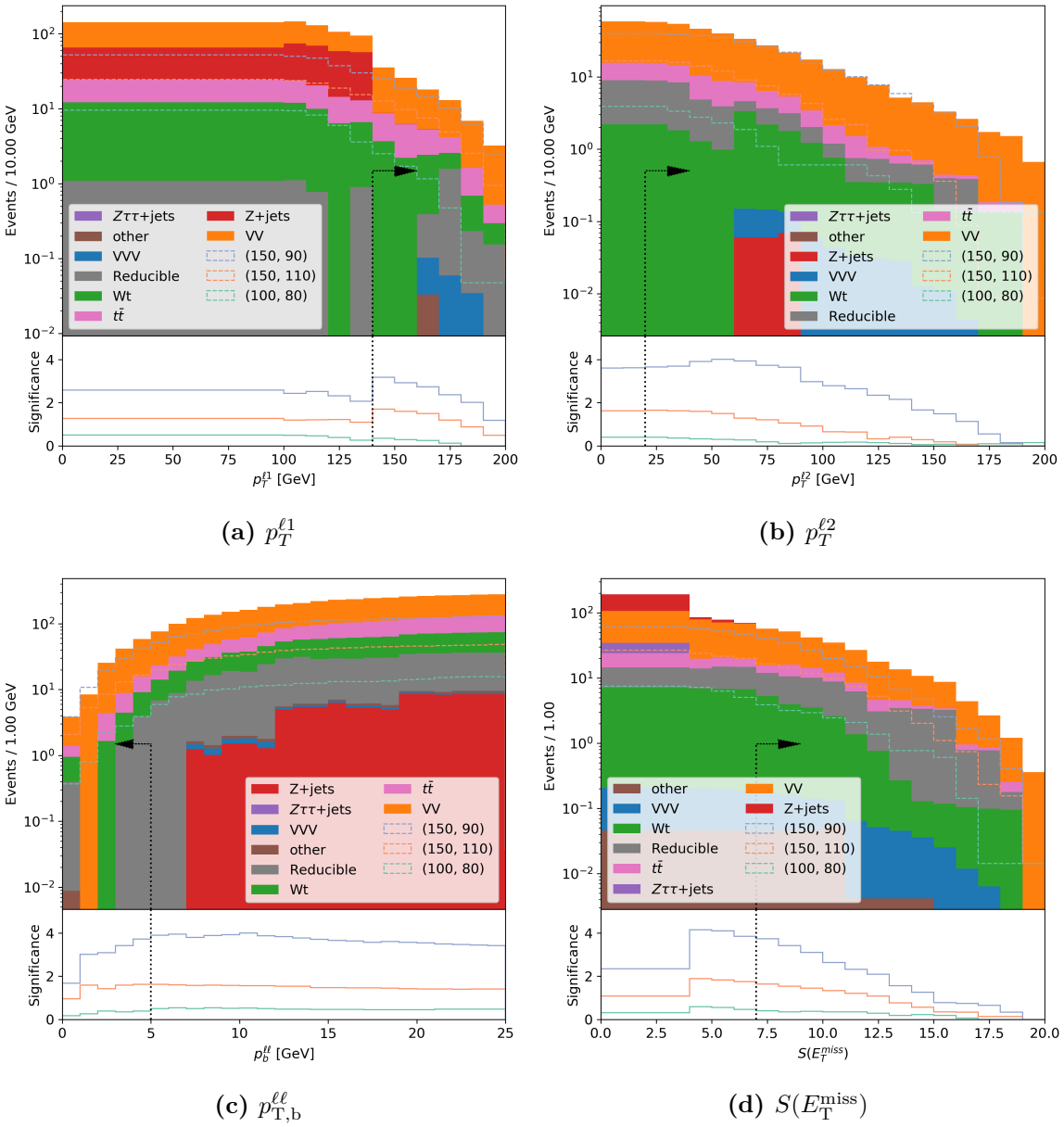

(a) $p_T^{\ell 1}$ **(b)** $p_T^{\ell 2}$

(c) $p_{\mathrm{T,b}}^{\ell\ell}$ **(d)** $S(E_{\mathrm{T}}^{\mathrm{miss}})$

Figure 6.18: Cumulative distributions of variables in the signal region in simulated SM and SUSY events. The arrow indicates the requirement applied to obtain the signal region.

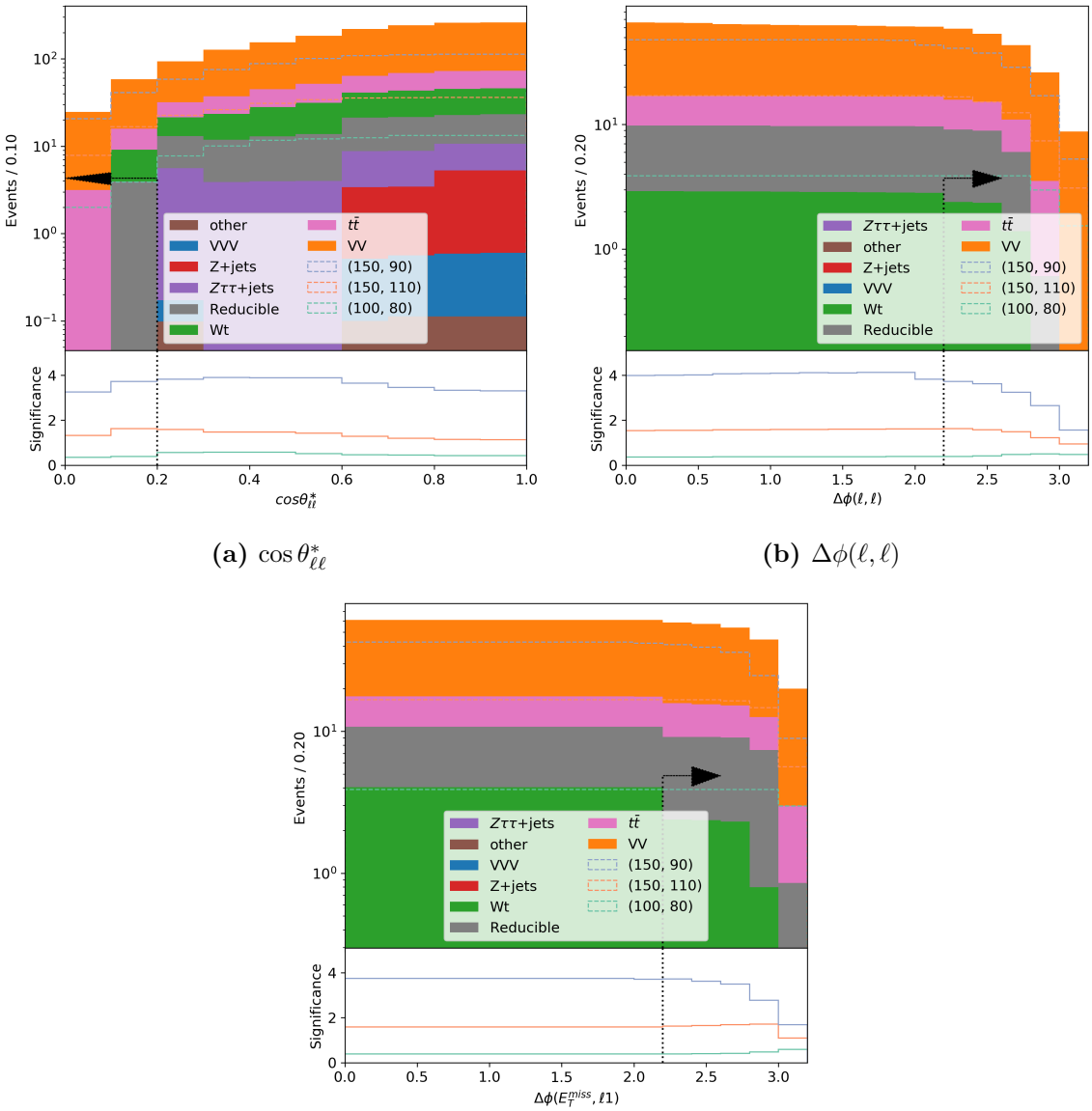

(a) $\cos\theta^*_{\ell\ell}$ **(b)** $\Delta\phi(\ell,\ell)$

(c) $\Delta\phi(E_{\mathrm{T}}^{\mathrm{miss}},\ell 1)$

Figure 6.19: Distributions of variables in the signal region in simulated SM and SUSY events. The arrow indicates the requirement applied to obtain the signal region.

6.6 Background estimation

In the signal process, events with a pair of same-flavour opposite-sign (SFOS) leptons and some $E_{\mathrm{T}}^{\mathrm{miss}}$ are expected. Backgrounds to this search are SM events with the same signature: they are classified as either irreducible flavour-symmetric, irreducible flavour-asymmetric, or reducible (cf. Section 6.2). The flavour-asymmetric and reducible backgrounds are estimated from MC simulation.

The VV processes ($V = W, Z$) contribute both flavour-symmetric and flavour-asymmetric events. Flavour-asymmetric events arise from WW decay, or from $WZ \to \ell\nu\ell'^{+}\ell'^{-}$ decays where a lepton from the Z is not reconstructed. Flavour-symmetric events arise from WZ decays when the W decays either hadronically or leptonically but its lepton is not reconstructed. The VVV processes contribute in a similar way when the third boson decays hadronically. The VV and VVV asymmetric contributions are estimated from MC simulation by subtracting the expected number of different-flavour events from that of same-flavour events.

The remainder of this section is devoted to the data-driven estimation of the flavour-symmetric backgrounds. Different-flavour opposite-sign (DFOS) events are used to estimate their contribution to the signal region. The contributing Standard Model processes have branching fractions to $e^{+}e^{-}$, $\mu^{+}\mu^{-}$, and $e^{\pm}\mu^{\mp}$ final states in a $\mathcal{B}(ee) : \mathcal{B}(\mu\mu) : \mathcal{B}(e\mu) = 1 : 1 : 2$ ratio due to lepton flavour universality. However the number of observed events in each flavour combination depends on lepton trigger, reconstruction, identification, and isolation efficiencies, which differ between lepton flavours. Therefore, assuming $4N$ of the contributing SM processes decay into ee, $\mu\mu$, and $e\mu$, then, accounting for trigger and reconstruction efficiencies[2], the number of events observed would be:

$$\begin{aligned} N_{ee} &= N\epsilon_{e}^{\mathrm{reco}}\epsilon_{e}^{\mathrm{reco}}\epsilon_{ee}^{\mathrm{trigger}} \\ N_{\mu\mu} &= N\epsilon_{\mu}^{\mathrm{reco}}\epsilon_{\mu}^{\mathrm{reco}}\epsilon_{\mu\mu}^{\mathrm{trigger}} \\ N_{e\mu} &= 2N\epsilon_{e}^{\mathrm{reco}}\epsilon_{\mu}^{\mathrm{reco}}\epsilon_{e\mu}^{\mathrm{trigger}}. \end{aligned} \tag{6.7}$$

Variable	CR-κ	CR-α	CR-F	CR-DF
N(jets)	< 2	< 2	$= 0$	$= 0$
N(OS leptons)	$= 2$, SF	$= 2$	$= 2$	$= 2$, DF
$p_T^{\ell 1}$ [GeV]	> 30	> 30	> 140	> 140
$p_T^{\ell 2}$ [GeV]	> 9	> 20	> 20	> 20
$S(E_{\mathrm{T}}^{\mathrm{miss}})$	> 6		> 7	> 7
$E_{\mathrm{T}}^{\mathrm{miss}}$ [GeV]		> 230		
$p_{\mathrm{T,b}}^{\ell\ell}$ [GeV]			> 7	< 5
$\cos\theta_{\ell\ell}^{*}$	> 0.2		> 0.5	< 0.2
$\lvert m_{\ell\ell} - m_Z \rvert$ [GeV]		> 15		> 15
$\Delta\phi(\ell,\ell)$				> 2.2
$\Delta\phi(E_{\mathrm{T}}^{\mathrm{miss}},\ell 1)$				> 2.2
Trigger	1L	$E_{\mathrm{T}}^{\mathrm{miss}}$	1L	1L

Table 6.12: Definitions of control regions used for the estimation of flavour-symmetric backgrounds. CR-κ and CR-α are used to measure the trigger and reconstruction efficiencies for the efficiency correction method. CR-F is used to measure the transfer factor for the transfer factor method. CR-DF is identical to SR-trad save its requirement for different-flavour lepton pairs. The efficiency correction method and the transfer factor method are applied to events in CR-DF to obtain an estimate for flavour-symmetric background contributions to the signal regions.

Rearranging the above and eliminating N, we can obtain:

$$\begin{aligned} N_{ee} &= \frac{1}{2} N_{e\mu} \frac{\epsilon_e^{\mathrm{reco}}}{\epsilon_\mu^{\mathrm{reco}}} \frac{\epsilon_{ee}^{\mathrm{trigger}}}{\epsilon_{e\mu}^{\mathrm{trigger}}} \\ N_{\mu\mu} &= \frac{1}{2} N_{e\mu} \frac{\epsilon_\mu^{\mathrm{reco}}}{\epsilon_e^{\mathrm{reco}}} \frac{\epsilon_{\mu\mu}^{\mathrm{trigger}}}{\epsilon_{e\mu}^{\mathrm{trigger}}}. \end{aligned} \tag{6.8}$$

The number of expected $e\mu$ events $N_{e\mu}$ is measured in control region CR-DF, which shares all the requirements of the signal region SR-trad save one: lepton pairs are required to be DFOS rather than SFOS.

Two methods of measuring the efficiency ratios were developed by collaborators. They are validated against each other and are shown to be consistent. The methods are described below, followed by a comparison of their results.

[2]The efficiencies of reconstruction, identification, and isolation are grouped into a single reconstruction efficiency ϵ^{reco}.

6.6.1 Efficiency correction method

This method was used previously in Ref. [183]. In order to facilitate measurement, Eqs. 6.8 are written

$$\begin{aligned} N_{ee}^{\text{exp}} &= \frac{1}{2} N_{e\mu} \frac{1}{\kappa(p_T^{\ell 1}, \eta)} \alpha(\eta) \\ N_{\mu\mu}^{\text{exp}} &= \frac{1}{2} N_{e\mu} \kappa(p_T^{\ell 1}, \eta) \alpha(\eta), \end{aligned} \tag{6.9}$$

where

$$\begin{aligned} \kappa &= \frac{\epsilon_\mu^{\text{reco}}}{\epsilon_e^{\text{reco}}} \sqrt{\frac{\epsilon_{\mu\mu}^{\text{trigger}}}{\epsilon_{ee}^{\text{trigger}}}} = \sqrt{\frac{\epsilon_\mu^{\text{reco}} \epsilon_\mu^{\text{reco}} \epsilon_{\mu\mu}^{\text{trigger}}}{\epsilon_e^{\text{reco}} \epsilon_e^{\text{reco}} \epsilon_{ee}^{\text{trigger}}}} = \sqrt{\frac{N_{\mu\mu}^{\text{CR}}}{N_{ee}^{\text{CR}}}} \\ \alpha &= \frac{\sqrt{\epsilon_{ee}^{\text{trigger}} \epsilon_{\mu\mu}^{\text{trigger}}}}{\epsilon_{e\mu}^{\text{trigger}}} \end{aligned} \tag{6.10}$$

under the assumption that these lepton efficiencies are independent.

The observables κ, and α are measured in dedicated control regions, the definitions of which are listed in Table 6.12. The details of their measurement are elaborated on below.

The κ factor encapsulates differences in reconstruction and trigger efficiencies, and is measured by the square root of the ratio of the number of $\mu^+\mu^-$ events to that of e^+e^- events. This measurement is made in control region `CR-`κ. Compared to the signal region `SR-trad`, looser requirements are made on $p_T^{\ell 1}$ and other variables in order to increase the number of expected events from flavour-symmetric backgrounds and it is made orthogonal to the signal region by inverting the $\cos\theta^*_{\ell\ell}$ requirement. The background composition in `CR-`κ is similar to that in `SR-trad`. The parameter κ was measured to be in the range 1.0655 ± 0.0089 to 1.440 ± 0.010, depending on the lepton $|\eta|$, where the uncertainties are statistical.

The α factor accounts for differences in the efficiency of the single-lepton triggers to ee, $e\mu$, and $\mu\mu$ events. The trigger efficiencies were measured by the ratio

$$\epsilon_{\ell\ell'}^{\text{trigger}} = \frac{N(E_{\text{T}}^{\text{miss}}\text{-triggered} \cap \text{single-lepton triggered} \cap \ell\ell')}{N(E_{\text{T}}^{\text{miss}}\text{-triggered} \cap \ell\ell')}$$

in the region `CR-`α, a $E_{\text{T}}^{\text{miss}}$-triggered two-lepton (with no flavour or sign requirement) sample which required $E_{\text{T}}^{\text{miss}} > 230\,\text{GeV}$, $p_T^{\ell 1} > 30\,\text{GeV}$, and $p_T^{\ell 2} > 30\,\text{GeV}$ to ensure the

$E_{\mathrm{T}}^{\mathrm{miss}}$ triggers and single-lepton triggers are fully efficient. The $E_{\mathrm{T}}^{\mathrm{miss}}$ triggers required are the primary triggers listed in Table 4.1. The measured α factors were found to be slightly dependent on lepton $|\eta|$, ranging from 0.962 ± 0.013 to 1.010 ± 0.020; the uncertainties shown are statistical.

6.6.2 Transfer factor method

In an alternative method, Eqs. 6.8 are rewritten such that the ratios of efficiencies are parametrised by *transfer factors* R:

$$\begin{aligned} \langle N_{ee} \rangle &= R_e \cdot N_{e\mu} \\ \langle N_{\mu\mu} \rangle &= R_\mu \cdot N_{e\mu} \\ \langle N_{SF} \rangle &= \langle N_{ee} \rangle + \langle N_{\mu\mu} \rangle = R \cdot N_{e\mu} = (R_e + R_\mu) \cdot N_{e\mu}, \end{aligned} \tag{6.11}$$

where $R_e = N_{ee}/N_{e\mu}$ and $R_\mu = N_{\mu\mu}/N_{e\mu}$ is the ratio of the number of ee ($\mu\mu$) events to the number of $e\mu$ events as measured in a control region `CR-F`. This region is close in definition to `SR-trad`, but made orthogonal to it by the requirements $p_{\mathrm{T,b}}^{\ell\ell} > 7\,\mathrm{GeV}$ and $\cos\theta_{\ell\ell}^{*} > 0.5$. The factors R_e and R_μ and their statistical uncertainties were measured to be 0.54 ± 0.07 and 0.43 ± 0.05 respectively.

6.6.3 Comparison of background estimates

Method	ee Events	$\mu\mu$ Events	Total
Efficiency correction factors	37.3 ± 4.5	32.9 ± 3.9	70.2 ± 8.3
Transfer factor	38.3 ± 6.7	30.5 ± 5.1	68.9 ± 11.8

Table 6.13: Expected flavour-symmetric background yields in `SR-trad` estimated using the events in `CR-DF`, which shares the same requirements as the signal region except DFOS lepton pairs are required. Two different methods were used: efficiency correction by κ and α factors, and estimation by transfer factors R_μ and R_e. Only statistical uncertainties are shown. This table was produced by collaborators in the analysis team.

The flavour-symmetric background estimate obtained by both methods is shown in Table 6.13. Both methods agree with each other within uncertainties, showing that

the background estimation is robust. The efficiency correction method is used in the results to follow.

6.7 Results

The estimated yields in the signal regions are listed in Table 6.14. In the machine-learning signal regions, all MC events were taken from the evaluation samples. No uncertainties were considered. The expected yields are higher when the data-driven symmetric background estimation is used. The flavour-symmetric backgrounds were estimated by the data-driven efficiency correction method.

The expected signal and background yields are used to compute the significance Z (cf. Eq. 6.1) for every signal point. The area in $(m_{\tilde{\ell}}, m_{\tilde{\chi}_1^0})$ that can be excluded at the 95% confidence level ($Z > 1.64$) assuming 10% uncertainty is shown in Figure 6.20. $\texttt{SR}_{20}$ and $\texttt{SR}_{40}$ have similar exclusion ranges in $(m_{\tilde{\ell}}, m_{\tilde{\chi}_1^0})$, both smaller than the other signal regions. Meanwhile $\texttt{SR}_{60}^{\texttt{low}}$ excludes more area in the target gap region, while $\texttt{SR}_{60}^{\texttt{high}}$ possesses more exclusion power for higher $m_{\tilde{\ell}}$ values, so they are complementary as intended; and their combined exclusion range is similar to that of `SR-trad` alone.

Sample	$\texttt{SR}_{20}$	$\texttt{SR}_{40}$	$\texttt{SR}_{60}^{\text{high}}$	$\texttt{SR}_{60}^{\text{low}}$	SR-trad
Expected with data-driven symmetric	6811.61	3018.76	963.21	647.64	79.24
MC Z+jets	646.50	569.58	40.46	17.79	0.11
Data-driven symmetric	5656.58	2294.15	828.35	576.50	68.28
MC VV asymmetric	354.29	88.19	75.56	15.30	4.04
MC VVV asymmetric	0.42	0.12	0.23	0.00	0.01
MC reducible	138.65	62.20	16.06	36.09	6.75
other	15.18	4.53	2.55	1.97	0.05
Expected MC-only	5962.23	2469.83	887.12	623.78	61.71
MC Z+jets	743.69	557.34	41.93	23.35	0.11
MC VV	2519.96	1066.08	413.50	280.00	42.78
MC VVV	6.02	1.30	1.94	0.64	0.13
MC $t\bar{t}$	1590.86	463.27	263.22	165.35	6.68
MC Wt	890.05	292.88	162.53	99.22	5.20
MC $Z\rightarrow \tau\tau$+jets	38.72	26.24	0.00	15.63	0.00
MC reducible	157.94	58.18	1.75	37.39	6.75
MC other	14.98	4.55	2.25	2.21	0.05
(150,110)	358.79	244.41	27.71	91.77	16.67
(150, 90)	1239.42	400.71	509.36	183.02	40.93
(100, 80)	96.78	65.24	0.00	32.39	3.89

Table 6.14: Expected yields in signal regions. No uncertainties were considered. In the machine-learning signal regions, all MC events were taken from the evaluation samples. The flavour-symmetric backgrounds were estimated by the data-driven efficiency correction method. The signal points are labelled by their masses $(m_{\tilde{\ell}}, m_{\tilde{\chi}_1^0})$ in GeV.s

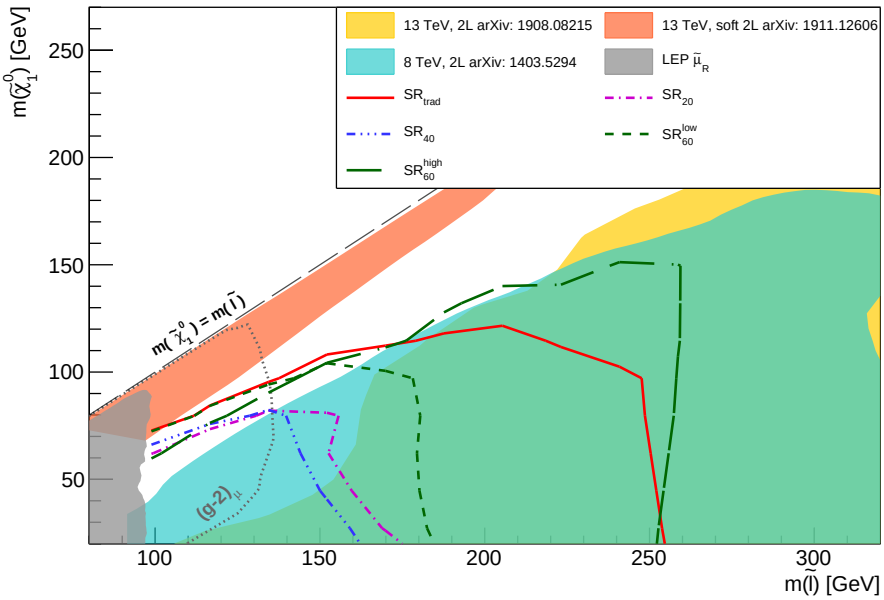

Figure 6.20: Exclusion limits computed from the signal regions are compared to previous ATLAS [5, 6, 173, 174] and LEP limits [43]. The model assumes four sleptons $\tilde{\ell} \in \{\tilde{e}_L, \tilde{e}_R, \tilde{\mu}_L, \tilde{\mu}_R\}$ of equal mass. Shown also is the parameter space favoured by $(g-2)_\mu$ as computed in Ref. [184]. For the expected limits, exclusion is defined as regions where $Z < 1.64$, and a 10% uncertainty was assumed. Flavour-symmetric backgrounds were estimated by a data-driven method, while all other backgrounds were taken from Geant MC.

6.8 Discussion

Comparing machine-learning and traditional signal regions Figure 6.21 compares the LGBM_{60} score distributions in signal and background events for SR-trad, $\mathtt{SR}_{60}^{\mathtt{low}}$, and $\mathtt{SR}_{60}^{\mathtt{high}}$. The distributions are normalised to unit area. All events are taken from Geant MC. Backgrounds have been taken from the whole of the Geant MC dataset, and all background contributions have been summed; The signal point $(m_{\tilde{\ell}}, m_{\tilde{\chi}_1^0}) = (150, 90)$ is chosen for this comparison as it lies just outside the exclusion range. The distribution of scores in SR-trad is very similar to that of $\mathtt{SR}_{60}$, indicating that most events in SR-trad fall into $\mathtt{SR}_{60}$.

Figures 6.22 and 6.23 show the same comparisons for the traditional kinematic variables. The shapes of variables in $\mathtt{SR}_{60}^{\mathtt{low}}$ are remarkably similar to those in SR-trad, except for variables such as $p_T^{\ell 1}$, $p_{\mathrm{T,b}}^{\ell\ell}$, and $\cos\theta_{\ell\ell}^*$ on which explicit requirements were made to define SR-trad. Meanwhile, events in $\mathtt{SR}_{60}^{\mathtt{high}}$ tend to be lower in $p_T^{\ell 1}$, $m_{\ell\ell}$, and smaller in the $\Delta\phi$ variables than events in the other two regions. In all regions, signal event variable distributions are similar to those of background events (except m_{T2}), showing again the difficulty of distinguishing one from the other.

Improving sensitivity with fit to $\mathbf{m_{T2}}$ $\mathtt{SR}_{60}^{\mathtt{low}}$ and $\mathtt{SR}_{60}^{\mathtt{high}}$ are bipartite in m_{T2}, which gives rise to their different regions of sensitivity. This sensitivity could potentially be improved by conducting a shape fit in m_{T2} in the union of $\mathtt{SR}_{60}^{\mathtt{low}}$ and $\mathtt{SR}_{60}^{\mathtt{high}}$.

Projected best-case scenario with small uncertainties In estimating the potential of the analysis, it should be noted that a 10% uncertainty could be pessimistic. Different-flavour events offer a way to obtain a high-precision data-driven estimate of the dominant, flavour-symmetric backgrounds; this estimate is limited by statistical uncertainty. Hence we also consider the case of a best-case scenario where the analysis is limited only by statistical uncertainties. Figure 6.24 shows the exclusion potential when Poisson uncertainties are assumed, that is when the absolute uncertainty is

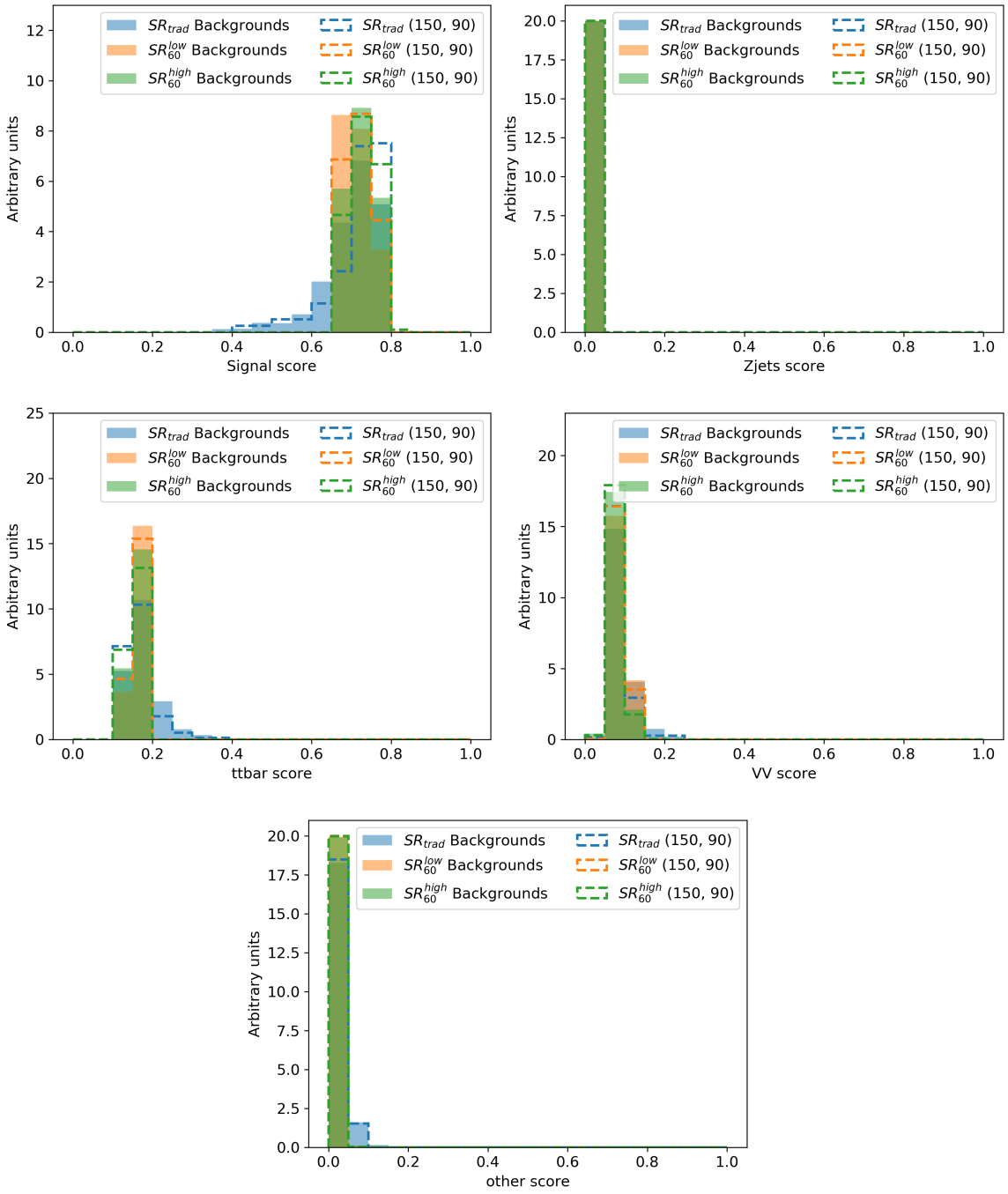

Figure 6.21: LGBM$_{60}$ score distributions of events in `SR-trad`, $\texttt{SR}_{60}^{\texttt{low}}$, and $\texttt{SR}_{60}^{\texttt{high}}$. Geant MC events from signal point $(m_{\tilde{\ell}}, m_{\tilde{\chi}_1^0}) = (150, 90)$ GeV are compared against Geant MC Standard Model events. All events in these signal regions fall within the same bin of Z+jets score.

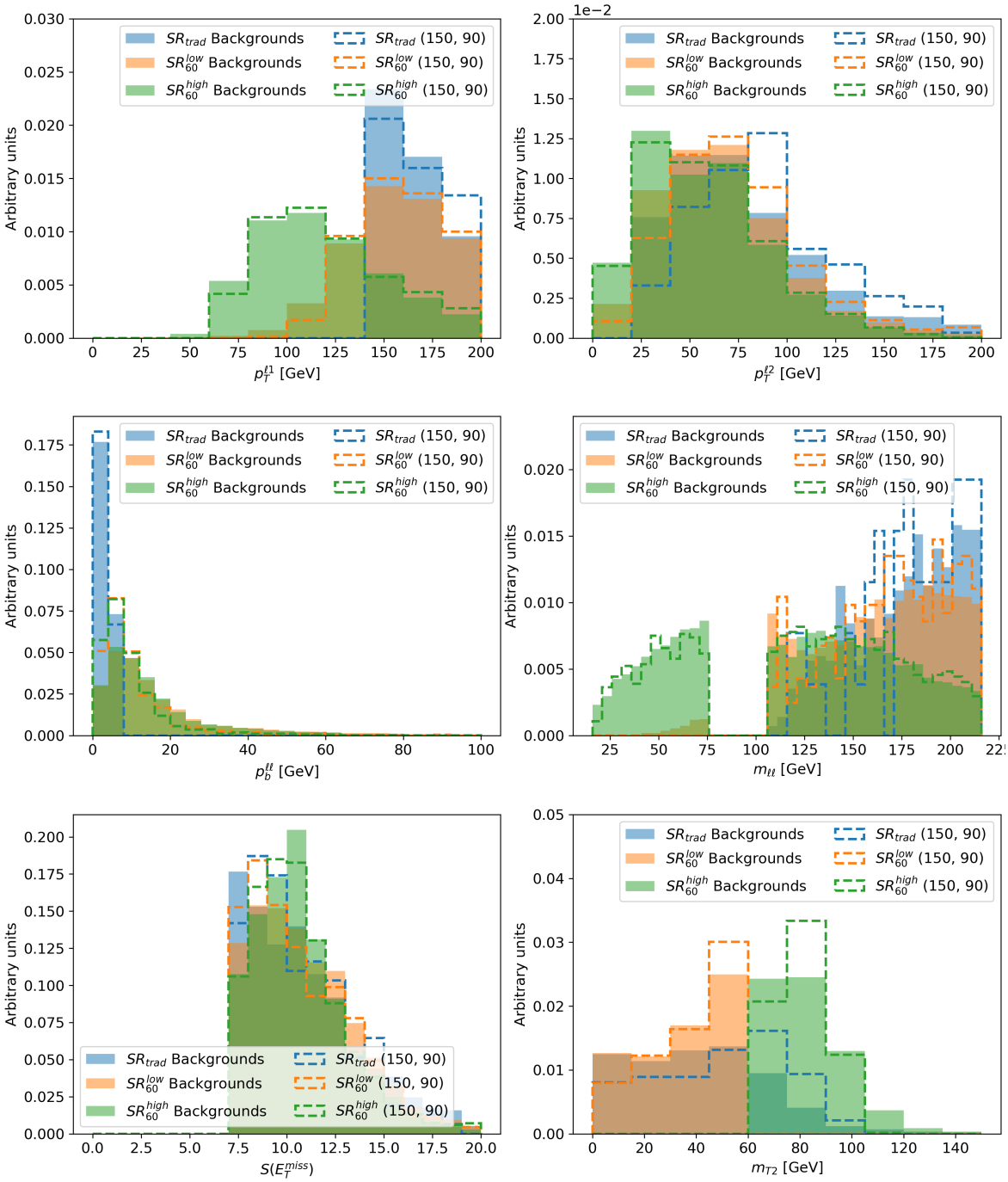

Figure 6.22: Variable distributions of events in `SR-trad`, $\texttt{SR}_{60}^{\texttt{low}}$, and $\texttt{SR}_{60}^{\texttt{high}}$. The distributions are normalised to unit area. Geant MC events from signal point $(m_{\tilde{\ell}}, m_{\tilde{\chi}_1^0}) = (150, 90)$ GeV are compared against Geant MC Standard Model events.

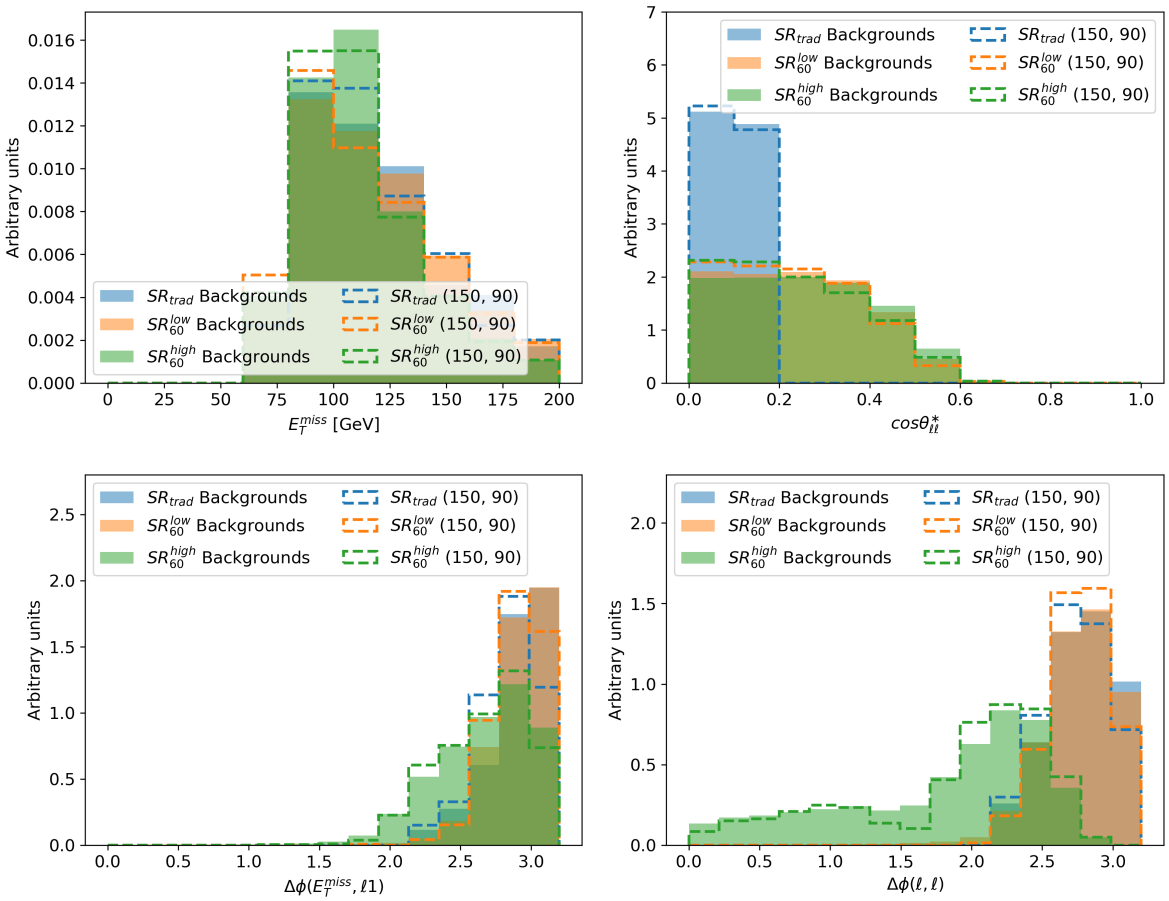

Figure 6.23: Variable distributions of events in `SR-trad`, $\texttt{SR}_{60}^{\texttt{low}}$, and $\texttt{SR}_{60}^{\texttt{high}}$. The distributions are normalised to unit area. Geant MC events from signal point $(m_{\tilde{\ell}}, m_{\tilde{\chi}_1^0}) = (150, 90)$ GeV are compared against Geant MC Standard Model events.

assumed to be the square-root of the total expected background $\sqrt{N_{\text{bkg}}}$. Under this assumption, the uncertainty on events yields in `SR-trad` is 11%; by comparison, the uncertainties in $\texttt{SR}_{20}$, $\texttt{SR}_{60}$, $\texttt{SR}_{60}^{\texttt{low}}$, and $\texttt{SR}_{60}^{\texttt{high}}$ are about 1.1%, 1.6%, 3.7%, and 3.1% respectively, much smaller than 10%.

In this data-driven background scenario, the exclusion power of all machine-learning-based regions extends to a much greater area in the gap with the same dataset. The improvement for $\texttt{SR}_{20}$ is particularly marked. The exclusion begins to overlap with the "soft 2L" analysis [6], and has sensitivity to smuon explanations of the $(g-2)_\mu$ anomaly [25, 32, 41, 42] as shown in Ref. [184].

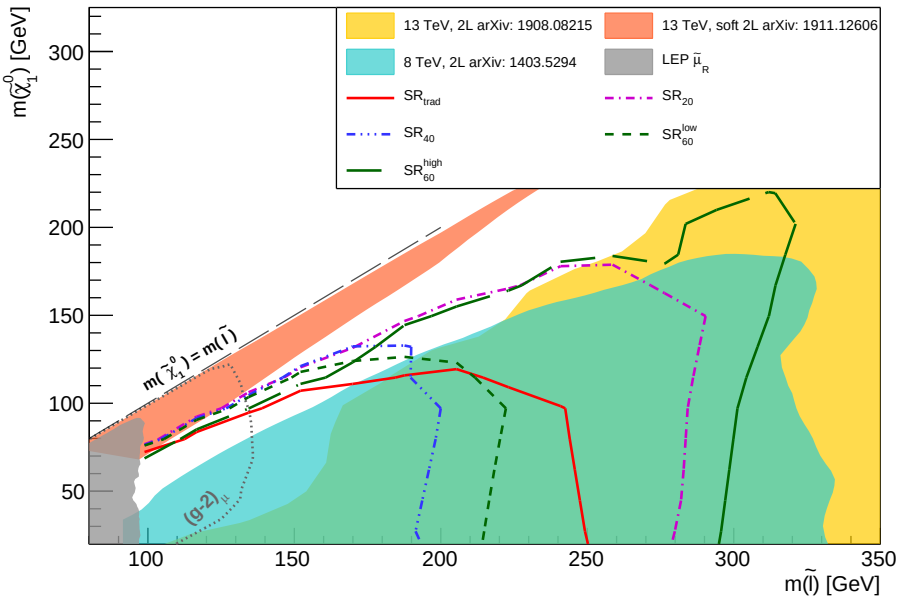

Figure 6.24: Exclusion limits computed from the signal regions are compared to previous ATLAS [5, 6, 173, 174] and LEP limits [43]. The model assumes four sleptons $\tilde{\ell} \in \{\tilde{e}_L, \tilde{e}_R, \tilde{\mu}_L, \tilde{\mu}_R\}$ of equal mass. Shown also is the parameter space favoured by $(g-2)_\mu$ as computed in Ref. [184]. For the expected limits, exclusion is defined as regions where $Z < 1.64$, and a $\sqrt{N_{\text{bkg}}}$ uncertainty was assumed. Flavour-symmetric backgrounds were estimated by a data-driven method, while all other backgrounds were taken from Geant MC.

Realistically, the dominant uncertainties for this analysis would be the the statistical uncertainty of the data-driven symmetric background estimate (which is roughly $1/\sqrt{N_{\text{bkg}}}$), and the systematic uncertainty of the machine-learning classifier (which requires further study). Uncertainties on the cross-section of SM backgrounds are likely to have a small effect as the dominant backgrounds are estimated by data. Object reconstruction uncertainties are also likely to be small because the main objects in this analysis, electrons and muons, are reconstructed with small uncertainties by ATLAS. The final exclusion curves could be optimistically expected to lie in between those presented in Figures 6.20 and 6.24.

Measuring sparticle properties It is interesting to note that $\texttt{SR}_{20}$ has about 85 times the number of events than `SR-trad`. It may be possible to take advantage of

these large event yields to perform some measurement of the properties of new particles, if they are found. For example, the variable $\theta^*_{\ell\ell}$ is sensitive to slepton spin [176]. To make this measurement, one would have to consider how the variable behaves after applying requirements on the classifier score.

6.9 Conclusion

This chapter presented a proposal for a machine-learning-based analysis to target a gap in ATLAS sensitivity to direct slepton production and decay. It was shown that, with a data-driven flavour-symmetric estimate, such an analysis is more powerful than one defined by traditional means given the same dataset, and it has the potential to be sensitive to almost the whole region in the model that is preferred by the $(g-2)_\mu$ result of Ref. [32] in the scenario where $m(\tilde{e}_L) = m(\tilde{e}_R) = m(\tilde{\mu}_L) = m(\tilde{\mu}_R)$. Moreover, the machine-learning signal regions, having O(10-100) more events than a traditionally-defined signal region, are more suited for the statistical measurement of new particle properties.

7
Conclusions

This thesis began by asking the big questions: Where did we come from? Why are we here? How did the universe come to be? Why is the universe the way it is? Now it concludes having made important but modest contributions to their answers.

The fundamental constituents of the universe as we know it are described by the Standard Model of Particle Physics. This model could be extended by supersymmetry, which has attractive features, including a solution to an instability inherent to the Standard Model and dark matter candidates. The LHC and the ATLAS experiment were used to search for deviations from the Standard Model and evidence for supersymmetry. None were found in the work described in this thesis.

Chapter 4 discussed the $E_{\mathrm{T}}^{\mathrm{miss}}$ trigger, a key system to the ATLAS Standard Model and beyond-the-Standard Model physics programs. An evaluation was presented of the trigger's performance under the challenging data-taking conditions between the years 2015 and 2018. Its excellent performance is owed to the introduction of new algorithms. Preparing the $E_{\mathrm{T}}^{\mathrm{miss}}$ trigger for future runs was also discussed: a much-needed software upgrade was described, and efforts to develop a new $E_{\mathrm{T}}^{\mathrm{miss}}$ trigger algorithm for future ATLAS runs were detailed.

Chapter 5 presented a search for new physics in events with four or more leptons. Through the optimisation efforts of the author, and in collaboration with fellow analysers, the exclusion reach of the analysis to various supersymmetric models was extended by between 150 and 250 GeV.

Chapter 6 proposed a machine-learning strategy to look for supersymmetry in events with two leptons and $E_{\mathrm{T}}^{\mathrm{miss}}$. This strategy fills a glaring gap in the ATLAS physics strategy, in which could reside a possible solution to the $(g-2)_{\mu}$ anomaly. This machine-learning-based approach was shown to be competitive with a traditional cuts-based approach in terms of exclusion power, but its signal regions would potentially have 10 to 100 times larger event yields, which would be beneficial for the measurement of the properties, such as spin, of new particles, if they exist.

As this thesis is submitted, the Large Hadron Collider and ATLAS are preparing for a new data-taking run beginning 2022, and ATLAS is still analysing the treasure trove of data it has collected to date. There are still exciting times ahead for particle physics. We look forward to getting ever closer to finding the answers to the big questions.

Bibliography

[1] ATLAS Collaboration, *Performance of the missing transverse momentum triggers for the ATLAS detector during Run-2 data taking*, JHEP **08** (2020) 080, arXiv: 2005.09554 [hep-ex] (cit. on pp. vi, 42–44, 49, 51–53, 64).

[2] ATLAS Collaboration, *Search for supersymmetry in events with four or more leptons in* $139\,fb^{-1}$ $\sqrt{s} = 13$ *TeV pp collisions with the ATLAS detector*, ATLAS-CONF-2020-040, 2020, URL: https://cds.cern.ch/record/2727861 (cit. on pp. vii, 70, 84).

[3] G. E. Gallardo, *Looking for SUSY in events with 4+ leptons at the ATLAS experiment*, 2020, URL: https://cds.cern.ch/record/2741131 (cit. on pp. vii, 70).

[4] ATLAS Collaboration, *Search for supersymmetry in events with four or more charged leptons in* $139\,fb^{-1}$ *of* $\sqrt{s} = 13$ *TeV pp collisions with the ATLAS detector*, (2021), submitted to the *Journal of High Energy Physics*, arXiv: 2103.11684, URL: http://arxiv.org/abs/2103.11684 (cit. on pp. vii, 70, 84, 97, 105, 108–111, 115, 116).

[5] ATLAS Collaboration, *Search for electroweak production of charginos and sleptons decaying into final states with two leptons and missing transverse momentum in* $\sqrt{s} = 13$ *TeV pp collisions using the ATLAS detector*, Eur. Phys. J. C **80** (2020) 123, arXiv: 1908.08215 [hep-ex] (cit. on pp. vii, 119, 122, 160, 165).

[6] ATLAS Collaboration, *Searches for electroweak production of supersymmetric particles with compressed mass spectra in* $\sqrt{s} = 13$ *TeV pp collisions with the ATLAS detector*, Phys. Rev. D **101** (2020) 052005, arXiv: 1911.12606 [hep-ex] (cit. on pp. vii, 42, 119, 122, 147, 160, 164, 165).

[7] ATLAS Collaboration, *ATLAS Simple Analysis tools*, URL: https://gitlab.cern.ch/atlas-sa (cit. on pp. viii, 126).

[8] M. Thomson, *Modern particle physics*, Cambridge University Press, 2013 (cit. on pp. 3–5, 14).

[9] S. P. Martin, *A Supersymmetry Primer*, Adv. Ser. Direct. High Energy Phys. **18** (1998) 1, arXiv: hep-ph/9709356 (cit. on pp. 3, 14–20).

[10] S. Weinberg, *The Quantum Theory of Fields*, Cambridge University Press, 1995 (cit. on pp. 4, 5).

[11] *Standard Model Summary Plots March 2021*, tech. rep. ATL-PHYS-PUB-2021-005, CERN, 2021, URL: https://cds.cern.ch/record/2758261 (cit. on p. 6).

[12] J. Liu, "Discovery strategies for dark matter and Higgsinos at the LHC", PhD thesis: University of Oxford, 2019, URL: https://ora.ox.ac.uk/objects/uuid:28e0016b-81b7-4f51-a065-22c743f301e4 (cit. on p. 5).

[13] D. Griffiths, *Introduction to Elementary Particles (2nd Edition)*, Wiley, 2008, ISBN: 9783527406012 (cit. on p. 5).

[14] S. F. Novaes, *Standard Model: An Introduction*, (2000), arXiv: 0001283 [hep-ph] (cit. on pp. 5, 12).

[15] A. Purcell, *Go on a particle quest at the first CERN webfest. Le premier webfest du CERN se lance à la conquête des particules*, (2012) 10, URL: https://cds.cern.ch/record/1473657 (cit. on p. 7).

[16] C. Rovelli, "Notes for a brief history of quantum gravity", *9th Marcel Grossmann Meeting*, July, 2000, arXiv: 0006061v3 [gr-qc] (cit. on p. 7).

[17] C. Rovelli, *Quantum Gravity*, Cambridge University Press, 2004 (cit. on p. 7).

[18] P. W. Higgs, *Broken symmetries, massless particlees and gauge fields*, Physics Letters **12** (1964) 132, ISSN: 00319163 (cit. on p. 8).

[19] P. W. Higgs, *Broken symmetries and the masses of gauge bosons*, Physical Review Letters **13** (1964) 508, ISSN: 00319007 (cit. on p. 8).

[20] F. Englert and R. Brout, *Broken symmetry and the mass of gauge vector mesons*, Physical Review Letters **13** (1964) 321, ISSN: 00319007 (cit. on p. 8).

[21] G. S. Guralnik, C. R. Hagen, and T. W. Kibble, *Global conservation laws and massless particles*, Physical Review Letters **13** (1964) 585, ISSN: 00319007 (cit. on p. 8).

[22] C. N. Yang and R. L. Mills, *Conservation of isotopic spin and isotopic gauge invariance*, Physical Review **96** (1954) 191, ISSN: 0031899X (cit. on p. 8).

[23] N. Cabibbo, *Unitary symmetry and leptonic decays*, Physical Review Letters **10** (1963) 531, ISSN: 00319007 (cit. on p. 12).

[24] M. Kobayashi and T. Maskawa, *CP-Violation in the Renormalizable Theory of Weak Interaction*, Progress of Theoretical Physics **49** (1973) 652, ISSN: 0033-068X (cit. on p. 12).

[25] P. Zyla et al., *Review of Particle Physics*, PTEP **2020** (2020) 083C01 (cit. on pp. 12–14, 18, 20, 24, 39, 164).

[26] R. S. Ellis, *Gravitational lensing: A unique probe of dark matter and dark energy*, Philosophical Transactions of the Royal Society A: Mathematical, Physical and Engineering Sciences **368** (2010) 967, ISSN: 1364503X (cit. on p. 13).

[27] D. Clowe et al., *A Direct Empirical Proof of the Existence of Dark Matter*, The Astrophysical Journal **648** (2006) L109, ISSN: 0004-637X, arXiv: 0608407 [astro-ph] (cit. on p. 13).

[28] V. C. Rubin, W. K. Ford, and N. Thonnard, *Rotational properties of 21 SC galaxies with a large range of luminosities and radii, from NGC 4605 (R=4kpc) to UGC 2885 (R=122kpc)*, The Astrophysical Journal **238** (1980) 471 (cit. on p. 13).

[29] F. Iocco, M. Pato, and G. Bertone, *Evidence for dark matter in the inner Milky Way*, Nature Physics **11** (2015) 245, ISSN: 17452481 (cit. on p. 13).

[30] G. Bertone, "Particle dark matter: Observations, models and searches", *Particle Dark Matter: Observations, Models and Searches*, Cambridge University Press, 2010 1, ISBN: 9780511770739 (cit. on p. 13).

[31] M. Lisanti, *Lectures on Dark Matter Physics*, (2017), arXiv: 1603.03797 (cit. on p. 13).

[32] G. W. Bennett et al., *Final report of the E821 muon anomalous magnetic moment measurement at BNL*, Physical Review D - Particles, Fields, Gravitation and Cosmology **73** (2006) 072003, ISSN: 15507998 (cit. on pp. 13, 164, 166).

[33] H. Georgi and S. L. Glashow, *Unity of all elementary-particle forces*, Physical Review Letters **32** (1974) 438, ISSN: 00319007 (cit. on pp. 14, 20).

[34] S. Weinberg, *Quantum Theory of Fields, Volume III: Supersymmetry*, Cambridge university press, 2005 (cit. on p. 15).

[35] M. E. Peskin, *Supersymmetry in Elementary Particle Physics*, (2008) 75, arXiv: 0801.1928, URL: http://arxiv.org/abs/0801.1928 (cit. on pp. 15, 19).

[36] ATLAS Collaboration, *Combined measurements of Higgs boson production and decay using up to* $80\,fb^{-1}$ *of proton–proton collision data at* $\sqrt{s} = 13\,TeV$ *collected with the ATLAS experiment*, Phys. Rev. D **101** (2020) 012002, arXiv: 1909.02845 [hep-ex] (cit. on p. 16).

[37] CMS Collaboration, *Combined measurements of Higgs boson couplings in proton–proton collisions at* $\sqrt{s} = 13\,TeV$, Eur. Phys. J. C **79** (2019) 421, arXiv: 1809.10733 [hep-ex] (cit. on p. 16).

[38] P. Meade, N. Seiberg, and D. Shih, *General gauge mediation*, Progress of Theoretical Physics Supplement (2009) 143, ISSN: 13474081, arXiv: 0801.3278 (cit. on pp. 17, 70).

[39] S. Dimopoulos, S. Raby, and F. Wilczek, *Supersymmetry and the scale of unification*, Phys. Rev. D **24** (1981) 1681 (cit. on p. 20).

[40] S. Dimopoulos and H. Georgi, *Softly broken supersymmetry and SU(5)*, Nucl. Phys. B **193** (1981) 150 (cit. on p. 20).

[41] A. Czamecki and W. J. Marciano, *Muon anomalous magnetic moment: A harbinger for "new physics"*, Physical Review D **64** (2001) 013014, ISSN: 05562821, arXiv: 0102122 [hep-ph] (cit. on pp. 20, 164).

[42] M. A. Ajaib, B. Dutta, T. Ghosh, I. Gogoladze, and Q. Shafi, *Neutralinos and sleptons at the LHC in light of muon* $(g-2)_\mu$, Physical Review D **92** (2015) 075033, ISSN: 1550-7998, arXiv: arXiv:1505.05896v3 (cit. on pp. 20, 119, 164).

[43] *SUSY March 2021 Summary Plot Update*, tech. rep. ATL-PHYS-PUB-2021-007, CERN, 2021, URL: https://cds.cern.ch/record/2758782 (cit. on pp. 21, 117, 119, 160, 165).

[44] ATLAS Collaboration, *Summary of the ATLAS experiment's sensitivity to supersymmetry after LHC Run 1 — interpreted in the phenomenological MSSM*, JHEP **10** (2015) 134, arXiv: 1508.06608 [hep-ex] (cit. on p. 21).

[45] ATLAS Collaboration, *Dark matter interpretations of ATLAS searches for the electroweak production of supersymmetric particles in* $\sqrt{s} = 8$ *TeV proton–proton collisions*, JHEP **09** (2016) 175, arXiv: 1608.00872 [hep-ex] (cit. on p. 21).

[46] H. Geiger and E. Marsden, *LXI. The laws of deflexion of a particles through large angles*, The London, Edinburgh, and Dublin Philosophical Magazine and Journal of Science **25** (1913) 604, ISSN: 1941-5982 (cit. on p. 23).

[47] D. Akerib et al., *The LUX-ZEPLIN (LZ) experiment*, Nuclear Instruments and Methods in Physics Research Section A: Accelerators, Spectrometers, Detectors and Associated Equipment **953** (2020) 163047, ISSN: 0168-9002 (cit. on p. 23).

[48] M. Aartsen et al., *The IceCube Neutrino Observatory: instrumentation and online systems*, Journal of Instrumentation **12** (2017) P03012 (cit. on p. 23).

[49] R. Aβmann, M. Lamont, and S. Myers, *A brief history of the LEP collider*, Nuclear Physics B - Proceedings Supplements **109** (2002) 17, ISSN: 09205632 (cit. on p. 23).

[50] W. Venus, "A LEP summary", ed. by D. Horváth, P. Lévai, and A. Patkós, vol. HEP2001, 2001 284 (cit. on p. 24).

[51] D0 Collaboration, *Observation of the top quark*, Physical Review Letters **74** (1995) 2632, ISSN: 00319007, arXiv: 9503003 [hep-ex] (cit. on p. 24).

[52] CDF Collaboration, *Observation of top quark production in* $\bar{p}p$ *collisions with the collider detector at fermilab*, Physical Review Letters **74** (1995) 2626, ISSN: 00319007, arXiv: 9503002 [hep-ex] (cit. on p. 24).

[53] C. Service graphique, *Overall view of the LHC*, URL: https://cds.cern.ch/images/OPEN-PHO-CHART-2014-006-1 (cit. on p. 25).

[54] Guinness World Records, *Largest machine*, URL: https://www.guinnessworldrecords.com/world-records/103591-largest-machine (visited on 02/04/2021) (cit. on p. 24).

[55] L. Evans and P. Bryant, *LHC Machine*, Journal of Instrumentation **3** (2008) S08001, ISSN: 17480221 (cit. on p. 25).

[56] R. Steerenberg et al., "Operation and performance of the CERN Large Hadron Collider during proton Run 2", *10th International Particle Accelerator Conference*, 2019 MOPMP031 (cit. on pp. 25, 26).

[57] ALICE Collaboration, *The ALICE experiment at the CERN LHC*, Journal of Instrumentation **3** (2008) S08002, ISSN: 17480221 (cit. on p. 25).

[58] LHCb Collaboration, *The LHCb detector at the LHC*, Journal of Instrumentation **3** (2008) S08005, ISSN: 17480221 (cit. on p. 25).

[59] CMS Collaboration, *The CMS experiment at the CERN LHC*, JINST **3** (2008) S08004 (cit. on p. 25).

[60] ATLAS Collaboration, *ATLAS data quality operations and performance for 2015–2018 data-taking*, JINST **15** (2020) P04003, arXiv: 1911.04632 [physics.ins-det] (cit. on p. 26).

[61] ATLAS Collaboration, *Luminosity determination in pp collisions at* $\sqrt{s} = 13$ *TeV using the ATLAS detector at the LHC*, ATLAS-CONF-2019-021, 2019, URL: https://cds.cern.ch/record/2677054 (cit. on p. 26).

[62] ATLAS Collaboration, *ATLAS Stand-Alone Event Displays*, URL: https://twiki.cern.ch/twiki/bin/view/AtlasPublic/EventDisplayStandAlone#2012_Z_mu_mu_event_with_high_pil (visited on 02/04/2021) (cit. on p. 27).

[63] J. Pequenao, *Computer generated image of the whole ATLAS detector*, URL: https://cds.cern.ch/record/1095924 (cit. on p. 28).

[64] ATLAS Collaboration, *The ATLAS experiment at the CERN large hadron collider*, J. Instrum. **3** (2008) S08003, ISSN: 17480221, URL: https://iopscience.iop.org/article/10.1088/1748-0221/3/08/S08003 (cit. on pp. 28, 30–35).

[65] T. S. Virdee, *Physics requirements for the design of the ATLAS and CMS experiments at the Large Hadron Collider*, Philos. Trans. R. Soc. A Math. Phys. Eng. Sci. **370** (2012) 876, ISSN: 1364503X (cit. on p. 30).

[66] P. Pequenao J; Schaffner, *How ATLAS detects particles: diagram of particle paths in the detector*, URL: https://cds.cern.ch/record/1505342 (cit. on p. 30).

[67] J. Stirling, *Parton luminosity and cross section plots*, The plot concerned is: Standard Model cross sections as a function of collider energy, with 125 GeV Higgs, URL: http://www.hep.ph.ic.ac.uk/~wstirlin/plots/plots.html (cit. on p. 29).

[68] ATLAS Collaboration, *Alignment of the ATLAS Inner Detector in Run-2*, Eur. Phys. J. C **80** (2020) 1194, arXiv: 2007.07624 [hep-ex] (cit. on p. 31).

[69] ATLAS Collaboration, *Performance of the ATLAS Transition Radiation Tracker in Run 1 of the LHC: tracker properties*, JINST **12** (2017) P05002, arXiv: 1702.06473 [hep-ex] (cit. on p. 32).

[70] B. Mindur, *ATLAS Transition Radiation Tracker (TRT): Straw tubes for tracking and particle identification at the Large Hadron Collider*, Nuclear Instruments and Methods in Physics Research, Section A: Accelerators, Spectrometers, Detectors and Associated Equipment **845** (2017) 257, ISSN: 01689002 (cit. on p. 32).

[71] X. Artru, G. B. Yodh, and G. Mennessier, *Practical theory of the multilayered transition radiation detector*, Phys. Rev. D **12** (5 1975) 1289 (cit. on p. 32).

[72] J. Pequenao, *Computer Generated image of the ATLAS calorimeter*, URL: https://cds.cern.ch/record/1095927 (cit. on p. 32).

[73] ATLAS Collaboration, *Topological cell clustering in the ATLAS calorimeters and its performance in LHC Run 1*, Eur. Phys. J. C **77** (2017) 490, arXiv: 1603.02934 [hep-ex] (cit. on pp. 33, 37, 44, 45).

[74] J. Pequenao, *Computer generated image of the ATLAS Muons subsystem*, URL: https://cds.cern.ch/record/1095929 (cit. on p. 34).

[75] ATLAS Collaboration, *Muon reconstruction and identification efficiency in ATLAS using the full Run 2 pp collision data set at* $\sqrt{s} = 13$ *TeV*, ATLAS-CONF-2020-030, 2020, URL: https://cds.cern.ch/record/2725736 (cit. on pp. 35, 38, 49, 80, 82, 127, 128).

[76] ATLAS Collaboration, *Muon reconstruction performance of the ATLAS detector in proton–proton collision data at* $\sqrt{s} = 13$ *TeV*, Eur. Phys. J. C **76** (2016) 292, arXiv: 1603.05598 [hep-ex] (cit. on p. 35).

[77] ATLAS Collaboration, *Performance of the ATLAS trigger system in 2015*, Eur. Phys. J. C **77** (2017) 317, arXiv: 1611.09661 [hep-ex] (cit. on pp. 35, 66).

[78] ATLAS Collaboration, *Operation of the ATLAS trigger system in Run 2*, Journal of Instrumentation **15** (2020), ISSN: 17480221, arXiv: 2007.12539 (cit. on pp. 35, 43).

[79] ATLAS Collaboration, *Performance of electron and photon triggers in ATLAS during LHC Run 2*, Eur. Phys. J. C **80** (2020) 47, arXiv: 1909.00761 [hep-ex] (cit. on pp. 36, 78).

[80] ATLAS Collaboration, *Performance of the ATLAS muon triggers in Run 2*, JINST **15** (2020) P09015, arXiv: 2004.13447 [hep-ex] (cit. on pp. 36, 78).

[81] ATLAS Collaboration, *Trigger Operation Public Results*, 2018, URL: https://twiki.cern.ch/twiki/bin/view/AtlasPublic/TriggerOperationPublicResults#2018_pp_at_13_TeV (cit. on p. 36).

[82] ATLAS Collaboration, *Electron reconstruction and identification in the ATLAS experiment using the 2015 and 2016 LHC proton–proton collision data at $\sqrt{s} =$ 13 TeV*, Eur. Phys. J. C **79** (2019) 639, arXiv: 1902.04655 [hep-ex] (cit. on pp. 37, 38, 49, 80, 82, 127, 128).

[83] T. G. Cornelissen et al., "The global $\chi 2$ track fitter in ATLAS", *Journal of Physics: Conference Series*, vol. 119, 3, Institute of Physics Publishing, 2008 032013 (cit. on p. 37).

[84] ATLAS Collaboration, *Vertex Reconstruction Performance of the ATLAS Detector at $\sqrt{s} = 13$ TeV*, ATL-PHYS-PUB-2015-026, 2015, URL: https://cds.cern.ch/record/2037717 (cit. on p. 37).

[85] ATLAS Collaboration, *Jet reconstruction and performance using particle flow with the ATLAS Detector*, Eur. Phys. J. C **77** (2017) 466, arXiv: 1703.10485 [hep-ex] (cit. on pp. 37, 39).

[86] ATLAS Collaboration, *Measurement of the photon identification efficiencies with the ATLAS detector using LHC Run 2 data collected in 2015 and 2016*, Eur. Phys. J. C **79** (2019) 205, arXiv: 1810.05087 [hep-ex] (cit. on p. 38).

[87] M. Cacciari, G. P. Salam, and G. Soyez, *The anti-k_t jet clustering algorithm*, JHEP **04** (2008) 063, arXiv: 0802.1189 [hep-ph] (cit. on pp. 39, 44, 50, 80, 127).

[88] ATLAS Collaboration, *Jet energy scale and resolution measured in proton–proton collisions at $\sqrt{s} = 13$ TeV with the ATLAS detector*, (2020), arXiv: 2007.02645 [hep-ex] (cit. on pp. 39, 45, 64).

[89] ATLAS Collaboration, *Reconstruction, Energy Calibration, and Identification of Hadronically Decaying Tau Leptons in the ATLAS Experiment for Run-2 of the LHC*, ATL-PHYS-PUB-2015-045, 2015, URL: https://cds.cern.ch/record/2064383 (cit. on p. 39).

[90] ATLAS Collaboration, *Identification of hadronic tau lepton decays using neural networks in the ATLAS experiment*, ATL-PHYS-PUB-2019-033, 2019, URL: https://cds.cern.ch/record/2688062 (cit. on pp. 39, 81–83).

[91] ATLAS Collaboration, *Performance of missing transverse momentum reconstruction with the ATLAS detector using proton–proton collisions at $\sqrt{s} = 13$ TeV*, Eur. Phys. J. C **78** (2018) 903, arXiv: 1802.08168 [hep-ex] (cit. on p. 40).

[92] ATLAS Collaboration, *Search for chargino and neutralino production in final states with a Higgs boson and missing transverse momentum at $\sqrt{s} = 13$ TeV with the ATLAS detector*, Phys. Rev. D **100** (2019) 012006, arXiv: 1812.09432 [hep-ex] (cit. on p. 42).

[93] ATLAS Collaboration, *Search for pair production of up-type vector-like quarks and for four-top-quark events in final states with multiple b-jets with the ATLAS detector*, JHEP **07** (2018) 089, arXiv: 1803.09678 [hep-ex] (cit. on p. 42).

[94] ATLAS Collaboration, *Search for a scalar partner of the top quark in the all-hadronic $t\bar{t}$ plus missing transverse momentum final state at $\sqrt{s} = 13$ TeV with the ATLAS detector*, Eur. Phys. J. C **80** (2020) 737, arXiv: 2004.14060 [hep-ex] (cit. on p. 42).

[95] ATLAS Collaboration, *Search for dark matter at $\sqrt{s} = 13$ TeV in final states containing an energetic photon and large missing transverse momentum with the ATLAS detector*, Eur. Phys. J. C **77** (2017) 393, arXiv: 1704.03848 [hep-ex] (cit. on p. 42).

[96] ATLAS Collaboration, *Measurements of WH and ZH production in the $H \to b\bar{b}$ decay channel in pp collisions at 13 TeV with the ATLAS detector*, (2020), arXiv: 2007.02873 [hep-ex] (cit. on p. 42).

[97] ATLAS Collaboration, *Search for invisible Higgs boson decays in vector boson fusion at $\sqrt{s} = 13$ TeV with the ATLAS detector*, Phys. Lett. B **793** (2019) 499, arXiv: 1809.06682 [hep-ex] (cit. on p. 42).

[98] J. Burr, "Searches for new physics involving massive invisible particles", PhD thesis, 2018, URL: https://cds.cern.ch/record/2648475 (cit. on pp. 43, 51, 53, 58).

[99] M. Cacciari, G. P. Salam, and G. Soyez, *FastJet user manual*, Eur. Phys. J. C **72** (2012) 1896, arXiv: 1111.6097 [hep-ph] (cit. on p. 44).

[100] ATLAS Collaboration, *Performance of pile-up mitigation techniques for jets in pp collisions at $\sqrt{s} = 8$ TeV using the ATLAS detector*, Eur. Phys. J. C **76** (2016) 581, arXiv: 1510.03823 [hep-ex] (cit. on p. 50).

[101] R. Bielski and ATLAS Collaboration, *ATLAS High Level Trigger within the multi-threaded software framework AthenaMT*, tech. rep. ATL-DAQ-PROC-2019-004, CERN, 2019, URL: https://cds.cern.ch/record/2674286 (cit. on p. 60).

[102] ATLAS Collaboration, *METMenuSequences.md*, Documentation of $E_{\mathrm{T}}^{\mathrm{miss}}$ trigger software, originally prepared by G. Gallardo, updated by various members of ATLAS., URL: https://gitlab.cern.ch/atlas/athena/-/blob/master/Trigger/TrigAlgorithms/TrigEFMissingET/doc/METMenuSequences.md (cit. on p. 61).

[103] ATLAS Collaboration, *Measurement of the four-lepton invariant mass spectrum in 13 TeV proton–proton collisions with the ATLAS detector*, JHEP **04** (2019) 048, arXiv: 1902.05892 [hep-ex] (cit. on p. 69).

[104] ATLAS Collaboration, *Search for Higgs boson pair production in the $WW^{(*)}WW^{(*)}$ decay channel using ATLAS data recorded at $\sqrt{s} = 13$ TeV*, JHEP **05** (2019) 124, arXiv: 1811.11028 [hep-ex] (cit. on p. 69).

[105] ATLAS Collaboration, *Measurements of the Higgs boson inclusive and differential fiducial cross sections in the 4ℓ decay channel at $\sqrt{s} = 13$ TeV*, Eur. Phys. J. C **80** (2020) 942, arXiv: 2004.03969 [hep-ex] (cit. on p. 69).

[106] ATLAS Collaboration, *Higgs boson production cross-section measurements and their EFT interpretation in the 4ℓ decay channel at $\sqrt{s} = 13$ TeV with the ATLAS detector*, Eur. Phys. J. C **80** (2020) 957, arXiv: 2004.03447 [hep-ex] (cit. on p. 69).

[107] CMS Collaboration, *Evidence for electroweak production of four charged leptons and two jets in proton–proton collisions at $\sqrt{s} = 13$ TeV*, Phys. Lett. B **812** (2021) 135992, arXiv: 2008.07013 [hep-ex] (cit. on p. 69).

[108] CMS Collaboration, *Observation of the production of three massive gauge bosons at $\sqrt{s} = 13$ TeV*, Phys. Rev. Lett. **125** (2020) 151802, arXiv: 2006.11191 [hep-ex] (cit. on pp. 69, 94).

[109] CMS Collaboration, *Search for a heavy pseudoscalar Higgs boson decaying into a 125 GeV Higgs boson and a Z boson in final states with two tau and two light leptons at $\sqrt{s} = 13$ TeV*, JHEP **03** (2020) 065, arXiv: 1910.11634 [hep-ex] (cit. on p. 69).

[110] CMS Collaboration, *Search for vectorlike leptons in multilepton final states in proton–proton collisions at $\sqrt{s} = 13$ TeV*, Phys. Rev. D **100** (2019) 052003, arXiv: 1905.10853 [hep-ex] (cit. on p. 69).

[111] CMS Collaboration, *Measurements of the Higgs boson width and anomalous HVV couplings from on-shell and off-shell production in the four-lepton final state*, Phys. Rev. D **99** (2019) 112003, arXiv: 1901.00174 [hep-ex] (cit. on p. 69).

[112] ATLAS Collaboration, *Search for R-parity-violating supersymmetry in events with four or more leptons in $\sqrt{s} = 7$ TeV pp collisions with the ATLAS detector*, JHEP **12** (2012) 124, arXiv: 1210.4457 [hep-ex] (cit. on p. 70).

[113] ATLAS Collaboration, *Search for supersymmetry in events with four or more leptons in $\sqrt{s} = 8$ TeV pp collisions with the ATLAS detector*, Phys. Rev. D **90** (2014) 052001, arXiv: 1405.5086 [hep-ex] (cit. on p. 70).

[114] ATLAS Collaboration, *Search for supersymmetry in events with four or more leptons in $\sqrt{s} = 13$ TeV pp collisions with ATLAS*, Phys. Rev. D **98** (2018) 032009, arXiv: 1804.03602 [hep-ex] (cit. on pp. 70, 74, 76, 78, 83, 84, 92, 93, 97, 107, 114, 116).

[115] CMS Collaboration, *Search for physics beyond the standard model using multilepton signatures in pp collisions at $\sqrt{s} = 7$ TeV*, Phys. Lett. B **704** (2011) 411, arXiv: 1106.0933 [hep-ex] (cit. on p. 70).

[116] CMS Collaboration, *Search for anomalous production of multilepton events in pp collisions at $\sqrt{s} = 7$ TeV*, JHEP **06** (2012) 169, arXiv: 1204.5341 [hep-ex] (cit. on p. 70).

[117] CMS Collaboration, *Search for Top Squarks in R-Parity-Violating Supersymmetry Using Three or More Leptons and b-Tagged Jets*, Phys. Rev. Lett. **111** (2013) 221801, arXiv: 1306.6643 [hep-ex] (cit. on p. 70).

[118] CMS Collaboration, *Search for anomalous production of events with three or more leptons in pp collisions at $\sqrt{s} = 8$ TeV*, Phys. Rev. D **90** (2014) 032006, arXiv: 1404.5801 [hep-ex] (cit. on p. 70).

[119] J. J. Junggeburth, "Searches for Supersymmetry in multi-leptonic and τ pair final states with the ATLAS experiment at the LHC at $\sqrt{s} = 13$ TeV", PhD thesis: Technische Universität München, 2020, URL: https://cds.cern.ch/record/2729360 (cit. on pp. 70, 97).

[120] J. Alwall, M.-P. Le, M. Lisanti, and J. G. Wacker, *Searching for directly decaying gluinos at the Tevatron*, Phys. Lett. B **666** (2008) 34, arXiv: 0803.0019 [hep-ph] (cit. on p. 70).

[121] J. Alwall, P. Schuster, and N. Toro, *Simplified models for a first characterization of new physics at the LHC*, Phys. Rev. D **79** (2009) 075020, arXiv: 0810.3921 [hep-ph] (cit. on p. 70).

[122] D. Alves et al., *Simplified models for LHC new physics searches*, J. Phys. G **39** (2012) 105005, arXiv: 1105.2838 [hep-ph] (cit. on p. 70).

[123] ATLAS Collaboration, *Search for pair production of higgsinos in final states with at least three b-tagged jets in $\sqrt{s} = 13$ TeV pp collisions using the ATLAS detector*, Phys. Rev. D **98** (2018) 092002, arXiv: 1806.04030 [hep-ex] (cit. on pp. 71, 114, 115, 117).

[124] ATLAS Collaboration, *Search for direct production of electroweakinos in final states with missing transverse momentum and a Higgs boson decaying into photons in pp collisions at $\sqrt{s} = 13$ TeV with the ATLAS detector*, JHEP **10** (2020) 005, arXiv: 2004.10894 [hep-ex] (cit. on p. 71).

[125] CMS Collaboration, *Search for supersymmetry using Higgs boson to diphoton decays at $\sqrt{s} = 13$ TeV*, JHEP **11** (2019) 109, arXiv: 1908.08500 [hep-ex] (cit. on p. 71).

[126] ATLAS Collaboration, *Formulae for Estimating Significance*, ATL-PHYS-PUB-2020-025, 2020, URL: https://cds.cern.ch/record/2736148 (cit. on pp. 76, 122).

[127] ATLAS Collaboration, *Observation and measurement of Higgs boson decays to WW^* with the ATLAS detector*, Phys. Rev. D **92** (2015) 012006, arXiv: 1412.2641 [hep-ex] (cit. on pp. 78, 93, 97).

[128] S. Agostinelli et al., GEANT4 – *a simulation toolkit*, Nucl. Instrum. Meth. A **506** (2003) 250 (cit. on pp. 79, 126).

[129] E. Bothmann et al., *Event generation with Sherpa 2.2*, SciPost Phys. **7** (2019) 034, arXiv: 1905.09127 [hep-ph] (cit. on pp. 80, 126).

[130] ATLAS Collaboration, *Multi-boson simulation for* 13 *TeV ATLAS analyses*, ATL-PHYS-PUB-2016-002, 2016, URL: https://cds.cern.ch/record/2119986 (cit. on pp. 80, 106, 126).

[131] R. D. Ball et al., *Parton distributions for the LHC run II*, JHEP **04** (2015) 040, arXiv: 1410.8849 [hep-ph] (cit. on pp. 80, 126).

[132] P. Nason, *A new method for combining NLO QCD with shower Monte Carlo algorithms*, JHEP **11** (2004) 040, arXiv: hep-ph/0409146 (cit. on pp. 80, 126).

[133] S. Frixione, P. Nason, and C. Oleari, *Matching NLO QCD computations with parton shower simulations: the POWHEG method*, JHEP **11** (2007) 070, arXiv: 0709.2092 [hep-ph] (cit. on pp. 80, 126).

[134] S. Alioli, P. Nason, C. Oleari, and E. Re, *A general framework for implementing NLO calculations in shower Monte Carlo programs: the POWHEG BOX*, JHEP **06** (2010) 043, arXiv: 1002.2581 [hep-ph] (cit. on pp. 80, 126).

[135] T. Sjöstrand et al., *An introduction to PYTHIA 8.2*, Comput. Phys. Commun. **191** (2015) 159, arXiv: 1410.3012 [hep-ph] (cit. on pp. 80, 126).

[136] D. de Florian et al., *Handbook of LHC Higgs Cross Sections: 4. Deciphering the Nature of the Higgs Sector*, (2016), arXiv: 1610.07922 [hep-ph] (cit. on p. 80).

[137] C. Anastasiou et al., *High precision determination of the gluon fusion Higgs boson cross-section at the LHC*, JHEP **05** (2016) 058, arXiv: 1602.00695 [hep-ph] (cit. on p. 80).

[138] C. Anastasiou, C. Duhr, F. Dulat, F. Herzog, and B. Mistlberger, *Higgs Boson Gluon-Fusion Production in QCD at Three Loops*, Phys. Rev. Lett. **114** (2015) 212001, arXiv: 1503.06056 [hep-ph] (cit. on p. 80).

[139] F. Dulat, A. Lazopoulos, and B. Mistlberger, *iHixs 2 – Inclusive Higgs cross sections*, Comput. Phys. Commun. **233** (2018) 243, arXiv: 1802.00827 [hep-ph] (cit. on p. 80).

[140] U. Aglietti, R. Bonciani, G. Degrassi, and A. Vicini, *Two-loop light fermion contribution to Higgs production and decays*, Phys. Lett. B **595** (2004) 432, arXiv: hep-ph/0404071 (cit. on p. 80).

[141] S. Actis, G. Passarino, C. Sturm, and S. Uccirati, *NLO electroweak corrections to Higgs boson production at hadron colliders*, Phys. Lett. B **670** (2008) 12, arXiv: 0809.1301 [hep-ph] (cit. on p. 80).

[142] M. Bonetti, K. Melnikov, and L. Tancredi, *Higher order corrections to mixed QCD-EW contributions to Higgs boson production in gluon fusion*, Phys. Rev. D **97** (2018) 056017, arXiv: 1801.10403 [hep-ph] (cit. on p. 80), Erratum: Phys. Rev. D **97** (2018) 099906.

[143] ATLAS Collaboration, *Measurement of the Z/γ^* boson transverse momentum distribution in pp collisions at $\sqrt{s} = 7$ TeV with the ATLAS detector*, JHEP **09** (2014) 145, arXiv: 1406.3660 [hep-ex] (cit. on p. 80).

[144] J. Pumplin et al., *New Generation of Parton Distributions with Uncertainties from Global QCD Analysis*, JHEP **07** (2002) 012, arXiv: hep-ph/0201195 (cit. on p. 80).

[145] ATLAS Collaboration, *ATLAS Pythia 8 tunes to 7 TeV data*, ATL-PHYS-PUB-2014-021, 2014, URL: https://cds.cern.ch/record/1966419 (cit. on pp. 80, 126).

[146] R. D. Ball et al., *Parton distributions with LHC data*, Nucl. Phys. B **867** (2013) 244, arXiv: 1207.1303 [hep-ph] (cit. on pp. 80, 126).

[147] J. Alwall et al., *The automated computation of tree-level and next-to-leading order differential cross sections, and their matching to parton shower simulations*, JHEP **07** (2014) 079, arXiv: 1405.0301 [hep-ph] (cit. on pp. 80, 126).

[148] ATLAS Collaboration, *Modelling of the $t\bar{t}H$ and $t\bar{t}V(V = W, Z)$ processes for $\sqrt{s} = 13$ TeV ATLAS analyses*, ATL-PHYS-PUB-2016-005, 2016, URL: https://cds.cern.ch/record/2120826 (cit. on p. 80).

[149] M. Beneke, P. Falgari, S. Klein, and C. Schwinn, *Hadronic top-quark pair production with NNLL threshold resummation*, Nucl. Phys. B **855** (2012) 695, arXiv: 1109.1536 [hep-ph] (cit. on p. 80).

[150] M. Cacciari, M. Czakon, M. Mangano, A. Mitov, and P. Nason, *Top-pair production at hadron colliders with next-to-next-to-leading logarithmic soft-gluon resummation*, Phys. Lett. B **710** (2012) 612, arXiv: 1111.5869 [hep-ph] (cit. on p. 80).

[151] P. Bärnreuther, M. Czakon, and A. Mitov, *Percent-Level-Precision Physics at the Tevatron: Next-to-Next-to-Leading Order QCD Corrections to $q\bar{q} \to t\bar{t} + X$*, Phys. Rev. Lett. **109** (2012) 132001, arXiv: 1204.5201 [hep-ph] (cit. on p. 80).

[152] M. Czakon and A. Mitov, *NNLO corrections to top-pair production at hadron colliders: the all-fermionic scattering channels*, JHEP **12** (2012) 054, arXiv: 1207.0236 [hep-ph] (cit. on p. 80).

[153] M. Czakon and A. Mitov, *NNLO corrections to top pair production at hadron colliders: the quark-gluon reaction*, JHEP **01** (2013) 080, arXiv: 1210.6832 [hep-ph] (cit. on p. 80).

[154] M. Czakon, P. Fiedler, and A. Mitov, *Total Top-Quark Pair-Production Cross Section at Hadron Colliders Through $O(\alpha_S^4)$*, Phys. Rev. Lett. **110** (2013) 252004, arXiv: 1303.6254 [hep-ph] (cit. on p. 80).

[155] M. Czakon and A. Mitov, *Top++: A program for the calculation of the top-pair cross-section at hadron colliders*, Comput. Phys. Commun. **185** (2014) 2930, arXiv: 1112.5675 [hep-ph] (cit. on p. 80).

[156] C. Anastasiou, L. J. Dixon, K. Melnikov, and F. Petriello, *High precision QCD at hadron colliders: Electroweak gauge boson rapidity distributions at next-to-next-to leading order*, Phys. Rev. D **69** (2004) 094008, arXiv: hep-ph/0312266 (cit. on p. 80).

[157] W. Beenakker, R. Höpker, M. Spira, and P. Zerwas, *Squark and gluino production at hadron colliders*, Nucl. Phys. B **492** (1997) 51, arXiv: hep-ph/9610490 (cit. on p. 80).

[158] A. Kulesza and L. Motyka, *Threshold Resummation for Squark-Antisquark and Gluino-Pair Production at the LHC*, Phys. Rev. Lett. **102** (2009) 111802, arXiv: 0807.2405 [hep-ph] (cit. on p. 80).

[159] A. Kulesza and L. Motyka, *Soft gluon resummation for the production of gluino-gluino and squark-antisquark pairs at the LHC*, Phys. Rev. D **80** (2009) 095004, arXiv: 0905.4749 [hep-ph] (cit. on p. 80).

[160] W. Beenakker et al., *Soft-gluon resummation for squark and gluino hadroproduction*, JHEP **12** (2009) 041, arXiv: 0909.4418 [hep-ph] (cit. on p. 80).

[161] W. Beenakker et al., *Squark and gluino hadroproduction*, Int. J. Mod. Phys. A **26** (2011) 2637, arXiv: 1105.1110 [hep-ph] (cit. on p. 80).

[162] B. Fuks, M. Klasen, D. R. Lamprea, and M. Rothering, *Gaugino production in proton-proton collisions at a center-of-mass energy of 8 TeV*, JHEP **10** (2012) 081, arXiv: 1207.2159 [hep-ph] (cit. on p. 80).

[163] B. Fuks, M. Klasen, D. R. Lamprea, and M. Rothering, *Precision predictions for electroweak superpartner production at hadron colliders with* RESUMMINO, Eur. Phys. J. C **73** (2013) 2480, arXiv: 1304.0790 [hep-ph] (cit. on p. 80).

[164] B. Fuks, M. Klasen, D. R. Lamprea, and M. Rothering, *Revisiting slepton pair production at the Large Hadron Collider*, JHEP **01** (2014) 168, arXiv: 1310.2621 [hep-ph] (cit. on p. 80).

[165] ATLAS Collaboration, *Selection of jets produced in 13 TeV proton–proton collisions with the ATLAS detector*, ATLAS-CONF-2015-029, 2015, URL: https://cds.cern.ch/record/2037702 (cit. on p. 80).

[166] ATLAS Collaboration, *ATLAS b-jet identification performance and efficiency measurement with $t\bar{t}$ events in pp collisions at $\sqrt{s} = 13$ TeV*, Eur. Phys. J. C **79** (2019) 970, arXiv: 1907.05120 [hep-ex] (cit. on p. 82).

[167] M. Baak et al., *HistFitter software framework for statistical data analysis*, Eur. Phys. J. C **75** (2015) 153, arXiv: 1410.1280 [hep-ex] (cit. on pp. 94, 114).

[168] S. Dittmaier et al., *Handbook of LHC Higgs Cross Sections: 2. Differential Distributions*, (2012), arXiv: 1201.3084 [hep-ph] (cit. on p. 106).

[169] R. D. Cousins, J. T. Linnemann, and J. Tucker, *Evaluation of three methods for calculating statistical significance when incorporating a systematic uncertainty into a test of the background-only hypothesis for a Poisson process*, Nucl. Instrum. Meth. A **595** (2008) 480, arXiv: physics/0702156 [physics.data-an] (cit. on p. 109).

[170] G. Cowan, K. Cranmer, E. Gross, and O. Vitells, *Asymptotic formulae for likelihood-based tests of new physics*, Eur. Phys. J. C **71** (2011) 1554, arXiv: 1007.1727 [physics.data-an] (cit. on p. 114), Erratum: Eur. Phys. J. C **73** (2013) 2501.

[171] A. L. Read, *Presentation of search results: the CL_S technique*, J. Phys. G **28** (2002) 2693 (cit. on p. 114).

[172] N. Aghanim et al., *Planck 2018 results*, Astronomy & Astrophysics **641** (2020) A6, ISSN: 1432-0746, URL: http://dx.doi.org/10.1051/0004-6361/201833910 (cit. on p. 119).

[173] ATLAS Collaboration, *Search for direct stau production in events with two hadronic τ-leptons in $\sqrt{s} = 13$ TeV pp collisions with the ATLAS detector*, Phys. Rev. D **101** (2020) 032009, arXiv: 1911.06660 [hep-ex] (cit. on pp. 119, 160, 165).

[174] ATLAS Collaboration, *Search for direct production of charginos, neutralinos and sleptons in final states with two leptons and missing transverse momentum in pp collisions at $\sqrt{s} = 8$ TeV with the ATLAS detector*, JHEP **05** (2014) 071, arXiv: 1403.5294 [hep-ex] (cit. on pp. 119, 160, 165).

[175] ATLAS Collaboration, *Object-based missing transverse momentum significance in the ATLAS Detector*, ATLAS-CONF-2018-038, 2018, URL: https://cds.cern.ch/record/2630948 (cit. on pp. 122, 123).

[176] A. J. Barr, *Measuring slepton spin at the LHC*, Journal of High Energy Physics **2006** (2006) 042, ISSN: 1029-8479, arXiv: hep-ph/0511115 (cit. on pp. 123, 166).

[177] C. G. Lester and D. J. Summers, *Measuring masses of semi-invisibly decaying particles pair produced at hadron colliders*, Phys. Lett. B **463** (1999) 99, arXiv: hep-ph/9906349 (cit. on p. 123).

[178] A. Barr, C. G. Lester, and P. Stephens, *A variable for measuring masses at hadron colliders when missing energy is expected; m_{T2}: the truth behind the glamour*, J. Phys. G **29** (2003) 2343, arXiv: hep-ph/0304226 (cit. on pp. 123, 125).

[179] ATLAS Collaboration, *Tagging and suppression of pileup jets with the ATLAS detector*, ATLAS-CONF-2014-018, 2014, URL: https://cds.cern.ch/record/1700870 (cit. on p. 128).

[180] G. Ke et al., *LightGBM: A Highly Efficient Gradient Boosting Decision Tree*, NIPS'17 (2017) 3149 (cit. on pp. 131, 133).

[181] A. Hoecker et al., *TMVA - Toolkit for Multivariate Data Analysis*, 2007, arXiv: physics/0703039 [physics.data-an] (cit. on p. 133).

[182] *scipy.stats.ks_2samp – SciPy v1.6.0 Reference Guide*, URL: https://docs.scipy.org/doc/scipy/reference/generated/scipy.stats.ks_2samp.html (cit. on p. 138).

[183] ATLAS Collaboration, *Search for new phenomena in events containing a same-flavour opposite-sign dilepton pair, jets, and large missing transverse momentum in $\sqrt{s} = 13$ TeV pp collisions with the ATLAS detector*, Eur. Phys. J. C **77** (2017) 144, arXiv: 1611.05791 [hep-ex] (cit. on p. 156).

[184] L. Beresford and J. Liu, *Photon collider search strategy for sleptons and dark matter at the LHC*, (2018), arXiv: 1811.06465 (cit. on pp. 160, 164, 165).